Conference Proceedings of the Society for Experimental Mechanics Series

Dario Di Maio
Javad Baqersad *Editors*

Rotating Machinery, Optical Methods & Scanning LDV Methods, Volume 6

Proceedings of the 39th IMAC, A Conference and Exposition on Structural Dynamics 2021

SEM

Springer

Conference Proceedings of the Society for Experimental Mechanics Series

Series Editor

Kristin B. Zimmerman, Ph.D.
Society for Experimental Mechanics, Inc.,
Bethel, CT, USA

The Conference Proceedings of the Society for Experimental Mechanics Series presents early findings and case studies from a wide range of fundamental and applied work across the broad range of fields that comprise Experimental Mechanics. Series volumes follow the principle tracks or focus topics featured in each of the Society's two annual conferences: IMAC, A Conference and Exposition on Structural Dynamics, and the Society's Annual Conference & Exposition and will address critical areas of interest to researchers and design engineers working in all areas of Structural Dynamics, Solid Mechanics and Materials Research

More information about this series at http://www.springer.com/series/8922

Dario Di Maio • Javad Baqersad
Editors

Rotating Machinery, Optical Methods & Scanning LDV Methods, Volume 6

Proceedings of the 39th IMAC, A Conference and Exposition on Structural Dynamics 2021

Springer

Editors
Dario Di Maio
MS3
University of Twente
ENSCHEDE, Overijssel, The Netherlands

Javad Baqersad
Kettering University
Flint, MI, USA

ISSN 2191-5644 ISSN 2191-5652 (electronic)
Conference Proceedings of the Society for Experimental Mechanics Series
ISBN 978-3-030-76334-3 ISBN 978-3-030-76335-0 (eBook)
https://doi.org/10.1007/978-3-030-76335-0

© The Society for Experimental Mechanics, Inc. 2022
This work is subject to copyright. All rights are solely and exclusively licensed by the Publisher, whether the whole or part of the material is concerned, specifically the rights of translation, reprinting, reuse of illustrations, recitation, broadcasting, reproduction on microfilms or in any other physical way, and transmission or information storage and retrieval, electronic adaptation, computer software, or by similar or dissimilar methodology now known or hereafter developed.
The use of general descriptive names, registered names, trademarks, service marks, etc. in this publication does not imply, even in the absence of a specific statement, that such names are exempt from the relevant protective laws and regulations and therefore free for general use.
The publisher, the authors, and the editors are safe to assume that the advice and information in this book are believed to be true and accurate at the date of publication. Neither the publisher nor the authors or the editors give a warranty, expressed or implied, with respect to the material contained herein or for any errors or omissions that may have been made. The publisher remains neutral with regard to jurisdictional claims in published maps and institutional affiliations.

This Springer imprint is published by the registered company Springer Nature Switzerland AG
The registered company address is: Gewerbestrasse 11, 6330 Cham, Switzerland

Preface

Rotating Machinery, Optical Methods & Scanning LDV Methods represents one of the nine volumes of technical papers presented at the 39th IMAC, A Conference and Exposition on Structural Dynamics, organized by the Society for Experimental Mechanics and held on February 8–11, 2021. The full proceedings also include volumes on Nonlinear Structures & Systems; Dynamics of Civil Structures; Model Validation and Uncertainty Quantification; Dynamic Substructures; Special Topics in Structural Dynamics & Experimental Techniques; Sensors and Instrumentation, Aircraft/Aerospace, Energy Harvesting & Dynamic Environments Testing; Topics in Modal Analysis & Parameter Identification; and Data Science in Engineering.

Each collection presents early findings from experimental and computational investigations on an important area within structural dynamics.

The organizers would like to thank the authors, presenters, session organizers, and session chairs for their participation in this track.

Flint, MI, USA — Javad Baqersad
Enschede, Overijssel, The Netherlands — D. Di Maio

Contents

Chapter 1
WaveAR: A Real-Time Sensor-Based Augmented Reality Implementation for Operating Deflection Shapes

Daniel Herfert and Kai Henning

Abstract We present WaveAR, the first sensor-based augmented reality system for structural dynamic measurements of operating deflection shapes. WaveAR offers a significant simplification of the configuration effort of vibration sensor measurements by an automatically sensor tracking coupled by an efficient 3D scan generation of the structure. AR markers are used for sensor tracking which are placed on the sensor. This allows the determination of the sensor pose relative to the scanned structure. For this purpose the vibration sensors must be covered with AR markers. This allows a universal easy application also for existing sensor equipment. For 3D scanning and sensor tracking, a low-cost stereo depth camera is used. Because the AR application should be independent from data acquisition hardware, we have implemented a universal HTTP Rest-API interface for data acquisition connection. Through this, it is also supported to use wireless sensors. Based on this configuration, a real-time visualization in the form of an augmented reality application of the operating deflection shapes can be performed under real operating conditions. This enables the user to view the measurement from different perspectives by moving the camera around the object to be examined.

Keywords Augmented reality · Data acquisition · Operating deflection shapes · Sensor pose tracking · 3D scanning

1.1 Introduction

At the current state of technology, the performance of a vibration analysis for construction, evaluation, or dynamic optimization of structures or buildings requires a lot of time and human resources. Especially when using many sensors and complex structures from a geometrical point of view, a large amount of time has to be planned for the whole measuring process. The structural dynamic validation of the measurement, especially the evaluation of the mode or operational deflection shapes, is currently performed after the measurements. Thus, errors within the measurement process can only be detected afterward.

The use of applications for real-time visualization in the form of an augmented reality (AR) representation is an essential point of interaction between the digital and analog worlds in the industrial environment in the age of Industry 4.0. Currently, these systems are used primarily for maintenance tasks, as digital manuals in service and maintenance, in plant and production planning, in training and further education, and in marketing, as well as at exhibitions. In most cases the systems are used as pure visualization and there is no consideration of other sensors. The use of AR systems in combination with other sensors offers an even more realistic interaction between the user and the digital application. The real-time visualization of essential sensor information at the scene of the event and always in relation to the structure under investigation are significant advantages of these systems.

These advantages would also be very useful for the field of structural dynamics within the construction phase of new structures, as well as in the optimization phase of existing structures which would allow a direct interaction with the structure. Thus the vibration response of the structure could be visualized directly during operation. Again, this procedure would significantly reduce the time needed to perform vibration analyses and would also allow direct analyses in real operation of the structure.

In the context of this publication, the AR system was applied to the modal analysis of a car rim and a steel plate. In addition to the results, the significant time savings in carrying out the measurement should be shown.

D. Herfert (✉) · K. Henning
Department of Structural Dynamics/Pattern Recognition, Society for the Advancement of Applied Computer Science, Berlin, Germany
e-mail: herfert@gfai.de; henning@gfai.de

D. Di Maio, J. Baqersad (eds.), *Rotating Machinery, Optical Methods & Scanning LDV Methods, Volume 6*, Conference Proceedings of the Society for Experimental Mechanics Series, https://doi.org/10.1007/978-3-030-76335-0_1

1.2 Background

In the field of structural dynamics, ever increasing demands are made on a realistic visualization of the natural and operational modes of vibration. This visualization is necessary to enable an optimal comparability with simulation results and is necessary to implement an even more precise analysis. The improved visualization possibilities of 3D animations, especially of computer games and movies, lead to higher and higher demands also on engineering software.

Currently, all forms of visualization as defined in the reality-virtuality continuum [1] are available, from a purely virtual vibration animation to a vibration animation in the real environment (see Fig. 1.1). In contrast to real-time visualization applications, these are only available after the measurement is complete. Therefore, a direct interaction with the structure during operation is not possible for the user.

To achieve these realistic representations, three things are necessary:

1. 3D reconstruction with high resolution and texture of the structure under investigation.
2. High measurement resolution, so that in the best case, one measurement point can be assigned to each point in the triangle mesh.
3. Textures from the real environment to project the results of the vibration analysis on the real background.

Currently, AR applications are technically only possible with electromechanical sensors. The optical methods for vibration measurement are currently not applicable for AR applications. For high-speed cameras, a real-time data stream via Ethernet is not feasible due to the large amount of data. With multipoint vibrometers, visualization or analysis of the measured data is also only possible after the measurement. The biggest disadvantages of electromechanical sensors are the significantly higher configuration effort, the measurement resolution, and the difficult surface measurement in comparison to optical methods. Thus, a fundamental aim of this work is to minimize these disadvantages compared to the optical sensors.

1.3 Technical Implementation

The aim of the work was the development of software components to accelerate and simplify the measurement chain for vibration analysis of mechanical structures by means of electromechanical sensors. To achieve this aim, three software components were created that can be used autonomously or in combination (see Fig. 1.2).

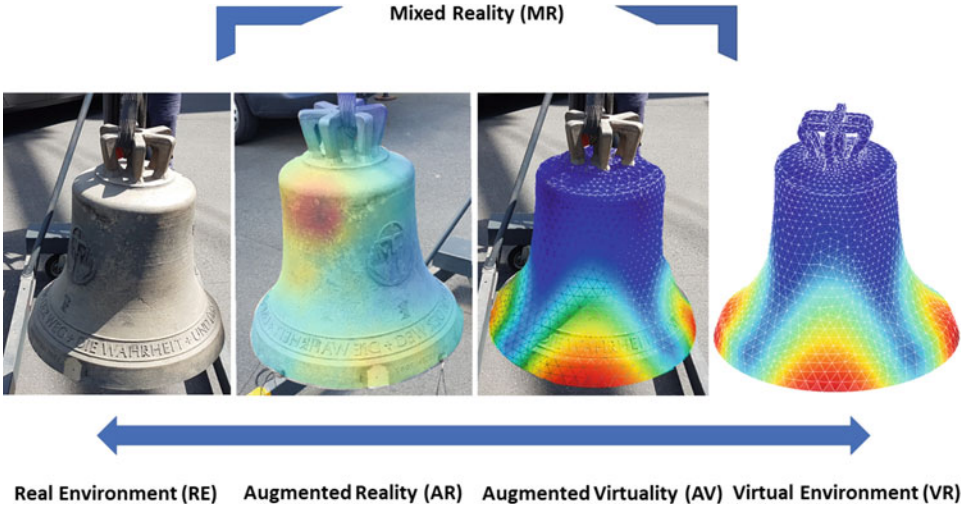

Fig. 1.1 Overview of all structural dynamic representation forms (reality, augmented reality, virtual reality, virtuality), created with the WaveImage software (gfai tech GmbH)

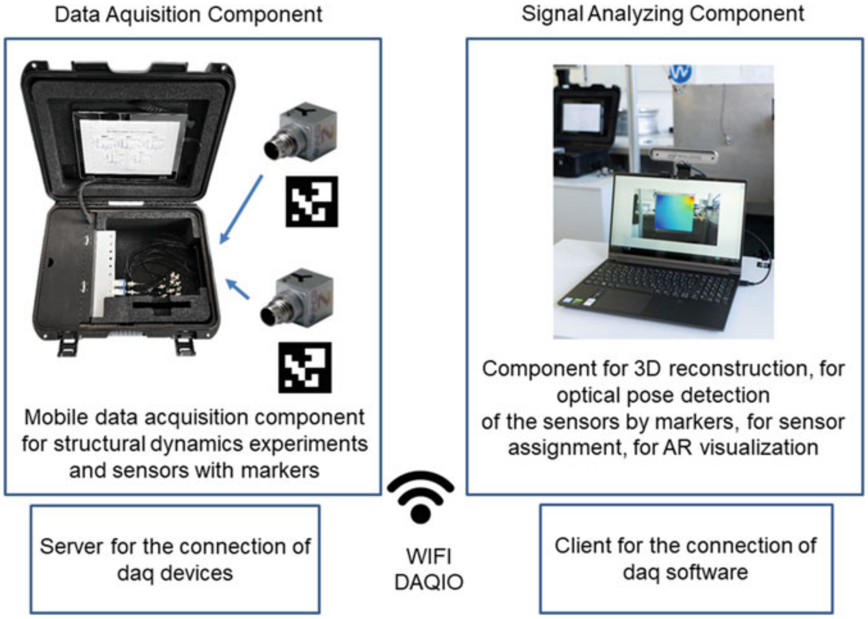

Fig. 1.2 Overview of all software and hardware components used to implement the data acquisition system for measurement configuration and realistic AR visualization

1.3.1 Acceleration and Simplification of the Measurement Configuration for Electromechanical Sensors

New concepts were implemented to improve the measurement configuration. These include an efficient 3D reconstruction, an automatic optical marker tracking of the vibration sensors, and the automatic assignment of the sensor poses to the triangular mesh of the structure under investigation. These work steps simplify the currently manually performed procedure for the configuration of the measurement setup in many ways.

Furthermore, this feature can be applied to existing data acquisition systems. To carry out the extension, only Arco markers have to be printed out and attached to the sensors. The Intel Real Sense D455 stereo camera has to be purchased and connected to a USB 3.0 port of the mobile measurement computer. With this hardware and the software WaveAR, the entire measurement configuration required to create the geometry and to assign the sensors to the geometry is possible. The created geometry and the corresponding sensor assignment can also be exported and used autonomously with external software components. But it can also be used as a measurement configuration for the following AR animation.

1.3.2 Universal Data Acquisition Interface

Furthermore, the transfer of the results to existing data acquisition systems is essential in order to ensure a wide applicability. Besides the use of existing sensors, the integration of already existing data acquisition hardware plays a special role. This is essential for the later user, because in most applications the data acquisition hardware has the highest costs for measuring equipment.

Therefore a standardized software development kit in C++ called DAQIO SDK was developed. This SDK contains all functions for the implementation of the DAQIO network protocol. With this SDK any data acquisition device can communicate with the visualization component in the future. This should standardize the communication of DAQ devices. Communication is understood to be the transfer of measurement data as well as the control. DAQIO provides a communication protocol for the data acquisition interface. With the SDK DAQ devices can be extended with the DAQIO protocol. The DAQIO protocol was implemented as a network protocol, so that the data acquisition device can be used via Ethernet or WLAN or as a local host on the measuring computer. Real-time visualization in the form of an AR application is only possible through wireless data transfer. This network protocol can also be used independently and represents an independent innovation.

Fig. 1.3 Mobile measuring case for structural dynamics

A mobile measuring case was developed for the AR application. This allows a complete structural dynamic measurement even outdoors without wired connection. The transfer of the measurement data from the acquisition unit to the visualization application is done via WLAN and with the DAQIO SDK. The mobile measuring case (see Fig. 1.3) is used for both indoor and outdoor measurements. For outdoor measurements it has a protected cable inlet and also works with closed lid. Therefore it is dust and water protected.

The measuring case called WaveCase consists of three separate components. The first component is a CompactDAQ package from National Instruments with up to 32 channels and a sampling rate per channel of 50 kHz. Eight measurement cards can be integrated into this housing. The possible measurement cards include various types of sensors and do not only cover the field of structural dynamics. Therefore this measurement case could be used for other applications with other sensors. The entire data acquisition system but also the visualization was designed in a modular way, so that the whole system would be transferable to other sensor data and thus could be used in other application areas.

The second component includes a commercially available tablet and is used to set up the server which is used to control the data acquisition device, synchronize data acquisition, store the measurement data locally, preprocess the measurement data, and transfer the measurement data to data acquisition clients.

The third component includes a high-performance rechargeable battery, which allows a minimum measurement time of 48 h. This battery supplies both the data acquisition device and the tablet and is easily replaceable. In addition, the measuring case offers storage space for the sensors and their cables and a Bluetooth keyboard and mouse for easier operation of the tablet.

1.3.3 Real-Time Visualization in the Form of an AR Application

The software WaveAR is the world's first AR application for structural dynamics (see Fig. 1.4). This form of real-time visualization enables for the first time a vibration animation by means of a color map, embedded in the video image. The color map is determined by means of current sensor values. In order to be able to assign sensor values to pixels or points of the geometry which were not measured, an interpolation [2] was implemented. This type of interpolation originally comes from the field of computer vision and is first used in the field of structural dynamics. This allows a much more realistic surface measurement even with electromechanical sensors.

By the computer-aided extension of the perception of reality in the form of an AR application, the operating deflection shapes can be shown directly in reality. This component requires the previously described components of the measurement configuration and universal data acquisition interface for the execution and therefore cannot be used independently.

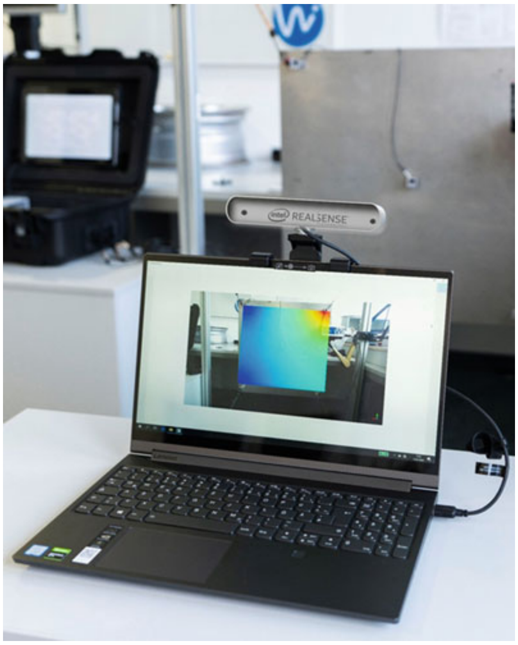

Fig. 1.4 Software user interface for time operating deflection shapes and visualization of a steel plate with WaveCase and Intel Real Sense D455 camera. The transfer of the measured values is done via Wi-Fi

1.4 Measurement Setup

The analysis of the system was carried out in the form of a modal analysis. The vibration response of a car rim and a steel plate to a selective force excitation was investigated to conduct the experimental modal analysis. For this purpose, a car rim and a steel plate were mounted freely suspended in an aluminum frame. The car rim and the steel plate were excited by an automated modal hammer (WaveHit$^{\mathrm{MAX}}$, gfai tech GmbH) [3] on a fixed position. This modal hammer offers the advantage of automated repetitions of single hit excitation with a defined and constant force amplitude. Equipped with a force sensor (PCB type 208C03), a plastic tip, and an additional mass of 60 g, a repeatable excitation of 500 N has been achieved in order to obtain the best signal-to-noise ratio at all measurement points.

The response of the car rim into z direction to the impact excitation was measured with five accelerometers (MMF KS943B.100). A series of three measurements with same input were carried out, each with five measuring points. First one part of the outer radius of the rim, then the second part of the outer radius, and then inner radius of the rim were measured. Due to the complete reproducibility of the excitation, the three measurements were combined into one measurement. The response of the steel plate only in z direction to the impact excitation was measured with five accelerometers (MMF KS943B.100).

1.5 Analysis

At the beginning of the two measurements, the automatic optical measurement configuration was performed with the support of the WaveAR system. For this purpose, five ArUco markers were glued to the inserted sensors. Another ArUco marker was used to position the box in which the 3D scan takes place. Furthermore, the Intel Real Sense D455 camera was connected to the USB 3.0 port. After that, the settings were made on the DAQ software. Among other things, this includes setting the sampling rate, the assignment between the marker ID and the associated channel of the DAQ device. After that, the test object was scanned (see Fig. 1.5). It should be noted that there is no post-processing of the 3D scan. If there are even higher demands on the visualization, an automated post-processing of the 3D scan would be possible. However, this would have no influence on the structural dynamic properties.

After scanning, the ArUco markers are then scanned to determine the relative pose of the sensors to the scanned structure. To scan the sensors, each sensor must appear in the camera image. If the user agrees with the determined sensor pose, it can be selected and continue with the scan of the next sensor pose afterward. If all sensors are to be determined with once, they all can be confirmed together (see Fig. 1.6).

To optimize the pose determination, an extended Kalman filter has been implemented, which can also compensate the pose if the sensor is not currently in the image. After the pose determination is finished by the user, the automatic assignment of

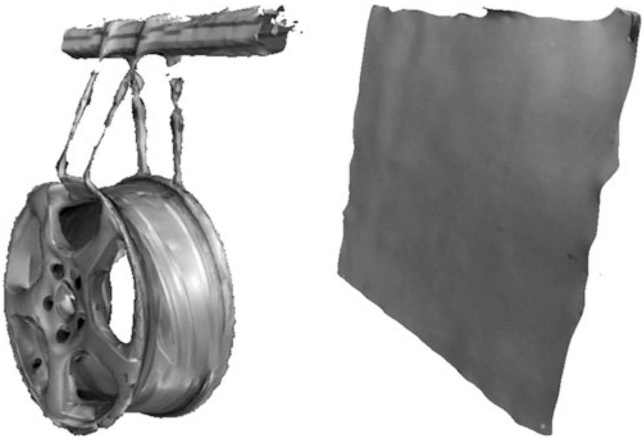

Fig. 1.5 3D scans with software WaveAR with Intel Real Sense D455 camera of a car rim (left) and steel plate (right) without mesh post-processing

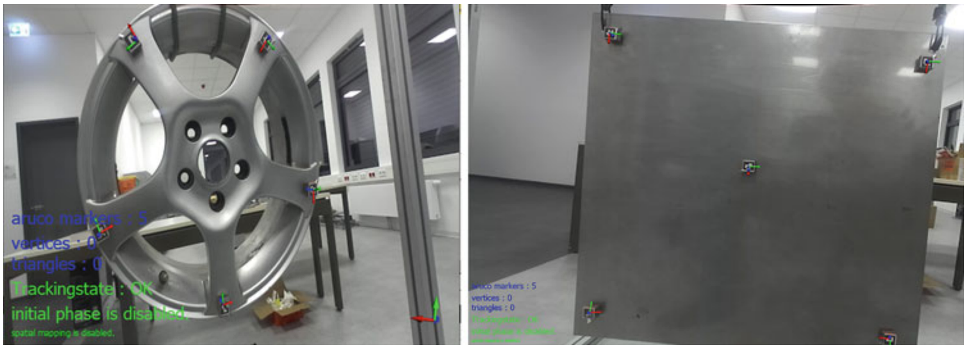

Fig. 1.6 Sensor pose detection with optical markers of a car rim (left) and steel plate (right)

the sensors to the 3D scan and the precalculation of the significant parameters of the interpolation for the later AR application are performed.

After the assignment is completed, the sensors were connected to the DAQ device of the WaveCase, and the impulse hammer was positioned at the test object. Then the measurement was started, allowing real-time visualization in the form of an AR application (see Fig. 1.4). The sensor values are transmitted wirelessly from the WaveCase to the AR computer. To validate the data, both measurements were exported and analyzed with the software WaveImage [4]. For this purpose the experimental modal analysis component of the software WaveImage (gfai tech GmbH) was used to extract the eigenfrequencies and mode shapes using the Complex Mode Indicator Function AI (CMIF-AI) algorithm [5]. In Fig. 1.7 the CMIF-AI results and in Table 1.1 all detected eigenfrequencies are shown.

For the car rim, ten and for the steel plate eight different modes could be identified.

The Modal Assurance Criterion (MAC) matrix (see Fig. 1.8) is used to validate the linear independence of the detected modes. In both measurements there is a dependency only between mode 2 and mode 5. Otherwise there are no significant dependencies between modes. This indicates that the measurement was performed correctly.

In Fig. 1.9 one mode shape per investigated object is presented. The mode shapes look quite realistic without a big effort for the geometry creation. Both measurements were feasible under 1 h, including the measurement setup, measurement configuration, data acquisition, and modal analysis by the WaveImage software. Without the WaveAR system, we would have needed much longer for the structural dynamic measurement of complex structures, such as the car rim.

1.6 Conclusion

In summary, this work has created a first research proposal on the following topics in the field of structural dynamics:

1. Automatic optical measurement configuration for structural dynamics for electromagnetic sensors.
2. Implementation of a universal data acquisition interface.
3. Real-time visualization in form of an AR application for electromagnetic sensors.

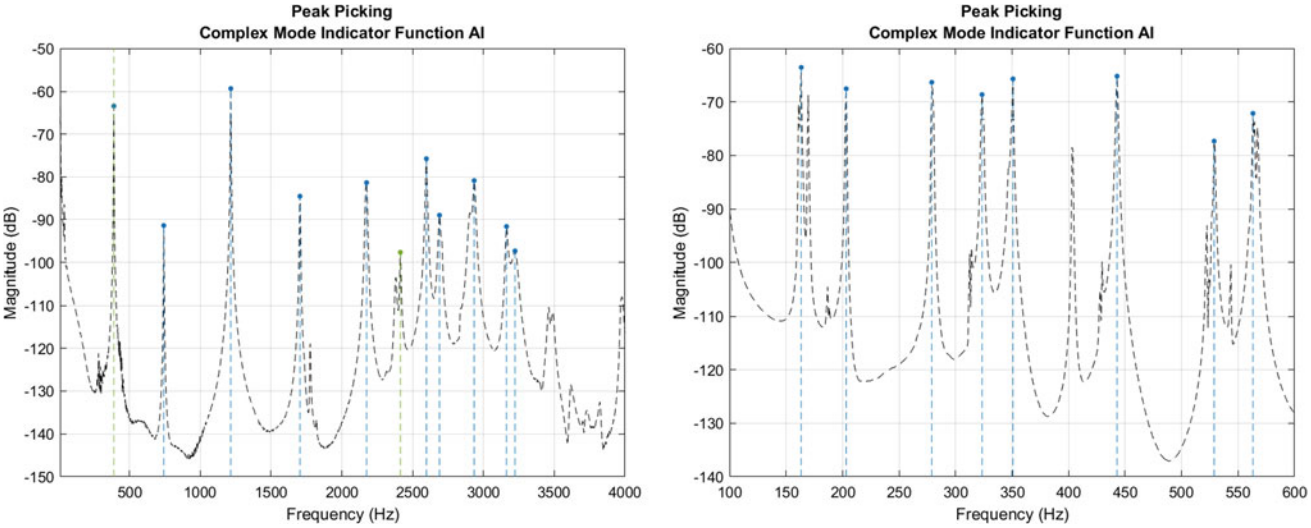

Fig. 1.7 Complex Mode Indicator Function AI (CMIF AI) of a car rim (left) and steel plate (right)

Table 1.1 Eigenfrequencies with the corresponding mode number of the car rim and the steel plate

Mode number	EMA frequency RIM (Hz)	EMA frequency steel plate (Hz)
1	388	163
2	741	203
3	1215	278
4	1703	323
5	2175	350
6	2597	442
7	2690	528
8	2935	563
9	3163	
10	3223	

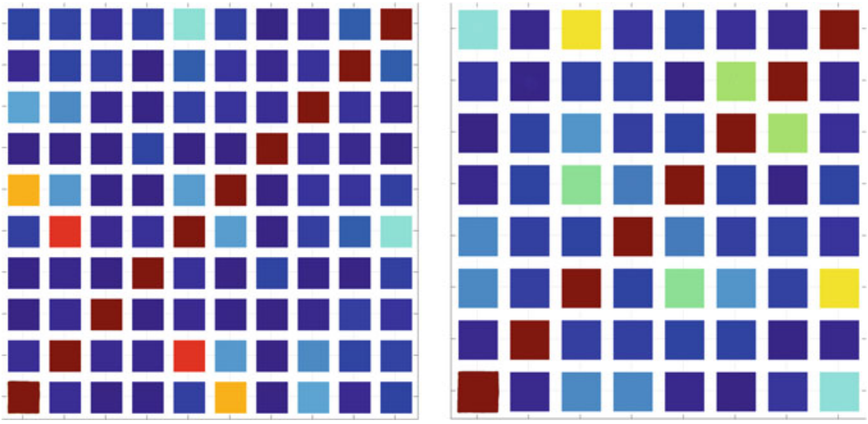

Fig. 1.8 Modal Assurance Criterion (MAC) matrix of the ten measured modes of car rim (left) and eight measured modes of steel plate (right)

With the current state of the work, an essential basis for the implementation of a cost-effective data acquisition system in the form of an AR application has been created. The possibilities for integration into existing data acquisition hardware and the low additional acquisition costs allow the current status to be used directly in applications in research and industry. Based on the achieved results, further steps of the measurement can be integrated into the system, but also existing methods can be improved and validated on new measurement applications. All in all, this system offers a new kind of interaction and assistance during and before the measurement, which does not exist in this form at this time. In addition, the measurement

Fig. 1.9 Three different views from the third mode (1215 Hz) of car rim. Seventh mode (528 Hz) of steel plate without texture

time can be significantly reduced with this system, and less expert knowledge is also required to perform the measurement. To protect the innovation, a detailed patent search and a patent application based on it were prepared and submitted. The patent was granted with the name "Method and System for Structural Dynamic Analysis" on September 5, 2019 (Germany patent no. DE102018103333, 2019).

References

1. Milgram, P.: A taxonomy of mixed reality visual displays. IEICE Trans. Inf. Syst. **77**(12), 1321–1329 (1994)
2. Herfert, D., Heimann, J., Henning, K.: Automatic interpolation for the animation of unmeasured nodes with differential geometric methods. In: Rotating Machinery, Optical Methods & Scanning LDV Methods, vol. 6, pp. 53–59. Springer International Publishing, Cham (2021)
3. Product Page of the WaveImage^{MAX}. https://wave-hit.com/
4. Product Page of the WaveImage Software. https://wave-image.com/?lang=en
5. Gollnick, M., Herfert, D., Heimann, J.: 9. Automatic modal parameter identification with methods of artificial intelligence. In: Topics in modal analysis & testing, vol. 8. Springer International Publishing, Cham (2021)

Chapter 2
Full-Field 3D Mode Shape Measurement Using the Multiview Spectral Optical Flow Imaging Method

Domen Gorjup, Janko Slavič, and Miha Boltežar

Abstract In some modal testing applications, image-based techniques offer compelling advantages compared to conventional sensors, particularly in cases where mass loading is problematic or a high spatial resolution is required. Still, the limited field of view of the well-established stereo DIC method can be a limiting factor in some measurements. By employing the principles of multi-view imaging, this constraint can be alleviated. For linear, time-invariant structures, multi-view triangulation can be performed in the frequency domain. The measurement field of view can in this way be arbitrarily extended using only a single moving camera imaging system. By using the simplified optical flow method in the displacement spectra identification step, a still-frame camera can be used for image acquisition, considerably lowering the complexity and cost of the imaging system. In this work, the spectral optical flow imaging and frequency-domain multi-view triangulation approaches are combined in an effort to identify mode shapes of a simple three-dimensional structure. The aim is to develop a robust and cost-effective single still-frame camera-based modal testing method.

Keywords Single camera · Multiview · Full-field measurement · Frequency-domain triangulation · Spectral optical flow imaging

2.1 Introduction

Image-based displacement measurement methods offer a viable alternative to traditional vibration measurement techniques, owing their appeal mainly to the high spatial resolution and the non-contacting nature of the measurement, especially important in cases where mass loading may impede the use of conventional transducers [1]. Due to an inherent limitation of 2D imaging systems, only the planar kinematics of the observed surface can be measured from a single camera point of view. With the introduction of stereo measurement methods (e.g., 3D Digital Image Correlation, DIC), this limitation is eliminated, but the field of view of the stereo camera pair remains limited to a single observed viewpoint [2].

Utilizing the principles of multi-view imaging [3], the field of view of an image-based vibration measurement can be extended for objects of arbitrary geometry. These methods extract spatial information from simultaneously acquired high-speed video frames of the observed process using triangulation. Alternatively, the mode shape data, captured by a moving stereo pair of high-speed cameras, can be used to extend the field of view of the measurement with a process called surface stitching [2]. When using these multi-view methods, possible distortions in the optical systems and time-synchronization errors with using multiple cameras can negatively affect the accuracy of the multi-view measurement [4]. This is the main motivation behind the so-called single-camera multi-view measurement methods. Using only a single digital camera, the complexity and cost of an imaging system are lowered. Single-camera multi-view systems however usually require additional light-splitting elements such as mirror adapters or prisms to project multiple views of the observed object on a single image sensor, sometimes resulting in lower spatial resolution [5]. The recently proposed method of frequency-domain triangulation for spatial vibration measurement offers an alternative single-camera measurement option [6]. Frequency-domain images of small harmonic motion can be used to reconstruct 3D deflection shapes of a linear, time-invariant mechanical structure under stationary excitation while arbitrarily extending the field-of-view of the measurement using only a single, moving image camera, preserving the full-field resolution of the result.

D. Gorjup (✉) · J. Slavič · M. Boltežar
Faculty of Mechanical Engineering, University of Ljubljana, Ljubljana, Slovenia
e-mail: domen.gorjup@fs.uni-lj.si; janko.slavic@fs.uni-lj.si; miha.boltezar@fs.uni-lj.si

D. Di Maio, J. Baqersad (eds.), *Rotating Machinery, Optical Methods & Scanning LDV Methods, Volume 6*, Conference Proceedings of the Society for Experimental Mechanics Series, https://doi.org/10.1007/978-3-030-76335-0_2

To extend the feasibility of high-speed imaging methods for measuring high frequency, as well as reduce the complexity and cost of high-speed imaging systems, various approaches to extending the frequency range of image-based measurement have been researched [7]. The Spectral Optical Flow Imaging (SOFI) method [8] has recently been used in a multi-view configuration to measure 3D operating deflection shapes (ODSs) of a vibrating specimen using a still-frame digital camera [9], with the frequency range of the measurement limited only by the frequency of a harmonically controlled light source.

In this paper, the possibility of using deflection shape images, obtained by the single-camera multi-view SOFI method, together with the excitation spectra, measured using a single force transducer, in a frequency-domain triangulation procedure to measure full-field 3D mode shapes of a mechanical structure is explored.

2.2 Theoretical Background

A method of measuring 3D ODSs using a single, moving still-frame camera is presented in [9]. Multiple images of the ODSs of a vibrating structure at selected frequencies of interest are acquired from various viewpoints using SOFI. Spatial operating deflection shapes $\boldsymbol{X}(\omega)$ of a linear, time-invariant structure are reconstructed from frequency-domain images of the observed

$$\boldsymbol{u}\left(\omega\right)=\Delta\boldsymbol{u}\left(\omega\right)+\boldsymbol{u}^{\mathrm{REF}}=\frac{1}{w}\,\mathbf{P}\left(\Delta\boldsymbol{U}\left(\omega\right)+\boldsymbol{U}^{\mathrm{REF}}\right) \tag{2.1}$$

spatial motion $\Delta\boldsymbol{U}(\omega)$, reconstructed from image data by frequency-domain triangulation of ODS images $\boldsymbol{u}(\omega)$:

$$\boldsymbol{X}\left(\omega\right)=\boldsymbol{U}\left(\omega\right)-\boldsymbol{U}^{\mathrm{REF}} \tag{2.2}$$

where w is the perspective scaling factor, assumed to be constant for small harmonic displacements $\Delta\boldsymbol{U}$ [6].

By adding a force transducer between the shaker and the structure in the measurement chain, as illustrated in Fig. 2.1, the excitation spectra can also be measured, and the frequency-response functions $H(\omega)$ can be computed for all the points, observed in the full-field optical measurement at the selected measurement frequencies. The mode shapes $\boldsymbol{\Psi}(\omega)$ can then be obtained, e.g., by using the least-squares frequency-domain (LSFD) method [10].

2.3 Preliminary Experiment

A concave steel object, composed of three 1-mm-thick 120 × 120 mm sheet metal planes, bent and welded along one edge was mounted onto an electrodynamic shaker through a PCB 208C01 force transducer. A single PCB SN 53358 accelerometer was mounted onto the object, in the middle of one of the three planes, facing away from the camera. The accelerometer was

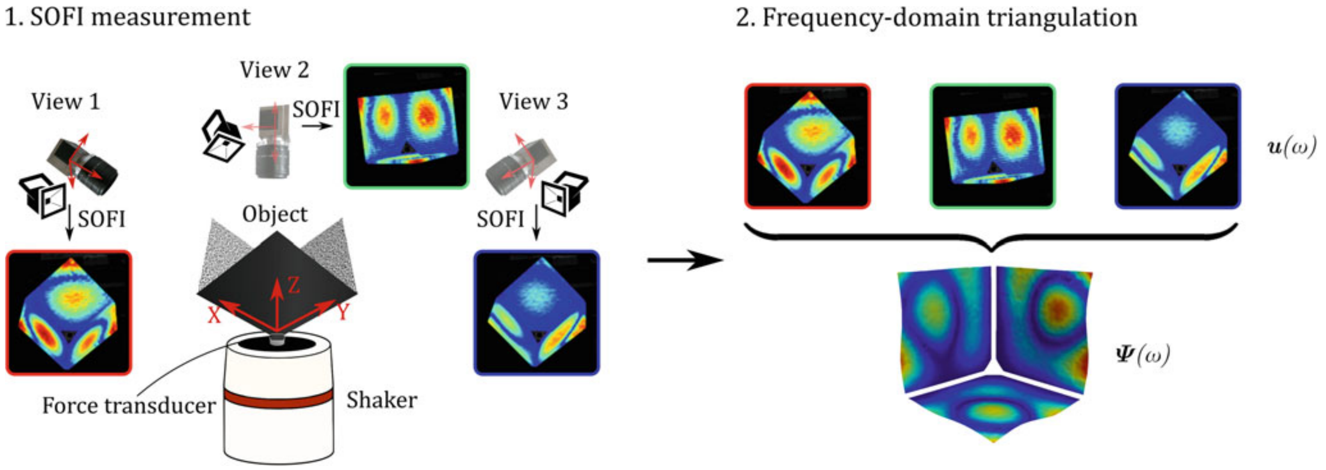

Fig. 2.1 Multi-view SOFI with frequency-domain triangulation for mode shape identification

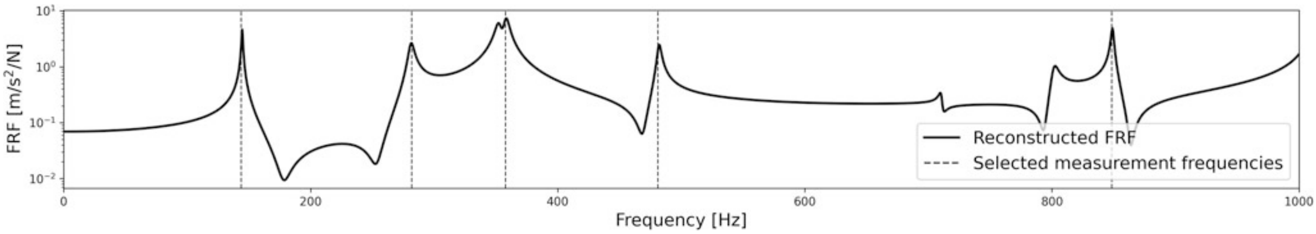

Fig. 2.2 Measured accelerance FRF of the observed object

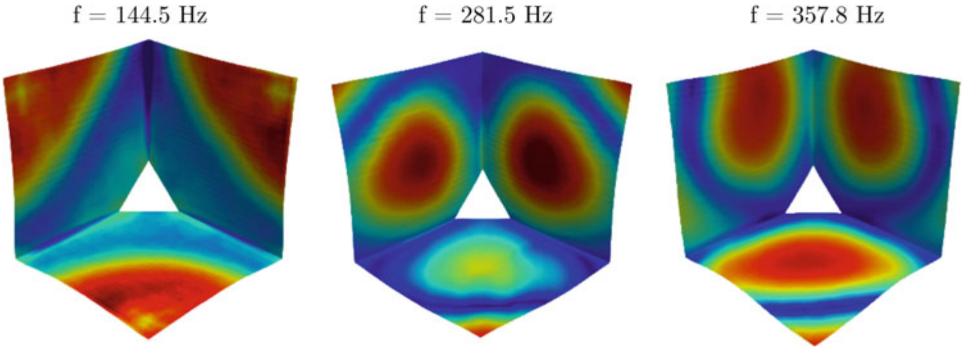

Fig. 2.3 Mode shapes, measured in the preliminary experiment

used to measure the FRF of the object in the 10–2000 Hz frequency band using sine-sweep excitation. It remained mounted to the object throughout the whole measurement process. Using the measured FRF, shown in Fig. 2.2, five measurement frequencies, corresponding to distinct resonant peaks, were selected for further analysis using multi-view SOFI.

A high contrast speckle pattern was applied to the object's three visible faces. The SOFI images were obtained at each selected frequency using a Basler Ace still-frame monochrome camera with a resolution of 4096 × 3000 pixels, with exposure period set to 2 s. The LED light source was controlled simultaneously with the shaker excitation, force, and image acquisition triggering, by external signals, generated using a single National Instruments 9263 output module. The process was repeated six times at each frequency, rotating the object on the shaker by approximately 60° between each measurement, to obtain six distinct views of the process. The multi-view system was calibrated using the perspective N-point algorithm [3].

A regular grid of 100 × 100 points was projected from the 3D model of the specimen onto each of the three visible faces in every view. A rectangular region of 175 × 175 pixels with the grid node in the center was analyzed using the multi-view SOFI method [9], to obtain the spatial response at each selected point for every measurement frequency. The resulting 3D ODS were used together with the force measurement to compute the full-field FRF values at the measurement frequencies. These were used to finally compute the 3D mode shapes of the observed object using the LSFD method. The results are shown in Fig. 2.3.

2.4 Conclusions

Although further analysis of the obtained results is required, the results of the preliminary experiment approximate the expected mode shapes of the observed object well, confirming the potential for future applications of the proposed method to 3D mode shape measurement. Multi-view SOFI enables single still-frame camera measurements of spatial mode shapes for linear, time-invariant mechanical structures by utilizing the properties of a stationary mechanical process to facilitate full-field 3D measurements without the need for precise time-synchronization of multiple video sequences, with the only additional equipment required being a controlled light source. The multi-view SOFI method measures the response of a vibrating specimen directly in the frequency domain, significantly reducing the amount of the acquired data and the post-processing times, compared to existing full-field spatial measurement methods.

References

1. Helfrick, M.N., Niezrecki, C., Avitabile, P., Schmidt, T.: 3D digital image correlation methods for full-field vibration measurement. Mech. Syst. Signal Process. **25**(3), 917–927 (2011). https://doi.org/10.1016/j.ymssp.2010.08.013
2. Patil, K., Srivastava, V., Baqersad, J.: A multi-view optical technique to obtain mode shapes of structures. Measurement. **122**, 358–367 (2018). https://doi.org/10.1016/j.measurement.2018.02.059
3. Hartley, R., Zisserman, A.: Multiple View Geometry in Computer Vision, 2nd edn. Cambridge University Press, New York, NY (2003)
4. Yu, L., Pan, B.: Single-camera stereo-digital image correlation with a four-mirror adapter: Optimized design and validation. Opt. Lasers Eng. **87**, 120–128 (2016). https://doi.org/10.1016/j.optlaseng.2016.03.014
5. Durand-Texte, T., Simonetto, E., Durand, S., Melon, M., Moulet, M.-H.: Vibration measurement using a pseudo-stereo system, target tracking and vision methods. Mech. Syst. Signal Process. **118**, 30–40 (2019). https://doi.org/10.1016/j.ymssp.2018.08.049
6. Gorjup, D., Slavič, J., Boltežar, M.: Frequency domain triangulation for full-field 3D operating-deflection-shape identification. Mech. Syst. Signal Process. **133**, 106287 (2019). https://doi.org/10.1016/j.ymssp.2019.106287
7. Barone, S., Neri, P., Paoli, A., Razionale, A.V.: Low-frame-rate single camera system for 3D full-field high-frequency vibration measurements. Mech. Syst. Signal Process. **123**, 143–152 (2019). https://doi.org/10.1016/J.YMSSP.2019.01.016
8. Javh, J., Slavič, J., Boltežar, M.: Measuring full-field displacement spectral components using photographs taken with a DSLR camera via an analogue Fourier integral. Mech. Syst. Signal Process. **100**, 17–27 (2018). https://doi.org/10.1016/j.ymssp.2017.07.024
9. Gorjup, D., Slavič, J., Babnik, A., Boltežar, M.: Still-camera multiview Spectral Optical Flow Imaging for 3D operating-deflection-shape identification. Mech. Syst. Signal Process. (2021). https://doi.org/10.1016/j.ymssp.2020.107456
10. Verboven, P.: Frequency-Domain System Identification for Modal Analysis, Ph.D. Thesis. Department of Mechanical Engineering, Vrije Universiteit Brussel, Brussels, Belgium (2002)

Chapter 3
Stereophotogrammetry Camera Pose Optimization

Bryan L. Witt, J. Justin Wilbanks, Brian C. Owens, and Daniel P. Rohe

Abstract Stereophotogrammetry makes use of calibrated camera pairs to obtain three-dimensional information from two-dimensional images. The accuracy of the extracted measurements is extremely dependent on the selection and setup of the camera system. For a given test object and desired viewing orientation, there is no one "correct" stereo camera setup, but rather a range of potential setups with some approaching an optimal system with respect to maximizing the measurement resolution. The open-ended nature of this test design exercise is compounded by equipment availability and the fact that many of the setup parameters have dependent characteristics, e.g., changing focal distance will affect stand-off distance, field of view, and image projection, among others. This work describes a planning tool that utilizes projective and Euclidian geometry to iteratively estimate optimal camera poses for available equipment, determines the most efficient image size, and also performs checks for lens diffraction, minimum focal distance, and adequate depth of field. Integrating a finite element model with these calculations further extends planning capabilities by allowing (1) an accurate definition of the volume to be imaged and (2) the ability to estimate response displacements in pixels due to an arbitrary excitation applied to the test object. This latter capability is critical for pre-test determination of the chosen camera setup's ability to successfully extract three-dimensional measurements. The theory and workflow are presented along with an experimental demonstration.

Keywords Stereo · Photogrammetry · Test planning · Camera pose · Displacement estimation

3.1 Introduction

Photogrammetry is well established as a diagnostic capability for quasi-static displacement and strain measurements as well as large-scale (integer pixel) motion tracking [1–4]. Optical measurement techniques have many benefits, such as being non-contact and very fast to field. Photogrammetry's use in structural dynamics, where higher frequency displacements are typically sub-pixel, is gaining popularity as camera technology and bespoke data processing methods are established [5–8]. A recent study [9] demonstrated that carefully constructed experimental modal tests using DIC can directly extract modal information from displacements as small as 0.001 pixel.

The resolution of any optical system is dependent of the field of view (FOV); optimizing the number of pixels across an imaged area of interest (AOI) is critical for measuring sub-pixel displacements. However, because there are an endless number of practical considerations for each unique optical test (e.g., camera sensor selection, lenses available, physical space around the test object, etc.), there is no single truly "optimized" configuration. Typically, the practitioner must rely solely on

---

Sandia National Laboratories is a multimission laboratory managed and operated by the National Technology and Engineering Solutions of Sandia, LLC., a wholly owned subsidiary of Honeywell International, Inc., for the US Department of Energy's National Nuclear Security Administration under contract DE-NA-0003525. This paper describes objective technical results and analysis. Any subjective views or opinions that might be expressed in the paper do not necessarily represent the views of the US Department of Energy or the US government.

B. L. Witt (✉) · D. P. Rohe
Experimental Structural Dynamics Department, Sandia National Laboratories, Albuquerque, NM, USA
e-mail: blwitt@sandia.gov; dprohe@sandia.gov

J. J. Wilbanks · B. C. Owens
Analytical Structural Dynamics Department, Sandia National Laboratories, Albuquerque, NM, USA
e-mail: jjwilba@sandia.gov; bcowens@sandia.gov

D. Di Maio, J. Baqersad (eds.), *Rotating Machinery, Optical Methods & Scanning LDV Methods, Volume 6*, Conference Proceedings of the Society for Experimental Mechanics Series, https://doi.org/10.1007/978-3-030-76335-0_3

their experience to select cameras and lenses and then determine their best pose in a stereo rig. Pose is defined here as the physical location and orientation of the cameras in space relative to each other as well as the test object.

It is entirely conceivable to set up a stereo system, collect and download images, and post-process the data only to find that the displacements of the test object never overcame the noise floor of the optical system. This work presents a photogrammetry pre-test planning workflow that will inform the selection of camera/lens pairs and the stereo poses that approximate their optimal setup in terms of measurement resolution. This process also considers lens minimum focus distances and depth of field (DOF) requirements and checks for lens diffraction limitations.

Finally, we use a finite element model (FEM) and the pose optimization results to determine what points in a bounding volume will be visible to both cameras and estimate their respective displacement amplitudes on a mode-by-mode basis for a given excitation. The modal displacement estimates can be directly correlated to the known (or estimated) noise floor of the camera system, easily identifying which modes may or may not be observable by the optical system. Armed with the information from the test planning workflow, the practitioner can easily iterate on the test setup (equipment, AOI, pose, excitation, etc.) to have the best opportunity to obtain the measurements of interest and meet the test objectives.

The following section provides background information on general stereo camera setups, including the coordinate systems which are utilized and a brief coverage of 3D–2D projective transformations. Section 3.3 presents the iterative pose optimization routine and demonstrates output results relative to an actual test. Section 3.4 provides a stand-alone FEM analysis to determine visible nodes and estimate displacements, using the final results from Sect. 3.3 as input. The reader is cautioned that these two sections use different variable definitions. The final section discusses conclusions and future work under consideration.

3.2 General Stereophotogrammetry Setup

The test planning workflow described in this work can be applied to a 2D photogrammetry using a single camera. However, a single camera test is usually much easier to setup and iterate upon; in this work we will focus on the more complex stereo camera setup utilizing two cameras for 3D photogrammetry measurements.

Consider a test article in 3D space which is defined in an arbitrary "world" Cartesian coordinate system, $\mathbf{O_w}$, as depicted in Fig. 3.1. It is usually extremely convenient to let the world coordinate system match that of the FEM global coordinate system, as is done in this work. Two cameras, denoted Camera 0 and Camera 1, are positioned such that their optical axes are pointed in the direction of the test article and have local coordinate systems $\mathbf{O}_i$ where i indicates the camera index 0 or 1, respectively. The baseline (BL) is the line formed between the origin points of $\mathbf{O}_i$ and lies on the same plane containing all points along both optical axes, $\mathbf{z}_i$. The camera rig is a fourth coordinate system, $\mathbf{O_r}$, and is defined at the center of the baseline, oriented such that $\mathbf{x_r}$ points from Camera 0 to Camera 1 and $\mathbf{y_r}$ is normal to the plane containing the baseline and optical axes. Finally, the image planes are located at the focal distance f_i along the optical axis $\mathbf{z}_i$. Ideally, the image center would lie on the optical axis $\mathbf{z}_i$ such that $(c_x, c_y)_i = (0, 0)$; typically there are slight offsets, but this is a reasonable approximation for

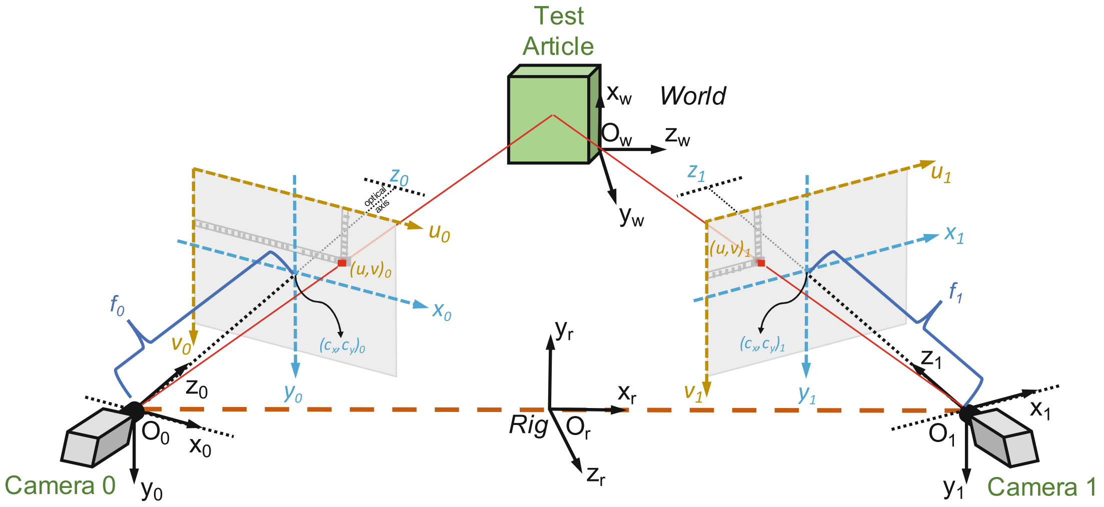

Fig. 3.1 Stereophotogrammetry setup

a planning tool. By convention, the integer pixel indexing in each image space is defined such that $(u, v)_i = (0, 0)$ is in the upper left corner as shown in Fig. 3.1.

As part of a stereophotogrammetry test, a camera calibration is performed prior to data collection, which establishes both the intrinsic and extrinsic parameters of the camera system. In the test planning workflow, we do not have equipment setup to perform a calibration, but the form of the results elucidates the parameters needed for planning purposes. The intrinsic parameters form $\mathbf{K}_i$ and comprise the optical center $(c_x, c_y)_i$, the focal lengths $(f_x, f_y)_i$, and a skew term q that is the tangent of the angle between the image axes. The extrinsic parameters form $[\mathbf{R}|\mathbf{T}]_{i\mathbf{r}}$ and comprise the rotation matrix and translation vector that transforms 3D coordinates $\mathbf{X}$ (in homogeneous coordinates) from $\mathbf{O_r}$ to $\mathbf{O}_i$. Thus, Eq. (3.1) describes the projective transform between a 3D point in the rig coordinate system to 2D pixels $\mathbf{u}$ in the image frame. The $\mathbf{u}$ results are also in homogeneous coordinates and should be divided by the homogeneous scalar a to obtain final pixel values. The form of this projection will be used throughout the process.

$$\begin{gathered}\mathbf{u}_i = \mathbf{K}_i[\mathbf{R}|\mathbf{T}]_{i\mathbf{r}}\mathbf{X}_\mathbf{r} \\ \begin{bmatrix} au \\ av \\ a \end{bmatrix}_i = \begin{bmatrix} f_x & q & c_x \\ 0 & f_y & c_y \\ 0 & 0 & 1 \end{bmatrix}_i \begin{bmatrix} r_{xx} & r_{xy} & r_{xz} & t_x \\ r_{yx} & r_{yy} & r_{yz} & t_y \\ r_{zx} & r_{zy} & r_{zz} & t_z \end{bmatrix}_{i\mathrm{r}} \begin{bmatrix} X \\ Y \\ Z \\ 1 \end{bmatrix}_\mathrm{r}\end{gathered} \tag{3.1}$$

3.3 Stereo Pose Optimization

An overview of the workflow is provided in Fig. 3.2. At a high level, the process is divided into four main segments: input, setup, pose estimation, and pose validation. The following section will elaborate on each segment, providing necessary details for those interested in recreating the tool in a programming language of choice.

3.3.1 User Inputs

First, specifications regarding the available imaging hardware are gathered. Specifically, the following information must be compiled:

- Camera sensor specifications:
  - Full image size (s_x, s_y) (pixels)
  - Pixel size, ϵ (mm)
- Camera orientation (landscape or portrait; see Sect. 3.3.3)
- Camera stand orientation (horizontal or vertical; see Sect. 3.3.3)
- A list of lenses available and their properties:
  - Make and model
  - Nominal focal length f (mm)
  - Minimum focal distance, $s_{\min}$ (mm)
  - Aperture f-stop values, N (minimum and maximum)

With the exception of the above hardware specifications, all of the other user inputs presuppose a knowledge of the planning process and will be described in detail in the following sections:

- Physical size or coordinates of a bounding box that encloses the surfaces to be imaged
- Bounding box margin
- Euler angles that describe the viewing orientation (i.e., how to “look at” test object)
- Space available around the part
  - Acceptable range for standoff distance (SOD)
  - Acceptable range for camera baseline (BL)
  - Acceptable range for camera perpendicular distance (PD)

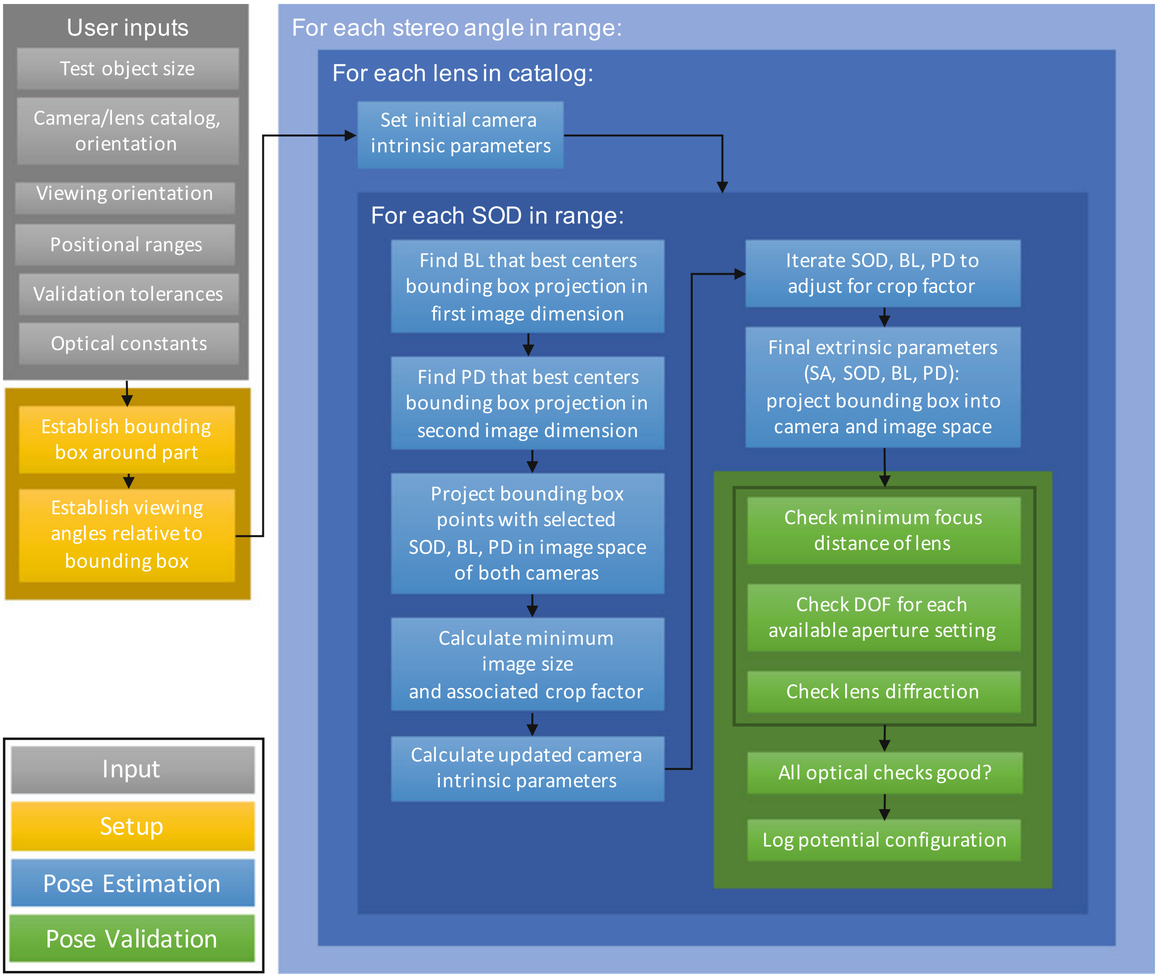

Fig. 3.2 Stereo pose optimization flowchart

- Acceptable range of camera stereo angles
- Tolerance ranges for optical validation parameters
  - Minimum focus distance
  - DOF
  - Lens diffraction
- Optical constants that will be used for DOF and lens diffraction estimations
  - Acceptable circle of confusion, c (mm)
  - Light wavelength, λ (mm)

There is a tradeoff between minimizing required user inputs and increasing the flexibility of the tool. The workflow presented here corresponds to the authors' current implementation but can easily be modified according to specific application needs.

3.3.2 *Setup: Establish Bounding Box*

For the purpose of test planning, we define an imaginary bounding box that contains all surfaces of the test object that are to be imaged. Consider an example test object, such as the Box Assembly with Removable Component (BARC) [10], from which the areas of interest (AOI) include all camera-facing surfaces. The corresponding bounding box is shown in

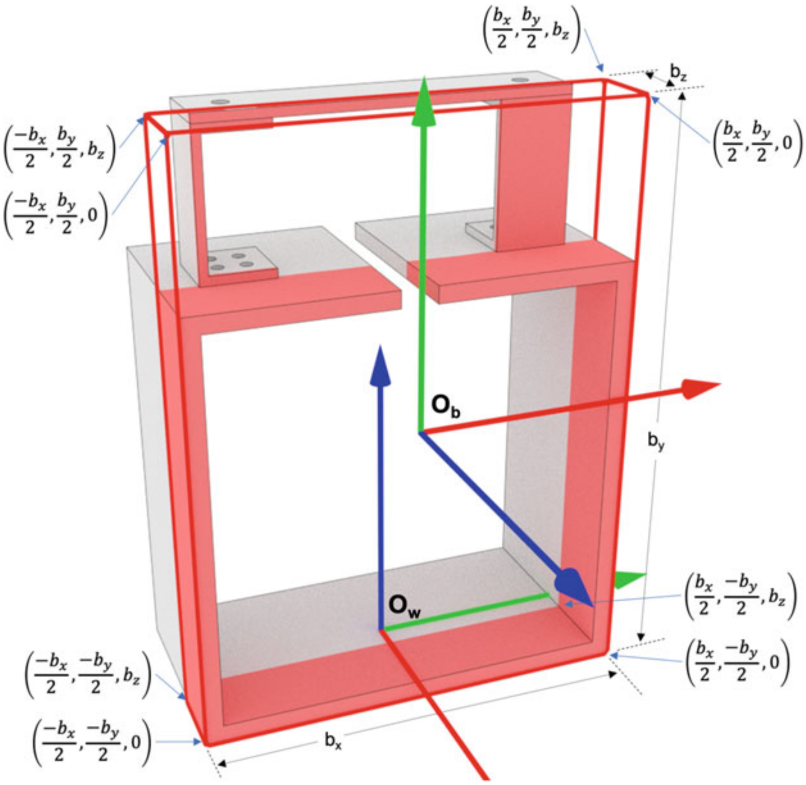

Fig. 3.3 Bounding box nodes in local coordinates

Fig. 3.3 as a red rectangular cube encompassing those surfaces; the entirety of the test object does not need to be included in the bounding box volume, only the surfaces to be imaged. The bounding box has its own coordinate system $\mathbf{O_b}$, which is centered on the front surface as shown in Fig. 3.3. The coordinates of the bounding box nodes are easily defined given its dimensions (b_x, b_y, b_z):

In practice, the box node coordinate values may be given in the world/FEM coordinate system along with the dimensions (b_x, b_y, b_z). In this case, first use the bounding box dimensions to compute the box node positions as shown in Fig. 3.3. Once the 3D coordinates are known in both $\mathbf{O_w}$ and $\mathbf{O_b}$, we compute the transformation between the two, $\mathbf{[R|T]_{bw}}$, for later use in Sect. 3.3.4. This is accomplished through least squares rigid motion (LSRM) transformation using multiple point correspondences [11].

Although the bounding box is defined by the test object's dimensions, in practice it is useful to allow the box to expand by some margin, which can be specified by the user in all three axes independently. This relaxes the degree of accuracy to which the cameras must be placed to retain all AOIs in the image frame. More importantly, this also allows for lens "focus breathing" which varies in both direction and severity from lens to lens (more details in Sect. 3.3.5). This is easily achieved by defining the bounding box "tight" on the test object as shown in Fig. 3.3 and then applying the specified margins to the box coordinates in $\mathbf{O_b}$.

The bounding box dimensions (b_x, b_y, b_z) are user-defined inputs. Similarly, the margin values associated with each box dimension are user-defined inputs.

3.3.3 Pose Estimation

Consideration must be given to the camera (sensor) orientation, relative to how it is defined by the user. For example, if the full image size is defined as (2048, 1920) pixels and the camera is mounted such that the 2048 pixels are in the u dimension of the image, the camera orientation is considered "landscape" (refer to Fig. 3.1). Conversely, if the 2048 pixels lie along the v dimension of the image, the camera orientation is considered "portrait." Thus, the relationship between the image size

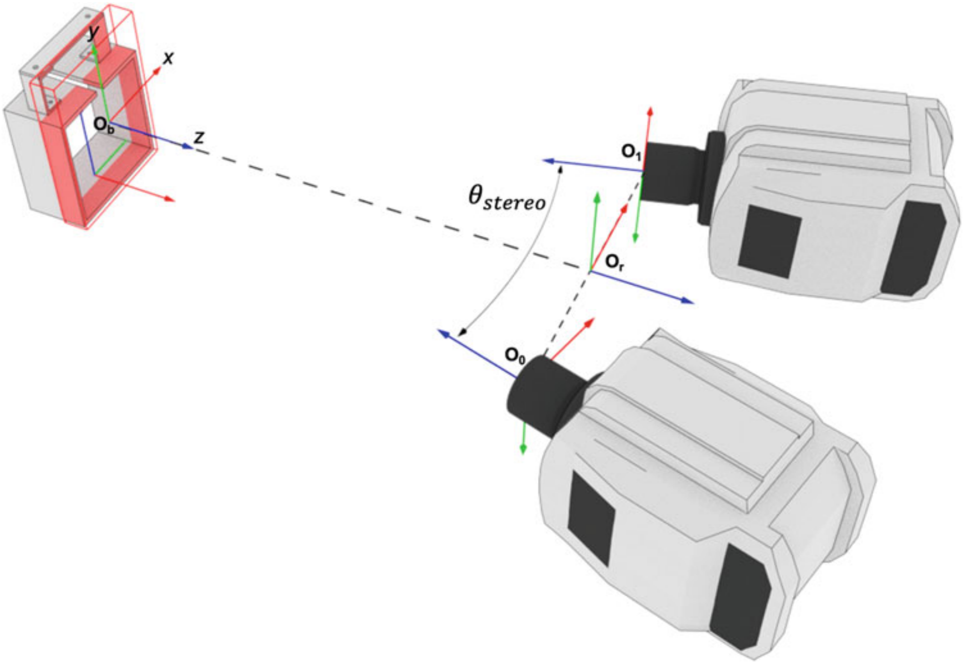

Fig. 3.4 Typical stereo setup with no view angle change

and the camera orientation defines which axis of the sensor corresponds to the image *u* and *v* dimensions. Either camera orientation may be used, and this is included as an option in the user-defined inputs.

Similarly, consideration is given to the camera stand orientation relative to the test object. When the cameras are aligned along the image *u* dimension, we refer to the stand orientation as "horizontal." Conversely, if the cameras are aligned along the image *v* dimension, we refer to the stand orientation as "vertical." This distinction will be important in determining the targets for centering the test object within the image frame in subsequent steps. The camera stand orientation is also a user-defined input.

The user is also responsible for the definition of the view angle with respect to $\mathbf{O_b}$. Consider the typical stereo pose where the camera rig is placed directly in front of the test object as depicted in Fig. 3.4; in this case it is trivial to place the camera rig in space using $\mathbf{O_b}$. However, if the camera rig needs to be positioned somewhere other than directly in front of the part, we can define a new coordinate system $\mathbf{O_v}$ that makes this task easier. A user-defined set of Euler angles describe a rotation matrix, $\mathbf{R_{vb}}$, to transform from $\mathbf{O_b}$ to $\mathbf{O_v}$. For example, to look down on the bounding box from the right side, the Euler angles (in this case using the Tait-Bryan convention with intrinsic rotations about the axes) $\left(\theta_y,\ \ \theta_{x'},\ \ \theta_{z''}\right) = (-10, 15, 0)^\circ$ would rotate into a coordinate frame in which the rig position is easily defined, as depicted in Fig. 3.5. The superscripts $'$ and $''$ on the angle subscripts denote the once and twice rotated coordinate frame, respectively.

To position the camera rig relative to the bounding box, three positioning dimensions are defined in $\mathbf{O_v}$:

- Standoff distance (SOD) is the distance along the *z*-axis of $\mathbf{O_v}$ to the camera rig.
- Baseline (BL) is two times the distance to either camera along the *x*-axis of $\mathbf{O_v}$ (we assume both cameras are equidistant from the rig origin of $\mathbf{O_r}$). This is equivalent to the normal definition of baseline which is simply the straight-line distance between camera origin points.
- Perpendicular distance (PD) is measured along the *y*-axis of $\mathbf{O_v}$.

The user defines the ranges that SOD, BL, and PD may fall within based on the space available around the test object. The camera positions with respect to $\mathbf{O_v}$ are shown in Eq. (3.2). The coordinates $\mathbf{C}_i$ are also the origin points of the respective camera coordinate systems $\mathbf{O}_i$. The stereo angle, θ_{stereo}, is the angle formed between the optical axes of the cameras (see Fig. 3.4). Typical stereo DIC tests will be performed in the ~20–30° stereo angle range [2] as this provides a balance between resolving out-of-plane motions and image correlation breakdown. For the planning workflow, the user defines the stereo angle or stereo angle range to consider. Referring back to Fig. 3.2, note that the stereo angle is not changed when iterating the SOD, BL, or PD; some configurations will obviously not properly frame the bounding box within the image and are rejected.

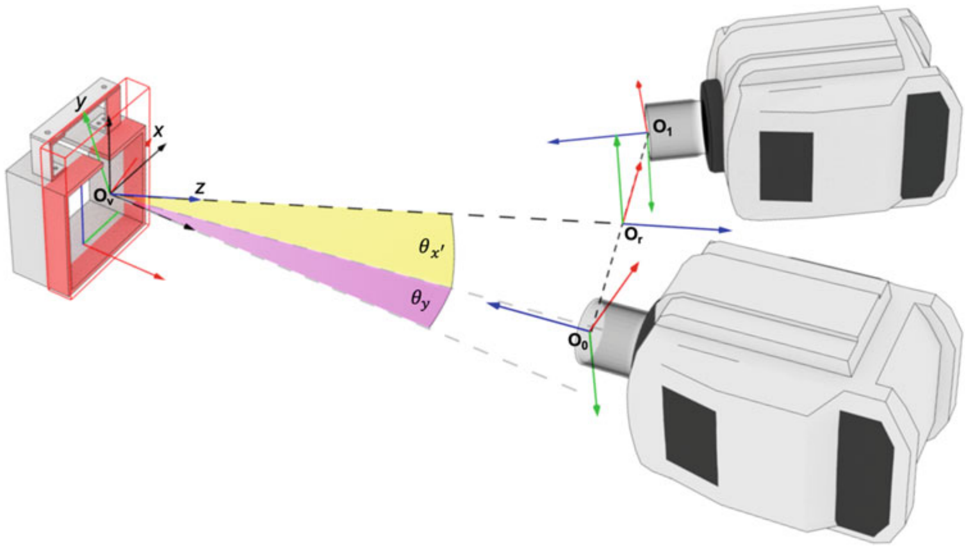

Fig. 3.5 Stereo setup with example view angle change

$$\left.\begin{aligned} \boldsymbol{C}_0 &= \left(\tfrac{-\mathrm{BL}}{2}, \mathrm{PD}, \mathrm{SOD}\right)^T \\ \boldsymbol{C}_1 &= \left(\tfrac{\mathrm{BL}}{2}, \mathrm{PD}, \mathrm{SOD}\right)^T \end{aligned}\right\} \text{if stand orientation is horizontal}$$
$$\left.\begin{aligned} \boldsymbol{C}_0 &= \left(\mathrm{PD}, \tfrac{-\mathrm{BL}}{2}, \mathrm{SOD}\right)^T \\ \boldsymbol{C}_1 &= \left(\mathrm{PD}, \tfrac{\mathrm{BL}}{2}, \mathrm{SOD}\right)^T \end{aligned}\right\} \text{if stand orientation is vertical} \tag{3.2}$$

We now have the tools necessary to project the bounding box 3D coordinates into image pixels for either camera. Referring to the form of Eq. (3.1) and noting that transformation matrices can be chained together, the 3D–2D projection from the bounding box to image space is:

$$\mathbf{u}_i = \mathbf{K}_i \mathbf{R}_{i\mathbf{v}} [\mathbf{I}|\mathbf{C}]_i \mathbf{R}_{\mathbf{vb}} \mathbf{X}_{\mathbf{b}}$$
$$\begin{bmatrix} au \\ av \\ a \end{bmatrix}_i = \begin{bmatrix} f_x & q & c_x \\ 0 & f_y & c_y \\ 0 & 0 & 1 \end{bmatrix}_i \begin{bmatrix} r_{xx} & r_{xy} & r_{xz} \\ r_{yx} & r_{yy} & r_{yz} \\ r_{zx} & r_{zy} & r_{zz} \end{bmatrix}_{i\mathrm{v}} \begin{bmatrix} 1 & 0 & 0 & C_\mathrm{x} \\ 0 & 1 & 0 & C_\mathrm{y} \\ 0 & 0 & 1 & C_\mathrm{z} \end{bmatrix}_i \begin{bmatrix} r_{xx} & r_{xy} & r_{xz} & 0 \\ r_{yx} & r_{yy} & r_{yz} & 0 \\ r_{zx} & r_{zy} & r_{zz} & 0 \\ 0 & 0 & 0 & 1 \end{bmatrix}_{\mathrm{vb}} \begin{bmatrix} X \\ Y \\ Z \\ 1 \end{bmatrix}_{\mathrm{b}} \tag{3.3}$$

where $\mathbf{R}_{i\mathbf{v}}$ takes into account the camera z-axis flip and stereo angle by rotating $\mathbf{O}_\mathbf{v}$ to $\mathbf{O}_i$ as described by the Euler angles (in radians):

$$\left.\begin{aligned} \left(\theta_x, \theta_{y'}, \theta_{z''}\right)_{0\mathrm{v}} &= \left(-\pi, \tfrac{-\theta_{\mathrm{stereo}}}{2}, 0\right) \\ \left(\theta_x, \theta_{y'}, \theta_{z''}\right)_{1\mathrm{v}} &= \left(-\pi, \tfrac{\theta_{\mathrm{stereo}}}{2}, 0\right) \end{aligned}\right\} \text{if stand orientation is horizontal}$$
$$\left.\begin{aligned} \left(\theta_x, \theta_{y'}, \theta_{z''}\right)_{0\mathrm{v}} &= \left(-\pi, \tfrac{\theta_{\mathrm{stereo}}}{2}, 0\right) \\ \left(\theta_x, \theta_{y'}, \theta_{z''}\right)_{1\mathrm{v}} &= \left(-\pi, \tfrac{-\theta_{\mathrm{stereo}}}{2}, 0\right) \end{aligned}\right\} \text{if stand orientation is vertical} \tag{3.4}$$

Since no actual camera calibration is performed in the planning workflow, we must make assumptions in order to populate $\mathbf{K}_i$. First, we assume the actual focal length of the lenses, f, is the nominal manufacturer value (e.g., 50 mm) and the pixel size is square such that $f_x = f_y = f/\epsilon$. Further, we assume the optical axis is aligned with the center of the image such that $c_x = s_x/2$ and $c_y = s_y/2$. Finally, in most test scenarios, the skew is negligible, and one can assume $q = 0$.

From right to left, the terms in Eq. (3.3) effectively take the 3D coordinates of the bounding box in $\mathbf{O_b}$, transform them into $\mathbf{O_v}$, translate them to the camera positions, rotate them into $\mathbf{O}_i$, and finally project them into image space. Thus, for a user-defined stereo angle and desired viewing angle, one can iterate over the camera positions $\mathbf{C}_i$ to find potential rig poses for which the bounding box is completely contained and centered in both camera images.

The iteration process is outlined in the blue boxes on the right side of Fig. 3.2. For each stereo angle considered, the workflow will loop over all lenses specified in the catalog, allowing the intrinsic matrices $\mathbf{K}_i$ to be formed. For a first pass, we assume the full sensor size will be used (no sensor cropping). Next, the workflow loops over each SOD in the range specified by the user. At each SOD step, first assume a PD of zero, and iterate over all BL values in the user-defined range to find which best centers the bounding box in both images using Eq. (3.3). The camera stand orientation will change which image dimension will be affected by a change in BL: u if stand is horizontal (c_x is the center target) and v if vertical (c_y is the center target). Hence, the optimal BL will minimize the difference between the center target and the mean of the projected bounding box points. This must be done for both cameras which will have competing "optimal" values, meaning the center target errors from both cameras should be evaluated together (e.g., minimizing the RMS error values from both cameras). Similarly, the next step is to assume the BL just calculated and iterate over each PD in the user-defined range, finding the value that best centers the bounding box in the associated image dimension depending on stand orientation.

This process produces the optimal BL and PD for the current SOD iteration; however, there is no guarantee yet that together these $\mathbf{C}_i$ values will project the bounding box completely within the image space. Thus, the optimal values for this SOD are passed into Eq. (3.3), and the projection is checked to see if all points fall within the (full) image size. At some instance, as SOD iterates outward, the entirety of the bounding box will fit within both camera images. Clearly, some configurations will run out of positional range before this occurs, in which case the current SOD is abandoned, and the next iteration begins.

Even when the bounding box is properly framed in the image, there will often be "wasted pixels" where the bounding box does not fill the image in both directions. In such cases, it makes sense to crop the sensor appropriately and minimize the image size. The optimal image size is easily determined since the bounding box pixel positions, and thus extent in both image directions, have already been calculated. However, cropping the image size necessitates recalculating new intrinsic camera matrices, $\mathbf{K}_i$. Further, a subroutine must be performed in which the current SOD iteration is increased slightly to account for the zoom effect of cropping the sensor, and the BL and PD optimization iterations are re-performed. The end result is an optimized image size and camera positions (for the current θ_{stereo}, lens, and SOD). Note the user-defined resolution of the steps in the ranges provided for SOD, BL, and PD will determine how accurately the algorithm can center the bounding box.

3.3.4 Pose Validation

Once a potential pose is established, the optical viability must be evaluated (green box, bottom right of Fig. 3.2). The current version of the planning workflow evaluates for lens minimum focal distance, DOF, and lens diffraction limitations.

The minimum focal distance and DOF checks can be easily accomplished by recognizing that the bounding box coordinates can be transformed into 3D camera coordinates $\mathbf{O}_i$ by leaving the $\mathbf{K}_i$ out of Eq. (3.3) as:

$$\mathbf{x}_i = \mathbf{R}_{i\mathbf{v}}[\mathbf{I}|\mathbf{C}]_i\mathbf{R}_{\mathbf{vb}}\mathbf{X}_\mathbf{b}$$
$$\begin{bmatrix} x \\ y \\ z \end{bmatrix}_i = \begin{bmatrix} r_{xx} & r_{xy} & r_{xz} \\ r_{yx} & r_{yy} & r_{yz} \\ r_{zx} & r_{zy} & r_{zz} \end{bmatrix}_{i\text{v}} \begin{bmatrix} 1 & 0 & 0 & C_\text{x} \\ 0 & 1 & 0 & C_\text{y} \\ 0 & 0 & 1 & C_\text{z} \end{bmatrix}_i \begin{bmatrix} r_{xx} & r_{xy} & r_{xz} & 0 \\ r_{yx} & r_{yy} & r_{yz} & 0 \\ r_{zx} & r_{zy} & r_{zz} & 0 \\ 0 & 0 & 0 & 1 \end{bmatrix}_{\text{vb}} \begin{bmatrix} X \\ Y \\ Z \\ 1 \end{bmatrix}_\text{b} \tag{3.5}$$

Once all bounding box points have been transformed to the camera CS, we can find the center value of their z-coordinates:

$$s_i = (\max(z_i) + \min(z_i))/2 \tag{3.6}$$

Ideally, the focused plane should lie at the center of the bounding box volume. Since the z-axis is the optical axis of the camera, s_i corresponds to the distance between the focused plane and the lens. Therefore, if the calculated focus distances are greater than or equal to the minimum focal distance of the lens, such that Eq. (3.7) is true, the pose is considered valid. Generally, a relaxation of the equality is beneficial in actual application, in the form of the user-defined tolerance (e.g., $\geq$0.95). Note that we have dropped the i subscript denoting individual cameras, but the check must be performed for both cameras.

$$s/s_{\min} \geq 1 \tag{3.7}$$

Next we consider DOF requirements to ensure the entire bounding box will be in focus for both cameras. Since the DOF is a function of the lens aperture setting, we must consider each *f*-stop value, *N*, of the lens under consideration. The estimated DOF for near and far points is [12]:

$$\begin{aligned} \mathrm{DOF}_{\mathrm{near}} &= \tfrac{Hs}{H+s} \\ \mathrm{DOF}_{\mathrm{far}} &= \tfrac{Hs}{H-s} \end{aligned} \tag{3.8}$$

where H is the hyperfocal distance, given as:

$$H = \frac{f^2}{Nc} \tag{3.9}$$

and c is the acceptable circle of confusion, which is a user-defined value. The circle of confusion is the largest diameter of a spot that will be perceived as a point; it can conservatively be set to the size of one pixel.

Using the coordinates of the bounding box in the camera CS from Eq. (3.5), we can check if the extrema in the z-dimension of both cameras are bounded by the calculated DOF for each aperture f-stop to determine if the configuration is valid within a user-defined tolerance:

$$\begin{aligned} &\tfrac{\min(\mathbf{z})}{\mathrm{DOF}_{\mathrm{near}}} \geq 1 \\ &\tfrac{\mathrm{DOF}_{\mathrm{far}}}{\max(\mathbf{z})} \geq 1 \end{aligned} \tag{3.10}$$

Finally, if both the minimum focus distance and DOF checks are valid, the lens diffraction is estimated. In an optical system with a circular aperture, a point is not imaged as a point but rather as an Airy disk, which has one central lobe and sequentially degrading concentric diffraction rings [13]. The diameter of the Airy disk is:

$$D = 2.44\lambda N \tag{3.11}$$

where λ is the wavelength of the light entering the lens. Since the Airy diameter represents the smallest theoretical spot size that can be imaged, we consider the optical system to be diffraction (lens) limited when D is greater than the pixel size, such that a valid configuration will satisfy the following equality within a user-defined tolerance:

$$\epsilon/D \geq 1 \tag{3.12}$$

If a pose configuration passes all three optical validation checks, it is flagged as viable, and all relevant parameters are recorded. The process is repeated for the next iteration of SOD → lens → stereo angle.

The camera positions in $\mathbf{O_v}$ are already given by SOD, BL, and PD values as given in Eq. (3.2). It may be more convenient to also record these coordinates in the bounding box system, $\mathbf{O_b}$, which may be easier to physically measure when actually positioning the cameras for a test:

$$\mathbf{G}_i = \mathbf{R_{vb}}^{\mathrm{T}}\mathbf{C}_i \tag{3.13}$$

where $^{\mathrm{T}}$ indicates the matrix transpose. Similarly, the camera positions can be recovered in the world (FEM) coordinate system $\mathbf{O_w}$ by use of the transformation between world and bounding box $\mathbf{[R|T]_{bw}}$ established in Sect. 3.3.2:

$$\begin{aligned} \mathbf{W}_i &= \begin{bmatrix} \mathbf{R} & \mathbf{T} \\ 0 & 1 \end{bmatrix}_{\mathbf{bw}}^{-1} \begin{bmatrix} \mathbf{G}_i \\ 1 \end{bmatrix} \\ \begin{bmatrix} aw_x \\ aw_y \\ aw_z \\ a \end{bmatrix}_i &= \begin{bmatrix} r_{xx} & r_{xy} & r_{xz} & t_x \\ r_{yx} & r_{yy} & r_{yz} & t_y \\ r_{zx} & r_{zy} & r_{zz} & t_z \\ 0 & 0 & 0 & 1 \end{bmatrix}_{\mathrm{bw}}^{-1} \begin{bmatrix} g_x \\ g_y \\ g_z \\ 1 \end{bmatrix}_{\boldsymbol{i}} \end{aligned} \tag{3.14}$$

A list of the primary results to record for each viable pose would include:

- Lens settings (N, s)
- θ_{stereo}
- Optimized image size (pixels, pixels)
- $\mathbf{C}_i$ camera positions in $\mathbf{O_v}$ (SOD, BL, PD)
- $\mathbf{G}_i$ camera positions in $\mathbf{O_b}$
- $\mathbf{W}_i$ camera positions in $\mathbf{O_w}$
- Optical validation parameter results
- Camera intrinsic matrices
- Transformation matrices used

3.3.5 Evaluating Output and Final Pose Selection

The workflow, as presented, will likely output many (thousands) viable pose configurations. For example, for a given stereo angle, there can be viable poses for each lens, at multiple SODs, and with multiple lens aperture settings. We can easily reduce the number of viable poses to a more refined set by realizing that only the pose with the minimum SOD is optimal in the sense that it maximizes the number of pixels across the bounding box. Simply flagging the first configuration with a SOD that results in a valid pose as optimal is recommended. Additionally, an "image" of how this pose projects the bounding box into the image space is useful and easily accomplished with Eq. (3.3). This reduces the output to contain only the best pose for each lens in the catalog and its corresponding range of N that will provide adequate DOF and prevent lens diffraction. From this reduced list, the user can easily pick which lens and aperture setting make the most sense for the test at hand.

As an example, if we wished to set up a test similar to that shown in Fig. 3.5 with the user inputs listed in Table 3.1, there are thousands of valid poses that are found (exact number will depend on the input parameters such as the number of lenses available, SOD/BL/PD range and step size, and number of stereo angles considered). The optimal set is reduced to the number of lenses in the user catalog (in this case 9). Examples from two different lenses are shown in Fig. 3.6. The red face represents the front (camera-facing) surface of the bounding box, with a line drawn to the origin of $\mathbf{O_b}$.

Table 3.1 User-defined inputs for example viewing angle shown in Fig. 3.5

Cameras	**Phantom v2640 UHS** – Sensor size = [2048, 1920] px – Pixel size = 0.0135 mm
Lenses	**Zeiss Milvus 2.8/18 mm** – Minimum focal dist = 250 mm – Aperture range = [22, 1.8]
	Zeiss Milvus 2.0/135 mm – Minimum focal dist = 800 mm – Aperture range = [22, 2.0]
Camera orientation	Horizontal
Camera stand orientation	Horizontal
Stereo angle (degrees)	30
Bounding box [b_x, b_y, b_z] (mm)	[152.4, 206.4, 38.1]
Bounding box margin %(x, y, z)	[0, 0, 0]
Viewing Euler angles (degrees; y, x', z'')	[−10, 15, 0]
SOD range (mm)	[200:5:5000]
BL range (mm)	[200:5:5000]
PD range (mm)	[−20:5:30]
Minimum focus check tolerance	0.95
DOF check tolerance	0.95
Lens diffraction check tolerance	0.95
Acceptable circle of confusion (mm)	0.0135
Lighting wavelength (mm)	6.00E−04

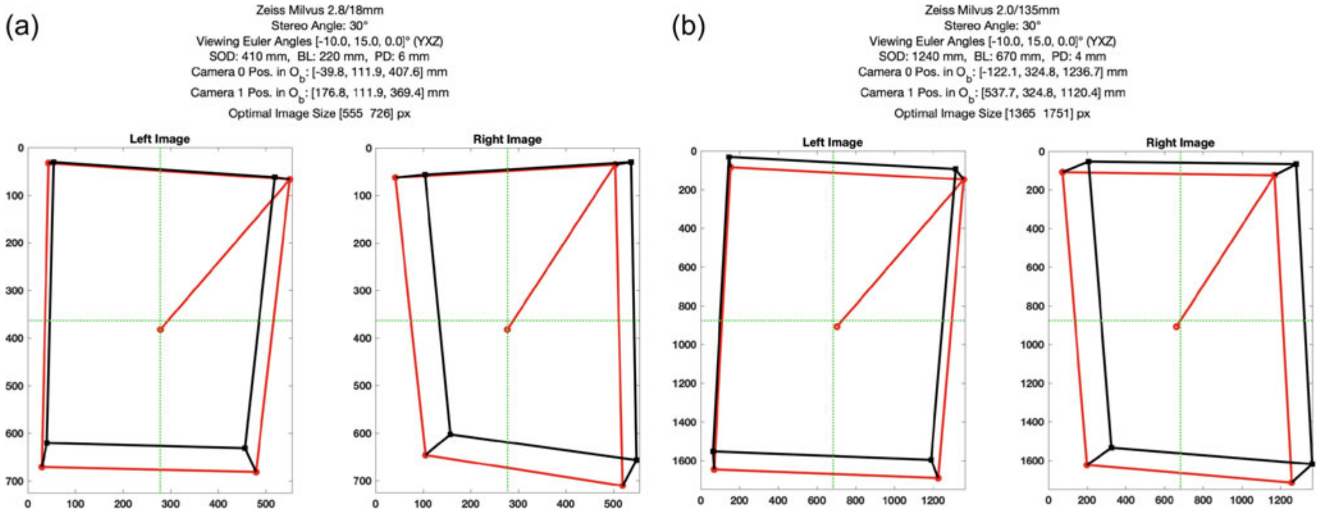

Fig. 3.6 Example results for optimal pose configurations for the example viewing angle shown in Fig. 3.5; (**a**) 18 mm lens, (**b**) 135 mm lens

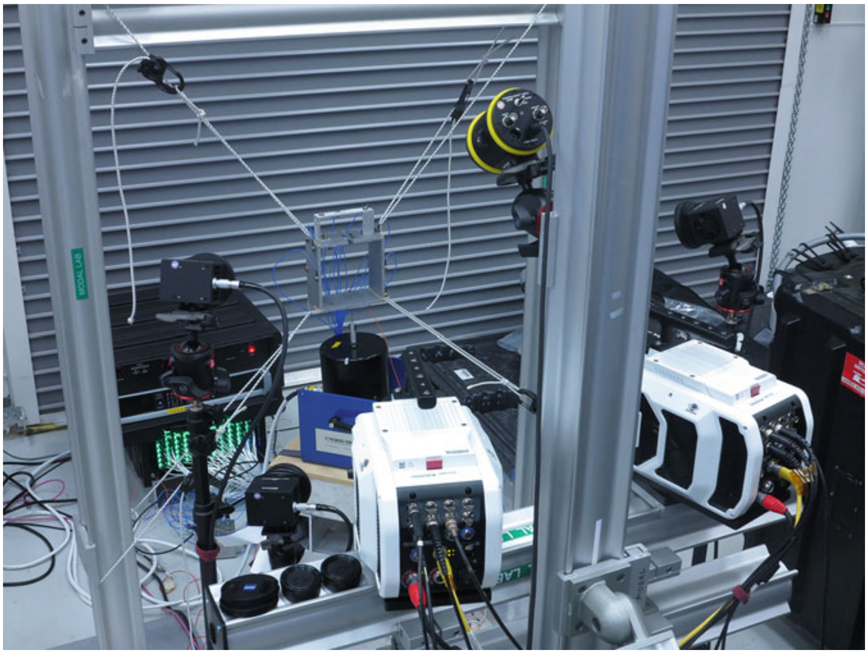

Fig. 3.7 Example stereo DIC test of the BARC structure

An example DIC test was performed on the BARC with the camera rig positioned directly in front of the test article, similar to the configuration depicted in Fig. 3.4, as shown in Fig. 3.7.

The test planning tool was used to estimate the optimal camera position for this test using the settings in Tables 3.1, 3.2 and 3.3. The optimized pose results (specifically the camera intrinsic and extrinsic parameters that locate the cameras with respect to the world coordinate system) were imported into an image rendering software, Blender [14], along with the FEM of the BARC. The rendered images are overlaid on the planning tool results for the optimized setup in Fig. 3.8, validating the selected pose for an idealized optical system and perfect camera placement in the real world.

However, in practice it is difficult to place the cameras in the exact locations specified by the planning tool output. Slight shifts in the actual placement are expected, along with asymmetry between the two cameras with respect to the rig origin. Another known difficulty with estimating the composition of the bounding box within the image frame is the phenomenon of lens "focus breathing" where the image composition changes as the focus distance is changed. Further confounding the issue is that, in some lenses, breathing will cause an apparent increase in magnification as focal distance increases, while

Table 3.2 Optimal vs. as-tested camera positions

	Camera 0				Camera 1			
Pose in Ob (mm)	Optimal	As-Tested	Error (mm)	Error (%)	Optimal	As-Tested	Error (mm)	Error (%)
X	−195	−219	24	13%	195	182	13	7%
Y	0	10	−10	–	0	9	−9	–
Z	728	768	−40	6%	728	777	−49	7%

Table 3.3 User-defined inputs for the stereo-DIC BARC test

Cameras	**Phantom v2640 UHS** – Sensor size = [1536, 1920] px – Pixel size = 0.0135 mm
Lenses	**Zeiss Milvus 1.4/85 mm** – Minimum focal dist = 800 mm – Aperture range = [16, 1.4]
Camera orientation	Horizontal
Camera stand orientation	Horizontal
Stereo angle (degrees)	30
Bounding box $[b_x, b_y, b_z]$ (mm)	[152.4, 206.4, 38.1]
Bounding box margin %(x, y, z)	[5, 5, 5]
Viewing Euler angles (degrees; y, x', z'')	[0, 0, 0]
SOD range (mm)	[200:5:5000]
BL range (mm)	[200:5:5000]
PD range (mm)	[−20:5:20]
Minimum focus check tolerance	0.95
DOF check tolerance	0.95
Lens diffraction check tolerance	0.75
Acceptable circle of confusion (mm)	0.0135
Lighting wavelength (mm)	6.00E−04

other lenses do exactly the opposite. The current tool only deals with this issue by applying a margin to the bounding box volume. As such, the user should be cognizant of the margin used and understand the degree to which the lenses available exhibit this behavior.

The as-tested pose configuration was quantified by performing a stereo camera calibration and importing the resulting intrinsic and extrinsic parameters (see Eq. 3.1) into Blender, as was done for the optimized configuration. The as-tested configuration was then synthesized within Blender allowing for the accurate calculation of the camera positions. The differences between the optimized and as-tested camera positions were found to be on the order of approximately 10%:

The (non-optimal) output from the test planning tool that most directly corresponded to the as-tested configuration with the actual test images overlaid is shown in Fig. 3.9. The effects of focus breathing are immediately observable, in that the estimated projections are not quite zoomed in far enough (apparent lens focal length is too small). The positioning errors are also observable, as evidenced by the actual test images not being exactly centered. Even with these issues, the test planning tool provided a very good first-order estimate of which lens to select and the corresponding camera positions which would properly frame the test object (refer to Fig. 3.8); from this estimate a successful, but not perfect, test setup was easily created.

The positioning errors are strictly a function of how much time the user devotes to the test setup. The focus breathing phenomenon is the primary source of uncertainty (barring massive lens distortions). Future revisions of the planning tool may look to make the focal length of the lens a function of focus distance in the iterative optimization routine, although this would require very thorough experimental characterizations of each lens by the user. As a rough validation, the planning tool was re-run with a lens focal length of 93 mm to account for focus breathing, and the test images were artificially shifted to center the BARC within the image frames, as shown in Fig. 3.10. While this is merely a qualitative comparison, it does provide a level of expectation that if focus breathing is accounted for and camera positioning is exact, the planning tool and actual images should align quite well.

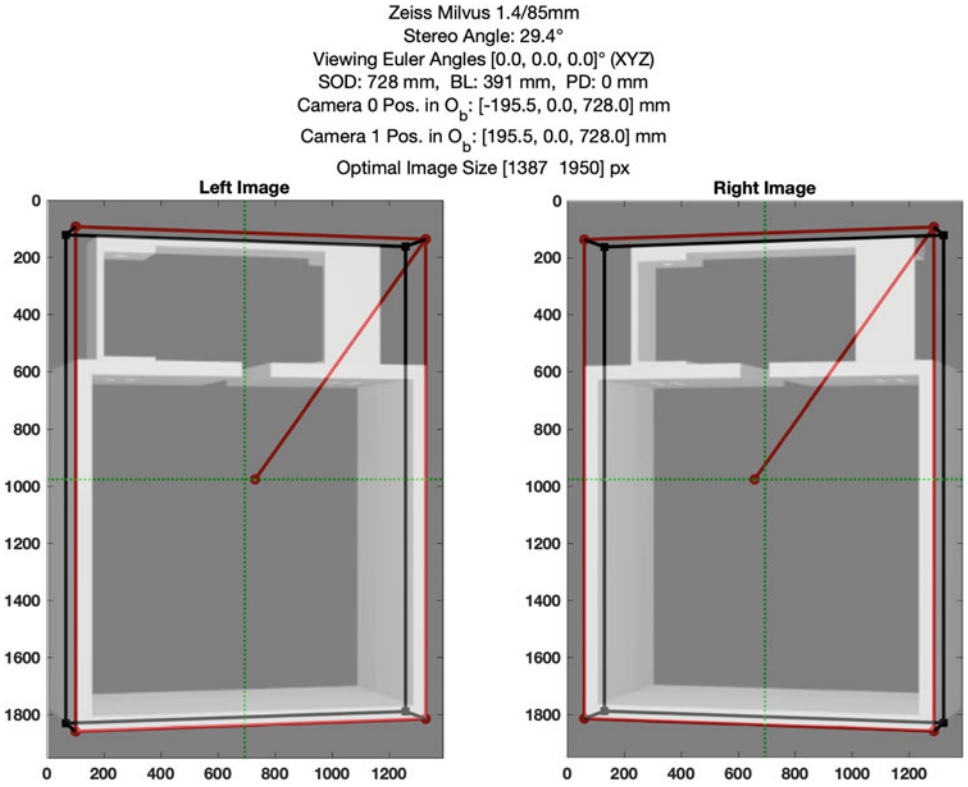

Fig. 3.8 Optimized pose selected for BARC stereo DIC test

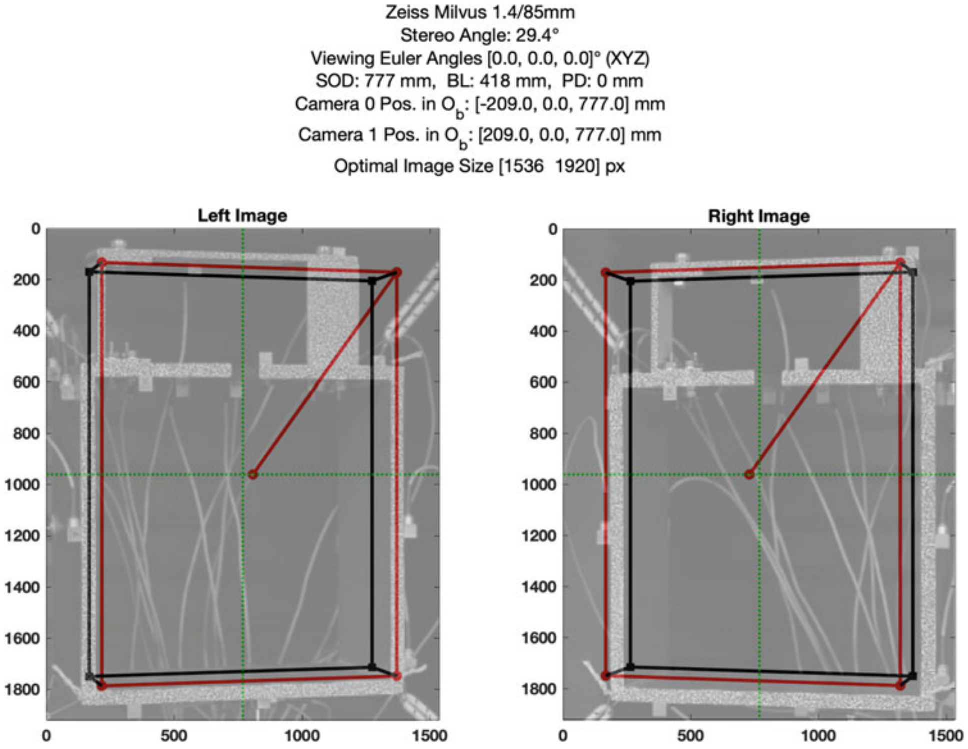

Fig. 3.9 As-tested pose for stereo DIC BARC test

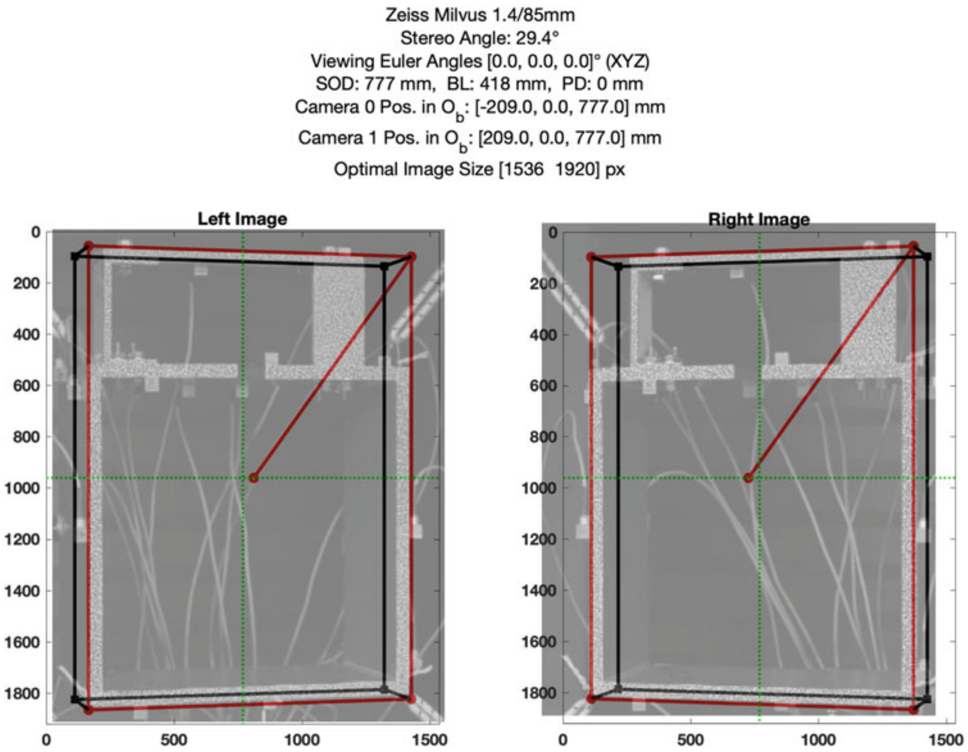

Fig. 3.10 As-tested pose artificially adjusted for camera translation and focus breathing ($f = 93$ mm)

3.4 Predicting Observable Pixel Displacements with FEM

Once the pose optimization has been performed as outlined in Sect. 3.3, a final camera pose is selected, and the resulting parameters are fed into the next stage of pre-test analysis which utilizes the FEM. In this section, all quantities are defined in the world (FEM) coordinate system $\mathbf{O_w}$. As a separate analysis, this section utilizes different variable definitions from those provided in Sect. 3.3, which are defined at the point of use. This analysis would also be performed prior to setting up any test equipment; the test examples shown in the previous section were to demonstrate the effectiveness of the pose estimation algorithm.

3.4.1 Algorithm to Determine Node Visibility from Camera Placements

The mesh of the test article of interest is created using CUBIT, a meshing toolkit produced by Sandia National Laboratories (SNL) [15]. Within CUBIT, the test article mesh is exported as an EXODUS file (*.exo) compatible with Sierra Structural Dynamics (SD) analyses, a SNL-produced module for the Sierra engineering mechanics simulation code suite [16]. In the definition of the mesh of the test article, the global placement of the mesh should be consistent with the coordinate system definitions and placement of the bounding box around the finite element model (FEM) in the camera setup tool discussed in Sect. 3.3. In the definition of the mesh, surfaces that are candidates for measurement with digital image correlation (DIC) can be defined as sidesets. The CUBIT mesh of the example test article is shown in Fig. 3.11a.

The mesh information, including node coordinate, connectivity, and model output data from a normal mode analysis, are imported into MATLAB. The nodes on the external sides of the test article model can be identified from the connectivity information to form a set of planes that represent the exterior of the test article, which is shown in Fig. 3.11b. This information along with the sideset representing prospective measurement nodes, shown as red points in Fig. 3.11c, comprises the user information required in order to predict the observable nodal displacements from a camera position.

In addition to the definition of the set of nodes and planes that form the exterior surface, as well as the prospective measurement nodes, camera placements are designated to represent the test setup geometry as provided by the iterative optimization process from Sect. 3.3. Figure 3.12 shows how lines are formed from each of the cameras placed, Camera 1

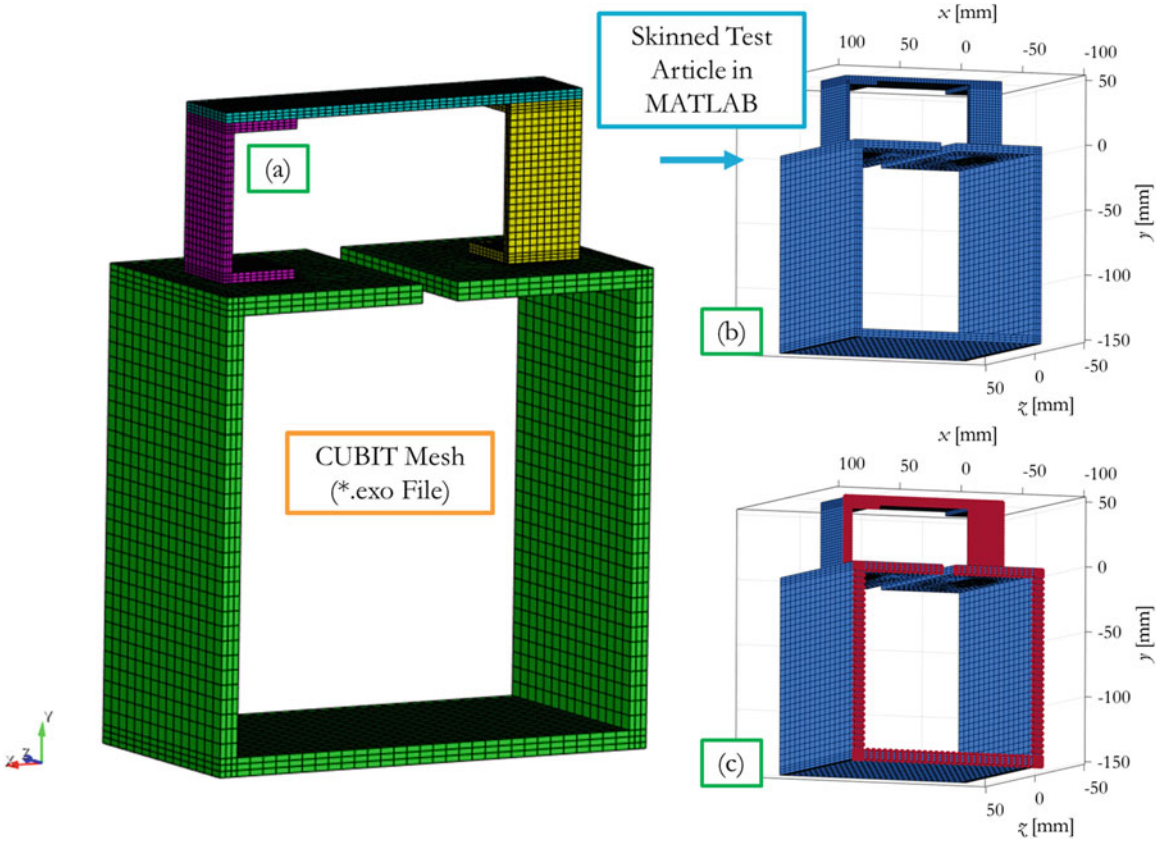

Fig. 3.11 Initial steps to determine observable nodes in FEM of test article based on camera parameters and test setup with a (**a**) mesh defined in CUBIT processed in MATLAB (**b**) without and (**c**) with the prospective measurement surface nodes highlighted

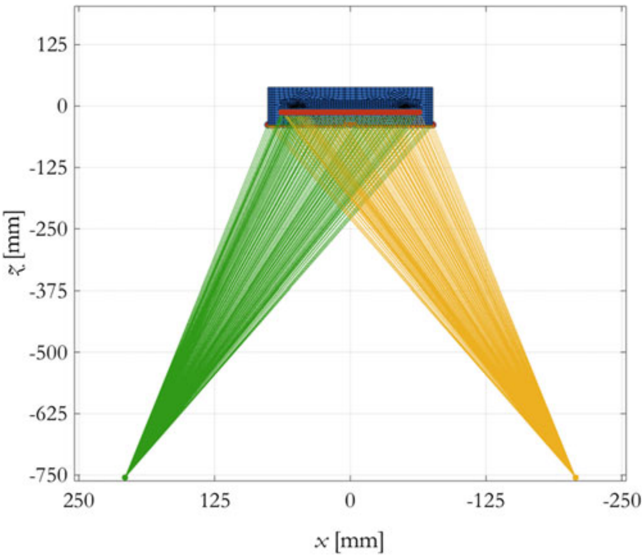

Fig. 3.12 Camera placement and definition of lines representing camera views of each node in a prospective speckling area

(green point) and Camera 0 (yellow point), to each of the prospective nodes, shown as red points, for example, digital image correlation setup and determination of visible nodes. This tool currently assumes small displacements, such that excitation of the part does not cause nodes to go in/out of visibility.

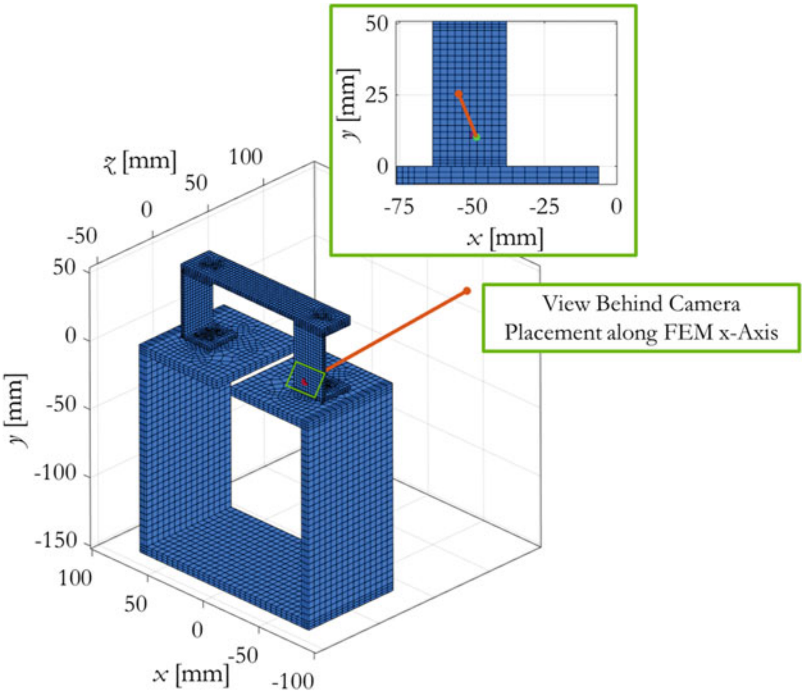

Fig. 3.13 Definition of single view line from camera to a node of interest from a poorly placed camera relative to surface of interest

The camera placements shown in Fig. 3.12 are an effective set for observing the prospective measurement points chosen. Figure 3.13 shows a poorly placed camera position (orange point, behind the area of interest) viewing the single red measurement point to show the detection of nonvisible nodes due to view obstructions. The green inset of Fig. 3.13 shows the view behind the poor camera placement, which highlights the detected intersection point in green.

Any intersection of a view line with an exterior surface of the model is calculated by checking to see if the view line intersects with any of the planes forming the exterior surface and if the intersection point falls within the edges of the element face being represented by the plane. The intersection shown in the inset of Fig. 3.13 is shown in greater detail in Fig. 3.14. Once the test article is skinned and prospective measurement nodes are defined, the toolset starts with determining if any intersections occur for the view line, or ray, from the camera position to each of the nodes of the prospective measurement set. The toolset can be used for hexahedral and tetrahedral meshes without significant user input since the script detects what mesh is used for each component of the test article. A slightly different approach is leveraged to detect what prospective measurement nodes are obstructed depending on the mesh type.

The intersection example shown in Fig. 3.14 is based on a hexahedral mesh, which is implemented on the BARC test article. Edge 1, $\mathbf{v_{12}}$, is defined between Vertex 1 (yellow point) and Vertex 2 (red point), and Edge 2, $\mathbf{v_{14}}$, is defined between Vertex 1 (yellow point) and Vertex 4 (gray point). Using the edge definitions, the plane normal can be defined as:

$$\mathbf{n} = [D, E, F] = \mathbf{v_{12}} \times \mathbf{v_{14}} \tag{3.15}$$

where D, E, and F denote the components of the normal vector for the plane being intersected. Once the normal $c =$ vector for the current plane is determined, the general form of the equation of the plane can be defined as:

$$D\mathbf{x} + E\mathbf{y} + F\mathbf{z} = 0 \tag{3.16}$$

which can be defined with the parametric definition of the camera view line to determine if the view line intersects the plane, is parallel to the plane, or exists in the plane when extending the plane to infinity.

The parametric line definition for the camera view is:

$$\begin{aligned} x_{CV}(s) &= x_c + Us \\ y_{CV}(s) &= y_c + Vs \\ z_{CV}(s) &= z_c + Ws \\ \mathbf{u_{Camera}} &= [U, V, W] = [x_{mn} - x_c, y_{mn} - y_c, z_{mn} - z_c] \end{aligned} \tag{3.17}$$

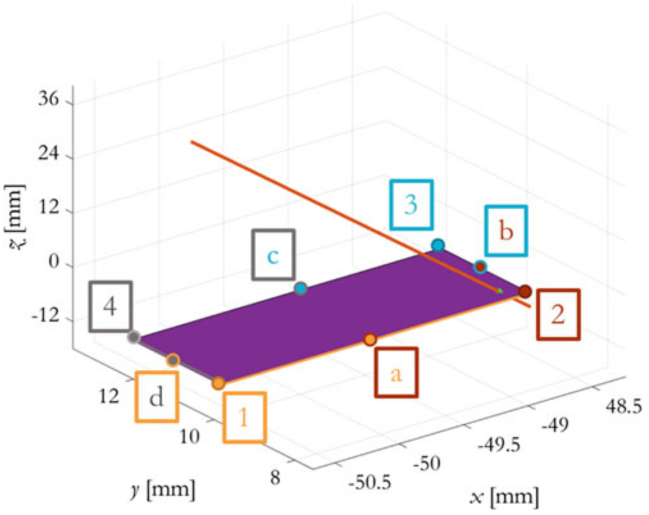

Fig. 3.14 An example of an intersection point and intersect exterior plane on the FEM of the test article based on poor camera placement

where $\mathbf{u}_{\mathbf{Camera}}$ denotes a vector representing the camera optical axis, $[x_c, y_c, z_c]$ is the camera position in Cartesian coordinates shown as the orange point in Fig. 3.13, and $[x_{mn}, y_{mn}, z_{mn}]$ is the location of the measurement node shown as the red point in Fig. 3.13. If $\mathbf{u}_{\mathbf{Camera}}$ is perpendicular to $\mathbf{n}$, the view line lies within the plane or is parallel to the plane at an offset. If the following equality is satisfied with $\mathbf{u}_{\mathbf{Camera}}$ perpendicular to $\mathbf{n}$:

$$\mathbf{n} \cdot \mathbf{r}_{\mathbf{Camera}} - \mathbf{n} \cdot \mathbf{r}_{\mathbf{1}} = 0 \tag{3.18}$$

where $\mathbf{r}_{\mathbf{1}}$ is the vector from the origin of the global Cartesian coordinate frame to Vertex 1 and $\mathbf{r}_{\mathbf{Camera}}$ the vector from the origin to the camera placement; then the camera view line is contained within the plane. Otherwise, $\mathbf{u}_{\mathbf{Camera}}$ being perpendicular to $\mathbf{n}$ implies that the camera view line is parallel to the current plane being analyzed on the exterior surfaces of the test article.

If the dot product of $\mathbf{u}_{\mathbf{Camera}}$ and $\mathbf{n}$ is nonzero, the infinite representation of the plane and camera optical axis intersects at a single point. The intersection point is defined as:

$$\mathbf{r}_{\mathbf{Intersection}} = \mathbf{r}_{\mathbf{Camera}} - \mathbf{u}_{\mathbf{Camera}} \left(\frac{-\mathbf{n} \cdot \mathbf{r}_{\mathbf{1}} + \mathbf{n} \cdot \mathbf{r}_{\mathbf{Camera}}}{\mathbf{n} \cdot \mathbf{u}_{\mathbf{Camera}}} \right) \tag{3.19}$$

where $\mathbf{r}_{\mathbf{Intersection}}$ defines the vector from the origin to the intersection point (I), which is shown as the green point in the plane in Fig. 3.14. Up to this point in the calculations, the only difference between processing tetrahedral and hexahedral meshes is the number of edges of the plane being reduced by one, due to the element faces being triangles instead of quadrilaterals and Edge 2 being defined between Vertex 1 and Vertex 3 in a tetrahedral mesh in the above calculations.

When determining if the intersection point is contained within the edges of an exterior element face of the model, the methods differ slightly depending on the mesh type. For a hexahedral mesh, Varignon's theorem is used alongside Heron's formula to determine if the intersection point is contained on the element face of interest [17]. Varignon's theorem is used to calculate the area of the face of a hexahedral mesh that can be a general quadrilateral, which states for Fig. 3.13 that the area of the element face being represented by the finite plane is given as the sum of the area of the parallelogram $\overline{abcd}$ and triangles $\overline{1ad}$, $\overline{2ba}$, $\overline{3cb}$, and $\overline{4dc}$. The points a, b, c, and d in Fig. 3.14 are defined as follows:

$$\begin{aligned}
\mathbf{r}_{\mathbf{a}} &= \tfrac{1}{2}\left(\mathbf{r}_1 + \mathbf{r}_2\right) \\
\mathbf{r}_{\mathbf{b}} &= \tfrac{1}{2}\left(\mathbf{r}_2 + \mathbf{r}_3\right) \\
\mathbf{r}_{\mathbf{c}} &= \tfrac{1}{2}\left(\mathbf{r}_3 + \mathbf{r}_4\right) \\
\mathbf{r}_{\mathbf{d}} &= \tfrac{1}{2}\left(\mathbf{r}_4 + \mathbf{r}_1\right)
\end{aligned} \tag{3.20}$$

where $\mathbf{r_a}$, $\mathbf{r_b}$, $\mathbf{r_c}$, and $\mathbf{r_d}$ are the vectors from the origin to points a, b, c, and d, respectively. In Eq. (3.20), $\mathbf{r_2}$, $\mathbf{r_3}$, and $\mathbf{r_4}$ denote the vectors from the origin to points 2, 3, and 4 in Fig. 3.14, respectively.

This area can then be compared to the sum of the areas of the four triangles formed from the intersection point and the vertices of the plane of interest ($\overline{1I2}$, $\overline{2I3}$, $\overline{3I4}$, and $\overline{4I1}$), which denotes that the intersection point is on the element face if equal. The area of all the triangles can be calculated with Heron's formula:

$$\begin{aligned} s_{\mathrm{P}} &= \tfrac{1}{2}\left(T_{\mathrm{S1}} + T_{\mathrm{S2}} + T_{\mathrm{S3}}\right) \\ A_{\mathrm{T}} &= \sqrt{s_{\mathrm{P}}\left(s_{\mathrm{P}} - T_{\mathrm{S1}}\right)\left(s_{\mathrm{P}} - T_{\mathrm{S2}}\right)\left(s_{\mathrm{P}} - T_{\mathrm{S3}}\right)} \end{aligned} \tag{3.21}$$

where s_{P} denotes the semiperimeter of the triangle, A_{T} the area of the triangle, and T_{S1}, T_{S2}, and T_{S3} the side lengths of the triangle [17]. In the case of a tetrahedral mesh, Heron's formula is used in place of Varignon's theorem to calculate the area of the plane representing the current element face being analyzed based on the camera view line. Singularities associated with Heron's formula are not expected to cause issues when a quality mesh is used with low aspect ratios throughout. The above process is iterated throughout all the exterior faces of the test article mesh for each view line specified based on the optimized camera rig position (the final selection from the pose optimization routine in Sect. 3.3) and prospective measurement nodes. Additional constraints include accounting for intersection points that occur beyond the length of the camera view line (i.e., behind the measurement node) and verifying that the intersection point is the prospective measurement node. The edge of the camera view is enforced by leveraging the information about the image size and pixel transformation from the camera setup tool discussed in Sect. 3.3.

Figure 3.15 shows an example of the impact of camera placement on the viewable nodes in a prospective set of measurement nodes. The red lines in Fig. 3.15 are the sideset representing the nodes that are contained in the area that will be patterned for DIC, and the purple, orange, and green points represent possible camera placements denoted as 1, 2, and 3, respectively. Placing a camera in an obscured view or too close to the part doesn't allow for the complete set of measurement nodes to be observed and causes the nodes with maximum overall displacement to be missed in the camera, which is shown by comparing the view from camera position 3 (green inset) to either camera position 1 (purple inset) or camera position 2 (orange inset). This simple example shows the toolset is functional with minimum user input, which allows for it to be leveraged in iterative optimization process as well as automated setup procedures.

3.4.2 Definition of Frequency Response Functions to Assess Arbitrary Inputs

Figure 3.16 shows the representative model definition for the BARC test setup shown in Fig. 3.7. As stated in Sect. 3.4.1, the mesh was created in CUBIT. The final hexahedral mesh is shown in blue in Fig. 3.16 and consists of 8-node hexahedral elements (HEX8). Once the mesh was created, an eigenanalysis in Sierra SD was utilized to determine the modes of the structure using the *eigen* solution type and to inform a subsequent *modalfrf* study [16]. Figure 3.16 also shows the prospective measurement nodes in red.

The modal analysis for the BARC test article in Sierra SD was defined with free-free boundary conditions to replicate the test configuration:

$$0 = \left(\left(\mathbf{K} - \sigma\mathbf{M}\right) - \boldsymbol{\mu}\mathbf{M}\right)\boldsymbol{\phi} \tag{3.22}$$

where $\mathbf{K}$ denotes the stiffness matrix, $\mathbf{M}$ the mass matrix, $\boldsymbol{\phi}$ the eigenvectors, and $\boldsymbol{\mu}$ the eigenvalues of the shifted problem with shift σ, which must be a large negative value to ensure $\mathbf{K} - \sigma\mathbf{M}$ is nonsingular without being too large to impact the eigenvalue solver [16]. The shifted problem shown in Eq. (3.22) is used with *eigen* in Sierra SD since $\mathbf{K}$ is singular in the unshifted problem. Original eigenvalues can be obtained with the simple expression:

$$\boldsymbol{\omega} = \left(\boldsymbol{\mu} + \sigma\right)^2 \tag{3.23}$$

where $\boldsymbol{\omega}$ is the original eigenvalues of the unshifted problem. Figure 3.17 provides the first six flexible modes from the modal analysis of the BARC model in Sierra SD.

The inputs for the simulation are applied to the node closest to the location where the shaker is attached in the experimental test setup being represented, which is shown as the pink point in Fig. 3.16. The axis of the shaker is parallel to the y-axis, which is shown as the green arrow in Fig. 3.16. The mass of the input location is approximated as a portion of the mass of the elements containing the node located at the pink point in Fig. 3.16. Bolts of the joints connecting the removable component

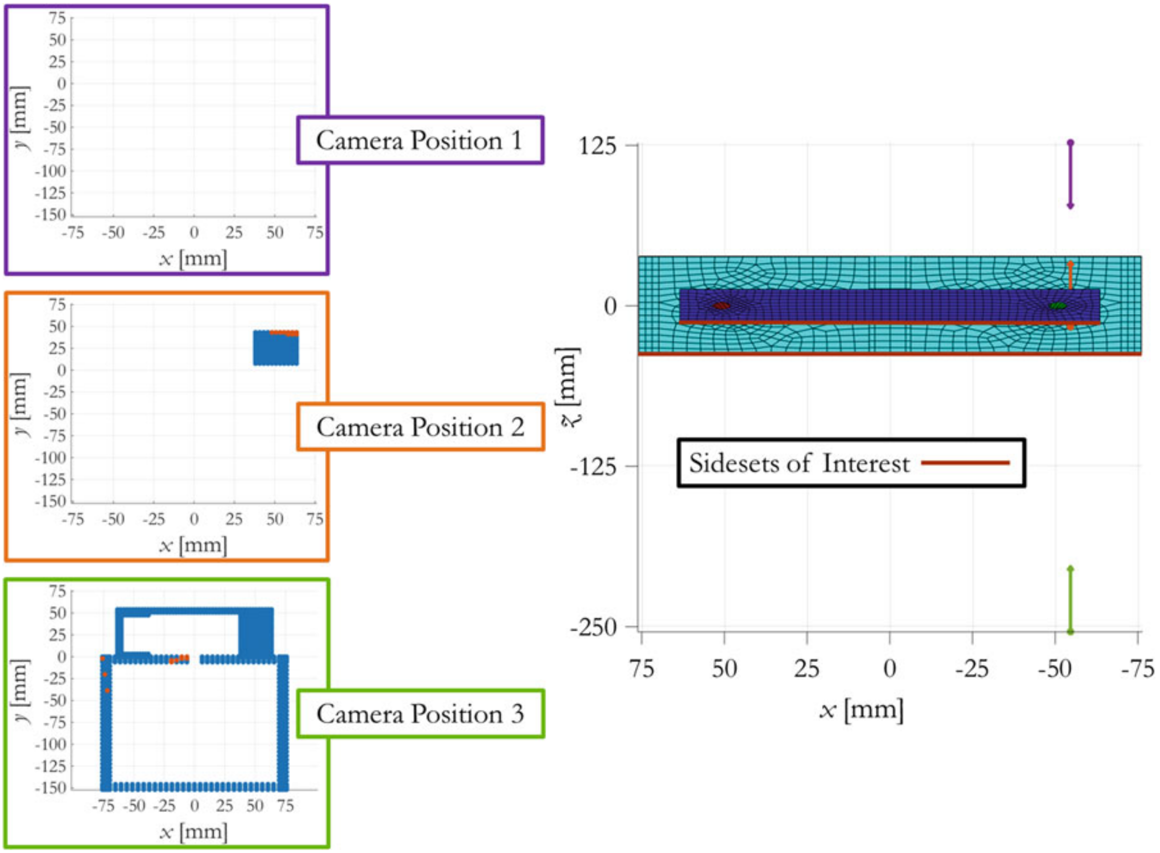

Fig. 3.15 Simulated impact of camera placement on valid measurement nodes in FEM

Fig. 3.16 Representation of BARC FEM for Sierra SD analysis

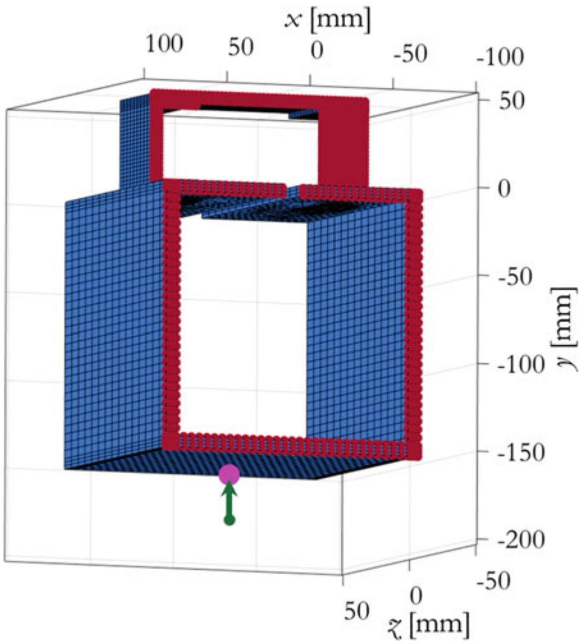

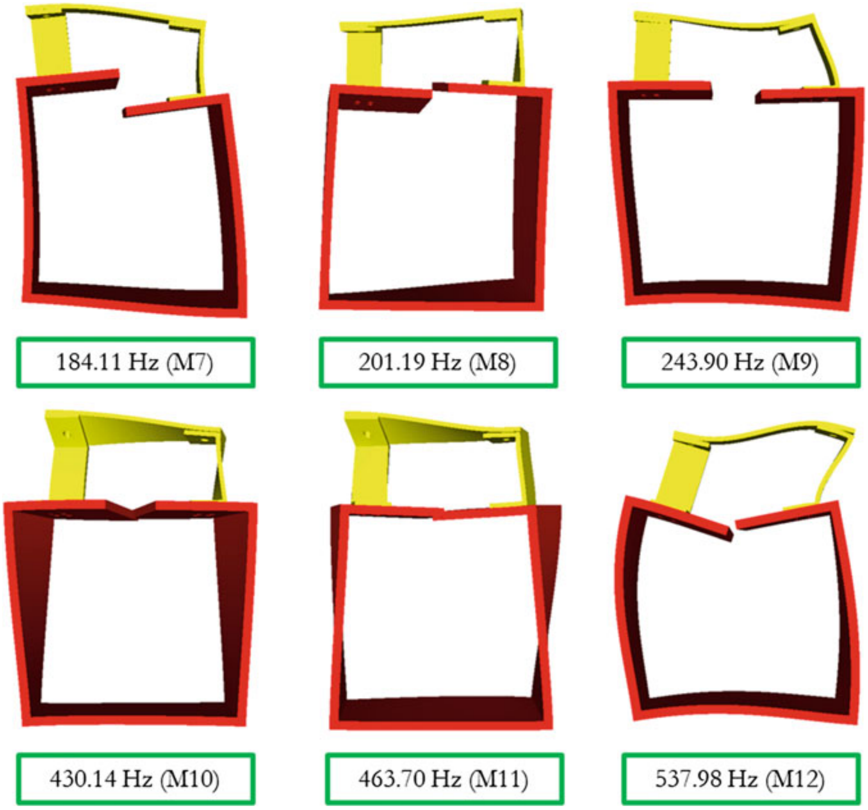

Fig. 3.17 First six analytical flexible modes of the BARC structure

(yellow component in Fig. 3.17) are defined using Joint2G elements, which provide the ability to define the constitutive behavior for each degree of freedom of the bolt represented by a node pair. The bolt representation is then connected to the bolt holes in CUBIT using the Spider command, which uses rigid bar elements, RBARS in Sierra SD, to represent the connections [15, 16]. A uniform modal damping ratio of 0.02 is applied to all real modes.

To determine the motion of each of the prospective measurement nodes, a frequency response function (FRF) study is completed in Sierra SD with the *modalfrf* solution type to define the transfer function matrix relating the input acceleration, or force, from the shaker to the displacement of the prospective measurement nodes. The response, or output, spectral density function matrix, $\mathbf{S_{mm}}$, due to an input acceleration at the shaker drive point, $\mathbf{S_{nn}}$, is expressed as:

$$\mathbf{S_{mm}}\left(\omega\right)=\mathbf{H_{mn}}\left(\omega\right)\mathbf{S_{nn}}\left(\omega\right)\mathbf{H_{mn}^{H}}\left(\omega\right) \tag{3.24}$$

where $\mathbf{H_{mn}}$ denotes the transfer function matrix between the response accelerations at the prospective measurement points and the input acceleration due to the shaker obtained with the FRF study with Sierra SD and $^{\mathbf{H}}$ denotes the complex conjugate transpose [18, 19]. Figure 3.18 provides the input auto-power spectral density (APSD) for the drive point acceleration measured in test to the node closest to the attachment point. Figure 3.19 shows a representative example for the resulting response of a prospective measurement node (Node 12,188), whose location is shown in the inset, for the *x*-axis (blue line), *y*-axis (orange line), and *z*-axis (yellow line).

3.4.3 Transformation to Modal Coordinates to Acquire Pixel Displacements for Modes of Interest

The root mean square (RMS) values arising from the responses at each measurement node obtained from the results of the FRF study can be used to determine which of the prospective nodes displace enough to surpass an expected noise floor of the optical system [8]. From experience, a displacement of 1/100 of a pixel can be used to extract modal information (in

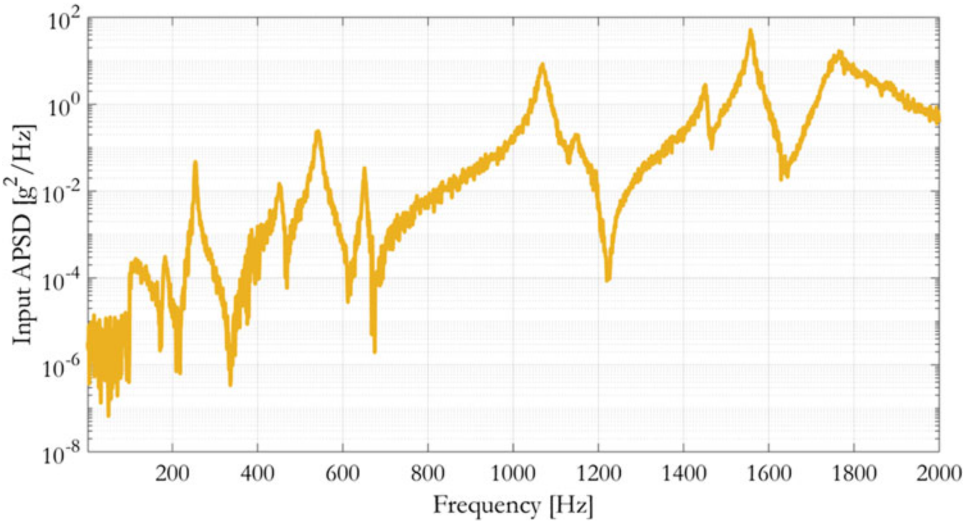

Fig. 3.18 Auto-spectral density function of input acceleration

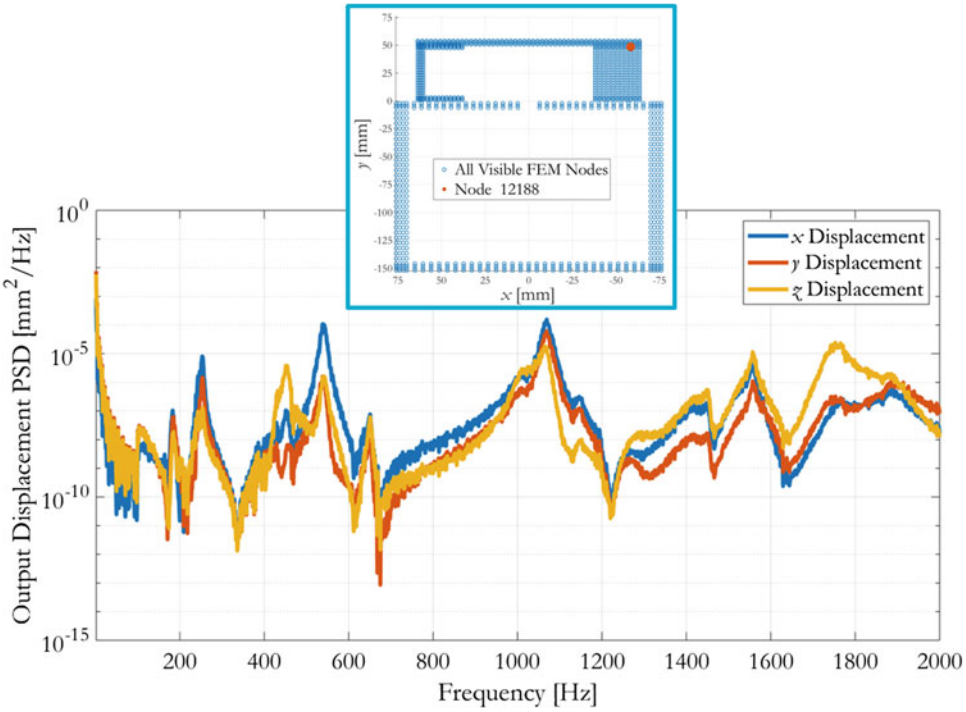

Fig. 3.19 Output APSD for a single node of the BARC FEM

optimal cases as low as 1/1000 of a pixel). The BARC test setup had an average of 8.8 px/mm for both cameras, resulting in an estimated noise floor of approximately 1.1E−3 mm. Modal filtering can be used to obtain the displacement of each pixel due to a mode of interest, which may then be compared directly to the noise floor to determine if that mode will be extractable. In the example shown in this section, the modes of interest are shown in Fig. 3.20.

A full modal filter can be applied to obtain the responses at each of the prospective measurement points in modal coordinates with the complete set of modes obtained with Sierra SD:

$$\mathbf{x} = \boldsymbol{\Phi}\mathbf{q} \tag{3.25}$$

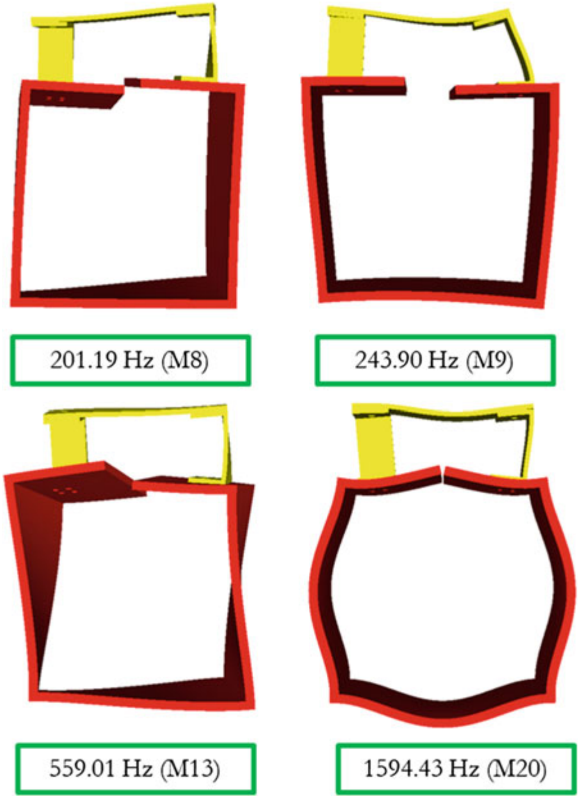

Fig. 3.20 Example mode shapes of interest in determining what nodal displacements surpass the assumed noise floor

where **x** denotes the displacements for prospective measurement nodes in Cartesian coordinates due to the applied APSD, **q** denotes the displacements for prospective measurement nodes in modal coordinates, and $\mathbf{\Phi}$ is the complete mode shape matrix containing the rigid body and flexible modes. The displacements in the modal coordinates can be obtained by calculating the pseudoinverse of, or $\mathbf{\Phi}^{+}$, and pre-multiplying Eq. (3.25) by the resulting matrix:

$$\mathbf{q} = \boldsymbol{\Phi}^{+}\mathbf{x} \tag{3.26}$$

The displacement in Cartesian coordinates for a specific mode can then be obtained as:

$$\mathbf{x}_{i\,\mathrm{RMS}} = \mathrm{RMS}\left(\boldsymbol{\Phi}_i \mathbf{q}_i\right) \tag{3.27}$$

where $\mathbf{\Phi}_i$ denotes the mode shape for a single mode at the prospective measurement nodes, $\mathbf{q}_i$ the response displacements for the measurement nodes due to the current mode of interest i in modal coordinates, and $\mathbf{x}_{i_{\mathrm{RMS}}}$ the root mean square (RMS) response displacement due to the mode of interest in physical Cartesian coordinates. Using Eqs. (3.25)–(3.27), the displacements of the prospective measurement nodes due to the modes of interest shown in Fig. 3.20 are calculated and compared to the noise floor to determine which nodes experience displacements that are observable; this result is shown in Fig. 3.21.

Additionally, the transformation to pixel coordinates can be completed to determine what nodes are indistinguishable from one another based on the camera placements, which is also enforced during this stage of the process. This transformation can be defined using the derivations from Sect. 3.3:

$$\mathbf{u}_i = \mathbf{K}_i \mathbf{R}_{i\mathbf{v}} [\mathbf{I}|\mathbf{C}]_i \mathbf{R}_{\mathbf{vb}} \mathbf{R}_{\mathbf{bw}} \mathbf{X}_{\mathbf{w}}$$

$$\begin{bmatrix} au \\ av \\ a \end{bmatrix}_i = \begin{bmatrix} f_x & q & c_x \\ 0 & f_y & c_y \\ 0 & 0 & 1 \end{bmatrix}_i \begin{bmatrix} r_{xx} & r_{xy} & r_{xz} \\ r_{yx} & r_{yy} & r_{yz} \\ r_{zx} & r_{zy} & r_{zz} \end{bmatrix}_{iv} \begin{bmatrix} 1 & 0 & 0 & C_x \\ 0 & 1 & 0 & C_y \\ 0 & 0 & 1 & C_z \end{bmatrix}_i \begin{bmatrix} r_{xx} & r_{xy} & r_{xz} & 0 \\ r_{yx} & r_{yy} & r_{yz} & 0 \\ r_{zx} & r_{zy} & r_{zz} & 0 \\ 0 & 0 & 0 & 1 \end{bmatrix}_{\mathrm{vb}} \begin{bmatrix} r_{xx} & r_{xy} & r_{xz} & t_x \\ r_{yx} & r_{yy} & r_{yz} & t_y \\ r_{zx} & r_{zy} & r_{zz} & t_z \\ 0 & 0 & 0 & 1 \end{bmatrix}_{\mathrm{bw}} \begin{bmatrix} X \\ Y \\ Z \\ 1 \end{bmatrix}_{\mathrm{w}} \tag{3.28}$$

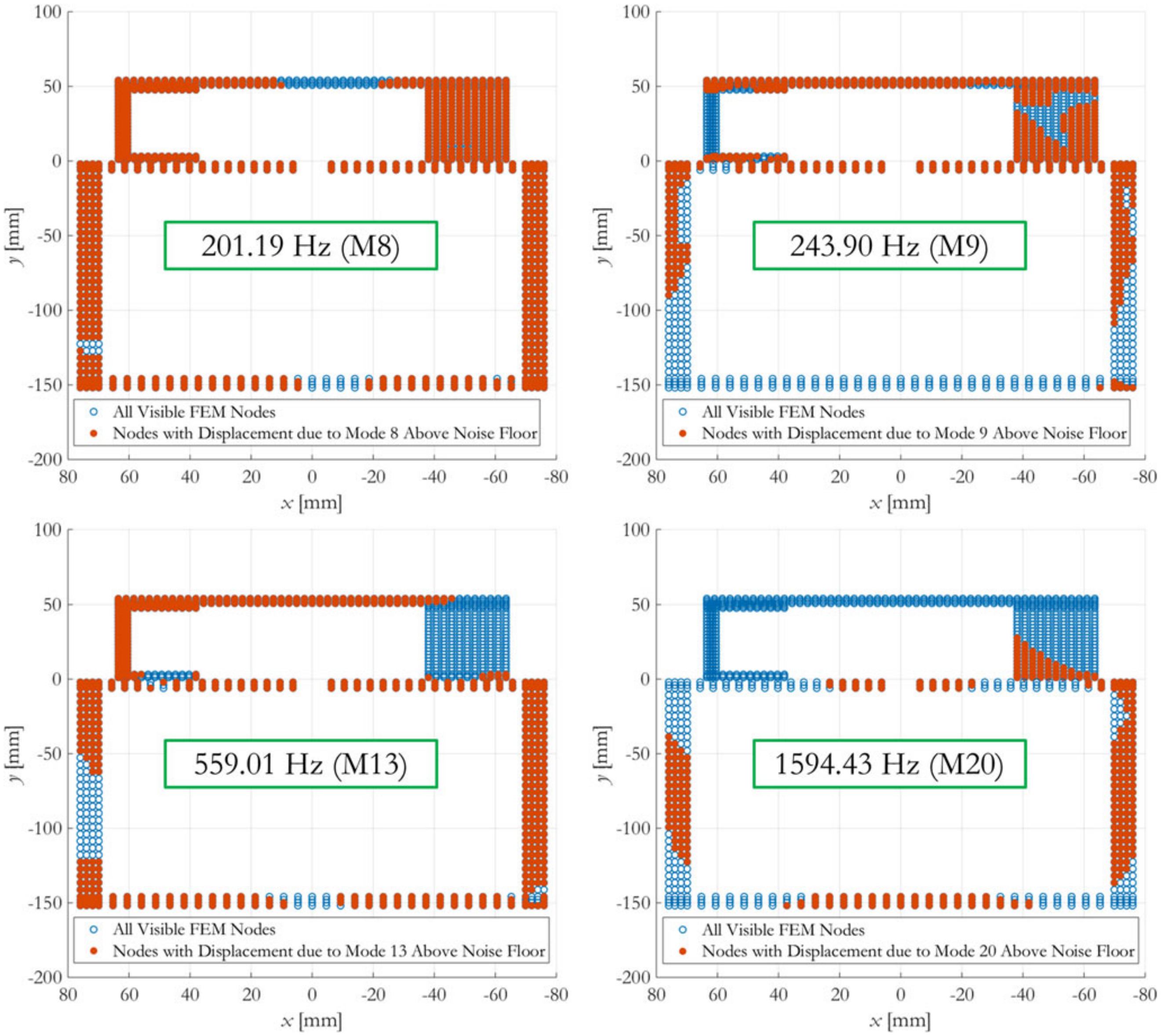

Fig. 3.21 Comparing nodal displacement to noise floor for example modes of interest

Accounting for the pixel transformation to Camera 1 (green point in Fig. 3.12) only reduces the number of visible nodes by 2.3% before comparing the displacements to the noise floor. It is estimated that 91% of the total prospective measurement points have observable displacements for Mode 8 (201 Hz) in comparison to 58%, 64%, and 29% for Modes 9 (243 Hz), 13 (559 Hz), and 20 (1594 Hz), respectively. A majority of the points do not have observable motion in the removable component for Mode 20 since the motion is dominated by the bottom box.

Alternatively, specific measurement points can be chosen to determine what modes do not result in observable motion for the chosen point. The locations of Node 8174 (green point) and Node 16296 (yellow point) are shown in Fig. 3.22. The resulting RMS displacements for Nodes 8174 and 16296 as a function of mode index are provided in Fig. 3.23. Node 8174 experiences detectable motion for 56% of the first 50 modes compared to the 50% for Node 16296. The percentage of modes that are indicated to be observable via this evaluation is highly dependent on which node is selected.

Evaluating the observable modes for prospective measurement nodes allows for the best area or points of the model to be chosen to measure specific modes of interest. The tools developed in this section can be used to validate measurement surfaces chosen or to leverage alongside an iterative optimization process to automate the selection of the optimal measurement points/area for a mode of interest.

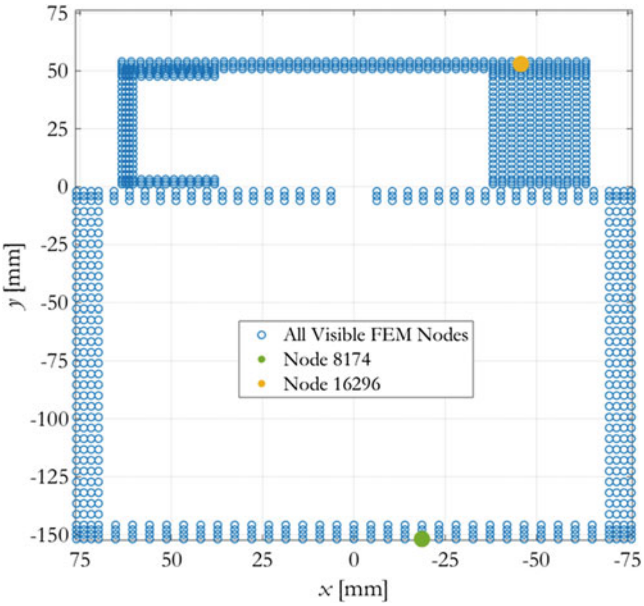

Fig. 3.22 Locations of nodes used in modal displacement comparison to the RMS noise floor for the first 50 flexible vibration modes

3.5 Conclusions and Future Work

A framework for iteratively determining a first-order approximation of a set of optimized stereo camera poses, given the optical hardware available to the practitioner, has been presented and demonstrated experimentally. The two primary difficulties lie in the ability to actually place the cameras in the exact locations specified by the planning tool results and in the phenomenon of lens "focus breathing."

The placement of the cameras is not a technical issue, but rather one of practicality; getting the cameras within centimeters of the optimal position was not found to be overly difficult, but certainly the time that would be spent getting much more accurate would outweigh the benefits. The authors are currently exploring the use of a portable coordinate measurement machine for test setups requiring very precise positioning of the cameras relative to the test object.

The current implementation of the planning tool only deals with lens breathing through the implementation of a margin around the bounding box volume. While effective, it leaves room for improvement, the most straightforward of which could be to treat the lens focal length as a function of the focus distance within the iteration. Unfortunately, due to the variations between lens designs, this would require the user to conduct a characterization of each lens to establish this relationship.

The pose optimization framework by itself is useful to a practitioner, but the addition of the FEM analysis presented in Sect. 3.4 provides an additional level of utility. The ability to check for occluded areas before testing can potentially save valuable test time. Clearly, the end analysis in this work is oriented toward experimental modal testing but could be applied to any analysis where displacements are a quantity of interest. Future developments could easily include strain estimations as well. Another future development being investigated is to use the FEM to determine the measurement points anywhere around a test object that are required for modal characterization (e.g., effective independence) and then determine the minimal set of camera poses necessary to measure them all.

The ultimate goal of a stereo camera pre-test analysis should be to not only determine where to put the equipment but also if the locations and quantities of interest will be observable—this can only be achieved with the additional FEM analysis. Considering the alternative for pre-test planning is a "guess-and-check" method where the practitioner must rely on their experience to create a viable test setup, the tools presented herein mark an appreciable improvement, even in their current state. Given the high level of automation and minimal user inputs, the pre-test analysis presented has been found to save more time that it consumes.

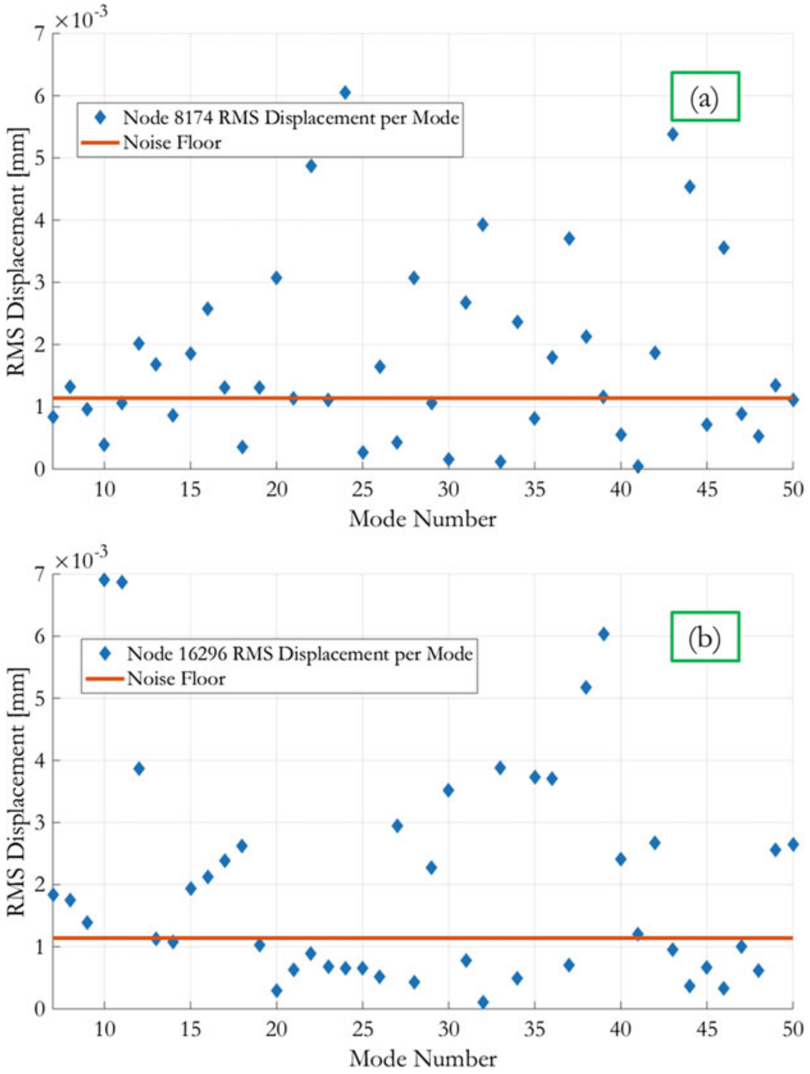

Fig. 3.23 Modal displacement comparison of (**a**) Node 8174 and (**b**) Node 16296 of FEM to the RMS noise floor for the first 50 flexible vibration modes

Acknowledgments This manuscript has been authored by National Technology and Engineering Solutions of Sandia, LLC. under Contract No. DE-NA0003525 with the US Department of Energy/National Nuclear Security Administration. The United States Government retains and the publisher, by accepting the article for publication, acknowledges that the United States Government retains a non-exclusive, paid-up, irrevocable, world-wide license to publish or reproduce the published form of this manuscript, or allow others to do so, for United States Government purposes.

References

1. Sutton, M., Orteu, J.J., Schreier, H.: Image Correlation for Shape, Motion and Deformation Measurements: Basic Concepts, Theory and Applications. Springer, New York (2009). https://doi.org/10.1007//978-0-378-78747-3
2. Jones, E.M.C., Iadicola, M.A. (eds.): A Good Practices Guide for Digital Image Correlation. International Digital Image Correlation Society, Portland, OR (2018). https://doi.org/10.32720/idics/gpg.ed1
3. Reu, P.: Introduction to digital image correlation: Best practices and applications. Exp. Tech. **36**, 3–4 (2012). https://doi.org/10.1111/j.1747-1567.2011.00798.x
4. Reu, P., Miller, T.: The application of high-speed digital image correlation. J. Strain Anal. Eng. Des. **43**, 673–688 (2008). https://doi.org/10.1243/03093247JSA414

5. Helfrick, M., Niezrecki, C., Avitabile, P., Schmidt, T.: 3D digital image correlation methods for full-field vibration measurement. Mech. Syst. Signal Process. **25**, 917–927 (2011). https://doi.org/10.1016/j.ymssp.2010.08.013
6. Molina-Viedma, A.J., Lopez-Alba, E., Felipe-Sese, L., Diaz, F.A.: Full-field modal analysis during base motion excitation using high-speed 3D digital image correlation. Meas. Sci. Technol. **28**(10), 105402 (2017). https://doi.org/10.1088/1361-6501/aa7d87
7. Lorenzo, E.D., Lava, P., Balcaen, R., Manzato, S., Peeters, B.: Full-field modal analysis using high-speed 3D digital image correlation. J. Phys. Conf. Ser. **012007**, 1149 (2018). https://doi.org/10.1088/1742-6596/1149/1/012007
8. Witt, B., Rohe, D.: Digital image correlation as an experimental modal analysis capability. Exp. Tech. (2020). https://doi.org/10.1007/s40799-020-00420-6
9. Rohe, D., Quintana, R., Witt, B., Halls, B.: Structural dynamic measurements using high-speed X-ray digital image correlation. In: Proceedings of the 39th International Modal Analysis Conference, Virtual (2021)
10. Rohe, D., Smith, S., Brake, M.R., deClerk, J., Blanco, M.A., Schoenherr, T.F., Skousen, T.: Testing summary for the box assembly with removable component structure. In: Proceedings of the 37th International Modal Analysis Conference, Orlando, FL (2019)
11. Arun, K.S., Huang, T., Blostein, S.: Least-squares fitting of two 3-D point sets. IEEE Trans. Pattern Anal. Mach. Intell. **PAMI-9**(5), 698–700 (1987)
12. Allen, E., Triantaphillidou, S.: The Manual of Photography. Taylor & Francis, Boca Raton, FL (2011). ISBN 978-0-240-52037-7
13. Greivenkamp, J.: Field Guide to Geometrical Optics. SPIE Press, Bellingham, WA (2004). ISBN 9780819452948
14. Rohe, D.: An optical test simulator based on the open-source Blender software. In: Proceedings of the 38th International Modal Analysis Conference, Houston, TX (2020)
15. Sandia National Laboratories: CUBIT 15.7 User Documentation. Sandia Technical Report, SAND2020-4156 W (2020)
16. Sandia National Laboratories: Sierra/SD – Theory Manual. Sandia Technical Report, SAND2020-3687 (2020)
17. Coxeter, H.S.M., Greitzer, S.L.: Geometry Revisited, pp. 52–54. MAA, Washington (1967). ISBN 978-0-88385-619-2
18. Wirsching, P.H., Paez, T.L., Ortiz, K.: Random Vibrations: Theory and Practice. Dover Publications Inc., Mineola, NY (2013). ISBN 9780486450155
19. Lin, Y.L.: Probabilistic Theory of Structural Dynamics. McGraw-Hill Book Co., New York (1967). ISBN 978-0882753775

Chapter 4
Simplified Finite Element Models of Pyramidal Truss Sandwich Panels with Welded Joints for Dynamic Analysis and Their Experimental Validation

Ke Yuan and Weidong Zhu

Abstract Pyramidal truss sandwich panels (PTSPs) are widely used in engineering structures, and their face sheets and core parts are generally bonded by the welding process. A large number of solid elements are usually required in the finite element model of a PTSP with welded joints to obtain its accurate modal parameters. Ignoring welded joints of the PTSP can save many degrees of freedom (DOFs) but significantly change its natural frequencies. This study aims to accurately determine modal parameters of a PTSP with welded joints with much fewer DOFs than its solid element model and to obtain its operational modal analysis results by avoiding missing its modes. Two novel methods that consider welded joints as equivalent stiffness are proposed to create beam-shell element models of the PTSP. The main step is to match stiffnesses of beam and shell elements of a welded joint with those of its solid elements. Compared with the solid element model of the PTSP, its proposed models provide almost the same levels of accuracy for natural frequencies and mode shapes for the first 20 elastic modes while reducing DOFs by about 98% for the whole structure and 99% for each welded joint. The first 14 elastic modes of a PTSP specimen that were measured without missing any modes by synchronously capturing its two-faced vibrations through use of a three-dimensional scanning laser vibrometer and a mirror experimentally validate its beam-shell element models created by the two proposed methods.

Keywords Finite element modeling · Sandwich panel · Pyramidal truss · Welded joint · Modal parameters

4.1 Introduction

Sandwich panels are a type of composite structures and widely used in commercial vehicles and aerospace and military industries. A typical sandwich panel consists of two face sheets that provide bending and in-plane shear stiffnesses and a core part that carries out-of-plane shear loads. According to types of core parts, sandwich panels can be classified as foams, corrugation, honeycombs, trusses, and so on. Compared with monolithic plate structures and other types of sandwich panels, truss sandwich panels have lower weights but higher stiffnesses and strengths [1]. Other physical properties of truss sandwich panels, such as the energy absorption capacity, the heat dissipation capability, and the heat transfer capability, have also been investigated by researchers [2].

Solid elements are generally used in finite element (FE) models of sandwich panels, and their high accuracies in static and dynamic analyses have been proved in many investigations. In this investigation, welded joints of a PTSP between its face sheets and truss core are made by the welding process. For this kind of sandwich panels, previous studies ignored welded joints in their FE models [3, 4]. However, dimensions of joints between face sheets and the core part of a sandwich panel can affect its static and dynamic characteristics [5, 6]. Based on above discussions, one can see that welded joints play an important role in modeling of sandwich panels. Shapes of welded joints are generally irregular during the fabrication process, but fillets are always used to simulate them in some fields, including fatigue assessment of welded joints and flow performance investigation of PTSPs. As shown in Fig. 4.1, fillets are created between the truss core and face sheets of the solid element model of the PTSP in this work, and dense meshes are applied to it to reduce errors caused by stress concentration when solid elements are used. As a result, much longer computation time and much larger computer memory are needed in FE analysis, especially for relatively large and complicated structures.

K. Yuan · W. Zhu (✉)
Department of Mechanical Engineering, University of Maryland, Baltimore County, MD, USA
e-mail: kyuan1@umbc.edu; wzhu@umbc.edu

D. Di Maio, J. Baqersad (eds.), *Rotating Machinery, Optical Methods & Scanning LDV Methods, Volume 6*, Conference Proceedings of the Society for Experimental Mechanics Series, https://doi.org/10.1007/978-3-030-76335-0_4

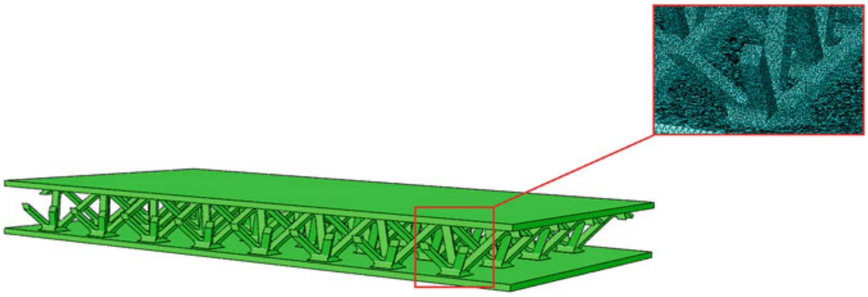

Fig. 4.1 Solid element model for the PTSP in this study with dense meshes applied to welded joints

One method to save time and memory in FE analysis is to use beam and shell elements to model a PTSP with welded joints, which are much more efficient than solid elements, since the number of degrees of freedom (DOFs) in a beam-shell element model is much fewer than that in a solid element model. Some researchers who focus on honeycomb-core sandwich panels usually use shell elements in their FE models due to characteristics of core parts [7]. However, Burlayenko and Sadowski [8] suggested that shell elements that save computation time have less accuracy than solid elements in calculation of natural frequencies of foam-filled honeycomb-core sandwich panels. Simplification of PTSPs is not always as easy as that of honeycomb-core sandwich panels due to existence of beam members in core parts of the PTSPs. Some researchers created FE models of PTSPs with shell elements in face sheets and solid elements in the truss core to obtain enough accuracy [9, 10], but DOFs of the FE models were not significantly reduced. Most of above studies focus on static analysis of PTSPs, and more studies on dynamic analysis of PTSPs modeled by beam and shell elements are needed, and modal tests of PTSPs need to be improved to resolve the missing mode problem [6].

This work aims to accurately determine modal parameters, including natural frequencies and mode shapes, of a PTSP with welded joints with a small number of DOFs and to improve accuracy of modal test results of the PTSP specimen by avoiding the missing mode problem. Two novel methods that consider the stiffness of welded joints created by solid elements as equivalent stiffnesses of beam and shell elements are developed to significantly simplify the solid element model. In these two methods, the equivalent stiffnesses are calculated by matching displacements of welded joints created by beam and shell elements with those created by solid elements. The equivalent stiffness of beam elements is simulated by adding extra beam elements with corresponding cross-sectional dimensions, while the equivalent stiffness of shell elements is simulated by updating their Young's modulus in one method and their thickness in the other method. In operational modal analysis of a PTSP specimen with simulated free boundary conditions, a speaker was used to excite it, and a 3D scanning laser vibrometer (SLV) was used to measure its vibration. In order to synchronously capture mode shapes of two face sheets of the specimen, vibration of the backface of the specimen is measured through its image in a mirror and combined with that of its frontface. Novelties of this work are summarized as follows. First, the FE model of a PTSP with welded joints is significantly simplified, and its modal parameters are accurately obtained. Second, the missing mode problem in the modal test of the PTSP is resolved by simultaneously measuring vibration of its two face sheets.

4.2 Methodology

The commercial finite element software ABAQUS is used in this study to build FE models of the PTSP with welded joints. Solid elements C3D4 are used in the solid element model, and beam elements B33 and shell elements S4R are used in beam-shell element models. Natural frequencies and mode shapes of PTSP models with free boundary conditions are extracted through the Lanczos approach. Equal dimensions of welded joints are assumed in numerical calculation.

As mentioned in Sect. 4.1, direct simplification methods have been used to model sandwich panels in some published works. For the directly simplified beam-shell element model of the PTSP in this study that ignores welded joints, its face sheets can be modeled by shell elements, and the truss core can be modeled by beam elements, as shown in Fig. 4.2. Both material properties and dimensions of the directly simplified model of the PTSP are kept the same as those of the solid element model. Besides, a "tie" is used as the constraint between beam and shell elements in the directly simplified model.

Based on the direct simplification method, two novel methods that consider the stiffness of welded joints created by solid elements as equivalent stiffnesses of beam and shell elements are proposed here. Modal parameters, such as natural frequencies and mode shapes, of a structure are mainly determined by its mass and stiffness. The approaches here mainly

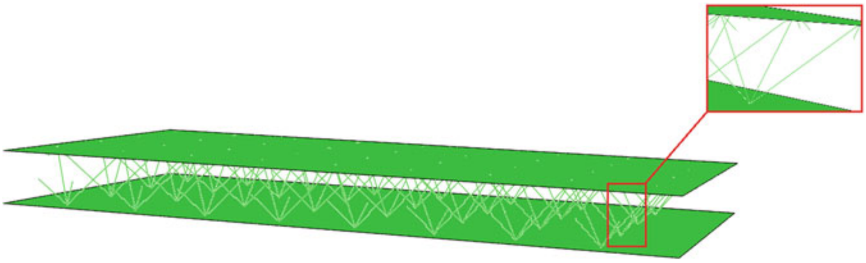

Fig. 4.2 Directly simplified beam-shell element model of the PTSP in Fig. 4.1: face sheets are created by shell elements, the truss core is created by beam elements, and welded joints are ignored

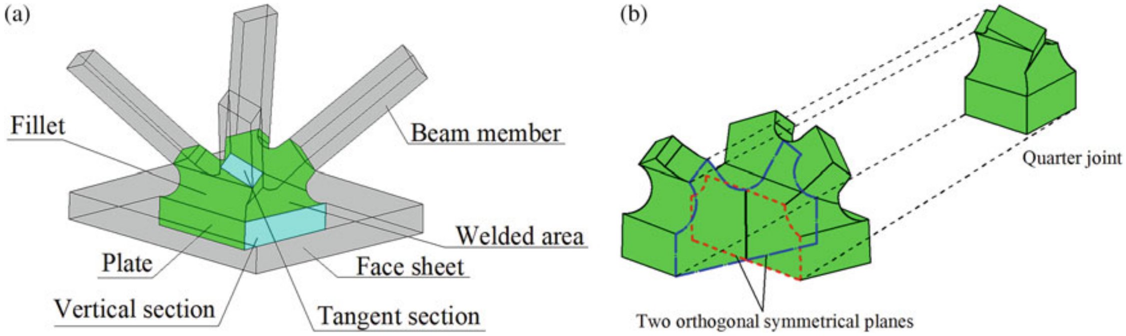

Fig. 4.3 (**a**) Components of a pyramidal truss unit of the solid element model of the PTSP and (**b**) single welded joint and its quarter part that is cut along its two orthogonal symmetrical planes

focus on predicting the equivalent stiffness introduced by welded joints, since the mass of the beam-shell element model of the PTSP can be easily matched with that of its solid element model by updating its density. Material properties or dimensions of beam and shell elements can be correspondingly changed to satisfy the stiffness equivalence. Note that the equivalent mass and stiffness of beam-shell element models of the PTSP are not updated based on experiment data but are updated based on numerical analysis of its solid element model.

As shown in Fig. 4.3a, a pyramidal truss unit of the solid element model of the PTSP in this work basically consists of a part of a thin face sheet, four beam members, and four fillets at a welded joint. By separating beam members and the face sheet from the welded joint at tangent sections and vertical sections in Fig. 4.3a, the welded joint can be solely analyzed to obtain its stiffness. A single welded joint is shown in Fig. 4.3b where two orthogonal symmetrical planes can be seen. A quarter of the welded joint with fixed boundaries on the symmetrical planes can be analyzed to obtain the stiffness of the whole joint, since one can assume that there is no deformation on the symmetrical planes.

The stiffness of the welded joint can be decomposed into two parts: the stiffness of beam members and that of the plate shown in Fig. 4.3a. Existence of the fillet makes the cross section of the beam variable and leads to its larger equivalent cross-sectional dimensions than those of the corresponding beam without the fillet. Therefore, the equivalent stiffness of the beam becomes larger when the effect of the fillet is considered. Similarly, the welded joint increases the equivalent thickness of the plate due to existence of the fillet and leads to augmentation of the plate stiffness. In this work, it is assumed that solid elements used in a welded joint can be substituted by sloped beam elements that have the same orientations and cross-sectional dimensions as original beam members in the pyramidal truss unit in Fig. 4.3a, vertical beam elements that offer an extra stiffness, and shell elements that have the equivalent bending stiffness to that of the original plate in the pyramidal truss unit, as shown in Fig. 4.4. A pin is used to connect the sloped beam and vertical beam, and a concentrated force F and a bending moment M are applied at the pin point, as shown in Fig. 4.5. Since cross sections of beam elements are rectangles, the equivalent stiffness of vertical beam elements can be calculated under loading conditions in two orthogonal planes referred to as the in-plane and out-of-plane, which are the plane formed by the sloped and vertical beams and that perpendicular to it, respectively, as shown in Fig. 4.5, and the equivalent stiffness of vertical beam elements can be expressed as their cross-sectional dimensions. The predictive modeling procedure for the equivalent out-of-plane stiffness, the equivalent in-of-plane stiffness, and the equivalent bending stiffness of the beam-shell element model of the welded joint is shown below.

As shown in Fig. 4.5, the sloped and vertical beams in the quarter welded joint are referred to as beam 1 and beam 2, respectively. When F and M are applied in the out-of-plane, force equilibria of the two beams are shown in Fig. 4.6a,

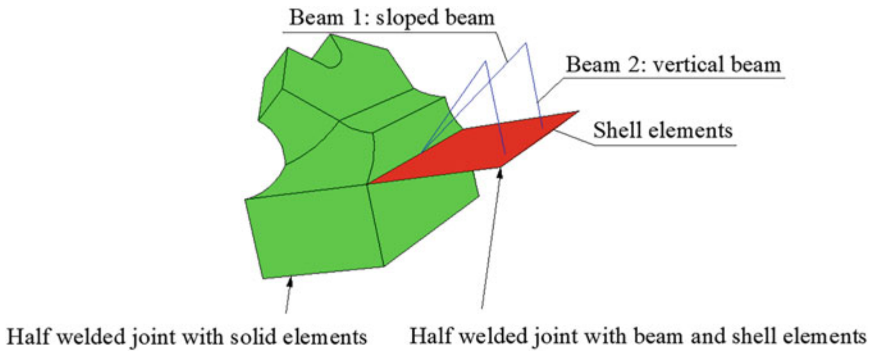

Fig. 4.4 Equivalent model of a welded joint with sloped beam elements, vertical beam members, and shell elements

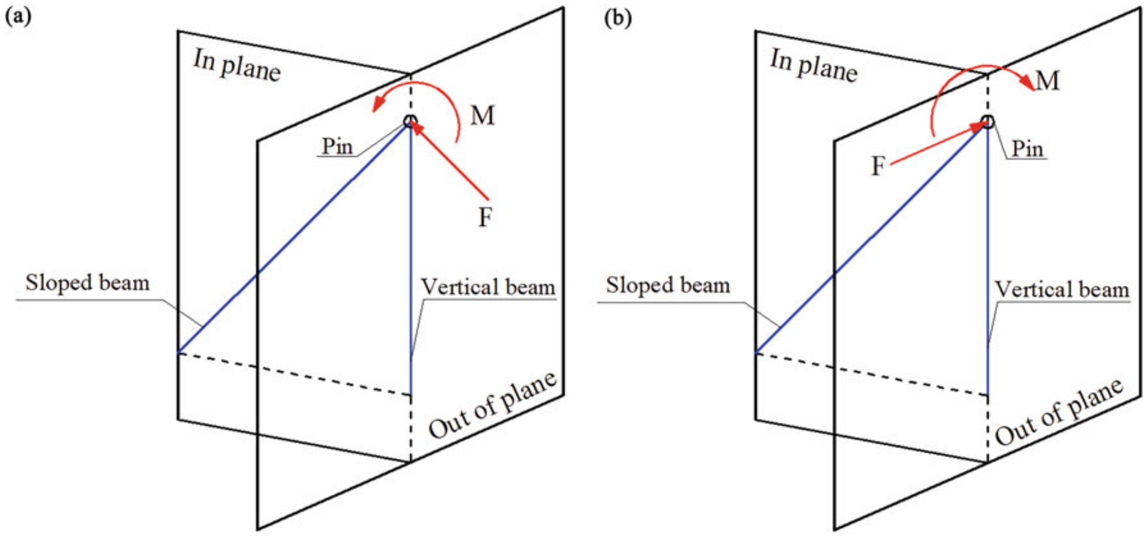

Fig. 4.5 Beam elements used to calculate the equivalent stiffness of the quarter welded joint: (**a**) an in-plane concentrated force and bending moment are applied at the pin and (**b**) an out-of-plane concentrated force and bending moment are applied at the pin

where U_1–V_1 and U_2–V_2 are local Cartesian coordinates of displacements for beams 1 and 2, respectively, and they can be transformed to each other through a transformation matrix that is a function of the angle α between the two beams. According to the analysis in Fig. 4.6a, relations between loads and beam displacements for beams 1 and 2 can be written as

$$K_1^{\text{out}}\begin{bmatrix} U_1^{\text{out}} \\ V_1^{\text{out}} \\ \theta_1^{\text{out}} \end{bmatrix} = \begin{bmatrix} \frac{A_1 E}{L_1} & 0 & 0 \\ 0 & \frac{12EI_1^{\text{out}}}{L_1{}^3} & -\frac{6EI_1^{\text{out}}}{L_1{}^2} \\ 0 & -\frac{6EI_1^{\text{out}}}{L_1{}^2} & \frac{4EI_1^{\text{out}}}{L_1} \end{bmatrix}\begin{bmatrix} U_1^{\text{out}} \\ V_1^{\text{out}} \\ \theta_1^{\text{out}} \end{bmatrix} = \begin{bmatrix} 0 \\ F - F_{\text{p}}^{\text{out}} \\ M \end{bmatrix} \tag{4.1}$$

$$K_2^{\text{out}}\begin{bmatrix} U_2^{\text{out}} \\ V_2^{\text{out}} \\ \theta_2^{\text{out}} \end{bmatrix} = \begin{bmatrix} \frac{A_2 E}{L_2} & 0 & 0 \\ 0 & \frac{12EI_2^{\text{out}}}{L_2{}^3} & -\frac{6EI_2^{\text{out}}}{L_2{}^2} \\ 0 & -\frac{6EI_2^{\text{out}}}{L_2{}^2} & \frac{4EI_2^{\text{out}}}{L_2} \end{bmatrix}\begin{bmatrix} U_2^{\text{out}} \\ V_2^{\text{out}} \\ \theta_2^{\text{out}} \end{bmatrix} = \begin{bmatrix} 0 \\ F_{\text{p}}^{\text{out}} \\ 0 \end{bmatrix} \tag{4.2}$$

respectively, where the superscript “out” denotes out-of-plane and subscripts “1” and “2” denote beams 1 and 2, respectively; U, V, and θ denote axial, transverse, and rotational displacements of either beam at its end at the pin, respectively; E is the Young’s modulus of the two beams; L, A, and I denote the length, cross-sectional area, and area moment of inertia of a cross-section of either beam, respectively; F_{p} denotes the reaction force on either beam from the pin along the transverse

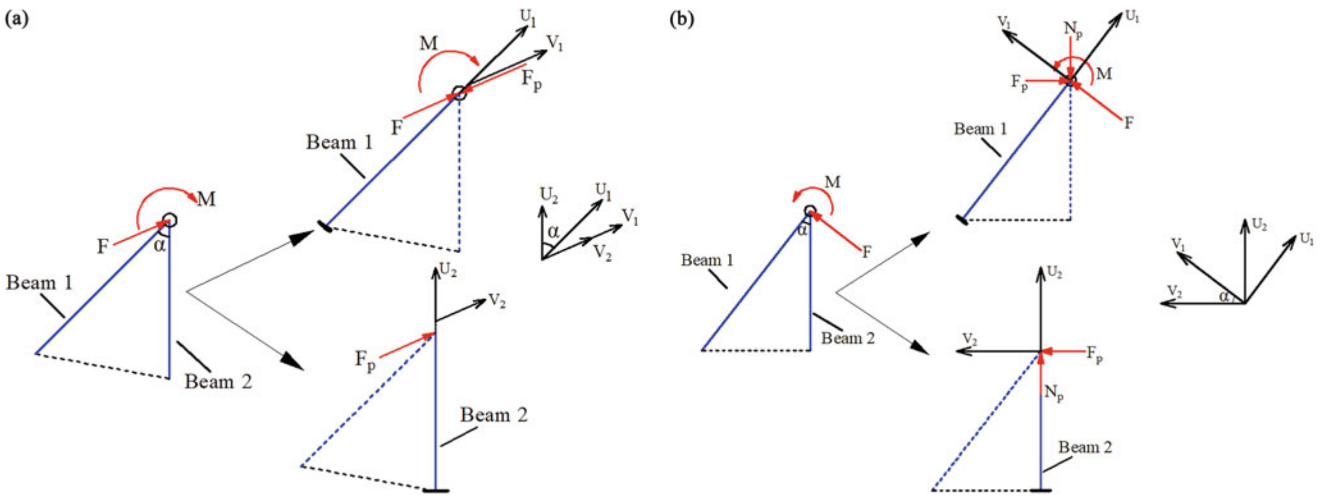

Fig. 4.6 Force equilibria of beams 1 and 2 when (**a**) the out-of-plane force and moment are applied at the pin and (**b**) the in-plane force and moment are applied at the pin

direction of the beam; and K denotes the stiffness matrix of either beam with its components shown there. There is no axial force in either beam when F and M are applied in the out-of-plane. The out-of-plane transverse displacement of beam 1 V_1^{out} is equal to that of beam 2 V_2^{out}. Therefore, Eqs. (4.1) and (4.2) can be simplified as

$$\begin{bmatrix} \frac{12EI_1^{\text{out}}}{L_1{}^3} & -\frac{6EI_1^{\text{out}}}{L_1{}^2} \\ -\frac{6EI_1^{\text{out}}}{L_1{}^2} & \frac{4EI_1^{\text{out}}}{L_1} \end{bmatrix} \begin{bmatrix} V_1^{\text{out}} \\ \theta_1^{\text{out}} \end{bmatrix} = \begin{bmatrix} F - F_{\text{p}}^{\text{out}} \\ M \end{bmatrix} \tag{4.3}$$

$$\begin{bmatrix} \frac{12EI_2^{\text{out}}}{L_2{}^3} & -\frac{6EI_2^{\text{out}}}{L_2{}^2} \\ -\frac{6EI_2^{\text{out}}}{L_2{}^2} & \frac{4EI_2^{\text{out}}}{L_2} \end{bmatrix} \begin{bmatrix} V_1^{\text{out}} \\ \theta_2^{\text{out}} \end{bmatrix} = \begin{bmatrix} F_{\text{p}}^{\text{out}} \\ 0 \end{bmatrix} \tag{4.4}$$

Since the rotational displacement of a beam affects more its behavior than axial and transverse displacements, only θ is selected to match the result from above analytical models and the numerical result from the solid element model of the quarter welded joint. In other words, θ_1^{out} in Eqs. (4.3) and (4.4) can be calculated from the solid element model of the quarter joint by applying the out-of-plane force and moment to it. As previously mentioned, beam 1 has the same cross section as original beam members in the pyramidal truss unit, which is rectangular and whose dimensions can be directly measured. The out-of-plane area moment of inertia of beam 1 I_1^{out} in Eq. (4.3) is $th^3/12$, where t and h are its cross-sectional dimensions. The out-of-plane transverse displacement of beam 1 V_1^{out}, the out-of-plane transverse reaction force $F_{\text{p}}^{\text{out}}$, the out-of-plane moment of inertia of beam 2 I_2^{out}, and the out-of-plane rotational displacement of beam 2 θ_2^{out} are four unknown variables that can be subsequently calculated from four equations in Eqs. (4.3) and (4.4).

Relations between in-plane loads and displacements of beams 1 and 2 can be similarly derived from Fig. 4.6b, which are

$$K_1^{\text{in}} \begin{bmatrix} U_1^{\text{in}} \\ V_1^{\text{in}} \\ \theta_1^{\text{in}} \end{bmatrix} = \begin{bmatrix} \frac{A_1E}{L_1} & 0 & 0 \\ 0 & \frac{12EI_1^{\text{in}}}{L_1{}^3} & -\frac{6EI_1^{\text{in}}}{L_1{}^2} \\ 0 & -\frac{6EI_1^{\text{in}}}{L_1{}^2} & \frac{4EI_1^{\text{in}}}{L_1} \end{bmatrix} \begin{bmatrix} U_1^{\text{in}} \\ V_1^{\text{in}} \\ \theta_1^{\text{in}} \end{bmatrix} = \begin{bmatrix} -N_{\text{p}}^{\text{in}}\cos\alpha + F_{\text{p}}^{\text{in}}\sin\alpha \\ F - N_{\text{p}}^{\text{in}}\sin\alpha - F_{\text{p}}^{\text{in}}\cos\alpha \\ M \end{bmatrix} \tag{4.5}$$

$$K_2^{\text{in}} \begin{bmatrix} U_2^{\text{in}} \\ V_2^{\text{in}} \\ \theta_2^{\text{in}} \end{bmatrix} = \begin{bmatrix} \frac{A_2E}{L_2} & 0 & 0 \\ 0 & \frac{12EI_2^{\text{in}}}{L_2{}^3} & -\frac{6EI_2^{\text{in}}}{L_2{}^2} \\ 0 & -\frac{6EI_2^{\text{in}}}{L_2{}^2} & \frac{4EI_2^{\text{in}}}{L_2} \end{bmatrix} \begin{bmatrix} U_2^{\text{in}} \\ V_2^{\text{in}} \\ \theta_2^{\text{in}} \end{bmatrix} = \begin{bmatrix} N_{\text{p}}^{\text{in}} \\ F_{\text{p}}^{\text{in}} \\ 0 \end{bmatrix} \tag{4.6}$$

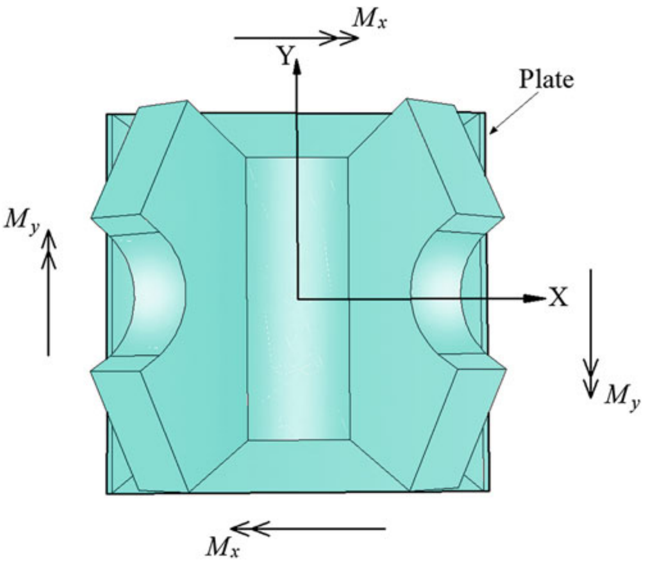

Fig. 4.7 Coordinate system established on the plane formed by the welded joint plate and moments applied to it along *X* and *Y* directions

respectively, where in-plane variables have similar meanings to out-of-plane variables previously discussed; N_p^in and F_p^in are in-plane reaction forces from the pin along axial and transverse directions of beam 2, respectively; I_1^in is the in-plane area moment of inertia of beam 1, whose calculation is similar to that of its out-of-plane area moment of inertia; and $I_1^\mathrm{in} = ab^3/12$ and $A_2 = ab$, respectively, in which a and b are cross-sectional dimensions of beam 2. As shown in Fig. 4.6b, transformations between axial and transverse displacements of beams 1 and 2 can be expressed as $U_2^\mathrm{in} = U_1^\mathrm{in}\cos\alpha + V_1^\mathrm{in}\sin\alpha$ and $V_2^\mathrm{in} = -U_1^\mathrm{in}\sin\alpha + V_1^\mathrm{in}\cos\alpha$, respectively, where α is the angle between beams 1 and 2. Then Eq. (4.6) becomes

$$\begin{bmatrix} \frac{abE}{L_2} & 0 & 0 \\ 0 & \frac{Eab^3}{{L_2}^3} & -\frac{Eab^3}{2{L_2}^2} \\ 0 & -\frac{Eab^3}{2{L_2}^2} & \frac{Eab^3}{3L_2} \end{bmatrix} \begin{bmatrix} U_1^\mathrm{in}\cos\alpha + V_1^\mathrm{in}\sin\alpha \\ -U_1^\mathrm{in}\sin\alpha + V_1^\mathrm{in}\cos\alpha \\ \theta_2^\mathrm{in} \end{bmatrix} = \begin{bmatrix} N_\mathrm{p}^\mathrm{in} \\ F_\mathrm{p}^\mathrm{in} \\ 0 \end{bmatrix} \tag{4.7}$$

Note that the out-of-plane moment of inertia of beam 2 I_2^out has been previously obtained; the relation between I_2^out and a and b is $I_2^\mathrm{out} = ba^3/12$. Similar to calculating the out-of-plane rotational displacement of beam 1 θ_1^out, θ_1^in that is the in-plane rotational displacement of beam 1 can be calculated from the solid element model of the quarter welded joint by applying the in-plane force and moment to it. Therefore, the seven unknown variables a, b, N_p^in, F_p^in, U_1^in, V_1^in, and θ_2^in can be solved from seven equations in Eqs. (4.5) and (4.7).

As shown in Fig. 4.7, a Cartesian coordinate system *X*–*Y* is created on the plane that is formed by the welded joint plate. In order to calculate the equivalent stiffness of shell elements in the welded joint, the first step is to calculate the bending stiffness of the welded joint plate by applying a couple M_x along the *X* direction and another couple M_y along the *Y* direction to it. Rotational displacements of the plate can be calculated from the solid element model of the whole welded joint to determine its bending stiffness. The second step is to create a beam-shell element model of the whole welded joint, where cross-sectional dimensions of vertical beam elements a and b are previously obtained, and to apply M_x and M_y to it. By updating the Young's modulus or thickness of shell elements, rotational displacements of the beam-shell element model of the welded joint can be matched with those of its solid element model. The updated Young's modulus or thickness of shell elements can be used to represent the equivalent bending stiffness of shell elements in welded joints of the whole PTSP created by beam and shell elements.

Based on above analyses and the matching process, the proposed method can be generally used to simplify the solid element model of a PTSP with welded joints. One can see that parameters of beam and shell elements in the simplified FE model of the PTSP, including their cross-sectional dimensions, Young's modulus, and thickness, are determined by geometrical sizes of its welded joints. Only solid element models of welded joints instead of the whole PTSP would be created. Steps of the proposed method are measuring geometrical sizes of welded joints in the PTSP, creating solid element models of welded joints, calculating parameters of beam and shell elements through the proposed method, and creating the beam-shell element model of the whole PTSP. The proposed method is numerically verified and experimentally validated in the following sections.

4.3 Results of Numerical Analysis

The material and dimensions of the PTSP in numerical analysis correspond to those of the actual PTSP specimen in Sect. 4.4; the material is aluminum that has a Young's modulus of 71.9 GPa, a density of 2700 kg/m^3, and a Poisson's ratio of 0.33. Dimensions of the solid element model of the PTSP are shown in Fig. 4.8. A face sheet of the PTSP has a length of 304 mm, a width of 162 mm, and a thickness of 3.5 mm. The distance between two face sheets is 30 mm. The distance between ends of two adjacent beams in a pyramidal truss unit is 35 mm along the length direction of face sheets and 40 mm along their width direction; the total number of pyramidal truss units is 8 × 4. As shown in Fig. 4.8b, the angle between two beams along the width direction of face sheets, which is determined by the air die shown in Fig. 4.1, is 66°. One can see from Fig. 4.8c that dimensions of the welded joint plate are 12 mm × 12 mm × 3.5 mm, the radius of fillets is 2 mm, and cross-sectional dimensions of beam members are 4 mm × 2 mm, which are approximate dimensions of welded joints in the actual PTSP specimen.

As discussed in Sect. 4.2, out-of-plane and in-plane bending moments of 10 N m and concentrated forces of 1000 N are applied to the solid element model of the quarter welded joint to calculate cross-sectional dimensions of beam 2. Lengths of beams 1 and 2 in Fig. 4.9 are 6 mm and 4.3 mm, respectively. The calculated out-of-plane and in-plane rotational displacements of beam 1 from the FE model are 0.0479 rad and 0.157 rad, respectively. As derived in Sect. 4.2, out-of-plane and in-plane moments of inertia of beam 2 can be calculated as 6.804×10^{-12} m^4 and 1.606×10^{-15} m^4, respectively. Therefore, cross-sectional dimensions of beam 2 are $a = 1.312 \times 10^{-4}$ m and $b = 8.538 \times 10^{-3}$ m. By inputting calculated cross-sectional dimensions of beam 2, a beam-shell element model of the whole welded joint can be created. Couples M_x and M_y along X and Y directions, respectively, which have the same value of 100 N m, are applied to the solid element

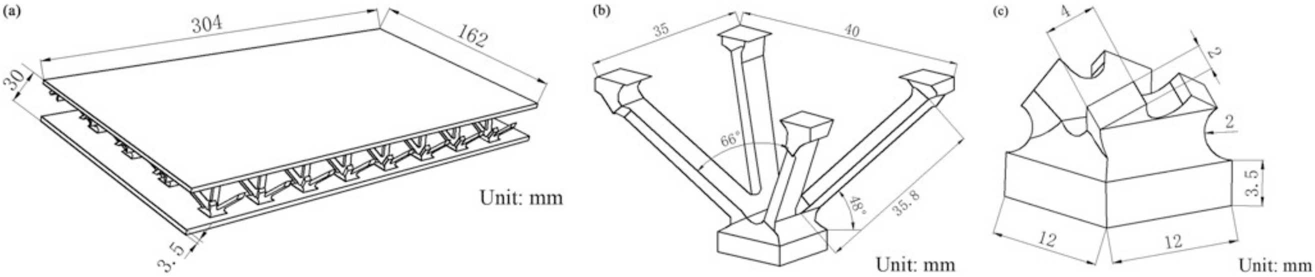

Fig. 4.8 Dimensions of the solid element model of the PTSP with welded joints: dimensions of (**a**) the whole PTSP, (**b**) a pyramidal truss unit, and (**c**) a welded joint

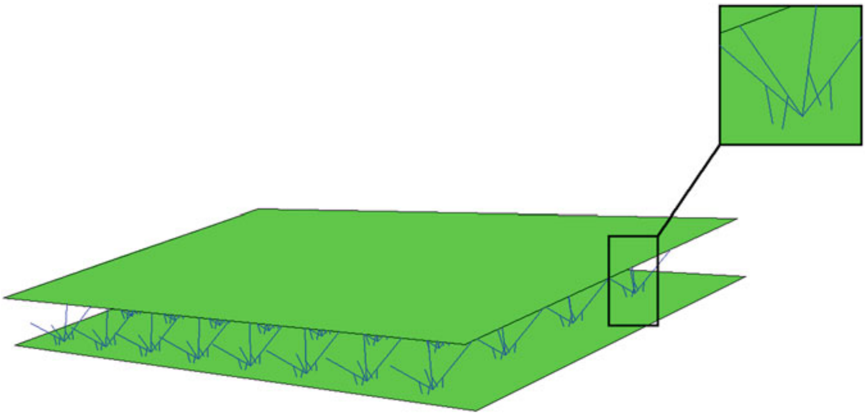

Fig. 4.9 Beam-shell element model created by method II or III

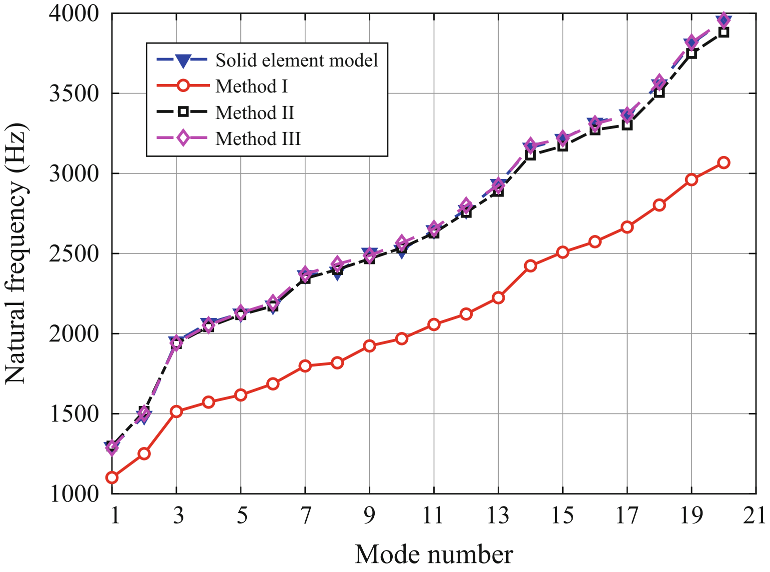

Fig. 4.10 Natural frequencies of the first 20 elastic modes of the PTSP from its beam-shell element models in methods I, II, and III and its solid element model

model of the whole welded joint to calculate its rotational displacements. The calculated rotational displacements of edges of the plate from the FE model are 0.129 rad and 0.119 rad along Y and X directions, respectively. In order to match the rotational displacement of edges of the beam-shell element model of the whole welded joint with that of edges of the plate in its solid element model, updating the Young's modulus and thickness of shell elements are used as two methods in this work. The initial Young's modulus and thickness of shell elements are the same as those of solid elements. The updated Young's modulus and thickness at intersections of relation curves and dashed lines are $E^* = 153.5$ GPa and $H^* = 3.88$ mm, respectively.

In this work, methods I, II, and III represent the direct simplification method, the updating Young's modulus method, and the updating thickness method, which are used to create beam-shell element models of the PTSP. The beam-shell element model of the PTSP created by method II or III is shown in Fig. 4.9. The total number of DOFs of the solid element model of the PTSP that is shown in Fig. 4.1 is 6,853,806, that of its beam-shell element model created by method I is 159,648, and that of its beam-shell element model created by method II or III is 162,912. This indicates that compared with the solid element model of the PTSP, DOFs are reduced by 97.7% for its beam-shell element models in methods I, II, and III. Compared with DOFs of the solid element model of a welded joint, those of beam-shell element models of the welded joint in method II and III are reduced by 99.1%.

Natural frequencies of the first 20 elastic modes of the PTSP from its beam-shell element models in methods I, II, and III are compared with those from its solid element model in Fig. 4.10. It can be seen that elastic natural frequencies from the beam-shell element model in method I are much smaller than those from the solid element model and differences between them become more significant for the third and higher elastic modes. Absolute values of errors between elastic natural frequencies from the beam-shell element model in method I and those from the solid element model are about 15% for the first two elastic modes, and they range from 20% to 25% for the third through 20th elastic modes. When methods II and III are used in creating FE models, however, elastic natural frequencies from beam-shell element models are within 2% of those from the solid element model. While DOFs of beam-shell element models of the PTSP in method II and III are larger than those in method I by 2% because welded joints are ignored in method I, its elastic natural frequencies calculated by methods II and III are at least 14% much more accurate than those by method I.

By using method I to create the beam-shell element model of the PTSP, diagonal MAC (modal assurance criterion) values in are lower than 90% for some modes and even decrease to about 40% for the 16th and 17th elastic modes. MAC values between mode shapes from the beam-shell element model in method II and those from the solid element model are all larger than 95% along the diagonal of the MAC matrix and close to 0 for off-diagonal elements of the matrix. Note that while it is not shown here, absolute values of errors between the 21st through 23rd elastic natural frequencies of the PTSP from its beam-shell element model in method II and those from its solid element model are 1.8%, 2.4%, and 2.7%, respectively, and corresponding diagonal MAC values between their 21st through 23rd elastic mode shapes are 97%, 99%, and 88%, respectively. This indicates that method II can provide good results of modal parameters of the PTSP for at least its first

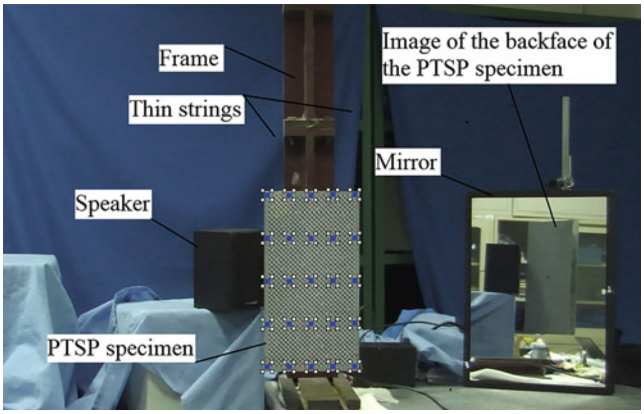

Fig. 4.11 Experimental setup for an operational modal analysis of a PTSP specimen

22 elastic modes. Although most diagonal MAC values are larger than 95% for the beam-shell element model in method III, diagonal MAC values decrease to about 70% for the 17th mode and even 40% for the 20th mode, which show weaker correlation between some higher mode shapes from the beam-shell element model in method III and those from the solid element model.

4.4 Experimental Validation

An operational modal analysis was conducted using a non-contact measurement technique to measure modal natural frequencies and mode shapes of a PTSP specimen to validate its beam-shell element models in methods II and III, with the experiment setup shown in Fig. 4.11. A speaker was used to excite the PTSP specimen, a 3D SLV Polytec PSV-500 with three scanning heads was used to measure 3D responses of measurement points on its two face sheets for capturing their possible 3D mode shapes, and a portable single-point laser vibrometer Polytec PDV-100 was used as a reference measurement. Two thin strings were symmetrically tied to the truss core of the specimen, and the specimen was hung by the strings on a stable heavy frame, which simulated free boundary conditions of the specimen.

In order to avoid missing modes of the specimen in operational modal analysis, especially for its high localized modes, some testing strategies were adopted to simultaneously excite and measure global and localized modes of its two face sheets in the experiment. The speaker that was used in the experiment has a relatively small power but a relatively wide bandwidth, so that both low and high elastic modes of the specimen can be excited. The speaker was placed at a side of the specimen instead of placing it in front or at back of its face sheets to simultaneously excite modes of the two face sheets. Another significant strategy to avoid missing modes of the specimen was to synchronously measure vibrations of its two face sheets. Since it is required to fix positions of the laser vibrometers, and the specimen during the experiment, a mirror was used to synchronously measure vibration of its backface, which is essential for two-faced vibration measurement.

The first 14 elastic natural frequencies of the specimen from the experiment are also compared with those from its beam-shell element models in methods I, II, and III, as shown in Fig. 4.12. Absolute values of maximum errors between the first 14 elastic natural frequencies from the experiment and those from beam-shell element models in methods I, II, and III are 27.2%, 4.7% and 4.1%, respectively, which occur for the fifth elastic mode in all the three methods. This indicates that ignoring welded joints in the beam-shell element model of the specimen in method I significantly underestimates its elastic natural frequencies, and considering them in methods II and III can provide their much better estimates.

By using method I, diagonal MAC values are over 95% for the first two global elastic modes; they are less than 80% for most localized elastic modes and less than 60% for some localized elastic modes, such as the fifth and tenth modes. By using methods II and III, however, diagonal MAC values are over 95% for the first two global elastic modes and over 85% for the 3rd through 14th localized elastic modes, which indicate that the first 14 elastic modes of the specimen were captured in the experiment without missing any modes and they have good correlation with those from its beam-shell element models in methods II and III. Therefore, methods II and III that consider welded joints in modeling of the PTSP are experimentally validated through above comparison between elastic natural frequencies and MAC matrices from the experiment and beam-shell element models in methods II and III.

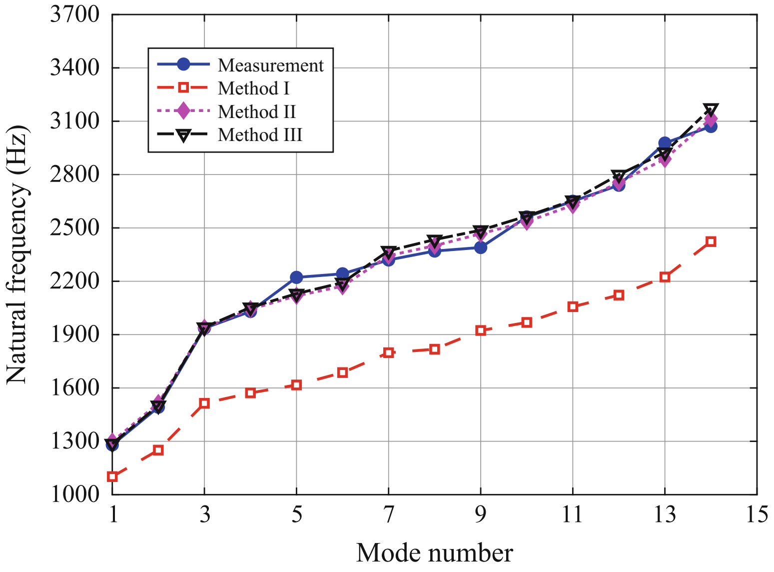

Fig. 4.12 First 14 elastic natural frequencies of the specimen from its beam-shell element models in methods I, II, and III and the experiment

4.5 Conclusion

Two novel methods that consider welded joints in the PTSP as equivalent stiffnesses of beam and shell elements are developed to create its beam-shell element models, which can significantly simplify its solid element model. In these methods, equivalent stiffnesses are calculated by matching rotational displacements of a welded joint created by beam-shell element models with that created by the solid element model. The equivalent stiffness of beam elements is simulated by adding extra beam elements with corresponding cross-sectional dimensions, and that of shell elements is simulated by updating their Young's modulus in one method and their thickness in the other method. Elastic natural frequencies and mode shapes of beam-shell models created by the proposed methods are compared with those from the solid element model and validated by operational modal analysis of a PTSP specimen. Main conclusions from this work are shown below:

1. Compared with the first 20 elastic natural frequencies from the solid element model of the PTSP, those from its directly simplified beam-shell element model that ignores welded joints are underestimated by 15–25%, while those from its beam-shell element models in the proposed methods are accurately determined and absolute values of errors are less than 2%, indicating that modeling of welded joints plays an important role in estimating natural frequencies of the PTSP. The first two elastic modes of the PTSP in this work are global modes, while the 3rd through 20th modes are localized modes in edge areas of its face sheets and have different shapes for the two face sheets. MAC values between mode shapes from the beam-shell element model by updating the Young's modulus of shell elements and those from the solid element model are all over 95% along the diagonal of the MAC matrix and close to 0 for off-diagonal elements of the matrix, while MAC values between mode shapes from the beam-shell element model by updating the thickness of shell elements and those from the solid element model are less than 70% along the diagonal of the MAC matrix for some high localized modes, indicating that the method by updating the thickness of shell elements is less accurate in simulating high localized mode shapes of the PTSP than that by updating the Young's modulus.
2. Compared with DOFs of the solid element model, those of beam-shell element models that are created by the proposed methods are reduced by 98% for the whole PTSP and 99% for each welded joint, indicating that the proposed methods can save large amounts of computation time and computer memory from the solid element model in FE analysis of the PTSP with welded joints.
3. The first 14 elastic modes of the PTSP specimen were captured in the experiment without missing any modes. Absolute values of errors between elastic natural frequencies of the specimen from beam-shell element models in the proposed methods and the experiment are less than 2% for the first two global modes and less than 5% for the 3rd through 14th localized modes. Diagonal MAC values are over 95% for the two global modes and over 85% for the localized modes. Accuracy of the proposed methods in estimating the first 14 elastic natural frequencies and mode shapes of the specimen is experimentally validated.

References

1. Evans, A.G., Hutchinson, J.W., Fleck, N.A., Ashby, M.F., Wadley, H.N.G.: The topological design of multifunctional cellular metals. Prog. Mater. Sci. **46**(3–4), 309–327 (2001)
2. Ma, Y., Yan, H., Xie, G.: Flow and thermal performance of sandwich panels with plate fins or/and pyramidal lattice. Appl. Therm. Eng. **164**, 114468 (2020)
3. Lu, L., Song, H., Yuan, W., Huang, C.: Baseline-free damage identification of metallic sandwich panels with truss core based on vibration characteristics. Struct. Health Monit. **16**(1), 24–38 (2017)
4. Yuan, W., Song, H., Lu, L., Huang, C.: Effect of local damages on the buckling behaviour of pyramidal truss core sandwich panels. Compos. Struct. **149**, 271–278 (2016)
5. Syam, W.P., Wu, J., Zhao, B., Maskery, I., Elmadih, W., Leach, R.: Design and analysis of strut-based lattice structures for vibration isolation. Precis. Eng. **52**, 494–506 (2018)
6. Yang, J.S., Ma, L., Chaves-Vargas, M., Huang, T.X., Schröder, K.U., Schmidt, R., Wu, L.Z.: Influence of manufacturing defects on modal properties of composite pyramidal truss-like core sandwich cylindrical panels. Compos. Sci. Technol. **147**, 89–99 (2017)
7. Wang, Y.J., Zhang, Z.J., Xue, X.M., Zhang, L.: Free vibration analysis of composite sandwich panels with hierarchical honeycomb sandwich core. Thin-Walled Struct. **145**, 106425 (2019)
8. Burlayenko, V.N., Sadowski, T.: Analysis of structural performance of sandwich plates with foam-filled aluminum hexagonal honeycomb core. Comput. Mater. Sci. **45**(3), 658–662 (2009)
9. Yin, S., Chen, H., Wu, Y., Li, Y., Xu, J.: Introducing composite lattice core sandwich structure as an alternative proposal for engine hood. Compos. Struct. **201**, 131–140 (2018)
10. Qi, G., Ma, L., Wang, S.Y.: Modeling and reliability of insert in composite pyramidal lattice truss core sandwich panels. Compos. Struct. **221**, 110888 (2019)

Chapter 5
Operational Modal Analysis of Rotating Structures Under Ambient Excitation Using Tracking Continuously Scanning Laser Doppler Vibrometry

L. F. Lyu and W. D. Zhu

Abstract A continuously scanning laser Doppler vibrometer (CSLDV) system is capable of rapidly obtaining spatially dense vibration measurement by continuously sweeping its laser spot along a path on a structure surface. This paper presents a new operational modal analysis (OMA) method for a rotating structure based on a rigorous rotating beam vibration theory, an image processing method, and a data processing method called the lifting method. A novel tracking CSLDV (TCSLDV) system was developed in this work to track and scan a rotating structure, and the real-time position of the rotating structure can be determined by image processing so that the TCSLDV system is capable of tracking a time-varying scan path on the rotating structure. The lifting method can transform raw TCSLDV measurement into measurements at multiple virtual measurement points as if they were measured by transducers attached to these measurement points. Modal parameters of the rotating structure with a constant speed, including damped natural frequencies, undamped mode shapes, and modal damping ratios, and operating deflection shapes (ODSs) of the structure with a constant or prescribed time-varying rotation speed can be determined by calculating and analyzing correlation functions with non-negative time delays among measurements at virtual measurement points. Experimental investigation is conducted using the TCSLDV system to study the OMA method with which modal parameters and an ODS of a rotating fan blade with different constant speeds, as well as an ODS of the rotating fan blade with a non-constant speed, are successfully estimated.

Keywords Tracking continuously scanning laser Doppler vibrometer system · Rotating beam vibration theory · Operational modal analysis · Lifting method · Operating deflection shapes

5.1 Introduction

Modal analysis studies modal parameters such as natural frequencies, mode shapes, and modal damping ratios of a linear structure [1]. Modal analysis methods can be divided into experimental modal analysis (EMA) methods and operational modal analysis (OMA) methods, depending on whether an excitation applied on the structure needs to be measured or not [2]. An EMA method requires excitation measurement, while an OMA method does not. Frequency response functions or impulse response functions of the structure are calculated and analyzed to estimate its modal parameters in EMA methods [1]. Correlation functions with non-negative time delays and their power spectra are calculated and analyzed to estimate modal parameters in OMA methods based on the natural excitation testing theory [3, 4]. Siringoringo and Fujino [5] proposed and investigated a time-synchronization technique to calculate correlation functions for simultaneously estimating modal parameters in OMA methods. Compared with EMA methods, modal parameters can be accurately estimated in OMA methods when the structure is assumed to be under white-noise excitation that is unknown or not measured. Hence OMA methods are more appropriate for structures under operating conditions or under ambient excitations.

A laser Doppler vibrometer that is considered to be one of the most accurate and reliable vibration measurement tools can measure the surface velocity of a point on a structure along its laser beam direction [6]. However, the measurement efficiency of a laser vibrometer becomes critical when there is a large and dense measurement grid. A laser vibrometer can be equipped with a scanner that has a set of orthogonal mirrors to increase its measurement efficiency [7]. The laser spot of the vibrometer is able to continuously sweep along a prescribed path on a structure to measure its surface velocity by rotating the mirrors that are controlled by a controller. When rotation angles of the mirrors continuously change, since the path and speed of the

---

L. F. Lyu · W. D. Zhu (✉)
Department of Mechanical Engineering, University of Maryland, Baltimore, MD, USA
e-mail: linfenl1@umbc.edu; wzhu@umbc.edu

D. Di Maio, J. Baqersad (eds.), *Rotating Machinery, Optical Methods & Scanning LDV Methods, Volume 6*, Conference Proceedings of the Society for Experimental Mechanics Series, https://doi.org/10.1007/978-3-030-76335-0_5

laser spot on the structure can be controlled, various scans of the laser spot can be created. The laser vibrometer, scanner, and controller of the scanner constitute a continuous scanning laser Doppler vibrometer (CSLDV) system [7–9]. When the sampling frequency of the CSLDV system is high, the system can efficiently perform spatially dense vibration measurement.

To analyze CSLDV measurements of structures undergoing different vibrations such as sinusoidal vibration, free vibration, and random vibration, various methods have been proposed. One method is the demodulation method [8, 10] for a structure undergoing sinusoidal vibration. The polynomial method [8, 10] is another method for a structure undergoing sinusoidal vibration, where real and imaginary parts of the ODS are represented by two polynomials. The demodulation method was later applied to identify damage in beams and plates undergoing sinusoidal vibration [11, 12]. Based on the demodulation method, Xu et al. [13] introduced a free response shape, which is a new type of vibration shapes. The free response shape corresponding to one mode of a structure can be used for baseline-free damage identification of the structure. A lifting method converts CSLDV measurement of a structure undergoing free vibration into measurements at multiple virtual measurement points as if there were transducers attached to these points for EMA [9]. An OMA method for a structure under ambient excitation was developed with a CSLDV system in Ref. [14], where harmonic transfer functions and harmonic power spectra [15] were employed. An OMA method that combines the lifting method and harmonic transfer functions was proposed in Ref. [16], where processing and interpretation of CSLDV measurement become simpler. Xu et al. [17] proposed a new OMA method for CSLDV measurement based on the lifting method to estimate modal parameters of damaged structures and detect local anomaly caused by damage on a scan path.

To estimate modal parameters of a rotating structure, encoders were used to track its angular position [18, 19]. Khalil et al. [18] proposed a method to track a rotating structure and measure its ODSs by attaching an encoder to it. Allen et al. [19] developed an EMA method to measure mode shapes of a rotating fan with an encoder attached to its shaft to track its angular position. However, it is difficult to attach an encoder to a rotating structure such as a large horizontal-axis wind turbine; a more convenient OMA method and CSLDV system for tracking the angular position of a rotating structure and estimating its modal parameters and ODSs are needed.

In this work, a new OMA method based on a rotating beam vibration theory, an image processing method, and the modal parameter estimation method in Ref. [17] is developed to estimate the rotation speed, modal parameters, and ODSs of a rotating structure under ambient excitation. A camera is used to capture images of the rotating structure so that a CSLDV system can track the structure by processing its images. Raw CSLDV measurement is transformed into measurements at multiple virtual measurement points using the lifting method. The OMA method can be used to estimate modal parameters of the rotating structure with a constant speed, including damped natural frequencies, undamped mode shapes, and modal damping ratios, by calculating and analyzing correlation functions between lifted measurements at virtual measurement points and a reference measurement point and their power spectra. It can also be used to estimate ODSs of the rotating structure with a constant or prescribed time-varying speed.

Experimental investigation of the OMA method was conducted on a rotating fan blade under ambient excitation using a new tracking CSLDV (TCSLDV) system that consists of a laser vibrometer, a scanner with its controller, and a camera. The fan was vertically mounted on a stationary frame, which can be considered as a model of a wind turbine. Modal parameters and the ODS of the fan blade with a constant rotation speed and the ODS of the fan blade with a non-constant rotation speed were estimated.

5.2 Methodology

As shown in Fig. 5.1, consider a fan blade that rotates about the z axis, which, without loss of generality, can be modeled as a uniform, rotating Euler-Bernoulli beam with a length l attached to a rigid hub with a radius b. Two coordinate systems are considered: an inertial coordinate system O-XYZ and a rotating coordinate system o-xyz whose origin o is at the center of the rigid hub, which is referred to as the rotation center; the z axis is parallel to the Z axis. The position of the origin O of the inertial coordinate system O-XYZ depends on the position of the camera of the TCSLDV system. Small transverse vibration of the beam along the z axis is considered and vibrations along x and y axes are neglected. The x axis passes through the rotation center and is tangent to the neutral axis of the beam at the point where the beam is attached to the hub. Assume that the beam has linear viscous damping in the z direction.

By following Refs. [20, 21], the governing equation of the uniform rotating Euler-Bernoulli beam under a distributed, external white-noise excitation force $f(x, t)$ in the z direction and its associated boundary conditions are derived using the extended Hamilton's principle:

Fig. 5.1 Schematic of a rotating structure

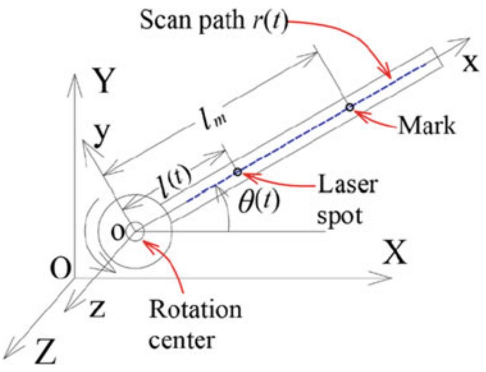

$$\begin{aligned}&\rho w_{tt}\left(x,t\right)+C\left[w_t\left(x,t\right)\right]+EIw_{xxxx}\left(x,t\right)\\&-\tfrac{1}{2}\rho\dot{\theta}^2(t)\left[\left((b+l)^2-x^2\right)w_{xx}\left(x,t\right)-2xw_x\left(x,t\right)\right]=f\left(x,t\right),b\le x\le b+l,t>0\end{aligned} \tag{5.1}$$

$$w\left(x,t\right)|_{x=b}=w_x\left(x,t\right)|_{x=b}=w_{xx}\left(x,t\right)|_{x=b+l}=w_{xxx}\left(x,t\right)|_{x=b+l}=0 \tag{5.2}$$

where the subscripts denote partial differentiation; an overdot denotes a time derivative; x is the spatial position along the x axis; t is time; $\theta(t)$ is the angle between x- and X-axes, as shown Fig. 5.1; w is the transverse displacement of the beam at the position x and time t along the z axis; ρ and EI are the mass per unit length and flexural rigidity of the beam, respectively; and $C(\cdot)$ is the damping operator. Note that Eqs. (5.1) and (5.2) are applicable to a rotating beam with a prescribed time-varying speed $\dot{\theta}(t)$. When $\dot{\theta}(t)=\varOmega$ is a constant, assume that the rotating beam is under a concentrated force $f_{\mathrm{a}}(t)$ applied at x_{a}; the solution to Eqs. (5.1) and (5.2) can be written as

$$w\left(x,t\right)=\sum_{i=1}^{\infty}\phi_i(x)\phi_i\left(x_{\mathrm{a}}\right)\int_0^t f_{\mathrm{a}}\left(\tau\right)g_i\left(t-\tau\right)\mathrm{d}\tau \tag{5.3}$$

where $\phi_i(x)$ is the i-th undamped mode shape of the rotating beam and $g_i(t)$ is the unit impulse response function of the beam corresponding to its i-th underdamped mode:

$$g_i\left(t\right)=\frac{1}{\omega_{d,i}}\mathrm{e}^{-\zeta_i\omega_i t}\sin\left(\omega_{d,i}t\right) \tag{5.4}$$

where ω_i, ζ_i, and $\omega_{d,i}=\omega_i\sqrt{1-\zeta_i^2}$ are the i-th real undamped natural frequency, modal damping ratio, and damped natural frequency of the rotating beam, respectively. Virtual measurement points are assigned on the fan blade in Fig. 5.1 along a time-varying scan path $r(t)$ when the TCSLDV system is used to periodically measure w by scanning its laser spot along the path $r(t)$. The TCSLDV system registers discrete measurements of w with a finite sampling frequency F_{sa}.

A scan path $r(t)$ is usually a straight line on a rotating structure, which is the case considered here. If a CSLDV system is used to scan along a stationary structure and positions of the laser spot can be considered to be linearly related to the rotation angle of a mirror (e.g., X-mirror) in the scanner in the CSLDV, only the X-mirror is needed to complete the scan, and the mirror signal can be directly used as the position of the laser spot on the scan path $r(t)$. However, both X- and Y-mirrors are needed to scan along a rotating structure such as the fan blade here; thus use of only one mirror signal is not enough to describe the position of the laser spot on the scan path $r(t)$. A simulated X-mirror signal for scanning a stationary structure is shown in Fig. 5.2a. Simulated X- and Y-mirror signals for scanning a rotating structure with a constant speed are shown in Fig. 5.2b. A new method is developed in this work to combine X- and Y-mirror signals to describe the position of a laser spot on the scan path $r(t)$ on a rotating structure.

A mark is attached to a structure that rotates with a constant speed to identify positions of the structure and scan path at any time instant (Fig. 5.1). Let the position of the rotation center relative to the inertial coordinate system XYZ be (u_0, v_0), the position of the mark be $(u_{\mathrm{m}}(t), v_{\mathrm{m}}(t))$, and the position of the laser spot be $(u(t), v(t))$; one has

$$\begin{cases}u_{\mathrm{m}}(t)-u_0=l_{\mathrm{m}}\cos\left(\theta(t)\right)=l_{\mathrm{m}}\cos\left(\varOmega t\right)\\v_{\mathrm{m}}(t)-v_0=l_{\mathrm{m}}\sin\left(\theta(t)\right)=l_{\mathrm{m}}\sin\left(\varOmega t\right)\end{cases}, \tag{5.5}$$

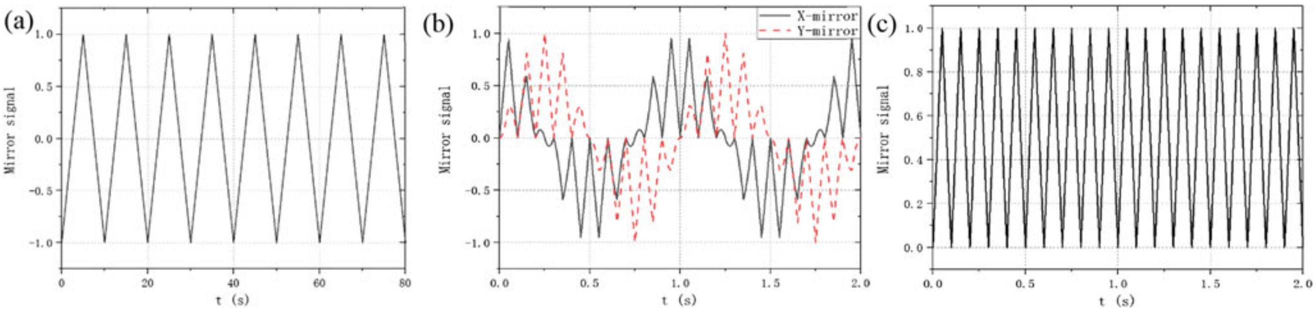

Fig. 5.2 Simulated mirror signals of a CSLDV system: (**a**) the X-mirror signal for scanning a stationary structure; (**b**) X- and Y-mirror signals for scanning a rotating structure; and (**c**) the processed mirror signal by combining mirror signals in (**b**)

$$\begin{cases} u(t) - u_0 = l(t)\cos(\theta(t)) = l(t)\cos(\Omega t) \\ v(t) - v_0 = l(t)\sin(\theta(t)) = l(t)\sin(\Omega t) \end{cases}, \tag{5.6}$$

where l_m is the distance between the rotation center and mark and $l(t)$ is the distance between the rotation center and laser spot at time t, which can be used to describe the position of the laser spot on the scan path $r(t)$. Since the scan path lies on a straight line through the rotation center, the distance between the rotation center and laser spot is

$$r(t) = \sqrt{(u(t) - u_0)^2 + (v(t) - v_0)^2} \tag{5.7}$$

where u and v are X- and Y-mirror signals, respectively. The position of the laser spot on the scan path $r(t)$ can be obtained by combining X- and Y-mirror signals using Eq. (5.7). The processed mirror signal by this method is shown in Fig. 5.2c. The method can also be applied to a structure that rotates with a prescribed time-varying speed. The solution w in Eq. (5.3) can be written as a function of $l(t)$ and t:

$$w\left[l(t), t\right] = \sum_{i=1}^{n} \phi_i\left[l(t)\right]\phi_i\left(x_\mathrm{a}\right)\int_0^t f_\mathrm{a}(\tau)\, g_i(t-\tau)\,\mathrm{d}\tau \tag{5.8}$$

where n is the number of modes that are measured in discrete measurements of w by the TCSLDV system, which is finite since F_sa is finite. The number of virtual measurement points N on the scan path $r(t)$ is determined by $N = F_\mathrm{sa}/F_\mathrm{sc}$ where F_sc is equal to the number of complete scans in 1 s. Multiple series of discrete measurements of w in Eq. (5.8) are formed by lifting them in the lifting method [9]. Each lifted w series corresponds to a virtual measurement point as if it were measured by a transducer attached to the rotating structure at that point. Note that N should be an integer since the laser spot needs to arrive at the same virtual points in each complete scan period; thus F_sa should be an integer multiple of F_sc. Therefore one has

$$l(t) = l\left(t + sT_\mathrm{sc}\right) \tag{5.9}$$

where $s = 0, 1, 2, \ldots$ and $T_\mathrm{sc} = 1/F_\mathrm{sc}$ is the duration of a complete scan period. A complete scan means that the TCSLDV system sweeps its laser spot back and forth once on the scan path $r(t)$. There is a constant sampling time difference $T_\mathrm{sa} = 1/F_\mathrm{sa}$ between two neighboring lifted w series, which means the lifted w series are not simultaneously registered by the TCSLDV system. Let measurement of w starts at $t = 0$ in Eq. (5.8) when the laser spot arrives at an endpoint of the scan path $r(t)$; the lifted w at the k-th virtual measurement point on the path $r(t)$ can thus be written as a function of sT_sc:

$$w_k^l\left(sT_\mathrm{sc}\right) = w\left[(k-1)\,T_\mathrm{sa} + (s-1)\,T_\mathrm{sc}\right] \tag{5.10}$$

where $k = 0, 1, \ldots K$ and $s = 0, 1, \ldots S$, in which K and S are numbers of measurement points and complete scans, respectively. Equation (5.10) shows that the laser spot arrives at the k-th virtual measurement point when $t = (k-1)T_\mathrm{sa} + (s-1)T_\mathrm{sc}$ and the sampling frequency of w_k^l is equal to F_sc. Let $w_{k_1}^l$ and $w_{k_2}^l$ be lifted w at the k_1-th and k_2-th virtual measurement points on the scan path $r(t)$. It can be shown that the correlation function between $w_{k_1}^l$ and $w_{k_2}^l$ can be expressed by [17, 22]

$$\tilde{R}_{k_1k_2}(T) = R\left[\sum_{j=1}^{n} \tilde{A}_j \phi_{j,k_2} \mathrm{e}^{(-\zeta_j\omega_{n,j}+\mathrm{i}\omega_{d,j})(k_2-k_1)T_{\mathrm{sa}}+(-\zeta_j\omega_{n,j}+\mathrm{i}\omega_{d,j})T}\right] \tag{5.11}$$

where $T = \left(m_{k_2} - m_{k_1}\right) T_{\mathrm{sc}}$, $R[\cdot]$ denotes the real part of a complex variable, $\tilde{A}_j$ is a complex factor, and $i = \sqrt{-1}$. By applying a standard OMA algorithm such as the PolyMAX algorithm [23] to power spectra associated with cross-correlation functions, $\omega_{d,j}$, ζ_j, and $\tilde{A}_j\phi_{j,k_2}\mathrm{e}^{(-\zeta_j\omega_{n,j}+\mathrm{i}\omega_{d,j})(k_2-k_1)T_{\mathrm{sa}}}$ in Eq. (5.11) can be estimated, the first two of which are the j-th damped natural frequency and modal damping ratio of the rotating structure, respectively, and ϕ_{j,k_2} in the third of which is the j-th undamped mode shape the rotating structure. The additional term $\mathrm{e}^{(-\zeta_j\omega_{n,j}+\mathrm{i}\omega_{d,j})(k_2-k_1)T_{\mathrm{sa}}}$ in the expression $\tilde{A}_j\phi_{j,k_2}\mathrm{e}^{(-\zeta_j\omega_{n,j}+\mathrm{i}\omega_{d,j})(k_2-k_1)T_{\mathrm{sa}}}$ can be eliminated to obtain ϕ_{j,k_2} with a scaling factor $\tilde{A}_j$ by multiplying the expression by $\mathrm{e}^{-(-\zeta_j\omega_{n,j}+\mathrm{i}\omega_{d,j})(k_2-k_1)T_{\mathrm{sa}}}$ since $\omega_{d,j}$ and ζ_j have been estimated and $(k_2 - k_1)T_{\mathrm{sa}}$ is known. Modal parameters of the rotating structure estimated are not affected by whether the structure is excited at one or multiple points, as long as the reference and measurement points and at least one excitation point are not nodal points of a mode of the structure of interest. ODSs of a rotating structure with a constant or time-varying speed can be estimated by analyzing correlation functions in Eq. (5.11) using the ODS module in the LMS Test.Lab software.

5.3 Experimental Setup

The TCSLDV system was developed in this work for measuring vibration of a rotating structure, and a fan blade with a rotating diameter of 139 cm was used as the rotating structure. The TCSLDV system consists of a Polytec OFV-533 laser Doppler vibrometer, a Cambridge 6240H scanner with an NI 9149 controller, and a Basler camera whose maximum frame rate was 50 Hz (Fig. 5.3a). The controller was connected to the scanner to control rotation angles of two orthogonal mirrors of the scanner. Since the laser beam of the vibrometer was reflected by the mirrors, horizontal and vertical positions of the laser spot on the structure could be controlled by changing rotation angles of X- and Y-mirrors, respectively. A control scheme was designed using the system engineering software LabVIEW so that various scan paths of the laser spot could be created by sending control signals to the scanner. The camera was used to capture images of the rotating fan in Fig. 5.3b with a frame rate of 50 frames per second. Since the TCSLDV system swept its laser spot from one end of the scan path to its other end, which was half of a complete scan, when the camera captured an image of the rotating fan, the number of complete scans in 1 s was half of the frame rate of the camera; therefore $F_{\mathrm{sc}} = 1/2 \times 50 = 25$ Hz. The scan frequency of the TCSLDV system could not exceed 25 Hz since the maximum frame rate of the camera was 50 frames per second, which means Nyquist frequency of the TCSLDV system was 12.5 Hz.

A black circular mark was attached to one blade of the rotating fan so that the TCSLDV system could track the position of the blade by determining the position of the mark. Lower left corners of images captured by the camera were used as references to determine the position of the black circular mark. Every time when the camera captured an image of a rotating fan blade, the image was processed by the LabVIEW software to determine the position of the mark on the blade. Images captured were converted to grayscale images by IMAQ Vision in LabView. IMAQ Find Circular Edge VI in IMAQ Vision could analyze the grayscale images and easily find the position of the black circular mark since it was the only circular item in the images. Since the surface of the blade was white while the mark was black, locations of the mark could be easily

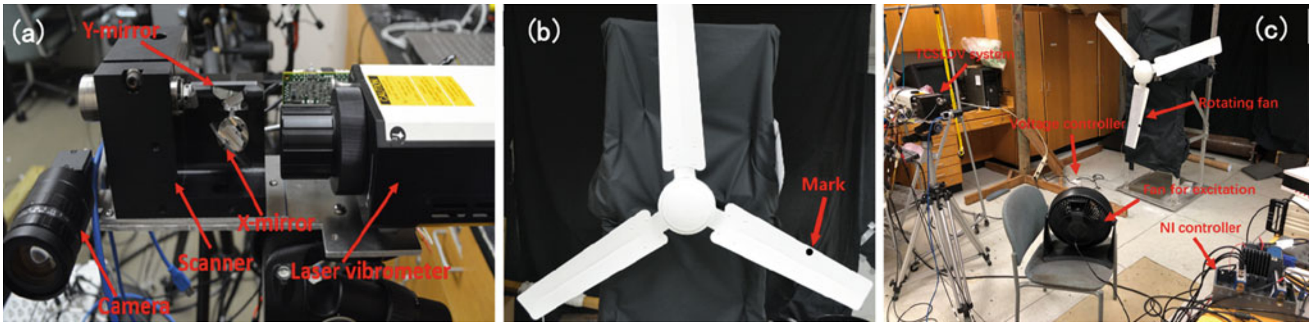

Fig. 5.3 Pictures of (**a**) the TCSLDV system for rotating structure vibration measurement, (**b**) the fan whose blade with a mark is tracked by the camera, and (**c**) the experimental setup

identified in these grayscale images. Since the mark was fixed on the rotating fan blade, the position of the blade could be determined as long as the position of the mark was determined. The controller could control the scanner to track the rotating fan blade and sweep its laser spot along it as the camera continuously captured its images (Fig. 5.3c). Every time when the TCSLDV system determined the position of the mark, it could sweep the laser spot from one end of the scan path to its other end. Since the rotating fan was sufficiently far away from the TCSLDV system and rotation angles of X and Y-mirrors were sufficiently small, horizontal and vertical positions of the laser spot could be considered to be linearly related to rotation angles of X- and Y-mirrors, respectively [17]. Feedback signals of the scanner that are registered in the form of voltage were used to indicate rotation angles of X- and Y-mirrors.

5.4 OMA Results

The first damped natural frequencies and modal damping ratios of the rotating fan blade with three different constant speeds are shown in Table 5.1, and the first undamped mode shapes of the rotating fan blade with the three different rotation speeds are shown in Fig. 5.4a. Revolutions per minute (RPM) was used to represent rotation speed. Spatial position on a scan path is denoted by *x*/*L* in Fig. 5.4 where *x* was the distance between the laser spot and end point of the scan path close to the rotation center and *L* was the length of the scan path. Since Nyquist frequency of the TCSLDV system was 12.5 Hz and the second damped natural frequency of the stationary fan blade measured by a laser vibrometer was about 27 Hz, only the first modal parameters were estimated. Note that to estimate modal parameters of the stationary fan blade, the fan was turned off and the fan blade was excited by the excitation fan in Fig. 5.3c. The fan blade was basically stationary, but slowly swung back and forth a bit about its downward equilibrium position due to fan excitation, and it was scanned by the TCSLDV system. Note also that undamped mode shapes estimated in this work were normalized by dividing their data by their maximum values. It was seen that there was more uncertainty in damping ratio measurement than damped natural frequency measurement as there was more uncertainty in damping modeling in Eq. (5.1). Compared with the damping of the stationary blade, there was larger damping when the blade rotates due to additional damping from air flow and friction

Table 5.1 First damped natural frequencies and modal damping ratios of the stationary fan blade and the rotating fan blade with three different constant speeds

RPM	Damped natural frequency (Hz)	Modal damping ratio (%)
Stationary	6.22	0.351
9.16 rpm	6.34	0.789
14.25 rpm	6.50	0.709
20.61 rpm	6.73	0.939

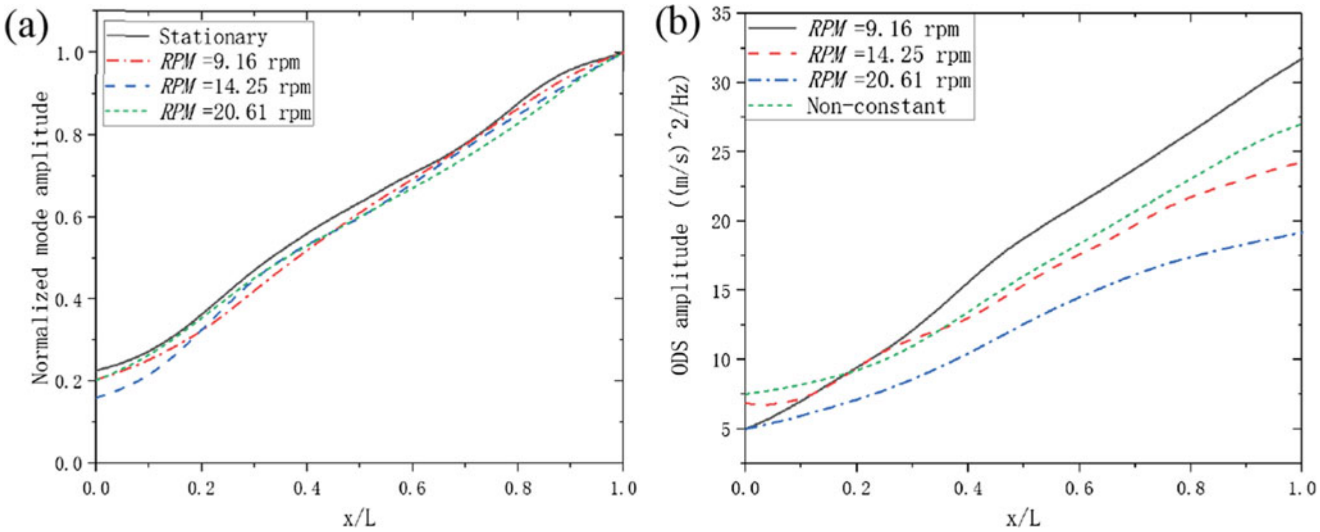

Fig. 5.4 (**a**) First normalized undamped mode shapes of the stationary fan blade and the rotating fan blade with three different constant speeds, and (**b**) ODSs of the rotating fan blade with three different constant speeds and a non-constant speed

damping in the fan motor. Therefore estimated modal damping ratios of rotating fan blade in Table 5.1 were larger than those of stationary fan blade. The estimated first damped natural frequency of the rotating fan blade increases with its speed due to the centrifugal stiffening effect. Estimated ODSs of the rotating fan blade in four tests with three different constant speeds and a non-constant speed are shown in Fig. 5.4b. The estimated ODS of the rotating fan blade with the non-constant speed had a similar shape to those of the rotating fan blade with constant speeds. Differences among ODSs of the rotating fan blade with different speeds in Fig. 5.4b were more pronounced than those among its first normalized undamped mode shapes in Fig. 5.4a, since ODSs depended on wind loads applied on the rotating fan blade and wind loads depended on its rotation speeds, while first normalized undamped mode shapes did not depend on wind loads.

5.5 Conclusion

A novel TCSLDV system was developed to track and scan a rotating structure, and a new OMA method based on a rotating beam vibration theory, an image processing method, and the lifting method is proposed to measure and estimate its modal parameters for a constant rotation speed and ODSs for constant and non-constant rotation speeds. The image processing method determines real-time positions of the rotating structure to calculate its speed and generate a scan path on the structure. The lifting method is used to transform TCSLDV measurement into measurements at multiple virtual measurement points. Correlation functions with non-negative time delays among lifted measurements are calculated and analyzed to estimate modal parameters and ODSs of the rotating structure. Modal parameters a rotating fan blade with a constant speed and ODSs of the fan blade with constant and non-constant speeds are successfully estimated using the new OMA method. A high-speed camera is needed to estimate modal parameters of a rotating structure with high natural frequencies using this OMA method. It is experimentally shown that estimated damped natural frequencies of the rotating fan blade increased with its speed.

Acknowledgments The authors are grateful for the financial support from the National Science Foundation through Grant No. CMMI-1763024. The authors would like to thank Daming Chen for some valuable discussion on the TCSLDV system.

References

1. Ewins, D.J.: Modal Testing: Theory, Practice and Application, 2nd edn. Research Studies Press, Hertfordshire, UK (2000)
2. Xu, Y.F., Zhu, W.D.: Efficient and accurate calculation of discrete frequency response functions and impulse response functions. J. Vib. Acoust. **138**(3), 031003 (2016)
3. Xu, Y.F., Liu, J., Zhu, W.D.: Accurate and efficient calculation of discrete correlation functions and power spectra. J. Sound Vib. **347**, 246–265 (2015)
4. James, G., Carne, T.G., Lauffer, J.P.: The natural excitation technique (NExT) for modal parameter extraction from operating structures. Modal Anal. **10**(4), 260–277 (1995)
5. Siringoringo, D.M., Fujino, Y.: Noncontact operational modal analysis of structural members by laser Doppler vibrometer. Comput. Aided Civ. Inf. Eng. **24**(4), 249–265 (2009)
6. Rothberg, S., Allen, M., Castellini, P.: An international review of laser Doppler vibrometry: Making light work of vibration measurement. Opt. Lasers Eng. **99**(1), 11–22 (2017)
7. Chen, D.M., Xu, Y.F., Zhu, W.D.: Damage identification of beams using a continuously scanning laser Doppler vibrometer system. J. Vib. Acoust. **138**(5), 05011 (2016)
8. Stanbridge, A., Ewins, D.: Modal testing using a scanning laser Doppler vibrometer. Mech. Syst. Signal Process. **13**(2), 255–270 (1999)
9. Allen, M.S., Sracic, M.W.: A new method for processing impact excited continuous-scan laser Doppler vibrometer measurements. Mech. Syst. Signal Process. **24**(3), 721–735 (2010)
10. Stanbridge, A., Ewins, D., Khan, A.: Modal testing using impact excitation and a scanning LDV. Shock. Vib. **7**(2), 91–100 (2000)
11. Chen, D.M., Xu, Y.F., Zhu, W.D.: Experimental investigation of notch-type damage identification with a curvature-based method by using a continuously scanning laser Doppler vibrometer system. J. Nondestruct. Eval. **36**, 38 (2017)
12. Chen, D.M., Xu, Y.F., Zhu, W.D.: Identification of damage in plates using full-field measurement with a continuously scanning laser Doppler vibrometer system. J. Sound Vib. **422**, 542–567 (2018)
13. Xu, Y.F., Chen, D.M., Zhu, W.D.: Damage identification of beam structures using free response shapes obtained by use of a continuously scanning laser Doppler vibrometer system. Mech. Syst. Signal Process. **92**, 226–247 (2017)
14. Yang, S., Allen, M.S.: Output-only modal analysis using continuous-scan laser Doppler vibrometry and application to a 20kw wind turbine. Mech. Syst. Signal Process. **31**, 228–245 (2012)
15. Wereley, N.M., Hall, S.R.: Frequency response of linear time periodic systems. In: 29th IEEE Conference on Decision and Control, Honolulu, HI, USA, vol. 6, pp. 3650–3655 (1990)
16. Yang, S., Allen, M.S.: Lifting approach to simplify output-only continuous-scan laser vibrometry. Mech. Syst. Signal Process. **45**(2), 267–282 (2014)

17. Xu, Y.F., Chen, D.M., Zhu, W.D.: Operational modal analysis using lifted continuously scanning laser Doppler vibrometer measurements and its application to baseline-free structural damage identification. J. Vib. Control. **25**(7), 1341–1364 (2019)
18. Gasparoni, A., Allen, M., Yang, S., Sracic, M., Castellini, P., Tomasini, E.: Experimental modal analysis on a rotating fan using tracking-CSLDV. In: AIP Conference Proceedings, vol. 60, (2010). https://doi.org/10.1063/1.3455482
19. Khalil, H., Kim, D., Nam, J., Park, K.: Operational deflection shape of rotating object using tracking laser Doppler vibrometer. In: 2015 IEEE International Conference on Electronics, Circuits, and Systems (ICECS), Cairo, pp. 693–696 (2015)
20. Zhu, W.D., Mote Jr., C.D.: Dynamic modeling and optimal control of rotating Euler-Bernoulli beams. ASME. J. Dyn. Syst. Meas. Control. **119**(4), 802–808 (1997)
21. Meirovitch, L.: Analytical Methods in Vibrations. The Macmillan Co, New York (1967)
22. Papoulis, A., Pillai, S.U.: Probability, Random Variables, and Stochastic Processes. Tata McGraw-Hill Education, New Delhi (2002)
23. Peeters, B., Van der Auweraer, H., Guillaume, P., Leuridan, J.: The PolyMAX frequency-domain method: A new standard for modal parameter estimation laser. Shock. Vib. **11**(3–4), 395–409 (2004)

Chapter 6
Delamination Detection in Fiber Metal Laminates Using Ultrasonic Wavefield Imaging

Casey Gardner, Young Ko, Michael Koutoumbas, Eric Flynn, Ian Cummings, and Phil Cornwell

Abstract This work presents a novel, non-destructive evaluation (NDE) method for detecting delaminations in fiber metal laminate (FML) plate-like structures. FMLs are rapidly replacing other materials in many aerospace applications because of their superior mechanical properties, including improved tolerance to fatigue, corrosion, and impact damage. However, delaminations can occur deep in the plate, and since access is limited to the composite face during most operations, the ability of traditional NDE techniques to discern these defects is limited. Many researchers have proposed using ultrasonic guided waves to image defects, but the anisotropic nature of wave propagation in FMLs and the subtlety of defects between metal and fiber-reinforced composite layers necessitate a new approach. In contrast to repeated transient excitations proposed in other literature, the method proposed here utilizes the full-field, steady-state response of an FML plate to ultrasonic excitation. Thus, the inspection time is shortened as the delay between measurements is removed, and a higher-energy input improves the signal-to-noise ratio. A 2D scanning laser Doppler vibrometer (LDV) is used to record the measurements at discrete points, while a piezoelectric transducer supplies the ultrasonic excitation. The steady-state response is processed to visualize defects on a pixel-by-pixel basis and locate potential regions of delamination in the FML plate. In this study, the one-dimensional response of a plate-like T800 graphite composite Ti-6Al-4V FML specimen with known areas of delamination is simulated. Two defect-detection features, based on simulated physical phenomena—detrended Hilbert envelope magnitude (DHEM) and low-pass local phase derivative (LLPD)—are subsequently evaluated over a wide range of excitation frequencies, to determine an optimal input for increased precision. Results from these simulations suggest potential guidelines to achieve a rapid and reliable NDE method for delamination detection in FML structures.

Keywords Ultrasonic inspection · Fiber metal laminate (FML) · Composite-overwrapped pressure vessel (COPV) · Acoustic wavenumber spectroscopy (AWS) · Laser Doppler vibrometer (LDV)

6.1 Introduction

Fiber metal laminates (FMLs) are rapidly replacing core structural materials in the aerospace industry. For instance, FMLs have been used to construct cryogenic propellant tanks in launch vehicles, sometimes referred to as composite-overwrapped pressure vessels (COPVs). Consisting of a metal substrate and fiber-reinforced composite layers, FMLs have a superior strength to weight ratio and improved tolerance to fatigue, corrosion, and impact damage compared to pure metals or pure fiber-epoxy composites [1, 2]. However, these hybrid materials are vulnerable to delamination, matrix cracking, and fiber

---

C. Gardner · Y. Ko · M. Koutoumbas
NSEC-EI, Los Alamos National Laboratory, Los Alamos, NM, USA

E. Flynn
ISR-2, Los Alamos National Laboratory, Los Alamos, NM, USA
e-mail: eflynn@lanl.gov

I. Cummings (✉)
NSEC-EI, Los Alamos National Laboratory, Los Alamos, NM, USA

ISR-2, Los Alamos National Laboratory, Los Alamos, NM, USA
e-mail: itc@lanl.gov

P. Cornwell
Department of Mechanical Engineering, U.S. Air Force Academy, Colorado Springs, CO, USA
e-mail: phil.cornwell@usafa.edu

D. Di Maio, J. Baqersad (eds.), *Rotating Machinery, Optical Methods & Scanning LDV Methods, Volume 6*, Conference Proceedings of the Society for Experimental Mechanics Series, https://doi.org/10.1007/978-3-030-76335-0_6

failure, representing a serious threat to the safety and reliability of the overall structure. Often, damage occurs deep beneath the surface, such as between the laminated composite and metal layers, and is not detectable by visual inspection. Thus, a critical challenge in ensuring the safety and quality of structural components is developing the ability to accurately and efficiently detect damage via non-destructive evaluation (NDE). Due to their complex manufacturing and mechanical nature, COPVs introduce additional challenges when considering high-risk operations such as space travel and military applications [2]. Defects that occur during their operation pose failure concerns which may risk human life or the destruction of launch vehicles and multi-billion dollar infrastructure. In September 2016, a SpaceX launch vehicle was destroyed when a COPV failed during fueling [3]. Although the ability of finite element models (FEMs) to predict FML behavior is continuously improving, a nominally functioning FML structure requires frequent NDE if it is intended for reuse.

This work describes two proposed delamination detection features and a process for choosing an optimal excitation frequency during experimental testing, based on simulated ultrasonic measurements of an FML. Section 6.2 provides a literature review of prior work detecting delaminations in composites and FMLs specifically. Section 6.3 describes the FEM used in this work. Section 6.4 motivates and discusses two proposed features that highlight delaminations, based on simulated results. Lastly, Sect. 6.5 discusses performance of the two proposed features as well as a procedure for validating and utilizing the findings for NDE of an FML article.

6.2 Literature Review

According to Montinaro et al., “The presence at the mesoscale of so diverse materials such as metals and plastic composites [in FMLs] has represented a great challenge in the quest to adapt or develop effective [NDE] techniques’” [1]. Since 2000, there has been significant discussion in the literature about potential solutions to this issue [4]. Both Montinaro et al. and Ibarra-Castanedo et al. proposed active thermographic inspection techniques [1, 5]. Others have proposed electromagnetic-based inspection techniques, including radiography [6], eddy current testing [7], and a novel conductance-based approach [8]. This paper contributes to the class of ultrasonic (UT) inspection techniques, which are popular for their relative speed and accuracy [9–16].

Ultrasonic waves have been widely employed for damage detection because of their high sensitivity to changes in geometry and ability to propagate long distances with minimal attenuation. In plate-like structures, propagating waves are often referred to as guided Lamb waves [17]. Many researchers have studied the use of guided Lamb waves’ amplitude, velocity, or local wavenumber (inverse of wavelength) to analyze damage. For instance, Gao et al. developed an NDE approach for delamination detection in a three-layer metal composite for manufacturing quality control, based on the amplitude of reflected Lamb waves [9]. However, Yeum et al. found that both delaminations and environmental temperature variations could affect the amplitude of propagating Lamb waves in a carbon fiber-reinforced polymer (CFRP) composite, potentially masking the effects of incipient delaminations [10]. Lee et al. extracted the propagation direction of incident waves from a transient excitation and used adjacent wave subtraction to image structural anomalies based on wave amplitude [18].

Numerous researchers have also found that, in the presence of delaminations and other defects, the velocity of propagating guided Lamb waves is decreased and proposed using time-of-flight (TOF) measurements for damage detection. Although the dispersive quality of guided Lamb waves increases the complexity of the analysis, many researchers have still found success using velocity as a damage detection feature. Yeum et al. compared TOF measurements along different wave propagation paths in a network of sensors, to obtain a baseline given current environmental conditions; a damage indicator was then developed based on the measured data [10]. Petculescu et al. quantified the effect of size and artificial delamination type on the velocity of guided Lamb waves in CFRP composite specimens [11]. Demcenko et al. and Shelke et al. also showed how TOF measurements could be used to detect delaminations in a three-layer GLARE FML and a two-layer bonded aluminum plate, respectively [12, 13]. Kim et al. used similar techniques in their modelling and experimental work but purposefully generated solitary waves rather than guided Lamb waves [14].

Wavenumber-based damage detection techniques are quickly gaining prominence in the literature, since they allow for both the location and quantitative size estimation of certain defects, including delaminations. Acoustic wavenumber spectroscopy (AWS) is one such technique, where guided Lamb wave propagation is measured with a non-contact laser Doppler vibrometer (LDV) to visualize the response of the test specimen. Flynn and Jarmer used AWS to examine the steady-state excitation of plate-like structures and found that AWS reduced the inspection time and improved the fidelity of measurements, compared with transient-excitation approaches [19]. Tian et al. combined phased array imaging with wavenumber-based methods to further minimize scan time, in a two-step process they referred to as the “global-local approach” [15]. LDV scans at discrete points were used to construct a phased array to globally locate damage, and then a higher-resolution scan was performed in that region to more precisely estimate local wavenumbers [15, 20]. However, most prior work with wavenumber-based techniques has been applied to relatively thin composite materials, and few researchers have applied these techniques to materials as thick and heterogeneous as the FMLs found in COPVs.

6.3 Model Setup

Abaqus CAE is a comprehensive finite element modelling, simulation, and post-processing software suite that allows for the simulation of coupled multiphysics phenomena and complex geometries. For this study, Abaqus was used to model the steady-state response of a two-dimensional FML model subjected to periodically varying pressure inputs. The model dimensions are chosen to match an existing FML plate test article, consisting of a 10.16-mm-thick T800-graphite composite bonded to a 0.813 mm Ti-6Al-4V metal backing. A linear perturbation analysis was employed to solve for the steady-state solution and quantify the complex response. The material properties used for carbon fiber-reinforced polymer (CFRP) and titanium are listed in Table 6.1, while the delamination was modelled as a rectangular void. The pressure source, representing the cross section of a PZT, is modelled as a line on the composite surface. In all simulations, the transducer was positioned near the left edge of plate, and the wave propagates from left to right.

Figure 6.1 shows the 2D through-thickness 10.3 × 254 mm rectangular geometry which was sectioned vertically into a 10.2-mm-thick composite panel and a 0.813-mm-thick titanium lamina. The delamination was located 127 mm from the left edge and was represented by a 1-mm-thick, 20-mm-long void. Some simplifying assumptions were made to make the simulation tractable and computationally efficient. Firstly, the CFRP section was assumed to have bulk properties, and no ply-by-ply modelling was employed. Secondly, a vertical, concentrated, complex sinusoidal force with complex magnitude $F = -1000 - 1000i\ N$ was used to generate the response. Thirdly, fixed boundary conditions were enforced on the two lower (titanium) corners of the plate; the edges were free to deform. Only the spatial velocity waveforms of the steady-state response on the top surface (composite side) were recorded and analyzed using MATLAB, to mimic the data available from an LDV scan. In order to avoid the near-field effects of the transducer, the leftmost 100 mm of the data is removed and not analyzed. Hence, spatial data will be trimmed starting at 100 mm from the leftmost end of the plate.

6.4 Feature Extraction Process

The spatial velocity waveforms exhibit diverse behavior over a range of excitation frequencies. Figure 6.2 shows two delamination-detection features evaluated from simulations driven by representative excitation frequencies. In all four cases, the model geometry and the location of the simulated delamination (at 264 mm from the left edge) remain unchanged. Figure 6.2a shows a significant increase in the magnitude of the spatial waveform at the delamination when excited at

Table 6.1 Engineering constants for carbon epoxy laminate used for simulation purposes

Young's modulus E_{11} [MPa]	Young's modulus $E_{22} = E_{33}$ [MPa]	Shear modulus $G_{12} = G_{13}$ [MPa]	Shear modulus G_{23} [MPa]	Poisson's ratio $\nu_{12} = \nu_{13}$	Poisson's ratio ν_{23}
138,000	9500	5200	1450	0.28	0.40

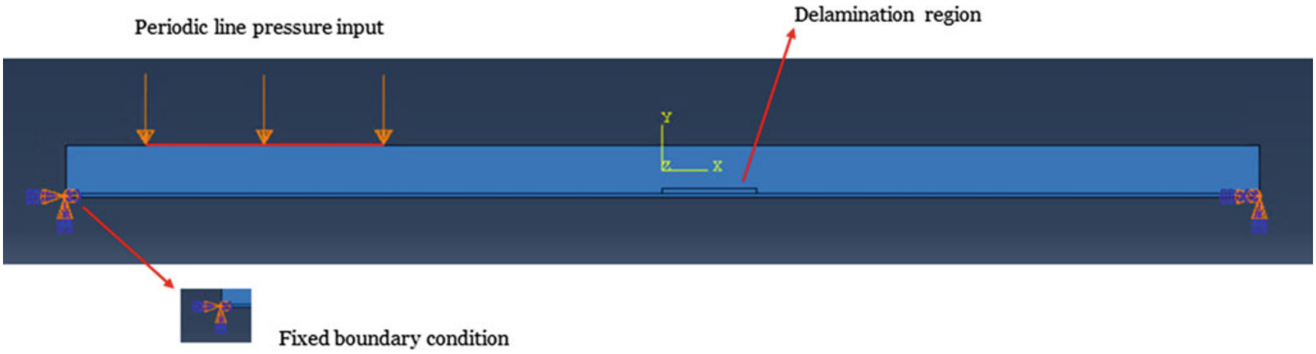

Fig. 6.1 Two-dimensional through-thickness geometry of Abaqus model

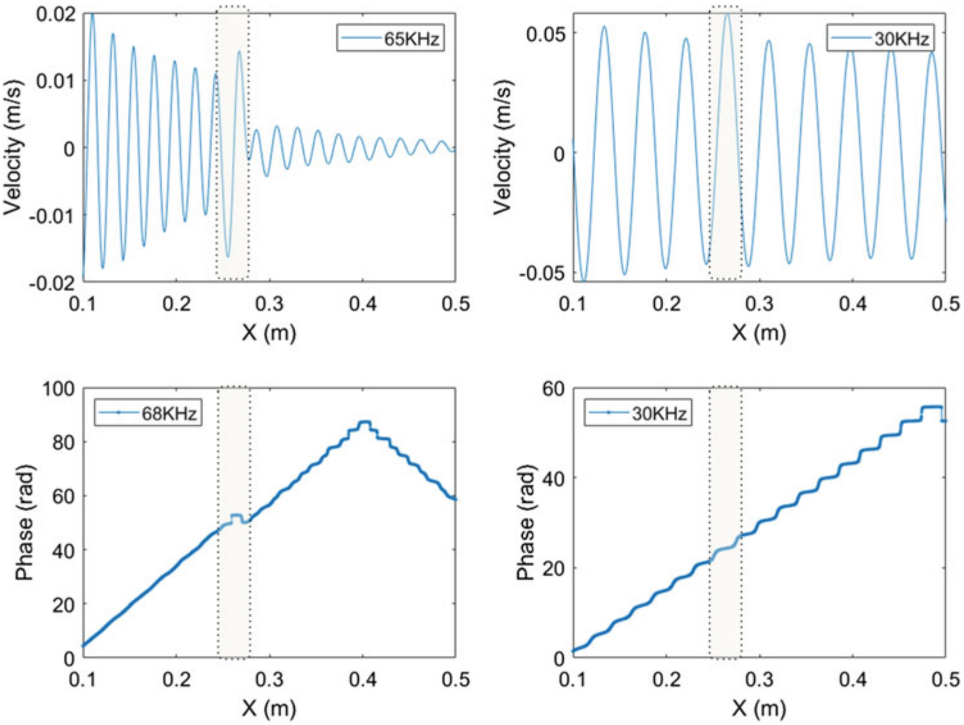

Fig. 6.2 Spatial velocity waveform obtained from the simulation in different forms: (**a**) magnitude at 65 kHz, (**b**) magnitude at 30 kHz, (**c**) phase at 68 kHz, (**d**) phase at 30 kHz

65 kHz, compared to Fig. 6.2b, which shows the same case excited at 30 kHz. Similarly, when the phase of complex velocity waveform is examined, Fig. 6.2c shows a plateau in the delamination region when the excitation frequency is 68 kHz. In contrast, no such plateau is observed in Fig. 6.2d when the excitation frequency is 30 kHz.

The observations shown in Fig. 6.2a, c only occur at specific frequencies, depending on the properties of the delamination and the feature being evaluated. Although multiple frequencies may highlight the delamination in terms of a specific feature, an optimal excitation frequency can be defined as the one that maximizes both the accuracy and effectiveness of the delamination detection. Therefore, the goal is to not only extract features but also find an optimal excitation frequency for each feature, depending on the properties of the delamination. To summarize, features are first evaluated over a range of frequencies following the process stated above. Next, the performance of each feature in highlighting the delamination is compared as a function of excitation frequency. This information is then used to determine which frequencies and features might be most effective for detecting delaminations in specific measurement scenarios.

In this study, two such features are designed and evaluated to highlight the location and size of a known, simulated delamination. The primary objective for feature design is to capture the two behaviors observed in Fig. 6.2. It is hypothesized that these behaviors are the result of resonant standing waves getting caught in the delamination region. In a delaminated region, the ultrasonic surface wave is exposed to a locally thinner material, and its speed changes abruptly. Shortly afterward, at the far edge of the delamination, the wave speed reverts to its original value because the full thickness is well bonded. This abrupt variation of velocity can trap a standing wave in that area, if the wavelength is comparable to the delamination size. The derivation of each feature and its correlation to the trapped standing wave is discussed in Sects. 6.4.1 and 6.4.2. The performance of each feature for delamination detection is evaluated in Sect. 6.5.

6.4.1 Detrended Hilbert Envelope Magnitude (DHEM)

The first feature described in this study, which we refer to as the Detrended Hilbert Envelope Magnitude (DHEM), is produced by detecting the envelope of the magnitude of the velocity and then detrending that envelope. At certain excitation frequencies, a significant magnitude increase is observed near the delamination, as seen in Fig. 6.2. In this case, it is hypothesized that the trapped standing wave undergoes constructive interference with the original wave from the transducer.

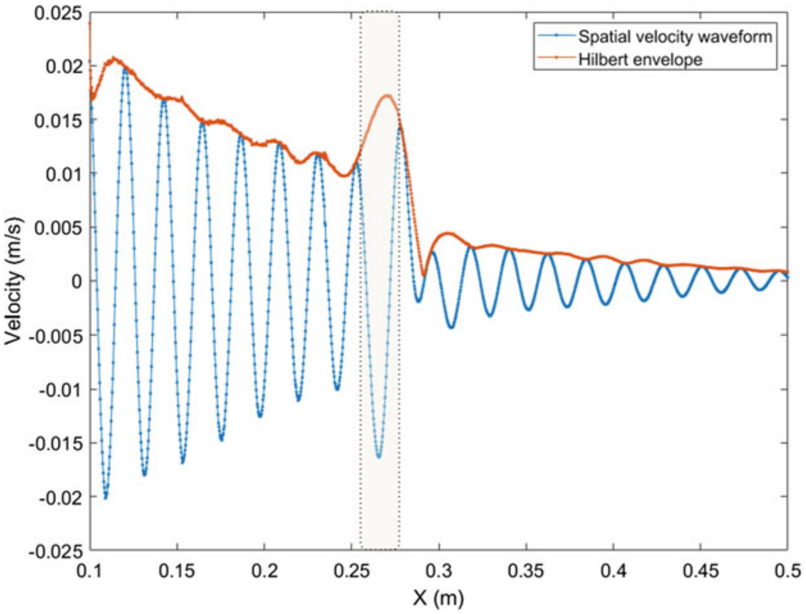

Fig. 6.3 Hilbert envelope applied to spatial velocity waveform at excitation frequency 65 kHz; (blue) spatial velocity waveform, (red) Hilbert analytic envelope

Waveforms generated at other excitation frequencies generally show decreasing magnitude as they propagate away from the transducer.

The Hilbert transform is applied to a complex-valued velocity waveform constructed from two real velocity waveforms, simulated a half period ($\pi/2$ radians) apart. In this way, one velocity waveform becomes the real part of complex velocity data, and the other serves as the imaginary part. The Hilbert envelope overwraps this complex velocity waveform, yielding upper and lower envelopes, which represent the extremes of the signal fluctuation. In this case, only the upper envelope is leveraged such that the perturbation can be expressed as a peak. Indeed, a local maximum is clearly observed in the enveloped result shown in Fig. 6.3.

Since the velocity magnitude of the wave decreases as it moves away from the transducer, the local maximum of the Hilbert envelope at the delamination location is not a global maximum. This decreasing trend can be seen in the red plot of Fig. 6.4 and can lead to difficulty in determining the most probable location of delamination. To mitigate this issue, the enveloped velocity waveform is detrended: the logarithm of the function is taken, a fitted first-order polynomial is subtracted, and lastly an exponential operator is applied to restore the original scaling. This process yields a global maximum corresponding to the delamination location. In Fig. 6.4, for example, the blue function is the DHEM resulting from the original Hilbert envelope shown in red. Both functions are normalized by their respective means for convenient comparison. A similar process, applied to a non-standing wave excitation frequency, does not exhibit this behavior and instead yields a nearly constant result. Thus, the DHEM feature is selected as the first feature for consideration, because it highlights the delaminated region with higher values.

6.4.2 *Low-Pass Local Phase Derivative (LLPD)*

The second proposed feature for delamination detection relies on the derivative of spatial velocity phase. To begin, discontinuities in the digital phase are removed by unwrapping the phase angles. Two examples of unwrapped phase are shown in Fig. 6.2c, d, with excitation frequencies at 68 kHz and 30 kHz, respectively.

Generally, the unwrapped phase increases as the wave propagates in a uniform direction, away from the transducer, as seen in Fig. 6.2d. However, it is not uncommon for the phase to trend downward as it approaches the right edge of the plate. The authors hypothesize that this trend reversal represents waves reflected from the edge of the plate and travelling in the opposite direction. Eventually, the original wave from the transducer and reflected wave meet, yielding a local maximum where the derivative of the phase becomes zero. This behavior was observed across multiple excitation frequencies. For clarity, this point will be referred to as the “reversal point” in future discussion.

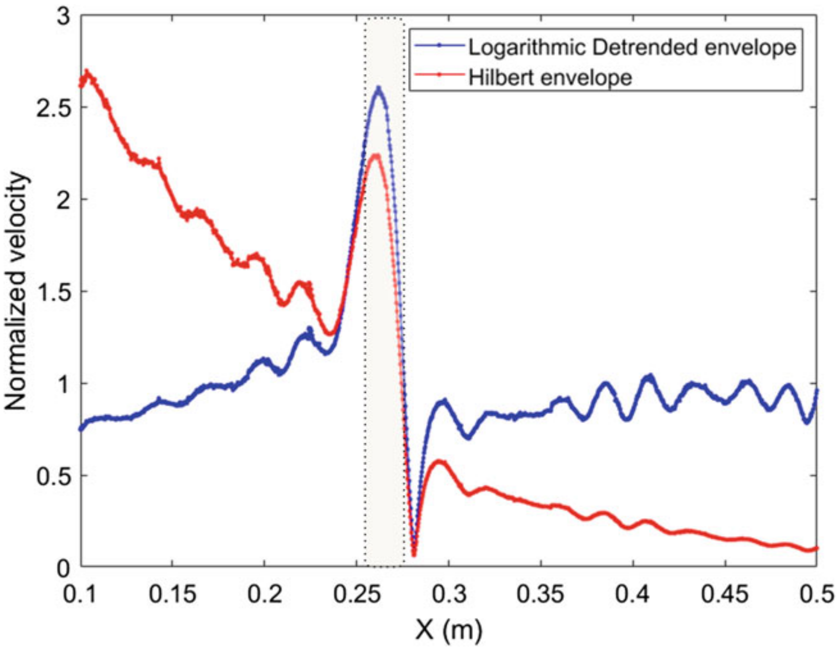

Fig. 6.4 Hilbert envelope (red) is logarithmically detrended to emphasize the peak (blue); velocity magnitude is normalized by its own mean

Similar phase reversals can also be used to detect delaminations. At certain excitation frequencies, such as the 68 kHz case shown in Fig. 6.2c, a second, local phase reversal occurs near the delamination (264 mm away from the left edge). The authors hypothesize that these "plateaus" are the result of a similar wave reflection phenomenon from a trapped standing wave. Therefore, it is useful to locate such plateaus as areas of delamination and distinguish them from any reversal points, which also yield a phase derivative of zero, due to the overall geometry of the plate.

To begin with, a finite impulse response (FIR) differentiator filter is used to differentiate the phase of the waveform. FIR differentiator filters take a band-limited signal as an input and output samples that represent the derivative of that signal, without significantly amplifying any random noise in the input. For the present effort, a low-pass filter (eighth-order Butterworth, with cutoff of 20 kHz) is also applied to reduce high-frequency noise. The low-pass filtered, unwrapped phase for an excitation frequency of 68 kHz is shown in Fig. 6.5 and is significantly smoother compared with the unfiltered phase originally shown in Fig. 6.2c and reproduced here. The derivative of both, calculated with an FIR filter, is shown in Fig. 6.6, where the delamination plateau and the reversal point are clearly separated from other areas of the plate.

In order to distinguish which zero derivative point corresponds to the reversal point and the delamination plateau, a sliding rectangular window is introduced prior to differentiation. While this window moves along the spatial domain, phase values within each window are extracted. With this isolated phase data for each window, the absolute difference between adjacent phase values is calculated. Finally, the mean of these differences is obtained to represent the phase derivative of the particular sliding window. This process, shown in Eq. 6.1 for a single window of size *N*, is termed the mean absolute difference (MAD) of these points and continues as the sliding window reaches the plate end. Given that phase differences are discretely averaged in each window, the specific reversal point where two counter-propagating waves collide does not appear in this approach. Multiple sliding windows encompass this point and the mean phase is obtained at each one of them. Therefore, the differences among mean phases near this local maximum are non-zero. In contrast, the plateau consists of multiple points that form a region of constant phase. Thus, the mean absolute difference at this region is still zero even after the sliding window is applied, enabling one to separate delamination plateaus from a reversal point.

$$\mathrm{MAD}(N) = \sum\nolimits_{i=0}^{N-1} \left| \frac{\phi(x)_i + \phi(x)_{i+1}}{N} \right| \tag{6.1}$$

Figure 6.7 displays the effect of the sliding window applied to the low-pass filtered phase, after which the mean absolute difference—described by Eq. 6.1—is calculated between mean phases at each window. In short, the second feature is composed of four consecutive steps: phase extraction, low-pass filtering, sliding window, and mean absolute difference.

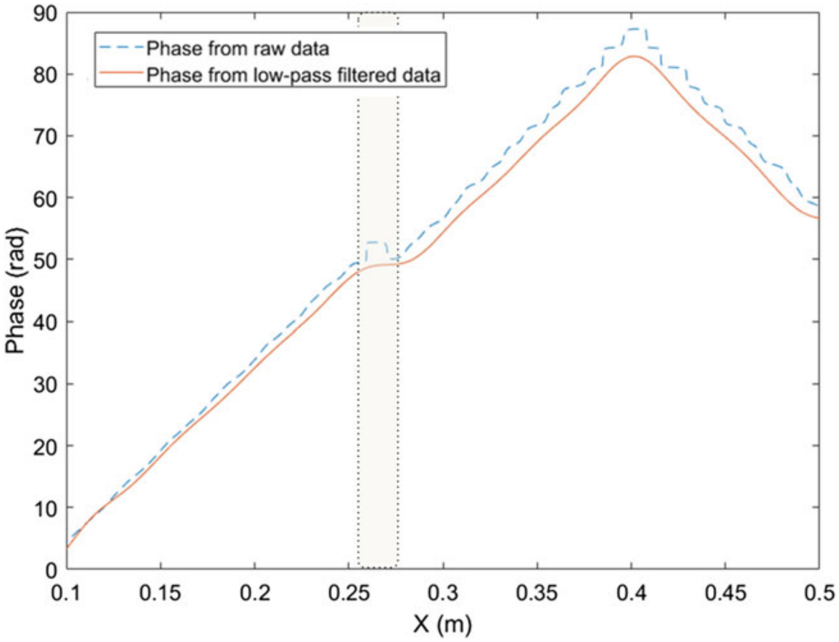

Fig. 6.5 Phase of spatial velocity waveform at excitation frequency 68 kHz from raw data (blue) and 20 kHz low-pass filtered data (red)

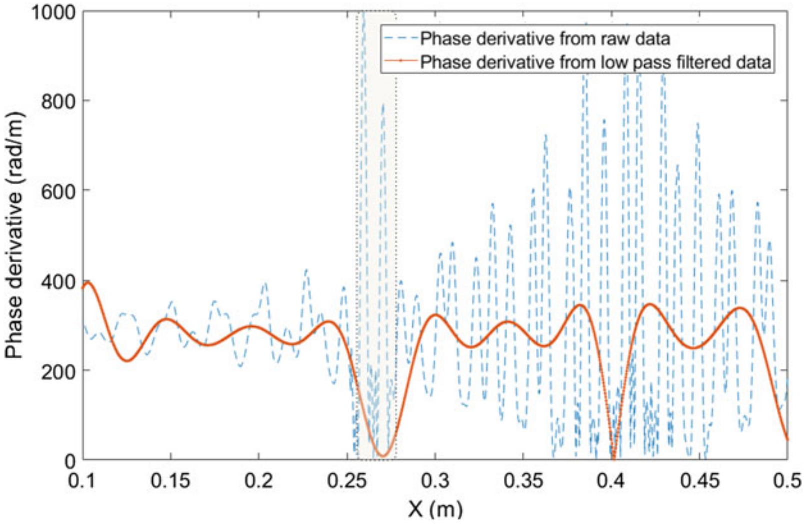

Fig. 6.6 Phase derivative of spatial velocity waveform at excitation frequency 68 kHz from raw data (blue) and 20 kHz low-pass filtered data (red)

As a result, the zero crossing at the reversal point is replaced with a positive, non-zero value, and the delamination plateau results in a global minimum. For ease of interpretation, this second delamination detection feature is inverted, as shown in Fig. 6.8, to clearly highlight the delamination plateau.

6.5 Qualitative Evaluation of the Feature Performance

The ability of the two features to detect a delamination in the FML plate is evaluated by comparing feature profiles over a range of excitation frequencies from 1 to 150 kHz. A total of 150 feature profiles are overlaid in one heat map as shown in Figs. 6.9 and 6.10 for the representative case (composite thickness of 10 mm, delamination length of 20 mm, and delamination location 264 mm from the left edge). The *x*-axis is the spatial domain, from 150 to 400 mm (at the right edge of

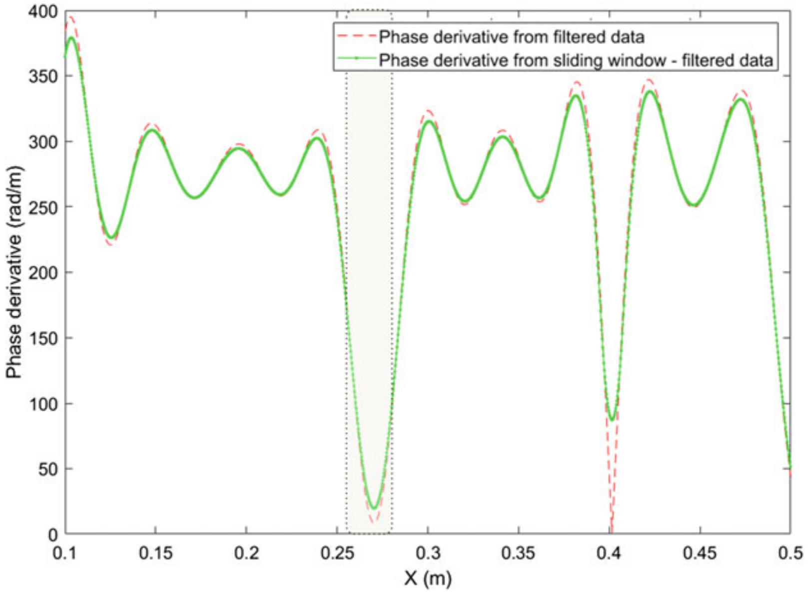

Fig. 6.7 Phase derivative of spatial velocity waveform at excitation frequency 65 kHz from only filtered data (red) and sliding window applied filtered data (green)

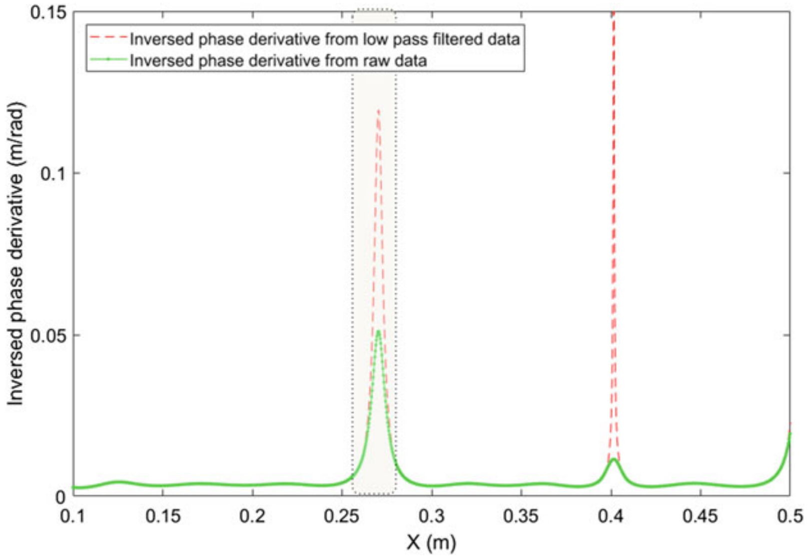

Fig. 6.8 Inverse of the phase derivative of spatial velocity waveform at excitation frequency 65 kHz from filtered data (red) and sliding window filtered data (green)

the plate), and the y-axis represents the excitation frequencies used. The leftmost 100 mm of the plate is intentionally removed to exclude exceptionally high feature values, due to local effects near the transducer. In both heat maps, the faded section represents the location and length of the delamination; this is referred to as the "delamination box" in further discussion. Two evaluation criteria are adopted to evaluate the features and determine an optimal excitation frequency for delamination detection. Firstly, the max of the feature peak should correspond with the delamination box (to prevent false negatives), and secondly, no other high feature region should exist apart from the delamination box at the chosen frequency (to prevent false positives).

First, Fig. 6.9 shows the distribution of the first feature, DHEM. Three distinct frequency paradigms can be observed. At lower frequencies (below 64 kHz), the feature does not seem to highlight the delamination. At approximately 64–65 kHz (marked by a red circle in the figure), a distinct, local maximum occurs that is well aligned with the delamination box. For higher frequencies (above 100 kHz), a strong but wide feature peak emerges as shown in a black rectangle in Fig. 6.9. Given

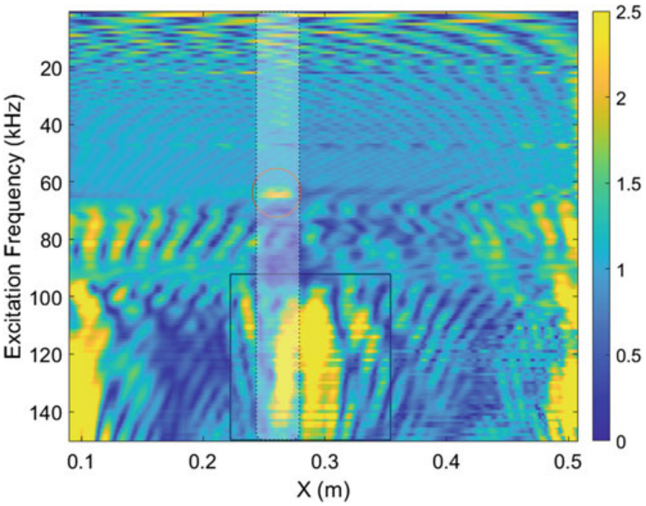

Fig. 6.9 Two-dimensional feature heat map for the DHEM

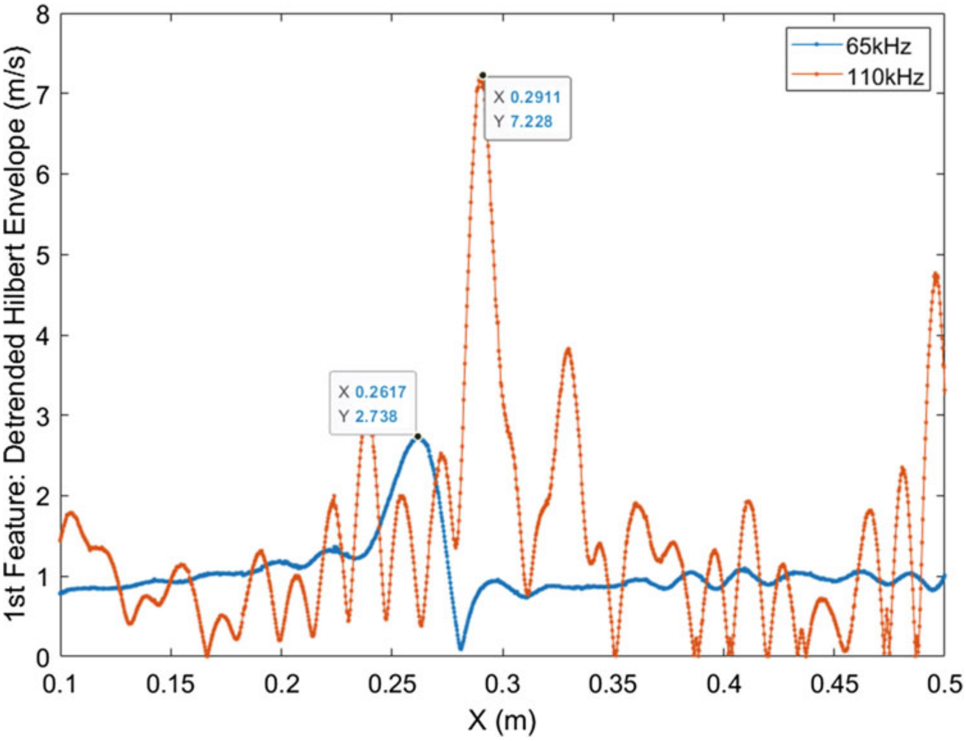

Fig. 6.10 The DHEM at two excitation frequencies: 65 kHz (blue) and 110 kHz (red)

that this broad yellow region only partially overlaps with the delamination box, the feature peak here is not appropriate for the delamination detection.

Comparing the two feature peaks observed in the delamination box region of the heat map shown in Fig. 6.9, the absolute value of the latter feature peak at 100–150 kHz is higher than that of the former feature peak at 64–65 kHz. Nevertheless, the spatial length of the latter feature peak is longer than the delamination length, spanning from 0 to 100 mm at its maximum. This is unfavorable for the detection purpose because one is unable to specify the exact location of delamination. In fact, the local maximum within this feature peak tends to lie outside the delamination location as shown in Fig. 6.10. Two feature profiles obtained at excitation frequencies, 65 and 110 kHz, are compared in this figure. Although the peak value is larger for 110 kHz, the peak location is quite far from the center of delamination, which is 264 mm in this case. On the contrary, the peak location for 65 kHz closely matches with this center. Thus, the stronger but wider feature peak at frequency range of

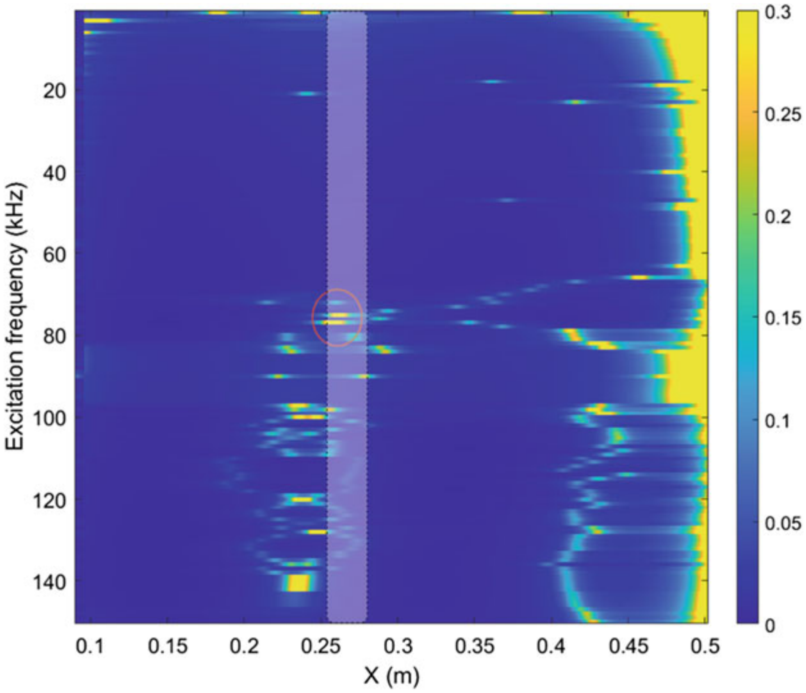

Fig. 6.11 Two-dimensional feature heat map for the LLPD, inverse phase derivative with 5 kHz low-pass filter

100–150 kHz is not considered ideal to detect delamination. Rather, 64–65 kHz is selected as an optimal excitation frequency for delamination detection since more compact feature peaks are found in the correct location.

One minor thing to notice in Fig. 6.9 is the exceptionally high feature values at the left and right edges. These are considered edge effects which are ignored while looking for the optimal excitation frequency. Consequently, at certain excitation frequencies, delaminations near the edge of a specimen would be difficult to detect, as feature peaks that might appear would likely be overwritten by the edge effect. This could be one limitation of the proposed delamination detection algorithm. Another interesting phenomenon is a feature dip between the red circle and the black rectangle. At this intermediate frequency range of 70–100 kHz, feature values become closer to zero as indicated by the dark blue region. Nevertheless, this lies between 250 and 280 mm, which corresponds with the center of delamination, at 264 mm, similar to the two feature peaks. Therefore, the feature dip could perhaps be utilized as a delamination indicator as well. Moreover, a sequence of feature peak, dip, and peak again could imply a unique pattern regarding the FML plate's response to ultrasonic guided waves. To elaborate, feature peak and feature dip may alternate at the delamination location as excitation frequency keeps increasing. Further simulation and experimental validation are necessary to examine this aspect.

Heat maps of the second feature, the LLPD, are displayed in Figs. 6.11 and 6.12. The difference between the two plots is the pass band frequency used for low-pass filtering. As mentioned earlier, pass band frequencies between 5 and 25 kHz are employed independently, by which different distributions of feature peaks appear. Two cases are shown in Figs. 6.11 and 6.12, for pass band frequencies of 5 kHz and 20 kHz, respectively. Until the excitation frequency reaches about 60 kHz, no apparent feature peaks are observed in either case. Then, distinct feature peaks appear at excitation frequencies of 60–80 kHz as highlighted by a red circle in the heat map. Apart from the feature peak at 68 kHz, where the extraction process for the LLPD is described in the previous section, there also exist strong feature peaks between 75 and 77 kHz. Feature peaks at this range of excitation frequency, 60–80 kHz, correspond well with the delamination box overlaid on the heat map. In contrast, no other feature peaks are found in the box after 60–80 kHz in both cases. Multiple feature peaks appear outside of the box, indicating the wrong location for potential delamination, but possibly indicating the presence of a delamination nonetheless. Therefore, for this simulated test article, we only consider excitation frequencies in the range of 60–80 kHz as possible candidates for delamination detection. In particular, 75 kHz is determined as an optimal excitation frequency based on the score metric devised to quantify the feature performance at a specific frequency. This is discussed in detail in Sect. 6.5.

The LLPD's behavior does not vary smoothly with excitation frequency, in contrast to the wide feature peak observed from the DHEM heat map in Fig. 6.9. Instead, shorter and sporadic feature peaks alternate with one another, as shown in the red circle. To be specific, two feature peaks are found in Fig. 6.11, whereas four sharp feature peaks reside in the circle in Fig. 6.12. Comparing the two figures, the latter is concluded to be better for delamination detection. The main reason is that

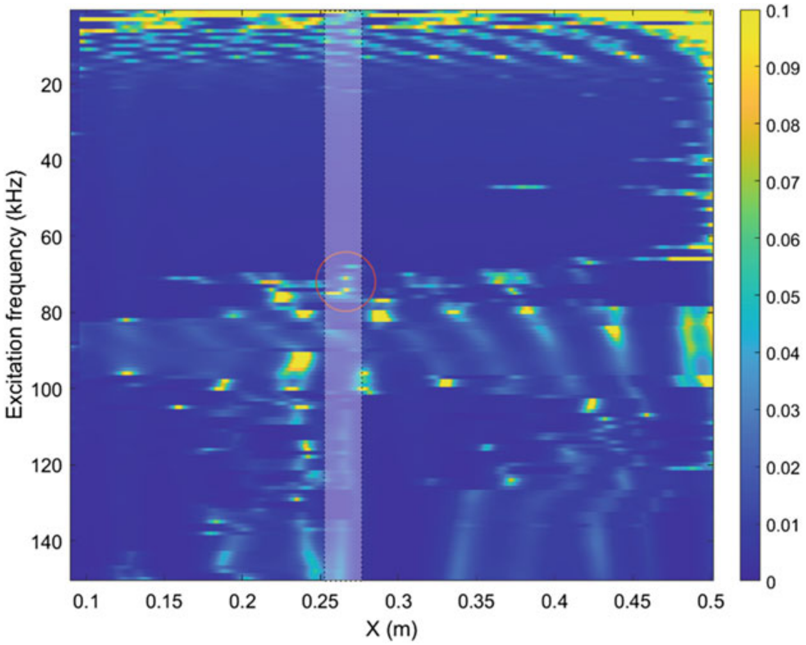

Fig. 6.12 Two-dimensional feature heat map for the LLPD, inverse phase derivative with 20 kHz low-pass filter

sharper feature peaks in Fig. 6.12 more precisely point out the delamination location. Moreover, less edge effect occurs at the right plate end in Fig. 6.12. That is, the strong yellow region tends to occupy the right end of the heat map in Fig. 6.11. Similarly to the DHEM feature, high feature values in the edge could be a limitation such that delamination near the edge could be covered by them. Thus, a pass band frequency of 20 kHz produces a better result for delamination detection using the second feature, LLPD.

6.5.1 Score Metric to Quantify the Feature Performance

The simple score metric is designed to quantify the feature performance in detecting delaminations over a range of excitation frequencies. The mathematical formula of the delamination detection score is shown in the following equation. For each excitation frequency, the ratio between the mean of feature values within the delamination and across the entire domain is measured as the score.

$$\text{Score}(f) = \frac{\text{Mean (feature value within delamination)}}{\text{Mean (feature value across entire domain)}} \tag{6.2}$$

This score is obtained for the two features, DHEM and LLPD, with respect to the excitation frequency (1–150 kHz) imposed in the simulation. The resulting score profiles are shown in Figs. 6.13, 6.14, and 6.15 for the representative simulation case. Figure 6.13 displays the score profile for DHEM, whereas Figs. 6.14 and 6.15 depict score profiles for LLPD with pass band frequencies of 5 kHz and 20 kHz, respectively.

From Fig. 6.13, two score peaks are observed at excitation frequency 65 and 122 kHz. This result corresponds to the qualitative analysis on Fig. 6.9, as the yellow feature peaks are located near the similar frequency. Although 65 kHz is concluded as an optimal excitation frequency in the previous section, 122 kHz has a higher score than 65 kHz in Fig. 6.13. However, the score peak at 122 kHz is wider than the score peak at 65 kHz. Also, several minor peaks exist near the score peak at 122 kHz. Hence, 65 kHz is still superior to 122 kHz when the accuracy of delamination detection is prioritized. In contrast, the potential location of delamination can be swiftly found using this simple score metric.

Comparing Figs. 6.14 and 6.15, feature peaks are observed at the same excitation frequency, 75 kHz. Therefore, among several feature peaks in Figs. 6.11 and 6.12, the feature peak at 75 kHz is found to be the most powerful for delamination detection. In addition, the feature peak using the 20 kHz pass band frequency is sharper than at a pass band frequency of

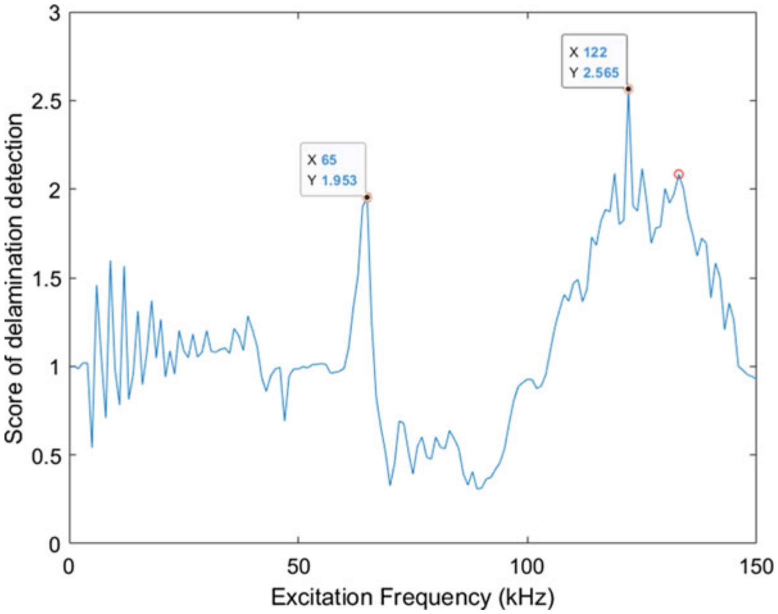

Fig. 6.13 Score profile for the DHEM

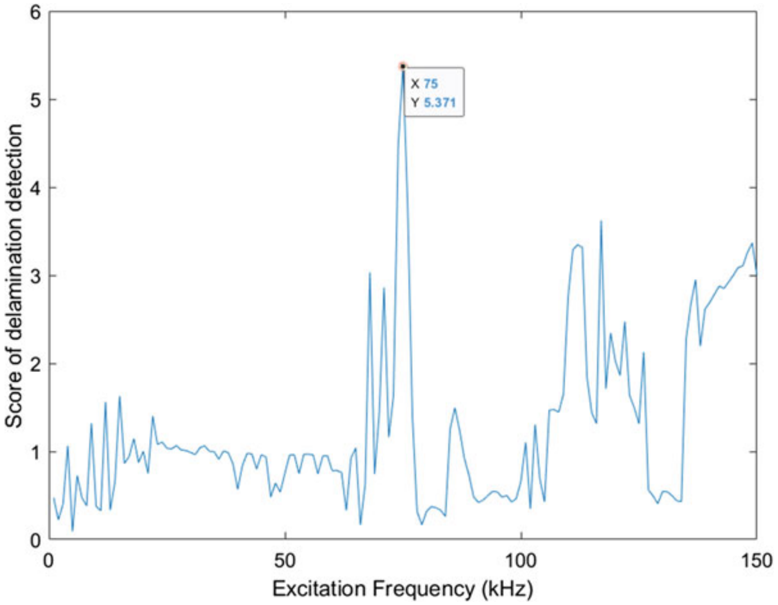

Fig. 6.14 Score profile for the LLPD with 5 kHz low-pass filter

5 kHz, indicating the same conclusion from previous qualitative analysis: a pass band frequency of 20 kHz is more highly optimized than a pass band frequency of 5 kHz.

6.5.2 Experimental Comparisons

The primary difficulty in evaluating the two features on experimental data is finding a comparable one-dimensional LDV-scan line, akin to an ultrasonic B-scan. Assuming the physical coordinates of the transducer on the plate are known, radial paths emanating from this point (essentially, considering the surface in polar coordinates) are the most direct comparison to the unidirectional wave propagation modelled in Abaqus CAE. Using linear interpolation of the grid points scanned by

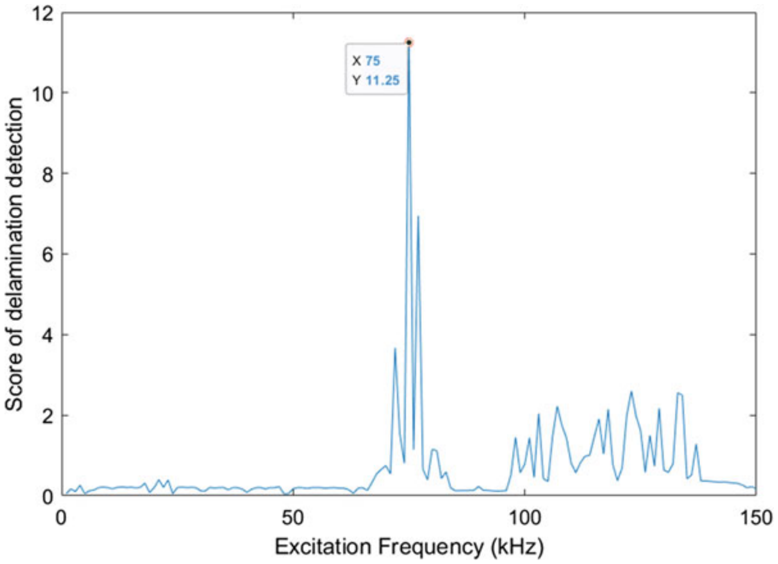

Fig. 6.15 Score profile for the LLPD with 20 kHz low-pass filter

the LDV, an arbitrary wave-path angle can be selected and evaluated. However, care must be taken into account for any anisotropic effects present in the composite (i.e., fiber direction, especially for plies nearest the surface). Additionally, due to coupling interactions, the area directly underneath and immediately adjacent to the transducer cannot be evaluated unless the transducer is moved to an alternate position.

For the current effort, only certain frequencies were available for processing, including 45, 90, and 135 kHz scans from both the front (composite laminate) and back (metal) sides. As shown in Figs. 6.9 and 6.12 (the heat maps for both DHEM and LLPD), none of these excitation frequencies appears to be optimal for highlighting the FML defects, based on the results of the simulated plate. Further experimental analysis of the sample FML plate using other excitation frequencies is planned to validate these results. By measuring the response of the sample to a more encompassing set of frequencies, and evaluating the damage-detection features proposed above on wave-paths that coincide with areas of known damage, the viability of this approach can be assessed. For a sample with known material properties and geometry, but unknown damage, the process proposed in this paper can be used to determine likely optimal frequencies at which to excite the sample.

6.6 Conclusion

In conclusion, this work demonstrates a novel approach and two proposed features for detecting delaminations in FMLs. FEM simulations imply a unique physical phenomenon, where a delamination can "trap" a standing wave; this phenomenon is then exploited to develop two novel detection features for highlighting delaminations. The first, DHEM, is based on the detrended envelope of the velocity magnitude. The second, LLPD, is based on a low-pass filtered, local phase derivative of the velocity profile. Furthermore, this process can be used to identify an optimal frequency for experimental testing, based on the geometry and material properties of the test specimen. Future work will include validating these results with experimental data and a sensitivity study on the effects of the delamination size, FML thickness, and excitation frequency.

Acknowledgments This research was funded by Los Alamos National Laboratory (LANL) through the Engineering Institute's Los Alamos Dynamics Summer School (LADSS). The Engineering Institute is a research and education collaboration between LANL and the University of California San Diego's Jacobs School of Engineering. This collaboration seeks to promote multidisciplinary engineering research that develops and integrates advanced predictive modelling, novel sensing systems, and new developments in information technology to address LANL mission-relevant problems. The authors would like to thank all of their LADSS colleagues for their feedback and support during this project.

References

1. Montinaro, N., Cerniglia, D., Pitarresi, G.: Detection and characterisation of disbonds on Fibre Metal Laminate hybrid composites by flying laser spot thermography. Compos. Part B Eng. **108**, 164–173 (2017). https://doi.org/10.1016/j.compositesb.2016.09.084
2. McLaughlan, P.B., Forth, S.C., Grimes-Ledesma, L.R.: Composite overwrapped pressure vessels, a primer. NASA. https://ntrs.nasa.gov/archive/nasa/casi.ntrs.nasa.gov/20110008406.pdf (March 2011)
3. Froust, J.: SpaceX Completes Rocket Explosion Investigation, Aims for Jan. 8 Launch. Space.com. https://www.space.com/35198-spacex-rocket-explosion-january-8-launch-date.html?TB_iframe=true&width=370.8&height=658.8 (January 2017)
4. Askaripour, K., Zak, A.: A survey of scrutinizing delaminated composites via various categories of sensing apparatus. J. Compos. Sci. **3**(4), 95–131 (2019). https://doi.org/10.3390/jcs3040095
5. Ibarra-Castanedo, C., et al.: Delamination detection and impact damage assessment of GLARE by active thermography. Int. J. Mater. Prod. Technol. **41**(1–4), 5–16 (2011). https://doi.org/10.1504/IJMPT.2011.040282
6. Léonard, F., et al.: Impact damage characterisation of fibre metal laminates by X-ray computed tomography. In: The Conference on Industrial Computed Tomography, Wels, Austria, 25–28 Feb 2014. https://www.researchgate.net/profile/Fabien_Leonard/publication/260137574_Impact_damage_characterisation_of_fibre_metal_laminates_by_X-ray_computed_tomography/links/0f317538b6b0853559000000.pdf
7. Bonavolonta, C., et al.: Eddy current technique based on HTc-SQUID and GMR sensors for non-destructive evaluation of fiber/metal laminates. IEEE Trans. Appl. Supercond. **19**(3), 808–811 (2009). https://doi.org/10.1109/TASC.2009.2019197
8. Matsuzaki, R., Yamamoto, K., Todoroki, A.: Delamination detection in carbon fiber reinforced plastic cross-ply laminates using crack swarm inspection: experimental verification. Compos. Struct. **173**, 127–135 (2017). https://doi.org/10.1016/j.compstruct.2017.04.014
9. Gao, H., Ali, S., Lopez, B.: Efficient detection of delamination in multilayered structures using ultrasonic guided wave EMATs. NDT & E Int. **43**(4), 316–322 (2010). https://doi.org/10.1016/j.ndteint.2010.03.004
10. Yeum, C.M., et al.: Instantaneous delamination detection in a composite plate using a dual piezoelectric transducer network. Compos. Struct. **94**(12), 3490–3499 (2012). https://doi.org/10.1016/j.compstruct.2012.06.003
11. Petculescu, G., Krishnaswamy, S., Achenbach, J.D.: Group delay measurements using modally selective Lamb wave transducers for detection and sizing of delaminations in composites. Smart Mater. Struct. **17**(1), 015007–015015 (2007). https://doi.org/10.1088/0964-1726/17/01/015007
12. Demcenko, A., et al.: Investigation of interaction of the Lamb wave with delamination type defect in GLARE composite using air-coupled ultrasonic technique. In: Proceedings of the Forum Acusticum Budapest: 4th European Congress on Acoustics, Budapest, Hungary, vol. 29, 29 Aug–2 Sept 2005. http://www.conforg.fr/acoustics2008/cdrom/data/fa2005-budapest/paper/604-0.pdf
13. Shelke, A., et al.: Mode-selective excitation and detection of ultrasonic guided waves for delamination detection in laminated aluminum plates. IEEE Trans. Ultrason. Ferroelectr. Freq. Control. **58**(3), 567–577 (2011). https://doi.org/10.1109/TUFFC.2011.1839
14. Kim, E., et al.: Solitary wave-based delamination detection in composite plates using a combined granular crystal sensor and actuator. Smart Mater. Struct. **24**(12), 125004–125012 (2015). https://doi.org/10.1088/0964-1726/24/12/125004
15. Tian, Z., Yu, L., Leckey, C.: Rapid guided wave delamination detection and quantification in composites using global-local sensing. Smart Mater. Struct. **25**(8), 085042–085052 (2016). https://doi.org/10.1088/0964-1726/25/8/085042
16. Tai, S., et al.: Modeling ultrasonic elastic waves in fiber-metal laminate structures in presence of sources and defects. J. Nondestruct. Eval. Diagn. Progn. Eng. Syst. **3**(4), 041102 (2020). https://doi.org/10.1115/1.4046946
17. Flynn, E.B., et al.: Structural imaging through local wavenumber estimation of guided waves. NDT & E Int. **59**, 1–10 (2013). https://doi.org/10.1016/j.ndteint.2013.04.003
18. Lee, J.-R., et al.: Laser ultrasonic anomalous wave propagation imaging method with adjacent wave subtraction: algorithm. Opt. Laser Technol. **44**(5), 1507–1515 (2012). https://doi.org/10.1016/j.optlastec.2011.12.008
19. Flynn, E.B., Jarmer, G.S.: High-speed, non-contact, baseline-free imaging of hidden defects using scanning laser measurements of steady-state ultrasonic vibration. In: Proceedings of the 9th International Workshop on Structural Health Monitoring, Stanford, CA, pp. 1186–1193, 10–12 Sept 2013. http://www.dpi-proceedings.com/index.php/shm2013/article/view/22912
20. Tian, Z., Leckey, C., Yu, L.: Multi-site delamination detection and quantification in composites through guided wave based global-local sensing. In: AIP Conference Proceedings, vol. 1806, no. 1, AIP Publishing LLC (2017)

Chapter 7
One-Dimensional Convolutional Neural Networks for Real-Time Damage Detection of Rotating Machinery

Onur Avci, Osama Abdeljaber, Serkan Kiranyaz, Sadok Sassi, Abdelrahman Ibrahim, and Moncef Gabbouj

Abstract This paper presents a novel real-time rotating machinery damage monitoring system. The system detects, quantifies, and localizes damage in ball bearings in a fast and accurate way using one-dimensional convolutional neural networks (1D-CNNs). The proposed method has been validated with experimental work not only for single damage but also for multiple damage cases introduced onto ball bearings in laboratory environment. The two 1D-CNNs (one set for the interior bearing ring and another set for the exterior bearing ring) were trained and tested under the same conditions for torque and speed. It is observed that the proposed system showed excellent performance even with the severe additive noise. The proposed method can be implemented in practical use for online defect detection, monitoring, and condition assessment of ball bearings and other rotatory machine elements.

Keywords Rotating machinery · Real-time monitoring · Ball bearings · Damage detection · Bearing defects · Convolutional neural networks · CNNs

7.1 Introduction and Overview of One-Dimensional CNNs

Condition monitoring and structural health assessment of structures have been an active topic of research in mechanical/civil/aerospace engineering fields over the decades [1–6]. Rotating machinery is no exception, and there has been constant attention specifically on rolling bearings as they are of great importance for continuous operation and extended service life of most machine elements [7–9]. This type of bearing is also called anti-friction bearings and they are utilized in a wide variety of machinery applications. While the condition assessment and health monitoring of rotating machinery have been an area of substantial research over a number of decades, there has been relatively more focus on early detection of damage with real-time methodologies. Vibration-based defect/anomaly detection utilizing acceleration data, as in many other applications [10–16], has been found to be an effective way to detect, locate, and quantify defects in rotating machinery. In addition to the existing model-based methods (involving classical physics) and data-driven methods [17–21] (involving feature extraction and classification) available in the literature, machine learning-based methods have been recently in use for bearing defect detection. Yet, the main downside of predominant machine learning-based techniques is simply their heavy reliance on

---

O. Avci (✉)
Civil, Construction and Environmental Engineering, Iowa State University, Ames, IA, USA
e-mail: oavci@vt.edu; oavci@iastate.edu

O. Abdeljaber
Department of Building Technology, Linnaeus University, Växjö, Sweden
e-mail: osama.abdeljaber@lnu.se

S. Kiranyaz
Department of Electrical Engineering, Qatar University, Doha, Qatar
e-mail: mkiranyaz@qu.edu.qa

S. Sassi · A. Ibrahim
Department of Mechanical Engineering, Qatar University, Doha, Qatar
e-mail: sadok.sassi@qu.edu.qa

M. Gabbouj
Department of Signal Processing, Tampere University of Technology, Tampere, Finland
e-mail: moncef.gabbouj@tuni.fi

D. Di Maio, J. Baqersad (eds.), *Rotating Machinery, Optical Methods & Scanning LDV Methods, Volume 6*, Conference Proceedings of the Society for Experimental Mechanics Series, https://doi.org/10.1007/978-3-030-76335-0_7

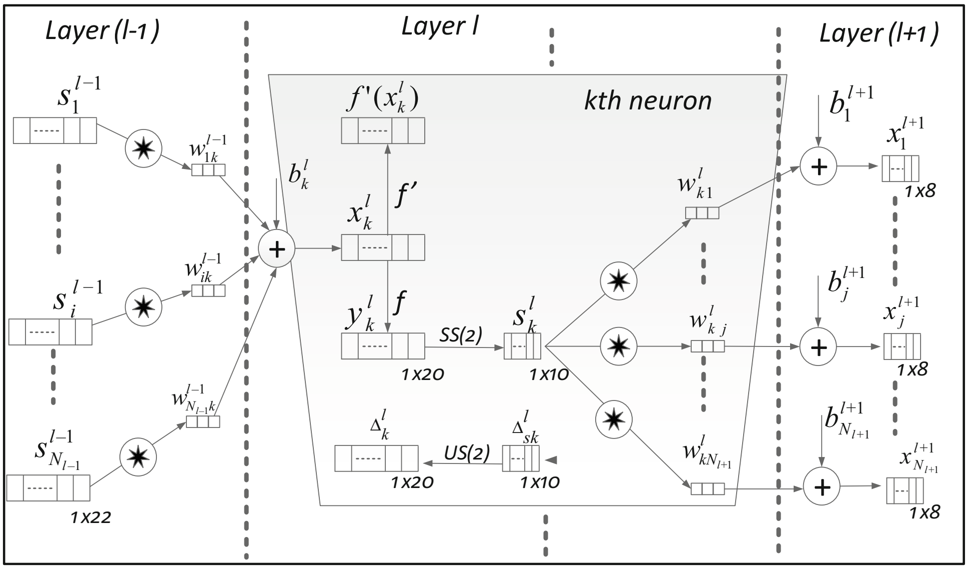

Fig. 7.1 The structure of 1D-CNN including three consecutive hidden CNN layers

hand-crafted attributes used in classifying vibration time histories. Determining the acceleration pattern characteristics for any type of acceleration data is mostly challenging which might very well bring in the risk of poor classification performance. Feature extraction and classification stages are blended into one unit in convolutional neural networks (CNNs) which were originally developed for pattern recognition and computer vision goals in 2D applications. For rotating machinery, initially deep 2D-CNNs were used for anomaly detection on bearings [22–28] for which various methods (e.g., vibration image, discrete Fourier transform) were used to convert the 1D acceleration signals to 2D. The drawback of these methods was the fact that they resulted in increased computational complexity which indicated that they were not good matches for online defect detection. Additionally, deep CNN training involved relatively larger training sets causing logistics issues for data augmentation, conflicting the use of purpose in practical applications. Compact 1D-CNNs eliminate most of the practicality issues and are reported to operate effectively over 1D signals in different engineering applications [29–36]. Compact 1D-CNNs have the ability to successfully detect defects, determine the location, and quantify the defect size in real time, with limited data for training, even with noise in the data [37–44]. In this paper, the methodology will be utilized in a case study where the damage conditions include both single and multiple bearing defect scenarios.

As the name implies, the 1D-CNNs are the counterparts of conventional 2D-CNNs which are a type of deep, feed-forward ANNs that are based on the way mammalian visual cortex operates. 1D-CNNs also have two types of layers: CNN layers and multi-layer perceptron (MLP) layers. In the CNN layers, the 1D convolutions and sub-sampling occur, whereas in the MLP layers, the classification task is performed. The architecture of a 1D-CNN is often developed by trial-and-error and is based on hyperparameters such as number of hidden CNN layers; hidden MLP layers; neurons in each CNN and MLP layers; subsampling factor; and filter kernel size.

Within the 1D-CNN structure, three consecutive hidden CNN layers are presented in Fig. 7.1 where the 1D filter kernel size is 3 and the sub-sampling factor is 2. The k^{th} neuron in the hidden CNN layer, l, primarily conducts a series of convolutions; and then the sum is run through the activation function, f, leaving the sub-sampling operation as the following step, where 1D arrays are replacing the 2D matrices for both feature maps and kernels. The CNN layers essentially operate over raw data, and they learn to extract features which are utilized by the MLP layers for classification operations. As a result, with 1D-CNNs, the feature extraction and feature classification are simply downsized to one single body to optimize the classification performance, resulting in a relatively lower computational complexity, enhancing the overall economy of the process. Here in this paper, the learning process is based on the bearing defect/fault/anomaly detection where the 1D-CNN structure processes feature extraction and "defect learning" tasks over raw one-dimensional accelerometer signals collected via sensors. The topology of the CNNs will allow variety in the input layer because the output CNN layer's sub-sampling factor is adaptively set [35]. Formulations and further information about the 1D-CNN architecture and forward-propagation and backward-propagation details can be found in [30, 35, 42, 45].

7.2 Proposed Methodology

The proposed methodology involves training of two separate 1D-CNNs. The first CNN is for the inner ring (CNN_i) and the second CNN is for the outer ring (CNN_o). The condition assessment of the inner and outer rings is assessed independently, based on the CNN results. The accelerations recorded by the accelerometers are simply the input for the CNN. The output generated by the independent CNN_i and CNN_o is utilized to produce the indexes P_i and P_o which are the probability of defect (probability of damage) values for the inner ring and the outer ring, respectively. Since the CNN_i and CNN_o values are produced independently, the P_i and P_o production is a decentralized process. Because the training data is collected once as an offline process, the following procedure is used for the very important step of training. Three sets of data are utilized to train 1D-CNN_i and 1D-CNN_o. The first dataset includes the acceleration data collected for the undamaged condition of the bearing rings ($\mathbf{C}_1$), whereas the second dataset includes the acceleration data collected for the most severely damaged condition of the inner ring ($\mathbf{C}_2$). The third dataset includes the acceleration data collected for the most severely damaged condition of the outer ring ($\mathbf{C}_3$).

$$\mathbf{C}_1 = \left[\mathbf{C}_{1,1}\ \ \mathbf{C}_{1,2}\ \ \cdots\ \ \mathbf{C}_{1,N1}\right] \tag{7.1}$$

$$\mathbf{C}_2 = \left[\ \mathbf{C}_{2,1}\ \mathbf{C}_{2,2}\ \cdots\ \mathbf{C}_{2,N2}\ \right] \tag{7.2}$$

$$\mathbf{C}_3 = \left[\ \mathbf{C}_{3,1}\ \mathbf{C}_{3,2}\ \cdots\ \mathbf{C}_{3,N3}\ \right] \tag{7.3}$$

While some of the existing CNN-based bearing fault detection methods [33, 46] necessitate the data for each damage condition for classifier training, the methodology presented in this paper requires acceleration data only for the most severe inner and most severe outer ring defect conditions. No data is needed for the “in-between” defect conditions for both the inner and outer rings. $\mathbf{C}_1$, $\mathbf{C}_2$, and $\mathbf{C}_3$ are divided into N_1, N_2, and N_3 number of non-overlapping frames, as a next step. Each frame has a length of n_s samples. With that, frames that belong to undamaged inner ring; damaged inner ring; undamaged outer ring; and damaged outer ring are defined and grouped as $\mathbf{U}_\text{i}$, $\mathbf{D}_\text{i}$, $\mathbf{U}_\text{o}$, and $\mathbf{D}_\text{o}$, respectively.

$$\mathbf{U}_\text{i} = \left[\ \mathbf{C}_{1,1}\ \mathbf{C}_{1,2}\ \cdots\ \mathbf{C}_{1,N1}\ \mathbf{C}_{3,1}\ \mathbf{C}_{3,2}\ \cdots\ \mathbf{C}_{3,N3}\ \right] \tag{7.4}$$

$$\mathbf{D}_\text{i} = \left[\ \mathbf{C}_{2,1}\ \mathbf{C}_{2,2}\ \cdots\ \mathbf{C}_{2,N2}\ \right] \tag{7.5}$$

$$\mathbf{U}_\text{o} = \left[\ \mathbf{C}_{1,1}\ \mathbf{C}_{1,2}\ \cdots\ \mathbf{C}_{1,N1}\ \mathbf{C}_{2,1}\ \mathbf{C}_{2,2}\ \cdots\ \mathbf{C}_{2,N2}\ \right] \tag{7.6}$$

$$\mathbf{D}_\text{o} = \left[\ \mathbf{C}_{3,1}\ \mathbf{C}_{3,2}\ \cdots\ \mathbf{C}_{3,N3}\ \right] \tag{7.7}$$

It is important to note that all frames are locally normalized (normalization takes place between -1 and 1) and later shuffled randomly to improve training efficacy. When $\mathbf{U}_\text{i}$, $\mathbf{D}_\text{i}$, $\mathbf{U}_\text{o}$, and $\mathbf{D}_\text{o}$ vectors are all normalized and shuffled, the resulting vectors are:

$$\mathbf{UN}_\text{i} = \left[\ \mathbf{UN}_{\text{i},1}\ \mathbf{UN}_{\text{i},2}\ \cdots\ \mathbf{UN}_{\text{i},N_1+N_3}\ \right] \tag{7.8}$$

$$\mathbf{DN}_\text{i} = \left[\ \mathbf{DN}_{\text{i},1}\ \mathbf{DN}_{\text{i},2}\ \cdots\ \mathbf{DN}_{\text{i},N_2}\ \right] \tag{7.9}$$

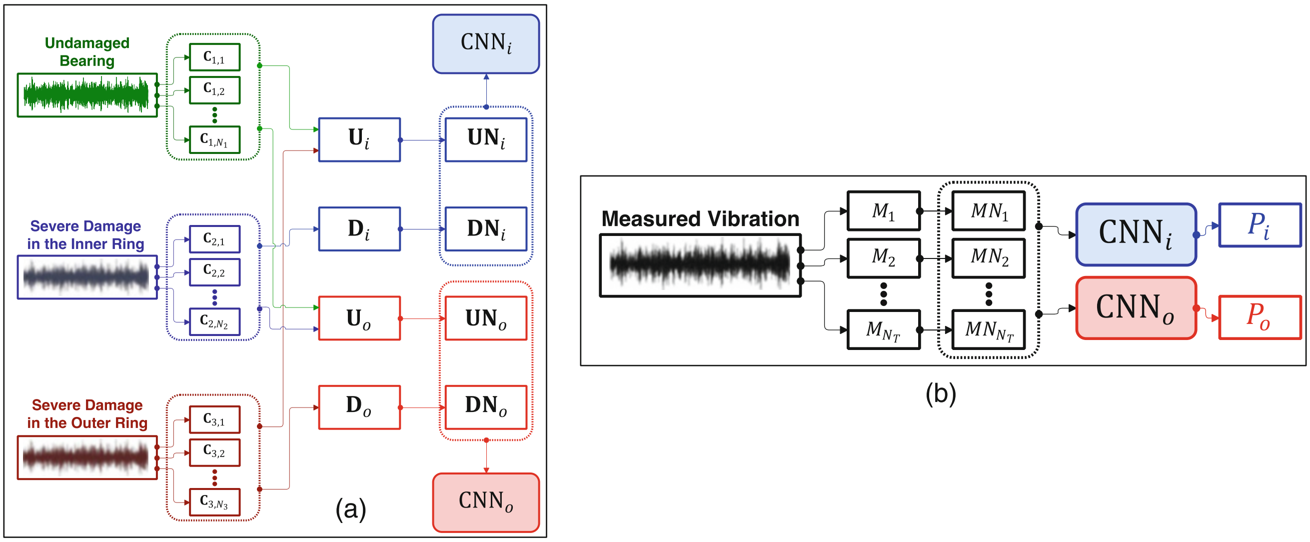

Fig. 7.2 (**a**) Summary of the CNN_i and CNN_o training; (**b**) summary of bearing condition monitoring; damage/defect detection

$$\mathbf{UN}_\mathrm{o} = \left[\,\mathbf{UN}_{\mathrm{i},1}\ \mathbf{UN}_{\mathrm{i},2}\ \cdots\ \mathbf{UN}_{\mathrm{i},N_1+N_2}\,\right] \tag{7.10}$$

$$\mathbf{DN}_\mathrm{o} = \left[\,\mathbf{DN}_{\mathrm{i},1}\ \mathbf{DN}_{\mathrm{i},2}\ \cdots\ \mathbf{DN}_{\mathrm{i},N_3}\,\right] \tag{7.11}$$

$\mathbf{UN}_\mathrm{i}$ and $\mathbf{DN}_\mathrm{i}$ are used to train the first classifier, CNN_i, which would determine whether there is a defect on the inner ring and quantify the level of damage, if any. Basically, what the CNN_i classifier is doing is processing the content of the input frame and checking if it is showing similarities with the inner ring conditions (no defect at all or the most severely damaged). Similarly, $\mathbf{UN}_\mathrm{o}$ and $\mathbf{DN}_\mathrm{o}$ are utilized to train the second classifier, CNN_o, which would determine whether there is a defect on the outer ring and quantify the level of damage, if any. As per adequate training, CNN_i will learn not to pick up the damage on outer ring because the frames including content for the severe outer ring defects are already present in $\mathbf{UN}_\mathrm{i}$. Likewise, for CNN_o, the classifier will not pick up the damage on the inner ring because the frames including content for the severe inner ring defects are already present in $\mathbf{UN}_\mathrm{o}$. In other words, $\mathbf{UN}_\mathrm{o}$ contains samples for acceleration data collected in the presence of a severe inner ring damage. As such, CNN_i and CNN_o trainings are processed per BP procedures that were presented in [30, 35, 42, 45]. The training of CNN_i and CNN_o is summarized in Fig. 7.2a.

After the training, for the inner ring, the first classifier CNN_i will have the capability to classify any input frame into either "Class 1: No damage on the interior ring" or "Class 2: Extreme damage on the interior ring." Likewise, for the outer ring, the second classifier CNN_o will be classifying the input frame into either "Class 3: No damage on the exterior ring" or "Class 4: Extreme damage on the exterior ring." The methodology of the bearing condition monitoring/condition assessment is summarized with the steps listed below and depicted in Fig. 7.2b:

1. The dynamic response of the bearing is collected via accelerometer and the signal time history is defined as **M**.
2. **M** is divided into N_T non-overlapping frames. Each frame will have n_s samples:

$$\mathbf{M} = \left[\,\mathbf{M}_1\ \mathbf{M}_2\ \cdots\ \mathbf{M}_{N_\mathrm{T}}\,\right] \tag{7.12}$$

3. **M** is normalized so that the maximum time history amplitude of each frame will be between −1 and 1:

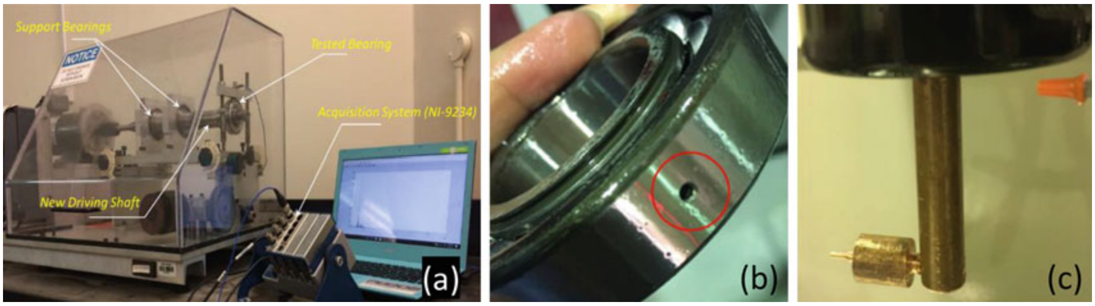

Fig. 7.3 (**a**) Bearing experimental setup; (**b**) outer ring bearing defect; (**c**) machining equipment

$$\mathbf{MN} = \left[\mathbf{MN}_1\ \mathbf{MN}_2 \cdots \mathbf{MN}_{N_\mathrm{T}}\right] \tag{7.13}$$

4. **MN** is fed into the $\mathrm{CNN_i}$ and $\mathrm{CNN_o}$ classifiers.
5. N_T frames are classified by $\mathrm{CNN_i}$ either into "Class 1: No damage on the interior ring" or "Class 2: Extreme damage on the interior ring." Likewise, N_T frames are classified by $\mathrm{CNN_o}$ either into "Class 3: No damage on the exterior ring" or "Class 4: Extreme damage on the exterior ring."
6. The probability of having damage on the surface of the interior ring is defined as P_i. The probability of having damage on the surface of the exterior ring is defined as P_o. Then, P_i and P_o can be formulated as:

$$P_\mathrm{i} = \frac{N_\mathrm{i}}{N_\mathrm{T}};\ P_\mathrm{o} = \frac{N_\mathrm{o}}{N_\mathrm{T}} \tag{7.14}$$

where
N_i = number of frames assigned by $\mathrm{CNN_i}$ to "Extreme damage on the interior ring (Class 2)"
N_o = number of frames classified by $\mathrm{CNN_o}$ to "Extreme damage on the exterior ring (Class 4)"

Based on the above, via the P_i and P_o calculations, bearing defect can be detected, localized, and quantified. When there is no defect at all, P_i and P_o are expected to have close to zero values. With the increase on the defect size, the probability of damage values is expected to increase (P_i will increase with the inner ring defect size and P_o will increase with the outer ring defect size). On another note, the inner ring defect should not be affecting P_o and the outer ring defect should not be affecting P_i.

7.3 Laboratory Setup for Bearing Tests

The test rig shown in Fig. 7.3a includes a driving shaft and support bearings to hold the rolling bearing in place. The experimental setup is designed to simulate and facilitate the bearing tests under various load and speeds. The acceleration signal was collected at 51,200 Hz sampling frequency with time intervals of 10 s via PCB accelerometers (PCB No. 352C33, 100 mV/g) which were connected to a NI-9234 controller. A sample outer ring bearing defect is shown in Fig. 7.3b, while the machining equipment utilized to introduce the bearing defects is shown in Fig. 7.3c. For brevity, this study focused on localized damage on bearing rings instead of widespread damage distributed throughout the surface of the interior and exterior rings.

7.4 Damage Detection Results

In this study, 27 damage scenarios were considered for bearing damage detection. These scenarios are categorized as shown below:

- Group 1: three similar undamaged bearings (reference damage condition for three scenarios)

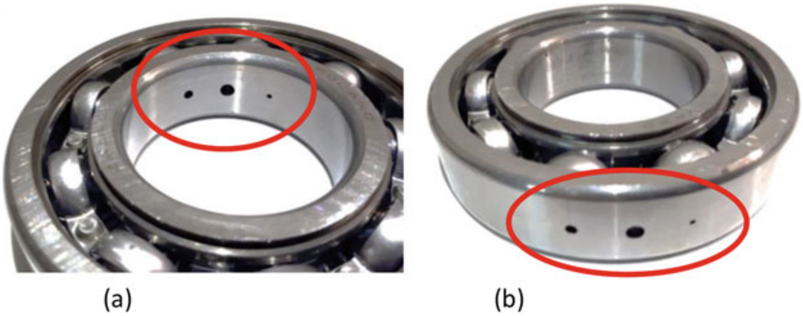

Fig. 7.4 (**a**) Interior ring defect example; (**b**) exterior ring defect example

- Group 2: Inner ring defects: nine increasing levels of defect size introduced on the inner ring: 0.35 mm, 0.40 mm, 0.50 mm, 0.58 mm, 1.00 mm, 1.50 mm, 2.00 mm, 2.50 mm, and 3.00 mm
- Group 3: Outer ring defects: nine increasing levels of defect size introduced on the outer ring: 0.35 mm, 0.40 mm, 0.50 mm, 0.58 mm, 1.00 mm, 1.50 mm, 2.00 mm, 2.50 mm, and 3.00 mm
- Group 4: Multiple damage scenarios (MDS): six scenarios corresponding to various combination of defects
    - MDS1: 0.50 mm interior ring damage + 2.00 mm exterior ring damage.
    - MDS2: 2.00 mm interior ring damage + 2.00 mm exterior ring damage.
    - MDS3: Three interior ring damage: 1.00 mm + 2.00 mm + 3.00 mm. Example is shown in Fig. 7.4a.
    - MDS4: 2.00 mm interior ring damage + 0.50 mm exterior ring damage.
    - MDS5: 1.00 mm interior ring damage + 1.00 mm exterior ring damage.
    - MDS6: Three exterior ring damage: 1.00 mm + 2.00 mm + 3.00 mm. Example is shown in Fig. 7.4b.

For each defect scenario, ten acceleration time histories were measured. Each acceleration time history was 10 s long and was recorded at 51,200 Hz sampling frequency. Time histories were filtered by a low-pass filter via 6400 Hz cutoff frequency and then down-sampled to 12,800 Hz, consequently compartmentalized to fixed length frames. Each frame had $n_s = 1024$ samples at the end.

The inner ring defects and the outer ring defects that are equal to or greater than 2.5 mm were accepted as "severe" damages on the bearing. Based on this, $\mathbf{C}_1$, $\mathbf{C}_2$, and $\mathbf{C}_3$ needed to train interior and exterior ring classifiers CNN_i and CNN_o can be explained as the following. As a reminder, $\mathbf{C}_1$ is the dataset for the undamaged condition of the bearing rings; $\mathbf{C}_2$ is the dataset for the most severely damaged condition of the inner ring; and $\mathbf{C}_3$ is the dataset for the most severely damaged condition of the outer ring.

- $\mathbf{C}_1$ comprises 5 time history data out of 30 (10 + 10 + 10 for three scenarios) available for Group 1 (undamaged condition corresponding to a "reference/datum"). Considering the fact that these 5 time history data correspond to undamaged bearing #1, it leaves remaining 5 time history data of undamaged bearing #1, 10 signals of the second undamaged bearing, and 10 signals of the third undamaged bearing. As a result, a total of 25 (5 + 10 + 10) time history data were dedicated for CNN evaluation.
- $\mathbf{C}_2$ comprises five out of the ten available time history data collected at 2.50 mm defect on the inner ring in addition to five out of the ten available time-history data acquired at 3.00 mm defect on the inner ring.
- $\mathbf{C}_3$ comprises five out of the ten available time history data collected at 2.50 mm defect on the exterior ring in addition to five out of the ten available time history data acquired at 3.00 mm defect on the exterior ring.

Only two extreme ends (undamaged and severely damaged cases) of the damage conditions were used for training. In other words, seven sets of time history data corresponding to the defects of 0.35 mm, 0.40 mm, 0.50 mm, 0.58 mm, 1.00 mm, 1.50 mm, and 2.00 mm on both inner ring and outer ring, in addition to six sets of time-history data corresponding to the multiple defect scenarios (categorized under Group 4, above), were not used for training. The time history data in the three sets ($\mathbf{C}_1$, $\mathbf{C}_2$, and $\mathbf{C}_3$) were divided into frames so that they have a length of $n_s = 1024$ samples. As a following step, the frames in the three sets were grouped, normalized, and shuffled as described before. As a result, both $\mathbf{UN}_\text{i}$ and $\mathbf{UN}_\text{o}$ comprised $(5 + 5 + 5) \times (12{,}800\ \text{Hz}) \times (10\ \text{s})/1024 = 1875$ frames. On the other hand, each $\mathbf{DN}_\text{i}$ and $\mathbf{DN}_\text{o}$ comprised $(5 + 5) \times (12{,}800\ \text{Hz}) \times (10\ \text{s})/1024 = 1250$ frames. For both classifiers, the structure of the CNN was compact. Specifically, two hidden convolutional layers and two MLP layers were used. 90% of the frames in $\mathbf{UN}_\text{i}$ and $\mathbf{DN}_\text{i}$ were utilized to train the CNN_i; meanwhile, 90% of the frames in $\mathbf{UN}_\text{o}$ and $\mathbf{DN}_\text{o}$ were utilized for classifier CNN_o training. In other words, 10% of the remaining data was utilized for testing. Classifier for the interior ring (CNN_i) and the classifier for the exterior ring

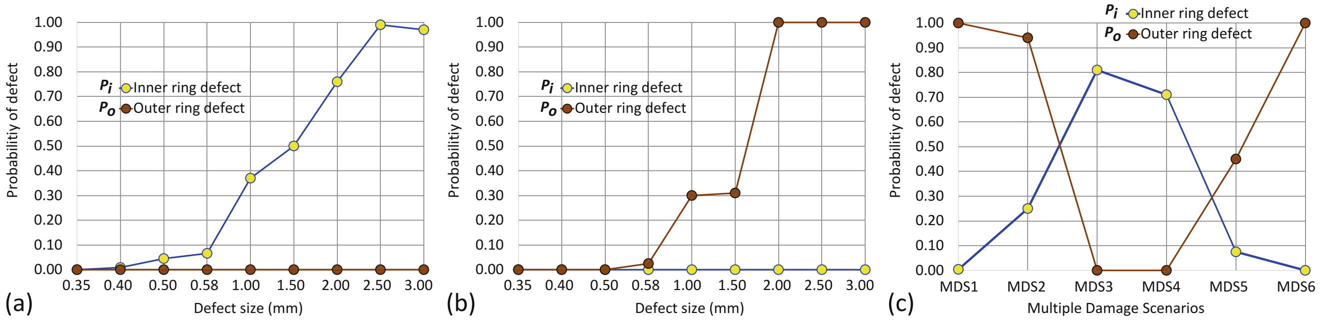

Fig. 7.5 P_i and P_o results per 1D-CNNs for (**a**) various damage sizes on the interior ring, (**b**) various damage sizes on the exterior ring, and (**c**) multiple damage conditions

(CNN$_o$) comprised (3, 3) neurons in the two hidden convolution layers and (10, 10) neurons in the two MLP layers. The subsampling factor was set to 20, while the kernel size was set to 40. The stopping criteria for the BP training were:

- 1% classification error
- Maximum 200 iterations for the BP process

The CNN training was conducted per the BP procedures described in [30, 35, 42, 45]. For CNN$_i$, the classification error was 0.53% for the training data and 0.64% for the validating data. For CNN$_o$, the classification error was 0% for training and validating data. Accuracy performance with more than 99% for the validating data was an excellent defect detection achievement.

The damage assessment procedure was run for the scenarios presented above. For each damage scenario, the time histories are separated into frames (1024 samples long) after which the frames are locally normalized and then fed into 1D-CNN classifiers, and probability of damage indices is calculated for interior and outer rings, P_i and P_o, respectively. In the presence of no damage, P_i and P_o values were correctly calculated as zero, revealing that the system did not come across any damage on the interior and exterior ring. As shown in Fig. 7.5a, for various damage sizes on the interior ring, the P_i values are reflecting the level of damage on the interior ring surfaces. As the defect size is increasing, the probability of damage values is also proportionally increasing. Meanwhile, when the interior ring is the only ring experiencing the damage, the P_o values for the outer ring are all zeros. For small defects up to 0.58 mm, probability of damage results varied from 0 to 0.066 indicating relatively smaller defect on the interior ring. For relatively larger damages on the interior ring (from 1 to 2 mm), the probability of damage values is changing from 0.37 to 0.76. For extreme damage sizes (from 2.5 and 3 mm), the probability of damage values is close to 1. Similarly, as shown in Fig. 7.5b, for the damages induced on the exterior ring, probability of damage values is in good correlation with the defect size. Again, it makes sense that the P_o values are reflecting the damages placed on the exterior ring; meanwhile the interior ring probability of damage values (P_i) is almost zero. Based on all this, the classifiers are proven successful for detecting, locating, and quantifying defects on the bearing rings which can be considered as an achievement because both CNN$_i$ and CNN$_o$ were trained with accelerations from two extreme ends (undamaged and extremely damaged conditions) only. This reveals a successful interpolation capability of the trained classifiers as per the presented methodology which is attempting to produce results with previously unseen data. This is an effective and feasible performance obviating the time and energy to be spent on the "in-between" damage scenarios. For the multiple damage scenarios of Group 4, the resulting P_i and P_o results are again found to be proportional to the size of the damage for each multiple damage cases, as presented in Fig. 7.5c, verifying the capability and accuracy of the proposed method on handling the six multiple damage conditions which were not originally used in the CNN training.

7.5 Performance Evaluation in the Presence of Noisy Data

In an attempt to examine the performance of the proposed methodology in the presence of various noise levels, the acceleration data for all damage conditions (excluding the data utilized for CNN training) are intentionally contaminated with various contents of noise, which is commonly represented by the SNR (signal-to-noise ratio):

Table 7.1 Probability of defect values for three undamaged bearing conditions in the presence of various noise levels

ID	SNR = 10 dB		SNR = 8 dB		SNR = 6 dB		SNR = 4 dB		SNR = 2 dB		SNR = 0 dB		SNR = −2 dB	
	P_i	P_o	P_i	P_o	P_i	P_o	P_i	P_o	P_i	P_o	P_i	P_o	P_i	P_o
1	0	0	0	0	0	0	0	0	0.002	0	0	0	0	0
2	0	0	0.002	0	0	0	0.004	0	0	0	0.002	0	0.002	0
3	0.003	0	0.005	0	0.003	0	0.002	0	0.008	0	0.004	0	0.002	0

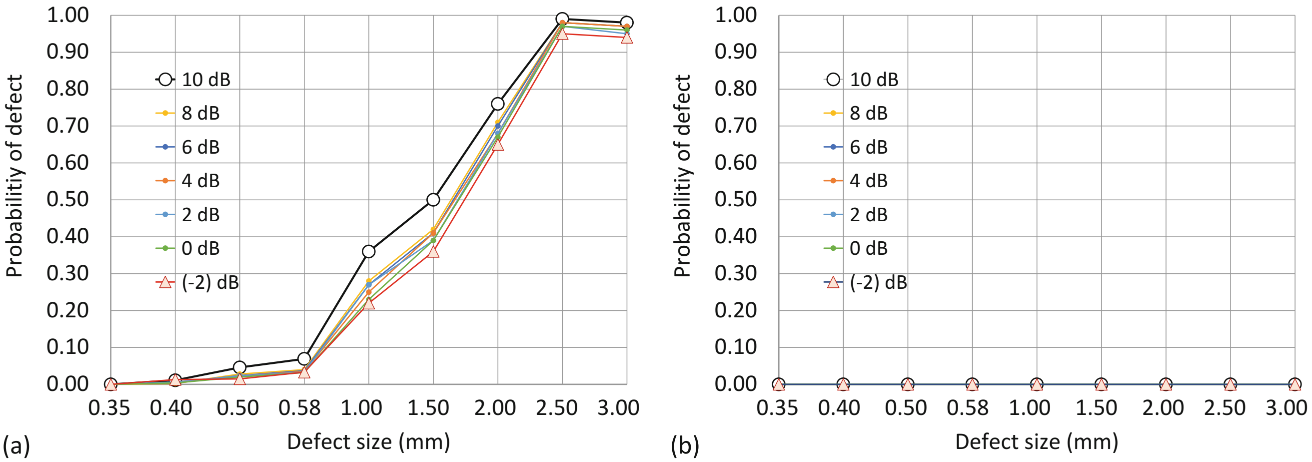

Fig. 7.6 Probability of defect values for the nine defect sizes on the inner ring in the presence of various noise levels: (**a**) P_i, (**b**) P_o

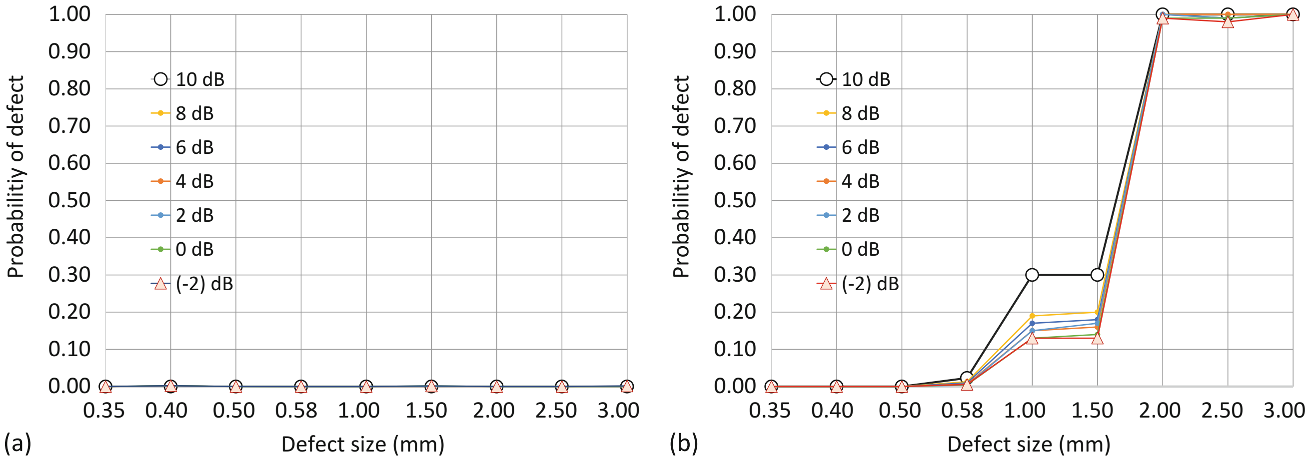

Fig. 7.7 Probability of defect values for the nine defect sizes on the outer ring in the presence of various noise levels: (**a**) P_i, (**b**) P_o

$$\mathrm{SNR} = 10\log_{10}\left(\frac{P_\mathrm{signal}}{P_\mathrm{noise}}\right) \tag{7.15}$$

In Eq. 7.15, P_noise represents the power of the white Gaussian noise, while P_signal represents the power of the acceleration signal. Probability of defect values for the three undamaged bearing conditions in the presence of various noise levels is presented in Table 7.1 for both inner and the outer rings. Probability of defect values for the nine defect sizes on the inner ring in the presence of various noise levels is plotted in Fig. 7.6. Similarly, the probability of defect values for the nine defect sizes on the outer ring in the presence of various noise levels are plotted in Fig. 7.7. Corresponding values for the six multiple damage scenarios are plotted in Fig. 7.8. Based on the results shown on Table 7.1 and Figs. 7.6, 7.7, and 7.8, it can be stated that the CNNs revealed excellent performance for damage detection, damage localization, and damage quantification, even with very noisy (−2 dB) acceleration data. This could be considered as an advantage over another similar approach [46], where the performance was dropping at and below 2 dB of SNR.

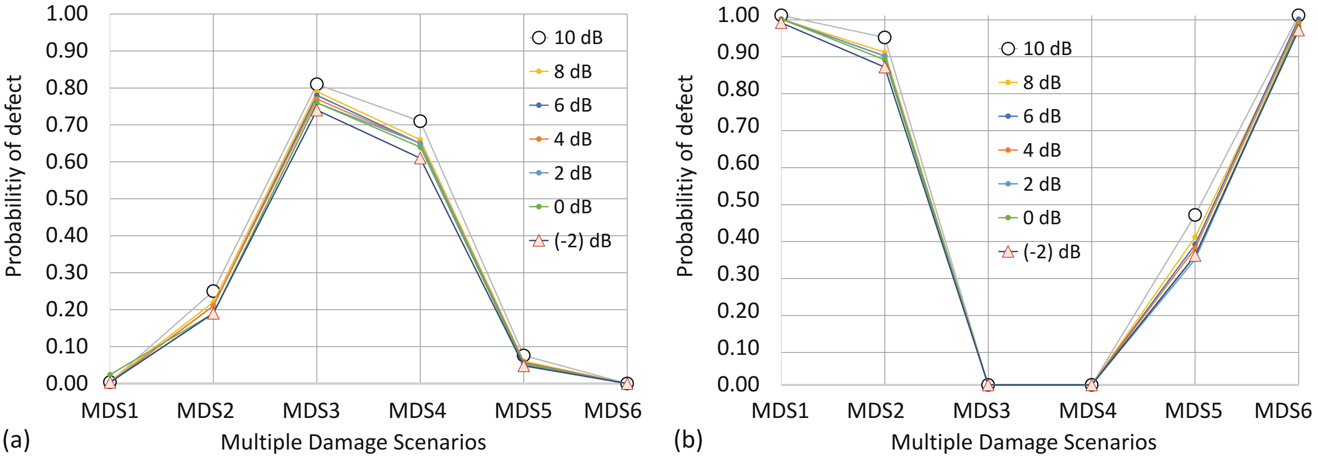

Fig. 7.8 Probability of defect values for the six multiple defect scenarios in the presence of various noise levels: (**a**) P_i, (**b**) P_o

7.6 Computational Complexity Analysis

The methodology presented in this paper is created via MATLAB and C++ by MS Visual Studio 2013 in 64 bit. Because compact 1D-CNNs are utilized, the work is actually a non-GPU task; yet, Intel-OpenMP API is utilized for multiprocessing via shared memory. The approach described in this paper runs forward-propagation and BP tasks pertinent to train and test 1D-CNNs. Codes written in MATLAB are deployed to extract raw acceleration arrays of $\mathbf{U}_i$, $\mathbf{D}_\mathbf{i}$, $\mathbf{U}_\mathbf{o}$, and $\mathbf{D}_\mathbf{o}$ and to compute the probability of defect values for the inner and outer rings via the raw acceleration data. Moreover, the experimental results are verified with a computer with I7-4910MQ at 8 cores-2.9 GHz and 32-GB memory. It is observed that the major advantage of 1D-CNN architecture in the vibration-based bearing defect detection method is simply the reduction of computation time and power required for acceleration signal classification. This has been successfully demonstrated via CNN_i when it was utilized to classify a 2-s acceleration signal collected per 12,800 Hz sampling frequency (the acceleration time history comprises 25,600 samples). The time history plot was partitioned into 25 frames, so that each frame ended up having $n_\mathrm{s} = 1024$ samples. The amount of time needed for the system to classify the 2-s signal was 0.24 s, which is almost eight times faster than requirements of real-time standards (1 s). This argument is also valid for the CNN_o counterpart, for the exterior ring.

7.7 Conclusions

A novel online monitoring system is presented in this paper for detection, quantification, and localization of rotational element damage. Even though rolling bearings are used in this paper, the procedure and methodology can be applied to any rotatory machine part. The methodology presented is based on two compact 1D-CNNs simply merging the feature extraction and corresponding classification tasks into one joint learning unit (as opposed to traditional defect monitoring systems where both tasks are taken care of separately). In doing so, the computational difficulties and issues regarding the hand-crafted features are eliminated, and the damage detection operation is optimized, in a sense. As a result, several important conclusions are made. The proposed methodology is capable of detecting, localizing, and quantifying the bearing defects on the interior and exterior rings of the bearing. The probability of damage values is in good correlation with the true damages placed on the rings of the bearing; which means the minimally trained 1D-CNN classifiers can successfully manage any induced damage. In addition to all this, the proposed system performed well even in the presence of severe noise in the acceleration data. On another note, the use of compact 1D-CNNs obviates training of large data and tasks like majority voting; dropout; batch normalization; data augmentation, etc. which makes the proposed system a convenient match for practical use in the industry, for other structural health monitoring applications.

References

1. Kankar, P.K., Sharma, S.C., Harsha, S.P.: Fault diagnosis of ball bearings using machine learning methods. Expert Syst. Appl. **38**, 1876–1886 (2011). https://doi.org/10.1016/j.eswa.2010.07.119
2. Bin, G.F., Gao, J.J., Li, X.J., Dhillon, B.S.: Early fault diagnosis of rotating machinery based on wavelet packets—empirical mode decomposition feature extraction and neural network. Mech. Syst. Signal Process. **27**, 696–711 (2012). https://doi.org/10.1016/j.ymssp.2011.08.002
3. Yan, R., Gao, R.X., Chen, X.: Wavelets for fault diagnosis of rotary machines: a review with applications. Signal Process. **96**, 1–15 (2014). https://doi.org/10.1016/j.sigpro.2013.04.015
4. Mansouri, M., Avci, O., Nounou, H., Nounou, M.: A comparative assessment of nonlinear state estimation methods for structural health monitoring. In: Conf. Proc. Soc. Exp. Mech. Ser. (2015). https://doi.org/10.1007/978-3-319-15224-0_5
5. Celik, O., Catbas, F.N., Do, N.T., Gul, M., Abdeljaber, O., Younis, A., Avci, O.: Issues, codes and basic studies for stadium dynamics. In: Proc. Second Int. Conf. Infrastruct. Manag. Assess. Rehabil. Tech., Sharjah, UAE (2016)
6. Abdeljaber, O., Avci, O.: Nonparametric structural damage detection algorithm for ambient vibration response: utilizing artificial neural networks and self-organizing maps. J. Archit. Eng. **22** (2016). https://doi.org/10.1061/(ASCE)AE.1943-5568.0000205
7. Liu, R., Yang, B., Zio, E., Chen, X.: Artificial intelligence for fault diagnosis of rotating machinery: a review. Mech. Syst. Signal Process. **108**, 33–47 (2018). https://doi.org/10.1016/j.ymssp.2018.02.016
8. Lei, Y., Yang, B., Jiang, X., Jia, F., Li, N., Nandi, A.K.: Applications of machine learning to machine fault diagnosis: a review and roadmap. Mech. Syst. Signal Process. **138**, 106587 (2020). https://doi.org/10.1016/j.ymssp.2019.106587
9. Nath, A.G., Udmale, S.S., Singh, S.K.: Role of artificial intelligence in rotor fault diagnosis: a comprehensive review. Artif. Intell. Rev. **54**, 2609–2668 (2021). https://doi.org/10.1007/s10462-020-09910-w
10. Abdeljaber, O., Avci, O., Do, N.T., Gul, M., Celik, O., Necati Catbas, F.: Quantification of structural damage with self-organizing maps. In: Conf. Proc. Soc. Exp. Mech. Ser. (2016). https://doi.org/10.1007/978-3-319-29956-3_5
11. Celik, O., Do, N.T., Abdeljaber, O., Gul, M., Avci, O., Catbas, F.N.: Recent issues on stadium monitoring and serviceability: a review. In: Conf. Proc. Soc. Exp. Mech. Ser. (2016). https://doi.org/10.1007/978-3-319-29763-7_41
12. Chaabane, M., Ben Hamida, A., Mansouri, M., Nounou, H.N., Avci, O.: Damage detection using enhanced multivariate statistical process control technique. In: 2016 17th Int. Conf. Sci. Tech. Autom. Control Comput. Eng. STA 2016—Proc. (2017). https://doi.org/10.1109/STA.2016.7952052
13. Abdeljaber, O., Hussein, M.F.M., Avci, O., Davis, B., Reynolds, P.: A novel video-vibration monitoring system for walking pattern identification on floors. Adv. Eng. Softw. **139**, 102710 (2020)
14. Alabbasi, S., Hussein, M., Abdeljaber, O., Avci, O.: A numerical and experimental investigation of a special type of floating-slab tracks. Eng. Struct. **215**, 110734 (2020). https://doi.org/10.1016/j.engstruct.2020.110734
15. Avci, O., Bhargava, A., Nikitas, N., Inman, D.: Vibrations assessment of existing building foundations due to moving trains in underground tunnels. In: IMAC XXXVIII, Int. Modal Anal. Conf. (2020)
16. Avci, O., Bhargava, A., Nikitas, N., Inman, D.J.: Vibration annoyance assessment of train induced excitations from tunnels embedded in rock. Sci. Total Environ. **711**, 134528 (2020). https://doi.org/10.1016/j.scitotenv.2019.134528
17. Patel, J.P., Upadhyay, S.H.: Comparison between artificial neural network and support vector method for a fault diagnostics in rolling element bearings. Proc. Eng. **144**, 390–397 (2016). https://doi.org/10.1016/j.proeng.2016.05.148
18. Prieto, M.D., Cirrincione, G., Espinosa, A.G., Ortega, J.A., Henao, H.: Bearing fault detection by a novel condition-monitoring scheme based on statistical-time features and neural networks. IEEE Trans. Ind. Electron. **60**, 3398–3407 (2013). https://doi.org/10.1109/TIE.2012.2219838
19. Mao, Z., Todd, M.D.: A Bayesian recursive framework for ball-bearing damage classification in rotating machinery. Struct. Health Monit. **15**, 668–684 (2016). https://doi.org/10.1177/1475921716656123
20. Ocak, H., Loparo, K.A., Discenzo, F.M.: Online tracking of bearing wear using wavelet packet decomposition and probabilistic modeling: a method for bearing prognostics. J. Sound Vib. **302**, 951–961 (2007). https://doi.org/10.1016/j.jsv.2007.01.001
21. Roan, M.J., Erling, J.G., Sibul, L.H.: A new, non-linear, adaptive, blind source separation approach to gear tooth failure detection and analysis. Mech. Syst. Signal Process. **16**, 719–740 (2002). https://doi.org/10.1006/mssp.2002.1504
22. Guo, X., Chen, L., Shen, C.: Hierarchical adaptive deep convolution neural network and its application to bearing fault diagnosis. Meas. J. Int. Meas. Confed. **93**, 490–502 (2016). https://doi.org/10.1016/j.measurement.2016.07.054
23. Janssens, O., Slavkovikj, V., Vervisch, B., Stockman, K., Loccufier, M., Verstockt, S., Van de Walle, R., Van Hoecke, S.: Convolutional neural network based fault detection for rotating machinery. J. Sound Vib. **377**, 331–345 (2016). https://doi.org/10.1016/j.jsv.2016.05.027
24. Hoang, D., Kang, H.: Convolutional neural network based bearing fault diagnosis, vol. 10362, pp. 105–111 (2017). https://doi.org/10.1007/978-3-319-63312-1
25. Wei, Z., Gaoliang, P., Chuanhao, L.: Bearings fault diagnosis based on convolutional neural networks with 2-D representation of vibration signals as input, vol. 13001, pp. 1–5 (2017)
26. Appana, D.K., Ahmad, W., Kim, J.-M.: Speed Invariant bearing fault characterization using convolutional neural networks, pp. 189–198 (2017). https://doi.org/10.1007/978-3-319-69456-6_16
27. Li, S., Liu, G., Tang, X., Lu, J., Hu, J.: An ensemble deep convolutional neural network model with improved D-S evidence fusion for bearing fault diagnosis. Sensors. **17**, 1729 (2017). https://doi.org/10.3390/s17081729
28. Lee, K.B., Cheon, S., Kim, C.O., Dalfino, L., Puntillo, F., Mosca, A., Monno, R., Luigia, M., Coppolecchia, S., Miragliotta, G., Bruno, F., Verstraete, D., Engineering, M., Engineering, M., Guo, M.F., Zeng, X.D., Chen, D.Y., Yang, N.C.: An adaptive deep convolutional neural network for rolling bearing fault diagnosis. Hindawi Shock Vib. **30**, 1–29 (2017). https://doi.org/10.1109/TSM.2017.2676245
29. Abdeljaber, O., Avci, O., Kiranyaz, M.S., Boashash, B., Sodano, H., Inman, D.J.: 1-D CNNs for structural damage detection: verification on a structural health monitoring benchmark data. Neurocomputing. **275**, 1308–1317 (2017). https://doi.org/10.1016/j.neucom.2017.09.069
30. Kiranyaz, S., Avci, O., Abdeljaber, O., Ince, T., Gabbouj, M., Inman, D.J.: 1D convolutional neural networks and applications: a survey. Mech. Syst. Signal Process. **151**, 107398 (2021). https://doi.org/10.1016/j.ymssp.2020.107398

31. Kiranyaz, S., Ince, T., Abdeljaber, O., Avci, O., Gabbouj, M.: 1-D convolutional neural networks for signal processing applications. In: ICASSP, IEEE Int. Conf. Acoust. Speech Signal Process.—Proc. (2019). https://doi.org/10.1109/ICASSP.2019.8682194
32. Avci, O., Abdeljaber, O., Kiranyaz, S., Hussein, M., Gabbouj, M., Inman, D.J.: A review of vibration-based damage detection in civil structures: from traditional methods to Machine Learning and Deep Learning applications. Mech. Syst. Signal Process. **147**, 107077 (2021). https://doi.org/10.1016/j.ymssp.2020.107077
33. Eren, L.: Bearing fault detection by one-dimensional convolutional neural networks. Math. Probl. Eng. **2017**, 8617315 (2017). https://doi.org/10.1155/2017/8617315
34. Li, D., Zhang, J., Zhang, Q., Wei, X.: Classification of ECG signals based on 1D convolution neural network. In: 2017 IEEE 19th Int. Conf. e-Health Networking, Appl. Serv. Heal. (2017). https://doi.org/10.1109/HealthCom.2017.8210784
35. Kiranyaz, S., Ince, T., Hamila, R., Gabbouj, M.: Convolutional neural networks for patient-specific ECG classification, in: Proc. Annu. Int. Conf. IEEE Eng. Med. Biol. Soc. EMBS (2015). https://doi.org/10.1109/EMBC.2015.7318926
36. Avci, O., Abdeljaber, O., Kiranyaz, S., Inman, D.J.: Convolutional neural networks for real-time and wireless damage detection. In: IMAC XXXVII, Int. Modal Anal. Conf., Springer International Publishing, Orlando, FL, USA (2019)
37. Avci, O., Abdeljaber, O., Kiranyaz, S., Boashash, B., Sodano, H., Inman, D.J.: Efficiency validation of one dimensional convolutional neural networks for structural damage detection using a SHM benchmark data. In: 25th Int. Congr. Sound Vib. (2018)
38. Abdeljaber, O., Sassi, S., Avci, O., Kiranyaz, S., Abulrahman, I., Gabbouj, M.: Fault detection and severity identification of ball bearings by online condition monitoring. IEEE Trans. Ind. Electron. **66**, 8136–8147 (2018). https://ieeexplore.ieee.org/document/8584489
39. Kiranyaz, S., Gastli, A., Ben-Brahim, L., Alemadi, N., Gabbouj, M.: Real-time fault detection and identification for MMC using 1D convolutional neural networks. IEEE Trans. Ind. Electron. (2018). https://doi.org/10.1109/TIE.2018.2833045
40. Ince, T., Kiranyaz, S., Eren, L., Askar, M., Gabbouj, M.: Real-time motor fault detection by 1-D convolutional neural networks. IEEE Trans. Ind. Electron. **63**, 7067–7075 (2016). https://doi.org/10.1109/TIE.2016.2582729
41. Kiranyaz, S., Avci, O., Abdeljaber, O.: Real-time structural damage detection by convolutional neural networks, US16031519 (2019). https://patents.google.com/patent/US20190017911A1/en
42. Abdeljaber, O., Avci, O., Kiranyaz, S., Gabbouj, M., Inman, D.J.: Real-time vibration-based structural damage detection using one-dimensional convolutional neural networks. J. Sound Vib. **388**, 154–170 (2017). https://doi.org/10.1016/j.jsv.2016.10.043
43. Avci, O., Abdeljaber, O., Kiranyaz, S., Inman, D.: Structural damage detection in real time: implementation of 1D convolutional neural networks for SHM applications. In: Niezrecki, C. (ed.) Struct. Heal. Monit. Damage Detect, vol. 7. Proc. 35th IMAC, A Conf. Expo. Struct. Dyn. 2017, pp. 49–54. Springer International Publishing, Cham (2017). https://doi.org/10.1007/978-3-319-54109-9_6
44. Avci, O., Abdeljaber, O., Kiranyaz, S., Hussein, M., Inman, D.J.: Wireless and real-time structural damage detection: a novel decentralized method for wireless sensor networks. J. Sound Vib. **424**, 158–172 (2018)
45. Avci, O., Kiranyaz, S., Abdeljaber, O.: StructuralDamageDetection.com (Public Website) (2019). http://www.structuraldamagedetection.com/
46. Zhang, W., Li, C., Peng, G., Chen, Y., Zhang, Z.: A deep convolutional neural network with new training methods for bearing fault diagnosis under noisy environment and different working load. Mech. Syst. Signal Process. **100**, 439–453 (2018). https://doi.org/10.1016/j.ymssp.2017.06.022

Chapter 8
A Practical Guide to Motion Magnification

Sean Collier and Tyler Dare

Abstract Numerous algorithms and software packages have been developed to detect and magnify small motions in video recordings with applications to structural vibration analysis. While some techniques follow naturally from intuition or mathematical duality, others seem overly complex at face value. Due to this, it can be difficult to assess the best tool for analysis, especially in terms of an intuitive understanding of how the results came to be. To facilitate the development of this intuition, input videos with different test articles and vibration characteristics were processed through selected magnification schemes. For each input, the outputs of the different methods were compared in order to assess their differences, amplification potentials, and limitations. Beginning with single regions of interest, the investigation then moved into more complicated scenarios involving multiple areas of localized motion. Variations such as coherence and scale for objects in the frame were also examined. Unlike previous review papers, these magnification tools are introduced in a framework that is more geared toward the working acoustician; in particular, intensity-, Fourier-, multi-resolution-, and Hilbert-based methods are evaluated in a structural-acoustic context to garner a better understanding of the underlying principles and idiosyncrasies. The main result is a thorough evaluation of each method's performance in order to develop a guide for choosing the best algorithm in a given scenario.

Keywords Motion amplification · Structural acoustics · Small motion · Practical understanding · Image processing

8.1 Introduction

The concept of pixel manipulation is not a novel one, with the paper by Rzeszotarski et al. from 1983 [1] being one of the earliest examples discussing the use of transforms to alter an image. This fundamental concept in image processing served as the motivation for motion magnification, introduced by the Computer Science and Artificial Intelligence Lab (CSAIL) at MIT [2]. Dr. Jeff Hay presented similar results shortly thereafter during his Ph.D. work at the University of Louisville [3]. Though the formulation was quite different than its MIT counterpart, these methods were both intensity-based, altering the raw image in order to enhance minute motions captured by the camera but invisible to the human eye. The MIT group made further progress by moving to phase-based methods [4], utilizing the results of Fleet and Jepson [5]. Specifically, Fleet and Jepson's evaluation of the correspondence between local phase and displacement facilitated CSAIL's efforts to detect and magnify motion in an Eulerian framework. Since 2014, the number of ways you are able to magnify small motions in video has increased dramatically, all touting extensions and reformulations capable of handling complex systems better than the last. In order to make sense of how these methods differ as well as know which is the best for your application, it is necessary to understand the inner workings of each, at least on a practical level.

While [1–4, 6] provide simplified, mainly 1D examples to mathematically motivate the inner workings of the algorithms, they lack the fine details within the implemented code. This is especially true for some of the more critical choices embedded in the community of those who developed them. Since many of the users and applications of these algorithms are outside of the field of computer vision, it becomes almost impossible to understand, recreate, and verify results without use of the source codes provided by CSAIL. This is problematic in that it encourages the black box mentality, such that when expansion and additions to the code are desirable and/or the question of which method to use becomes apparent, the answer and ability are often lost to the experimentalist. Rather than these 1D analytical examples, we provide explanation and understanding in

---

S. Collier (✉) · T. Dare
Graduate Program in Acoustics, College of Engineering, The Pennsylvania State University, State College, PA, USA
e-mail: smc604@psu.edu; tpd10@psu.edu

D. Di Maio, J. Baqersad (eds.), *Rotating Machinery, Optical Methods & Scanning LDV Methods, Volume 6*, Conference Proceedings of the Society for Experimental Mechanics Series, https://doi.org/10.1007/978-3-030-76335-0_8

a different context, beginning with intuitive magnification routes and building up to the complexities of the multiscale- and Hilbert-based methods. The paper proceeds as follows: Methodologies introduces the four fundamental methods, examples of their capability, and evaluation of their results; General Guidelines for Use is a comparison of the different methods and a general prescription for when each will perform best for a given application; and finally is the conclusion.

8.2 Methodologies

For each description and evaluation, a 1000 frames-per-second video of an acoustically excited drum head is used as the test subject. The high resolution, high sample rate with nice contrast, textured surface, and overall size within the frame make it a fitting subject to compare performance characteristics across the methods. The first frame of the video can be seen below in Fig. 8.1.

8.2.1 Intensity

We begin with the intensity-based method described by Hay [3]. This involves nothing more than the raw values output by the image sensor used in the camera and is based primarily on how subsequent pixel values vary from some reference. This reference can be chosen as the first image, the average of all of the images in the sequence (the DC component), the median image, or some other point in the sequence corresponding to the zero crossing if it happens to be known. Regardless, it is this variation about some value that is studied here, and its representation can be seen in Fig. 8.2 for the oscillating drum head.

Fig. 8.1 Still frame of vibrating, acoustically excited drum head

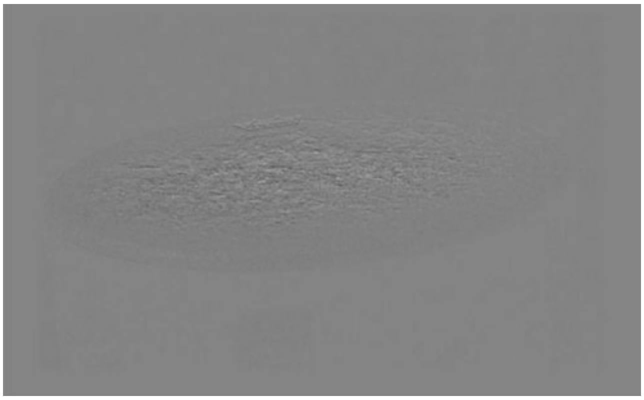

Fig. 8.2 What gets processed: difference of intensity (pixel) values of current frame from reference

Physical intuition would imply that there is an inherent link between the intensity value registered by the camera and the displacement of the object being recorded. In Jeff Hay's version of intensity-based magnification, the intensity of the pixel is shown to be directly proportional to the displacement, assuming small motion with constant illumination (between time steps). Therefore, if you scale the value of the pixel intensity over time, you will scale the displacement. Since the bit depth—the range and discretization of intensity—of the rendered image is limited, the magnitude of the amplified intensity is as well.

For example, an 8-bit image can take on values from 0 to 255, with 0 being black and 255 being white; in this case, the amplified intensities are bounded by the original 8-bit image and must fall within that usable range. Further still, it is important to realize that the motion is about the stationary intensity value of the surface, not 0. This complicates things further as a lighter surface is already closer to the 255 extreme, meaning there exists even less potential for amplification, especially when working with lower bit depths; however, re-scaling is an option if the overall appearance of the magnified video needs not be as it was in the original frame.

It is clear to see that in order for this method to work in its basic state, the motion must be incredibly small, less than one pixel, and ideally be recorded with a high bit depth. This is the easiest method to implement and the most physically intuitive. While simple, it is highly plagued by noise, significantly altering any extracted displacement signals and inhibiting the amplification potentials.

The MIT group published similar results to Hay's a year later [7]; however, their approach also incorporates a multiscale decomposition through successive blurring and downsampling. They go further than Hay and define limits for amplification, most notably its direct dependence to the amount of spatial shift (displacement) across the image. Since the amplification is dependent on the spatial shift, downsampling reduces motion that originally spanned multiple pixels to a smaller range (as we're capturing the same information with fewer pixels), implying increased magnification potential and fewer artifacts. Moreover, since the high spatial frequencies are removed during the downsampling (to avoid spatial aliasing), the bound increases, furthering magnification potential for the smoother transitions within the image. The multiscale implementation is not essential for rendering motion-magnified videos but does help with some of the limitations described above. With this, CSAIL's magnification factor is scaled along with the image, such that higher spatial frequencies are not magnified as much as their lower counterparts. This means the issue of bit depth is circumvented somewhat but will still come up if the amplification is pushed far enough.

8.2.2 Fourier Transform

Most similar to the intensity-based method, we transform the video and make use of the spatial analog of the Fourier shift theorem [1]. This should be familiar to all structural acousticians and is normally presented in the temporal context seen in Eq. 8.1

$$\xi\left(t-\tau\right) \iff e^{j\omega\tau}\,\Xi\left(\omega\right) \tag{8.1}$$

with its spatial analog being

$$\xi\left(x-\delta\right) \iff e^{j\omega_x\delta}\,\Xi\left(\omega_x\right) \tag{8.2}$$

with ω_x being the spatial frequency (wavenumber) and δ being some shift in space, much like τ being a shift in time for the temporal case. In both cases, we are altering the phase of the Fourier transform to render some shift in the primal domain. Now, instead of focusing on how the raw intensity values vary from some reference image, we look at how the spatial phase varies from the same reference, as seen in Fig. 8.3.

In this method, the image sequence is processed through a 2D spatial Fourier transform, followed by analyzing the spatial phase through time. The procession of steps for the (unwrapped) phase involves amplifying the signal via the shift theorem, which then implies a spatial shift in pixel location, resulting in an overall magnification of the motion present in the video. This method also assumes small deviations, and as the Fourier transform is global in nature, this method will only work when the region of interest (ROI) is undergoing simple translation [8]. If there exists more than one ROI, they must be in phase. If this is not the case, the Fourier transform may force them to appear in phase due to the global curve fit of the bases.

It is a natural progression, then, to attempt a solution to the global dilemma by again invoking our more familiar temporal signal processing, that is, creating the spatial analog of the spectrogram/short time Fourier transform (STFT). Much like the

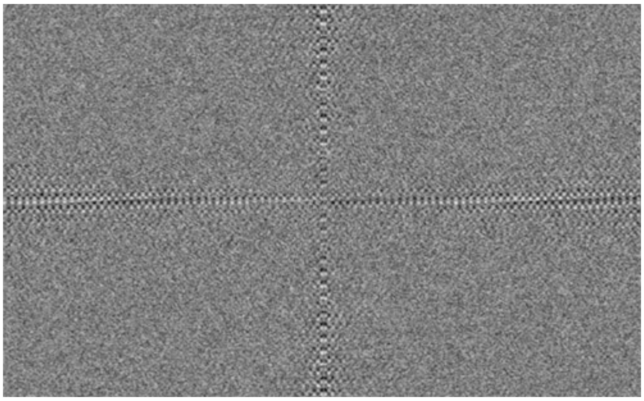

Fig. 8.3 What gets processed: phase difference of current frame from some reference, with both frames being processed through the 2D spatial Fourier transform prior to difference

temporal version, this involves windowing regions of the image to enhance locality; however, you must recall that since both of these methods are based on the Fourier transform, they are bound by the uncertainty principle, $\Delta t \Delta f = 1/N$ for temporal processing, such that there still exists some limitation between how localized you can be in the primal domain and how fine a resolution can be achieved in the dual.

8.2.3 Complex Steerable Pyramid

Eero Simoncelli, William Freeman, Edward Adelson, and David Heeger recognized this dilemma and succeeded in realizing the locality of the STFT while avoiding the uncertainty. The success was founded in wavelet theory, which had solved this problem many years prior and thus served as the basis for their development of the complex steerable pyramid (CSP) used in [4]. While the developmental jump between the STFT and the CSP may seem immense on first pass, they are actually quite similar. In truth, the main difference is the incorporation of scale, such that the deconstruction via the windowed bases is no longer constant over all of time-(spatial) frequency space; further, the amount of scaling and blurring (partitioning of spatial frequency space) can be made finer or more coarse, leading to octave or sub-octave representations.

In the CSP, we first form an image pyramid by iteratively downsampling and smoothing each frame in the image sequence. This is followed by multiscale convolutions with oriented (steerable) complex filters. In fact, it is not so far from the STFT with a Gaussian window, as both are pulling from the idea of a localized basis composed of windowed sinusoids. While these filters may seem complicated in nature, they are practically a summation of a (spatial) bandpass and its Hilbert transform in order to render the localized spatial phase needed for processing. The multiscale approach allows for the partitioning of fine details and larger structures, as well as helps deal with motion larger than a pixel in the original image sequence (by reasoning similar to the intensity-based method). Following the construction of the pyramid, we extract how the phase develops over time in our ROI(s), as described by Fleet and Jepson. Further, the magnification follows similarly to section B with an analogous shift theorem.

Never minding all of the complications, the goal remains the same as in section B: extract how the (now localized) spatial phase varies over time from some reference, and amplify this signal to make a motion-magnified video. While complex in nature and implementation, the idea and inspiration are identical to that of the Fourier transform; therefore, the fundamental understanding across the two is consistent. The described phase variations can be seen in Fig. 8.4. Notice the localization in phase as compared to Fig. 8.3, where features from the original image can now be seen, similar to Fig. 8.2.

Experimentally, this method allows for better localization in space and frequency without much influence from the uncertainty principle; however, note that as the spatial support (width of the windowing Gaussian) increases, we lose the locality, and with a wide enough window, the CSP approaches a frequency domain representation similar to that of the Fourier transform. The spatial support also plays a role in how the algorithm handles hard edges (a large difference between adjacent pixels), as the filters with smaller support have an impulse response that shows up as ringing in the magnified video. This implies that if an image has many hard edges, such as from white to black, it's better to use wider spatial filters (finer partitioning in the dual domain), even though this means a slight decrease in localization.

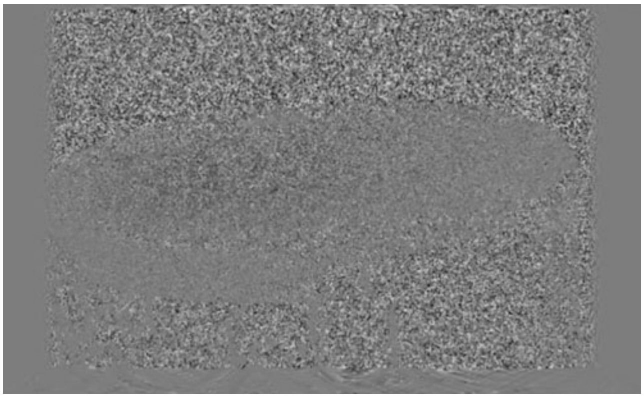

Fig. 8.4 What gets processed: phase difference at a particular orientation of current frame from some reference, with both frames being processed through the CSP prior to difference

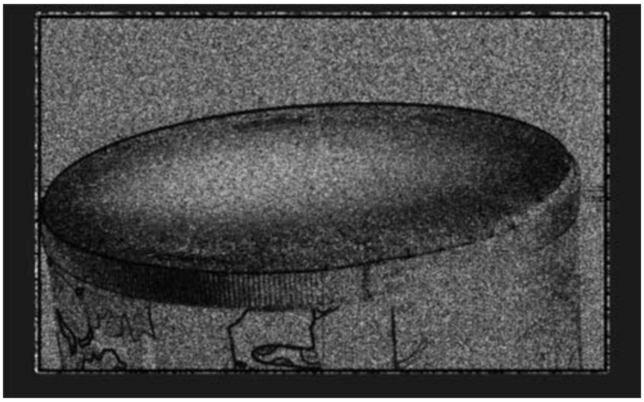

Fig. 8.5 What gets processed: phase difference of current frame from some reference, with both frames being processed through the Riesz transform prior to difference

8.2.4 Riesz Pyramid

The final fundamental technique is similar in nature to the CSP, but rather than use complex filters to render a spatial phase, the 2D analog of the Hilbert transform (Riesz transform) is used on the image to produce the necessary complex component [6]. Note this is simply a different means to the same end, as the resulting phase between the two methods is identical for the two-orientation CSP used in J. Chen et al. [9]. With this, the Riesz implementation also involves finding and only magnifying the direction of dominant orientation. While this may seem daunting or even impossible, the use of quaternions and clever equivalences removes the need for human input, and these calculations are handled as part of the algorithm. Again, the end goal remains the same as sections B and C; the related phase variation from some reference can be seen in Fig. 8.5, but do note that the presented phase is then broken down further for the quaternionic implementation.

Other than the use of the Hilbert transform, the method acts in the same way as the two-orientation CSP: multi-resolution, magnification of a pixel's value over time and finally inverting the transform. The true marvel here is the directionality of the magnification, leading to better handling of large motion in some circumstances as well as the better use of memory due to the fewer orientations and operations involved.

8.3 General Guidelines for Use

We motivate our guidelines with an extreme-case example, seen below in Fig. 8.6. In this, we have the same drum as above, now being impulsively excited, rather than acoustically. For this, we have large motion in the form of the translating stick and a noisy background, but otherwise ideal conditions with the ROI being large in the frame and well-textured. This video

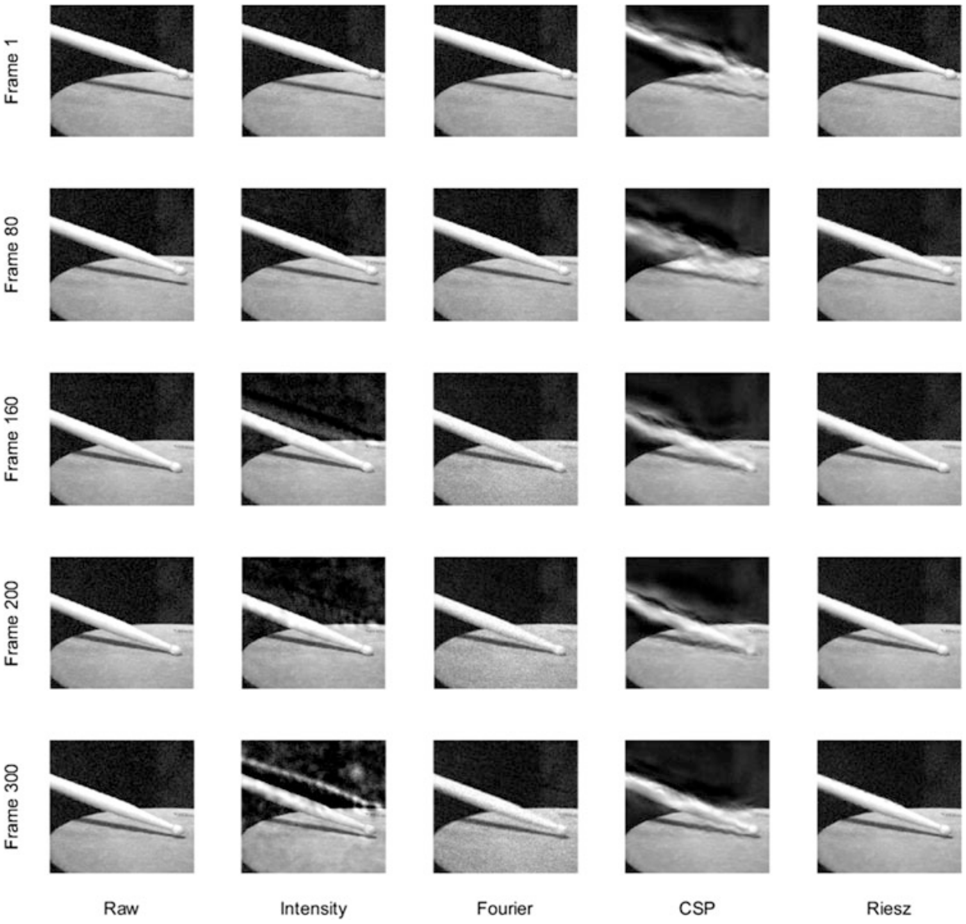

Fig. 8.6 Comparison plot of the four fundamental methods on an extreme case involving large motion and noisy frames

is processed through each of the four fundamental methods with the same frequency cutoffs, and the amplification factor was consistent for all of the phase-based methods, with the amplification factor for the intensity method being chosen separately due to its methodology. As is convention with the CSAIL papers, the reference image chosen for the algorithms was the first frame in the video.

Below, a few things can be noticed quite quickly. Firstly, and perhaps most importantly, the "ghosting" or "ringing" artifacts surrounding the drum stick resulting from the filter response and/or large motion can obstruct otherwise pertinent motion, here being the drumhead vibrations. Moreover, the intensity-based method seems to retain and then expand upon subsequent artifacts as the large motion deviates more from the reference, seen in the progressing frames. Secondly, the Fourier transform, being a global transform with numerous mathematical assumptions being broken inherently via image processing, develops an extreme amount of noise as the video develops. Lacking any usefulness for locality to begin with, introducing large, local motions complicates things further. With this, as we are manipulating spatial phase, seen above in Fig. 8.3, any hard edges in the original image appear in the phase signal as strong lines. In the Fourier-based method, these lines can appear in the inverted transform and cause similar artifacts to the ghosting; looking closely, you can see these in the progressing frames. The CSP, intentionally designed for small, imperceptible motion, struggles incredibly with large phase variations. While bounds may be placed to not amplify these large shifts (and thus reduce the artifacts), we found that this could lead to other issues with the magnified video. The Riesz-based method, given its directional magnification and quaternionic implementation, seemed to perform best here with a stark lack of artifacts compared to the other three; it should be noted that this is certainly not a general trend given that the Riesz transform is expected to behave much like the two-orientation CSP [6].

Given all of this, we are under the impression that so long as the motion is small, with constant illumination (between time steps), for a single ROI, all methods will adequately magnify motions invisible to the human eye. With this, if large motion is present, but not containing or contained within the ROI, all methods should again perform well. When moving into more complex scenarios, such as multiple (out-of-phase) ROIs, large motion contaminating the ROI, or (multiple) hard

Table 8.1 Summary of guidelines. Adequate denotes reliable feasibility in producing a quality motion-magnified video; inadequate denotes the inverse. For the CSP involving ROIs contained within large motions, further measures are required to produce quality magnification

Method	Single ROI	Multiple ROI	Large motion, not contained	Large motion, contained	All variants present
Intensity	Adequate	Adequate	Adequate	Inadequate	Inadequate
Fourier	Adequate	Inadequate	Adequate	Inadequate	Inadequate
CSP	Adequate	Adequate	Adequate	Conditionally adequate	Conditionally adequate
Riesz	Adequate	Adequate	Adequate	Adequate	Inadequate

edges filling the frame, the CSP or Riesz implementation should be chosen. Finally, for the most incredibly complex video sequences with a lack of clear, dominant orientation, the sub-octave, multi-directional CSP with added bounds on phase variation will outperform all other measures, but at the cost of computation time. A summarizing table follows (Table 8.1).

8.4 Conclusion

We have qualitatively described what we consider to be the four fundamental methods for magnifying motion in an Eulerian framework. These included simple Fourier-, intensity-, multiscale wavelet-, and Hilbert-based algorithms, each with their own quirks, limitations, and shining moments. While the underlying mathematics may have been waved away somewhat, it is our hope that this linear, simple-to-complex introduction in a more familiar framework has facilitated a greater understanding than what existed before. Most importantly, we hope that the working professional now feels some sense of comfort in understanding and explaining how and why these methods work to their colleagues and employers. While the black-box mentality may work for standardized algorithms in your favorite programming language, the key differences and potential consequences illustrated here provide adequate rationale for why these methods deserve greater attention, especially in terms of physical application.

Acknowledgments We would like to thank the ARL Walker Assistantship program for supporting this work.

References

1. Rzeszotarski, M.S., Royer, F.L., Gilmore, G.C.: An introduction to two-dimensional fast Fourier transforms and their applications. Behav. Res. Methods Instrum. **15**, 308–318 (1983)
2. Liu, C., Torralba, A., Freeman, W.T., Durand, F., Adelson, E.H.: Motion magnification. In: ACM Transactions on Graphics, (Proceedings SIG-GRAPH, 2005) 24 (2005)
3. Hay, J.: High dynamic range imaging for the detection of motion. In: Electronic Theses and Dissertations Paper 589 (2011)
4. Wadhwa, N. Rubinstein, M., Durand, F., Freeman, W.T.: Phase-based video motion processing. In: ACM Trans. Graph. (Proceedings SIGGRAPH 2013) 32 (2013)
5. Fleet, D.J., Jepson, A.D.: Computation of component image velocity from local phase information. Int. J. Comput. Vis. **5**, 77–104 (1990)
6. Wadhwa, N. Rubinstein, M., Durand, F., Freeman, W.T.: Riesz pyramids for fast phase-based video magnification (2014)
7. Wu, H., Rubinstein, M., Shih, E., Guttag, J., Durand, F., Freeman, W.T.: Eulerian video magnification for revealing subtle changes in the world. In: ACM Transactions on Graphics (Proc. SIGGRAPH 2012) 31 (2012)
8. Lazar, A.A., Ukani, N.H., Zhou, Y.: A motion detection algorithm using local phase information. Comput. Intell. Neurosci. **2016**, 7915245 (2016)
9. Chen, J.G., Wadhwa, N., Cha, Y.-J., Durand, F., Freeman, W.T., Buyukozturk, O.: Structural modal identification through high speed camera video: motion magnification. In: Proceedings of the 32nd International Modal Analysis Conference (2014)

Chapter 9
Squeeze Film Damper Experimental and Numerical Correlation: Test Setup Description and Parameter Identification of Dry System

Jason Cook, Jay Basinger, Thomas Hazelwood, Claire Luttrell, Blake Van Hoy, and Adolfo Delgado

Abstract The process of characterizing a damper involves both experimental techniques and model simulation. Experiments characterize dynamic behavior of a system through empirical modal analysis using impact and shaker testing. The layout of the test setup is crucial for a low-mass, nonlinear system. Physical arrangement, orientation of the system, and instrumentation affect the results that are discussed in this paper. These results can be used to validate a numerical simulation of the same system. With a validated model, important physical input parameters and modeling techniques can be determined and implemented in future designs. In other words, this modeling can be used with confidence to design alternative dampers that may be difficult, costly, and time-consuming to characterize experimentally.

Keywords Damper · Modal analysis · Modeling · Validation · Empirical

9.1 Introduction

Squeeze film dampers (SFD) reduce vibration at critical speeds and increase stability margin in rotating equipment [1]. An SFD is composed of a fluid film, generally oil, surrounding the outer race of a rolling element bearing or the housing of a fluid film bearing. These devices are typically assembled in parallel with a structural support (squirrel cage) centering the damper with respect to the bearing. Figure 9.1 shows a schematic view of an SFD. The literature on dampers with centering devices is extensive. Della Pietra and Adiletta [2, 3] present a comprehensive review of the literature on SFDs. SFD-centering devices allow lateral motions but restrict moments (i.e., whirling motion in the SFD land is cylindrical). In the case of damper support with a single pivot point, the motion at the damper land is conical. Limited documentation exists of the performance of this type of end supports and the effect on the SFD performance. A test rig was designed and built to evaluate this damper configuration.

The first step in the dynamic characterization of SFDs is to identify the structural parameters of the system before adding the lubricant (i.e., dry system) [4, 5]. Once the dry damper has been dynamically characterized through experiments and numerical modeling, the damping fluid is added to evaluate the fluid film forces.

The goal of creating and validating a model is to develop the ability to design future SFDs with confidence in predicting their dynamic characteristics. This is useful not only in validating the results of the model with measurements but also in establishing a model process or methodology for future damper designs. This is also true for establishing reliable

---

This manuscript has been authored by UT-Battelle, LLC, under contract DE-AC05-00OR22725 with the US Department of Energy (DOE). The US government retains and the publisher, by accepting the article for publication, acknowledges that the US government retains a nonexclusive, paid-up, irrevocable, worldwide license to publish or reproduce the published form of this manuscript, or allow others to do so, for US government purposes. DOE will provide public access to these results of federally sponsored research in accordance with the DOE Public Access Plan (http://energy.gov/downloads/doe-public-access-plan).

J. Cook (✉) · J. Basinger · T. Hazelwood · C. Luttrell · B. Van Hoy
Machine Dynamics Group, Oak Ridge National Laboratory, Oak Ridge, TN, USA
e-mail: cookjt@ornl.gov; basingerja@ornl.gov; hazelwoodtj@ornl.gov; vanhoybw@ornl.gov

A. Delgado
Mechanical Engineering Department, Texas A&M University, College Station, TX, USA
e-mail: adelgado@tamu.edu

D. Di Maio, J. Baqersad (eds.), *Rotating Machinery, Optical Methods & Scanning LDV Methods, Volume 6*, Conference Proceedings of the Society for Experimental Mechanics Series, https://doi.org/10.1007/978-3-030-76335-0_9

Fig. 9.1 SFD concept

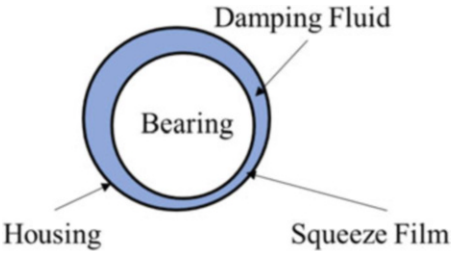

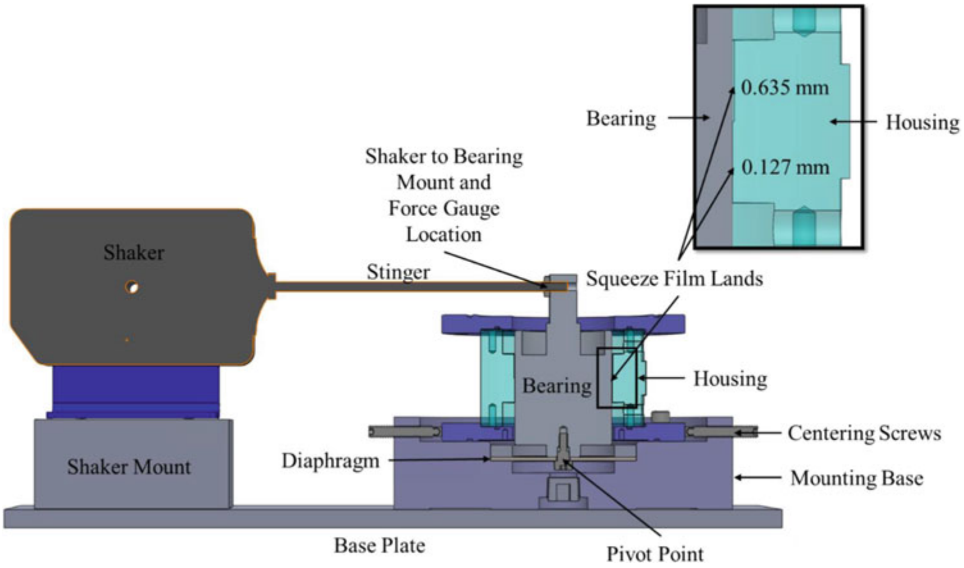

Fig. 9.2 Damper test stand

measurement techniques and processes to dynamically characterize a damper. Once a design has been created through modeling, a prototype may be built to confirm the results of the model.

This paper discusses the steps necessary to perform the dynamic experiments and numerical modeling for the dry damper. The authors also note additional considerations when characterizing this system in both obtaining the physical measurements and creating and executing the numerical models. A closed-form solution for calculating stiffness is also investigated for the dry damper.

9.2 Damper Test Stand Description

Figure 9.2 shows a schematic of the damper test stand depicting its major components comprising a base plate, mounting base, bearing, diaphragm, housing, shaker, and shaker mount. The bearing is bolted to the center of a circular diaphragm located at the top of the mounting base. An electrodynamic shaker applies a harmonic force via a slender rod (stinger) connected to the top of the damper bearing through a load cell, as shown in Fig. 9.2. The damper bearing pivots about a diaphragm clamped around its periphery, which provides angular and lateral stiffnesses. The mounting base allows adjustments for centering the bearing and housing relative to each other via centering screws. Adjustments to the bearing are also made at the attachment to the diaphragm. The housing is constructed from Lexan which allows for visualization of the squeeze film and cavitation formation. The damper land (50.8 mm) features two land diameters: one with a 0.127 mm diametral clearance (25.4 mm axial length) and the second with a 0.635 mm diametral clearance (25.4 mm axial length). This will allow characterization of the influence of oil supply grooves and evaluation of fluid inertia effects.

Four eddy current proximity probes are mounted to the housing; two are in parallel with the shaker motion, and two are orthogonal to it. The housing has an upper and lower port for adding the damping fluid. Data acquisition and shaker control software along with data acquisition hardware were used to collect and analyze the data from the damper test stand. Figure 9.3 shows the location of the probes and ports in the damper test stand.

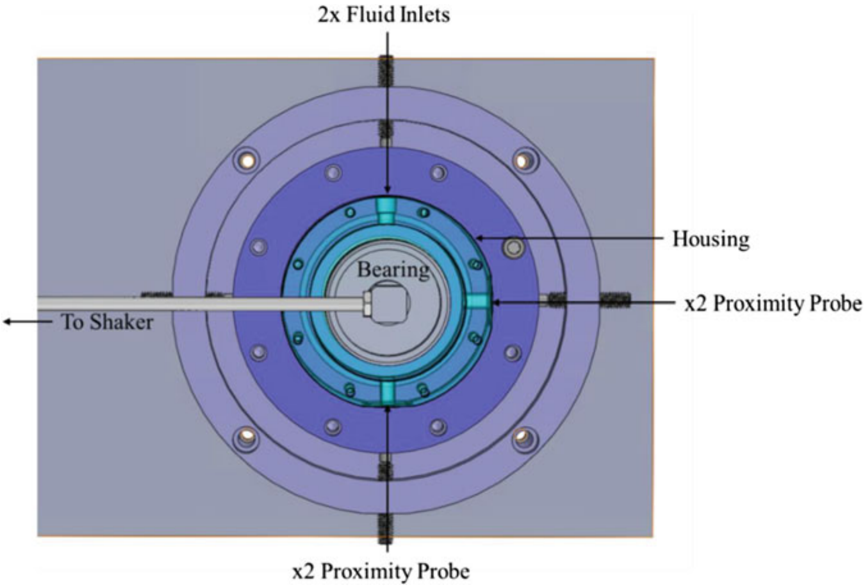

Fig. 9.3 Top view of the damper and location of probes

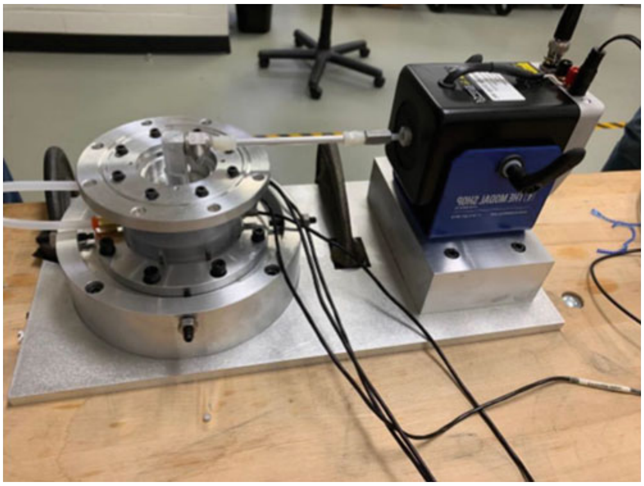

Fig. 9.4 Damper test stand

A photo of the test stand is shown in Fig. 9.4. A thin rubber isolation pad (not shown) was added between the table and base plate. The base plate was attached to the table through C-clamps.

9.3 Closed-Form Solution

A closed-form solution was used to estimate trunnion stiffness of the damper diaphragm in comparison with the numerical model and experimental results. The diaphragm is modeled as a circular plate under a linearly varying load, with the outer boundary of the plate clamped at a set radius, *a* [6]. An inner radius, *b*, which was considered to be absolutely rigid, was represented in two different cases as either the bearing bolt radius (below the plate) or the bearing contact radius (above the plate) (Fig. 9.11).

The angular/trunnion stiffness for such a plate can be expressed as $k_T = M/\varphi$, where *M* is the moment on the rigid inner radius and φ is the angle between two adjacent shaft sections of the trunnion represented by the inner radius. From Darlow et al. [7],

$$k_{\mathrm{T}}=\frac{\pi E t^3}{3\left(1-\mu^2\right)}\left[\frac{\left(\beta^2-1\right)}{\left(\beta^2+1\right)}-\ln \beta\right]^{-1}, \tag{9.1}$$

where E is the elastic modulus of the material, μ is the Poisson's ratio, t is the plate thickness, and β is the ratio of inner and outer radii, $\beta = b/a$.

Using the values $E = 193$ GPa, $\mu = 0.31$, $t = 1.9$ mm, and $a = 26.7$ mm (clamped radius), k_{T} was solved at the inner radius of $b = 8.9$ mm (bearing trunnion radius) and $b = 5.2$ mm (bolt head radius). These measurements match existing dimensions and material parameters in the finite element (FE) model. The resulting trunnion stiffness values from the closed-form solution were $k_{\mathrm{T}} = 2186$ N-m/rad (for $b = 5.2$ mm) and $k_{\mathrm{T}} = 5177$ N-m/rad (for $b = 8.9$ mm).

A simple FE model was created to compare with the closed-form solution results. The FE model consisted of two circular plates bonded together as shown in Fig. 9.5. The smaller circular plate acted as rigid body on which a fixed rotation was applied. The fixed rotation in radians and the resulting reaction moment were used to calculate the trunnion stiffness of the larger circular plate. Figure 9.6 shows a comparison between the closed-form-predicted and the FE-model-predicted trunnion stiffness for a range of β values. Both the closed-form solution and the FE model compare well over the β range considered. However, the trunnion stiffness was significantly overpredicted based on the assumptions in these two approaches.

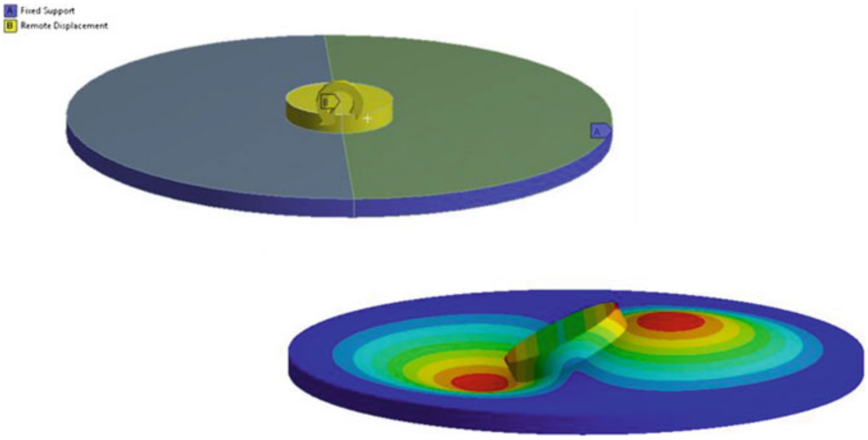

Fig. 9.5 Simplified FE setup and results for a circular plate with clamped edges and an infinitely stiff trunnion

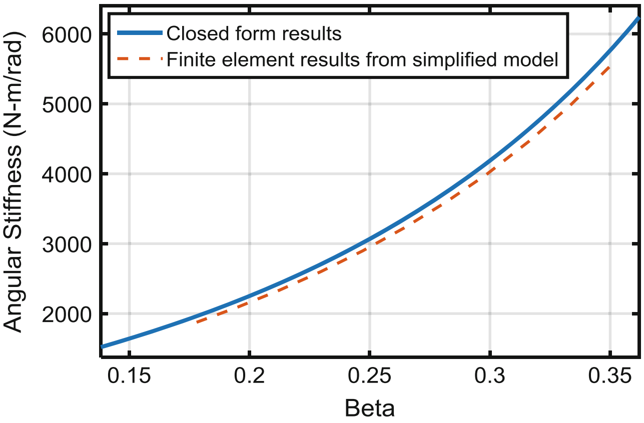

Fig. 9.6 Comparison of FE stiffness results for the simplified bearing plate model with a closed-form solution for similar plate dimensions and material properties. The ratio of the inner trunnion diameter to the outer clamped diameter is represented by β

9.4 Experimental Procedure and Results

An impact test was performed to determine the natural frequencies of the dry damper. This provided a baseline for further testing and identified the frequency range of the mode shape that will excite the squeeze film. The damper bearing was instrumented with a piezoelectric accelerometer attached horizontally in line with the shaker's stinger, as shown in Fig. 9.2. Note that the shaker and stinger were not connected to the bearing during the impact tests. A calibrated impact hammer was used to excite the damper bearing, and the frequency response function (FRF) of the accelerometer output is shown in Fig. 9.7. This testing identified a cantilever mode that was relatively radially symmetric from the horizontal accelerometers at approximately 230 Hz. Because the cantilever mode is what will be exciting the fluid film of the damper, the frequency range for further testing was determined to be 10–400 Hz.

Random and step sine shaker tests were performed on the dry-damper test rig to further illuminate the impact test response over the frequency of interest. A piezoelectric force gauge was mounted on the post on top of the damper bearing, and a stinger was mounted between the force gauge and the electromagnetic shaker. All subsequent empirical measurements used the force gauge as the excitation signal and the four eddy current proximity probes (shown in Fig. 9.3) as the response signals.

The first shaker excitation was random at a low energy level. Random testing provided an excellent snapshot of the frequency response of the damper within a few minutes of testing, but because random excitation can hide nonlinearities within the system, further testing was necessary.

The stepped sine excitation was employed to further characterize the dry damper at each integer frequency value within the range of interest. The authors decided to control the shaker amplitude based on the displacement measured from the top eddy current proximity probe in line with the shaker. The displacement value was parametrically increased to investigate the damper's linearity and to avoid overexciting the test stand. With the parametric study of excitation level and type completed, a representative FRF was chosen to compare with the closed-form solution and the numerical modeling. The rotational stiffness of the diaphragm was 1511 N-m/rad based on results from the stepped sine test. The resulting FRF generated from the stepped sine tests from 0 to 400 Hz is shown in Fig. 9.8. Both the impact test and stepped sine shaker test were in good agreement, measuring a natural frequency of approximately 230 Hz.

9.5 Numerical Modeling Procedure and Results

ANSYS Mechanical was used to model the dry-damper test stand [8]. The solid models used to build the parts for the test stand were used to develop the FE model. Some of the detailed features of the parts were simplified to reduce the number of elements needed to discretize the system.

Several numerical models were created to characterize the dry-damper configuration. A static structural model was created to determine the system's static stiffness to be compared with the measure results. A modal and harmonic analysis was conducted to establish the structure's natural frequencies along with corresponding mode shapes. The harmonic analysis also indicated how the dynamic force changes with frequency and was compared to the measured FRF.

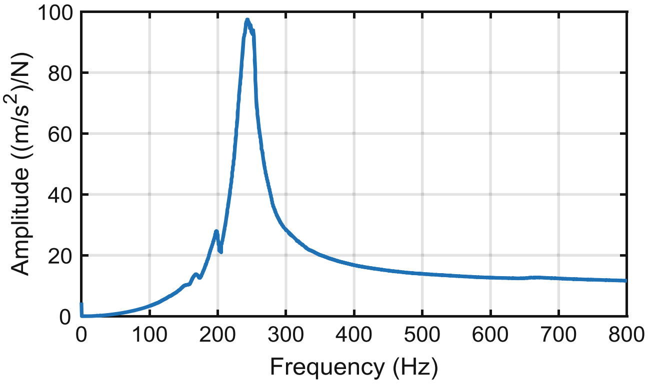

Fig. 9.7 FRF of the accelerometer output from the impact hammer test

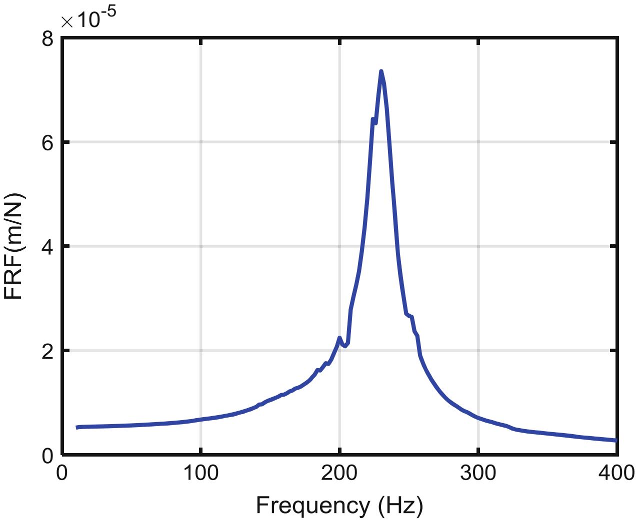

Fig. 9.8 FRF based on test results

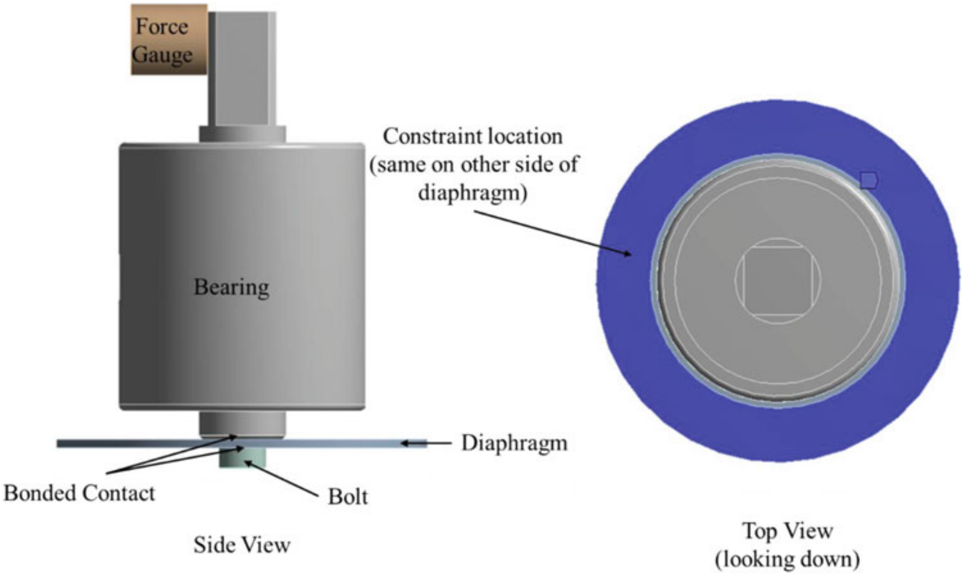

Fig. 9.9 Numerical model components and boundary conditions

9.5.1 Model Description

The same model was used for all the analyses, including the boundary conditions and mesh. The only components needed for the dry-model characterization were the bearing, diaphragm, bolt, and force gauge. The bearing was made from aluminum 6061-T6, the bolt was steel, and the diaphragm was made from 316 stainless steels. The force gauge was included to account for the additional inertia on the damper. The edge of the diaphragm was split where it would be clamped in the test stand so that a fixed constraint could be applied. The bolt attaching the bearing to the diaphragm was included and connected though bonded contact. Figure 9.9 shows the model used in the numerical analyses.

A coarse mesh was applied to the bearing, and a finer mesh was applied to the diaphragm. The diaphragm undergoes bending when a lateral force is applied to the bearing. A finer mesh is required to accurately capture this rotation. All elements are higher order, containing midside nodes for increased accuracy. Figure 9.10 shows the mesh used in the analyses.

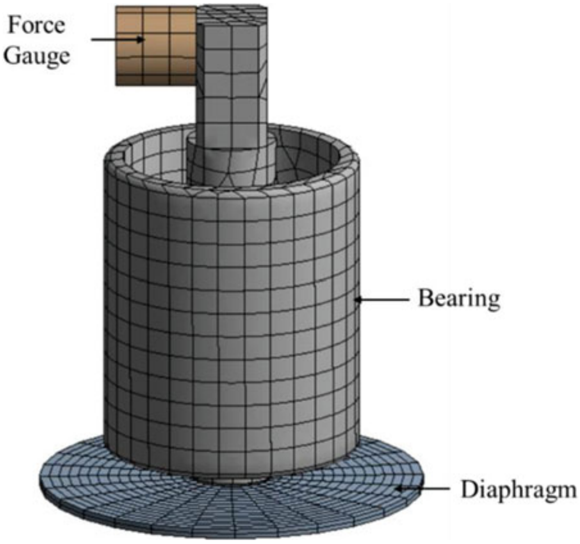

Fig. 9.10 Mesh used in analysis

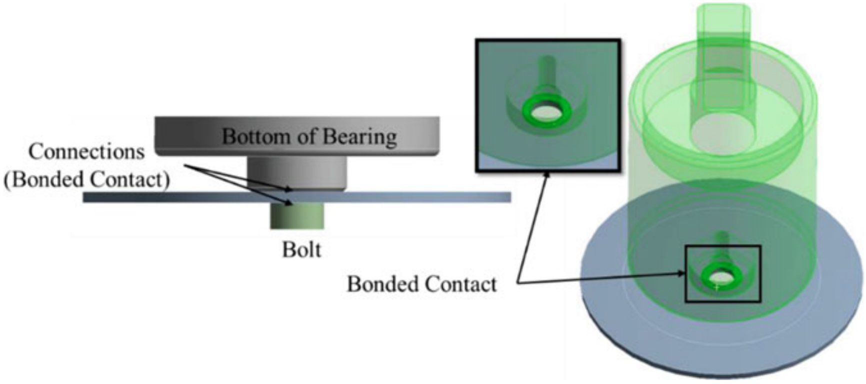

Fig. 9.11 Bonded contact area for connection between bearing and diaphragm

9.5.2 Diaphragm Stiffness from Model

The trunnion stiffness is determined by applying a force to the shaker stinger mount location. The resulting displacement is used to estimate the rotation at the diaphragm. The force is multiplied by the length between the shaker stinger mount and the connection to the diagram to obtain the moment. Once the moment and rotation are known, the diaphragm rotational stiffness can be determined.

The bond between the bearing and diaphragm was a critical feature in matching the model stiffness with the measured stiffness. The bonding surfaces were modified to capture the actual clamping area when they are bolted together. Because the diameter of the bolt and the bottom of the bearing are not identical, the clamping area is somewhere between the two diameters. The bonded contact area was determined by matching the model-diaphragm stiffness to test-calculated stiffness. Figure 9.11 shows the bonded contact area used in the analysis.

An 8.9-N force was applied to the stinger attachment location at the top of the bearing, and the resulting displacement was used to calculate the diaphragm stiffness. Figure 9.12 shows the resulting deformation due to the load (amplified for visualization). The average displacement at the force gauge and stinger location was 0.0475 mm. The resulting moment and rotation at the connection between the bearing and diaphragm were 0.8 N-m and 5.29×10^{-4} rad, respectively. The resulting rotational stiffness of the diaphragm was 1512 N-m/rad.

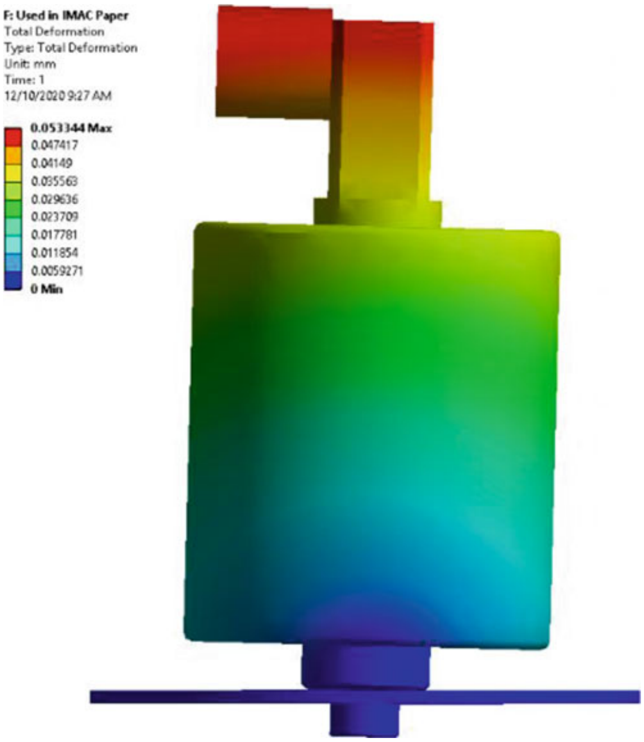

Fig. 9.12 Bearing and diaphragm deformation used in stiffness calculation

9.5.3 Numerical Modal and Harmonic Analysis

A modal analysis was used to determine the natural frequencies of the bearing and diaphragm. The modal analysis assumes no excitation force nor damping in the system. The harmonic analysis looks at the response of the system over a frequency range. This type of numerical analysis is similar to the stepped sine shaker test described above. A sinusoidal force is applied to the top of the bearing over a set frequency range. Damping can also be implemented in a harmonic analysis as an input. Because no fluid is present and the only source of damping is hysteretic, damping was initially assumed to be zero for this analysis.

The results from the numerical modal analysis help illustrate the mode shapes of the structure at several of its natural frequencies. Figure 9.13 shows the mode shape of the lowest natural frequency at 229 Hz, rotation about the diaphragm, from the modal analysis, which is also the main one of interests for this study. The next natural frequency is an axial mode that is approximately 1000 Hz. The stepped sine shaker test did not consider frequencies above 400 Hz.

A harmonic analysis on the model was performed. A sinusoidal force of 4.4 N was applied to the stinger hole at the top of the bearing. An FRF was calculated over the frequency range of 1–400 Hz. Figure 9.14 shows the FRF generated from the model with no damping. Note that the FRF is in terms of lateral force and displacement at the shaker attachment point. The result of this analysis agrees with the modal analysis results previously shown, indicating that the structure has a natural frequency at approximately 229 Hz.

9.6 Comparison

Recall that the closed-form solution and simpler FE model predicted a trunnion stiffness between 2186 and 5177 N-m/rad for the damper test rig. The agreement between the simpler FE model and the closed-form solution for trunnion stiffness indicates that the added compliance of the bearing body and connection between it and the diaphragm are nonnegligible. This added fidelity to the model acts to further reduce dry-damper stiffness beyond what is calculated when modeling the damper plate and small trunnion joint alone. Thus, the idealized close-form solution can significantly overpredict structural stiffness for more complicated structures.

Fig. 9.13 First mode shape of the bearing and diaphragm

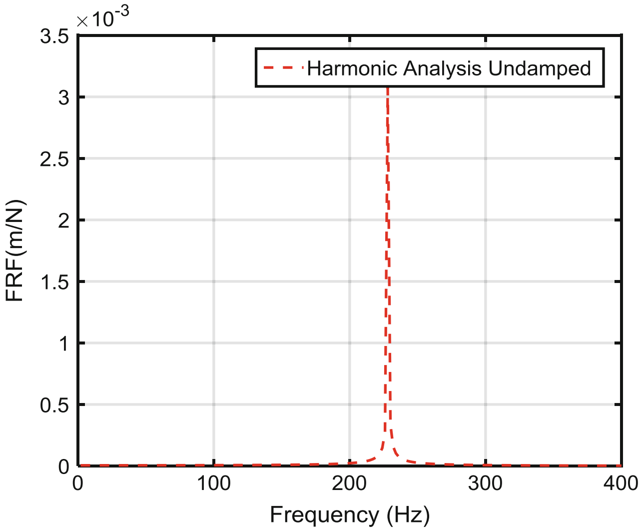

Fig. 9.14 Model-predicted FRF with no damping

Because the closed-form solution significantly overpredicted the diaphragm rotational stiffness, only the FE results of the actual damper were compared with the test data. Damping was added to the harmonic analysis to match the peak shape of the FRF to account for the hysteretic damping in the actual test damper. The diaphragm rotational stiffness was 1511 N-m/rad based on test data and 1512 N-m/rad from the numerical model. Both the test data and the model predict the first natural frequency to be approximately 230 Hz. Figure 9.15 shows a comparison plot of the FRF calculated from the test data and from the harmonic analysis with damping.

A damping ratio of 3.5% was added to the harmonic analysis to obtain the close prediction of the measured results over the frequency range considered. The damping is likely due to the bolted joint between the bearing and diaphragm and the clamped joint between the diaphragm and housing. The amplitude and natural frequency predicted from the model compare well with the measured data. Slight differences in the tolerance of components, mass, and the connections between them, which are idealized in the numerical model, account for some of the minor differences between the numerical simulation and physical system in the FRF.

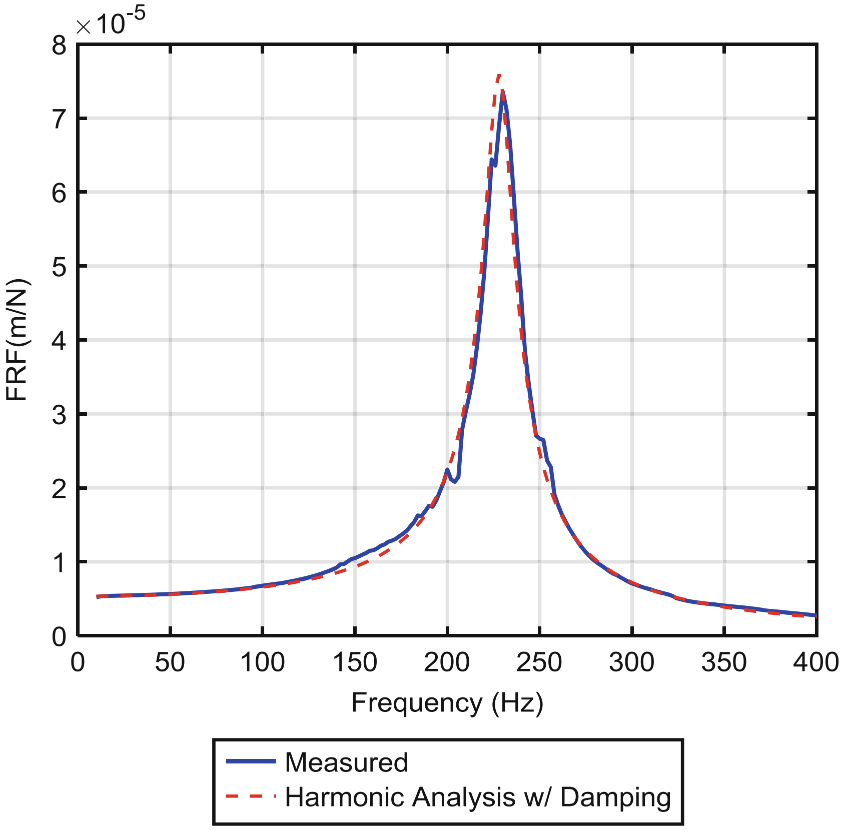

Fig. 9.15 FRF comparison between the test data and numerical model

9.7 Conclusion

A test stand was built to establish a methodology for determining SFD dynamic characteristics and validating numerical models (structure and damper). Once the numerical models are validated, these can be used with confidence in predicting the dynamic performance of future damper designs. This paper details the dynamic characterization of the "dry" damper, which is the first step to evaluate the performance of the SFD fluid film forces.

A closed-form solution and a numerical model simulation were performed to compare with test data from the damper test stand. The closed-form solution overpredicted the diaphragm stiffness because it assumed an infinitely stiff connection between the bearing and the diaphragm. The numerical model predicted the stiffness accurately after adjusting the contact area between the bearing and diaphragm. Both the test data and numerical analysis of the test stand estimated its natural frequency to be approximately 230 Hz. The FRF between the numerical model with damping and the test data is very close over the frequency range considered. The discrepancy is attributed to slight differences in component tolerancing, mass, and the connections between the numerical model and physical system. The next step will be to perform the shaker tests and numerical simulations on the damper test stand with fluid.

Acknowledgments This material was sponsored by the US Department of Energy, Office of Science. Oak Ridge National Laboratory is managed by UT-Battelle LLC, for the US Department of Energy.

References

1. Hamzehlouia, S., Behdinan, K.: Squeeze film dampers executing small amplitude circular-centered orbits in high-speed turbomachinery. Int. J. Aerosp. Eng. **2016**, 5127096 (2016)
2. Della Pietra, L., Adiletta, G.: The squeeze film damper over four decades of investigations. Part I: characteristics and operating features. Shock Vibrat. Digest. **34**(1), 3–26 (2002)

3. Della Pietra, L., Adiletta, G.: The squeeze film damper over four decades of investigations. Part II: rotordynamic analyses with rigid and flexible rotors. Shock Vibrat. Digest. **34**(2), 97–126 (2002)
4. Roberts, J., Homes, R., Mason, P.: Estimation of squeeze-film damping and inertial coefficients from experimental free-decay data. Proc. Inst. Mech. Eng. C: J. Mech. Eng. Sci. **200**(2), 123–133 (1986)
5. Delgado, A., San Andrés, L.: Identification of force coefficients in a squeeze film damper with a mechanical seal: large seal contact force. ASME J. Tribol. **132**(3), 032201 (2010)
6. Timoshenko, S. Woinoswsky-Krieger, S.: Theory of Plates and Shells, 2nd edn, pp. 285–289 (1959)
7. Darlow, M.S., et al.: Extension of the transfer matrix method for rotordynamic analysis to include a direct representation of conical sections and trunnions. Trans. ASME. **102**(1), 122 (1980)
8. ANSYS Release 19.2 Mechanical. www.ansys.com/-/media/ansys/corporate/resourcelibrary/brochure/ansys-capabilities-192.pdf

Chapter 10
Full-Field Modal Analysis by Using Digital Image Correlation Technique

Davide Mastrodicasa, Emilio Di Lorenzo, Simone Manzato, Bart Peeters, and Patrick Guillaume

Abstract At the state of art, the design validation of mechanical products in automotive, aerospace, and other advanced manufacturing industries is made by using vibration measurements and experimental modal analysis. The structures' dynamic behavior is investigated mostly using contact transducers (accelerometers, strain gauges, load cells, ...). Optical methods such as Digital Image Correlation (DIC) have recently received special attention in the structural dynamics field because it can be used to obtain full-field measurements. However, DIC can only measure vibrations in the camera field of view, which causes problems for hidden parts or in case the structure is too large to fit into the field of view. Therefore, it is of paramount importance to combine DIC with other traditional sensors such as accelerometers and strain gauges. Complex 3D test articles and structures need to be measured from many different directions. The knowledge gained by developing a heterogeneous sensor measurement system can significantly reduce the time and cost associated with pointwise sensor instrumentation. In this paper, DIC technique is used to get the full-field displacement. The sensor merging, DIC + pointwise sensors, is investigated. This information is then used to derive the modal characteristic of the structure (e.g. natural frequencies, damping ratios, and full-field mode shapes) that can be used for a more reliable FE model validation.

Keywords Digital Image Correlation (DIC) · Full-field modal analysis · Image processing

10.1 Introduction

Optical methods such as Digital Image Correlation (DIC) has recently received special attention in the structural dynamics field because it can be used to obtain full-field measurements, [1, 2]. Particularly DIC for vibration analysis was mostly performed on aerospace and automotive components [3–7] and rotating structures [8] like turbine blades [9], helicopter rotors [1]. Placing transducers is a labor-intensive and time-consuming task, and it could introduce electrical noise to the measured signals due to the extensive and unavoidable wiring. This is one of the reasons behind the development of image processing techniques to perform modal analysis of mechanical structures without contact and without having to instrument the specimen. Another reason for advancing the research in this field is connected to the damage detection and evaluation in lightweight structures, [7]. In fact, for this type of systems such as composite materials and 3D printed structures it is mandatory to avoid adding weight by placing sensors on their surface. This allowed the development of noncontact measurement techniques. The instrumentation of a test for DIC modal analysis has pros and cons with respect to the traditional contact transducers. The required equipment for the test is composed of the cameras setup and a speckled and well-illuminated surface. Therefore, a fairly large space is required for the full instrumentation around the structure to be analyzed and the surface must be appropriate to be speckled. This is not always possible, e.g. for hidden parts, like inside an aircraft wing, where it is not possible to use a DIC setup, or for foam structures, where the speckle cannot be applied.

D. Mastrodicasa (✉)
Siemens Industry Software NV, Leuven, Belgium

Acoustic & Vibration, Vrije Universiteit Brussel, Brussels, Belgium
e-mail: davide.mastrodicasa@siemens.com

E. Di Lorenzo · S. Manzato · B. Peeters
Siemens Industry Software NV, Leuven, Belgium

P. Guillaume
Vrije Universiteit Brussel, Brussels, Belgium

D. Di Maio, J. Baqersad (eds.), *Rotating Machinery, Optical Methods & Scanning LDV Methods, Volume 6*, Conference Proceedings of the Society for Experimental Mechanics Series, https://doi.org/10.1007/978-3-030-76335-0_10

This is one of the reason why DIC has to be combined with the already established and well-known contact transducers in a hybrid way for structural dynamics applications. In some cases, the purpose is just to analyze the full-field behavior on a certain area and obtain a discretized behavior of the structure in other regions. This is especially true for damage detection and junction characterization where we want to look accurately just to the small parts of structures.

In this paper, DIC technique is used to get the full-field displacement time histories of the unities under test. The information is after used in combination with the pointwise sensors to obtain the FRFs for the modal parameter estimation with Polymax algorithm, [10]. A first attempt of combining accelerometers sensors and DIC was conducted in SISW on a demo airplane and a car tire.

10.2 Background

10.2.1 Low Speed Camera for High Frequency Behavior Characterization

In this paper, low speed camera is used to investigate vibrations at frequency higher with respect to the camera Nyquist frequency. The under-sampling and remapping the time histories method was used to measure high frequency vibrations.

A fundamental hypothesis behind this method is that the signal that we want to reconstruct has to be periodic. When a signal is periodic, it is possible to reconstruct it at a lower frequency using signal aliasing. If we want to measure the blue signal in Fig. 10.1a having a frequency $f = f_{signal}$ and we sample it with a sampling frequency $f_{sample} < f_{signal}$ we obtain the purple signal, Fig. 10.1b having a frequency f_r related both to f_{signal} and f_{sample} and equal to

$$f_r = f_{signal} \cdot f_{sample} \cdot (f_{sample}^{-1} - f_{signal}^{-1}) \tag{10.1}$$

An important property of the reconstructed signal is that the shape of the reconstructed signal has the same shape of the original one but scaled along the time axis. The purple signal is described by the equation:

$$S_r(t) = S_{signal}\left(\frac{f_r}{f_{signal}} \cdot t\right) \tag{10.2}$$

Therefore, using Eq. (10.2) we can derive Eq. (10.3) and reconstruct one period of the desired signal, obtaining the one in Fig. 10.1c.

$$S_{artif}(t) = S_r\left(\frac{f_{signal}}{f_r} \cdot t\right) \tag{10.3}$$

From the experimental point of view, the structure was excited with a periodic pseudo random signal having a maximum frequency minor than the used camera sample frequency. Therefore, the excitation signal was reconstructed using the method previously exposed.

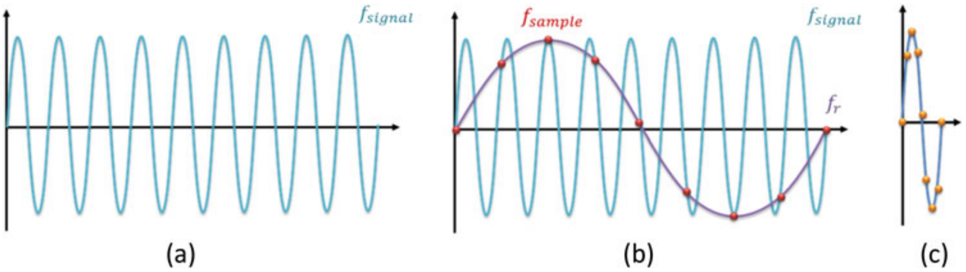

Fig. 10.1 Signal reconstruction process. (**a**) Original signal. (**b**) Original and sampling signals. (**c**) Reconstructed signal

10.3 Experimental Setup and Results

DIC was performed on two different structures, a demo airplane and a car tire. In both the cases, together with DIC, some pointwise sensors (accelerometers) were used as a reference measurement system for the modal parameters and to analyze the possibility to merge these two datasets.

10.3.1 Demo Airplane

Using the MatchID post processing DIC software, it was possible to obtain the full field displacement data signals to perform modal analysis. The test bed, previous the speckling process, it is shown in Fig. 10.2a. The same specimen after the application of the white coat, needed to create enough contrast after applying the speckles (i.e. features), is shown in Fig. 10.2b. Finally, the structure used for the test is shown in Fig. 10.2c. The structure was suspended using soft bungees for simulating free-free boundary conditions.

The full experimental setup, including the 2 cameras, the lights, and the acquisition systems, is shown in Fig. 10.3. Two acquisition systems, the SCADAS, from Siemens Industry Software NV, and the TriggerBox, from MatchID, were used. These 2 systems were interconnected together for synchronizing the cameras (triggered by the MatchID TriggerBox) with the shaker (triggered by the Siemens SCADAS). A sine signal is sent from the SCADS to the TriggerBox. The latter, knowing the sine frequency, locks onto it based on the zero crossing and the positive slope. In this way, the two systems are synchronized. Meanwhile a periodic signal, multiple Chirps in our case, is sent to the structure through the shaker. For each period, following the method exposed in Sect. 10.2.1, a certain number of pictures is grabbed in order to reconstruct the chirp signal using a camera sample frequency minor with respect to the maximum chirp frequency. The acquisition parameters and the signals specifications used in this measurement campaign are shown in Table 10.1.

From Fig. 10.2c it is also possible to see that some accelerometers were attached to the bottom face of the structure. The accelerometers output were used to obtain a reference result to compare with the DIC estimated modal parameters and for the mode shapes merging. Particularly, 22 accelerometers and 1 force cell attached to the stinger head were attached to the structure. The force cell output signal was used as a reference for the FRFs calculation, both for DIC and accelerometers.

The synchronization between the 2 systems was checked recording the sine both with the MatchID TriggerBox and the Siemens SCADAS. A small misalignment between the 2 systems was solved in a post processing phase finding the number of samples to be delayed in order to obtain the maximum correlation between the Testlab and MatchID sine signals. Therefore the Testlab sine was aligned onto the MatchID sine. Based on these results, also the time output signal from the force cell to be used for the FRFs with the displacements was delayed. 9 natural frequencies and mode shapes were identified in the bandwidth of interest. From the first investigation, it was noticed that the stable poles at a frequency higher than 105 Hz represent a dynamic behavior different than the one found with the accelerometers. This is probably due to the too low displacement at that frequency, and therefore the displacement signal is lower than the camera noise floor. This behavior is still under investigation. The modal parameters obtained from DIC and accelerometers are compared together in Fig. 10.4 and Table 10.2.

It is possible to see that there is a good correlation between the 2 measurement systems up to the 6th mode in terms of mode shapes and for all the modes in terms of natural frequencies (the % error is below the 5%). It has to be highlighted

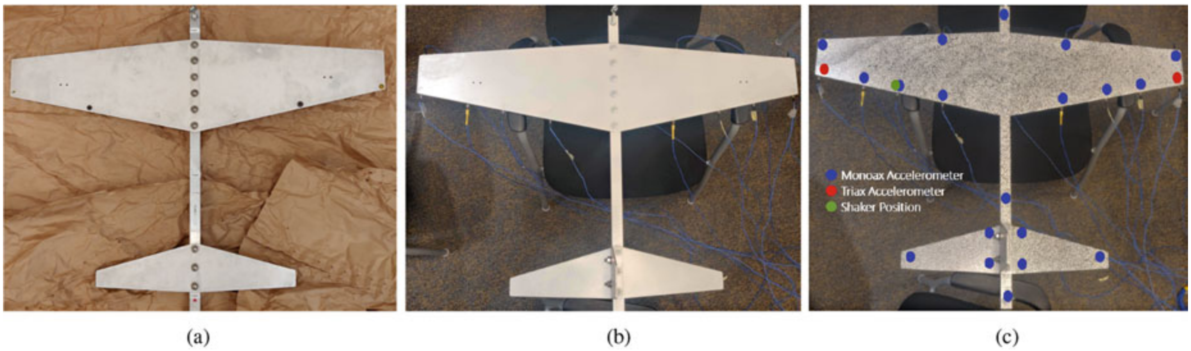

Fig. 10.2 Process of speckling. (**a**) Virgin structure. (**b**) White coated structure. (**c**) Speckled structure with sensors location

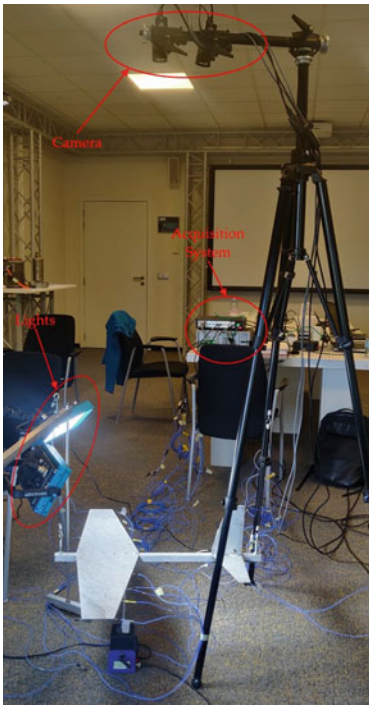

Fig. 10.3 Experimental setup

Table 10.1 Acquisition parameters

Signals specification	
Parameters	*Value*
Sine frequency	0.25 Hz
Sine amplitude	3 V
Chirp frequency	1–200 Hz
Chirp amplitude	0.3 V
Testlab acq. parameters	
Parameters	*Value*
Bandwidth	256 Hz
Spectral lines	256
Acquisition time	1 s
MatchID acq. parameters	
Parameters	*Value*
Sampling frequency	512 Hz
Camera frequency	8 Hz

that the lack of correlation on the 7th, 8th, 9th mode shapes are mainly due to the fact that these modes are hidden under the vertical displacement of the full mockup. Therefore, the correlation, for these modes it is not good.

In Fig. 10.5, it is possible to see the 2nd and 5th mode shape.

Particularly, in the 5th mode shape it is possible to understand the importance of merging pointwise sensors and DIC. This mode shape is mainly a mode of the fin. Due to the field of view of the stereo setup, it was not possible to measure this part of the structure with DIC. However, with the accelerometer it was possible to detect and identify this mode shape.

10.3.2 *Car Tire*

In this experimental setup, a car tire was suspended using bungees for simulating free-free boundary conditions. The measurement setup is shown in Fig. 10.6. In this case, 8 accelerometers were used as a comparison with the DIC results and for the mode shapes merging between the two measurement systems. The structure was excited using a Shaker on the

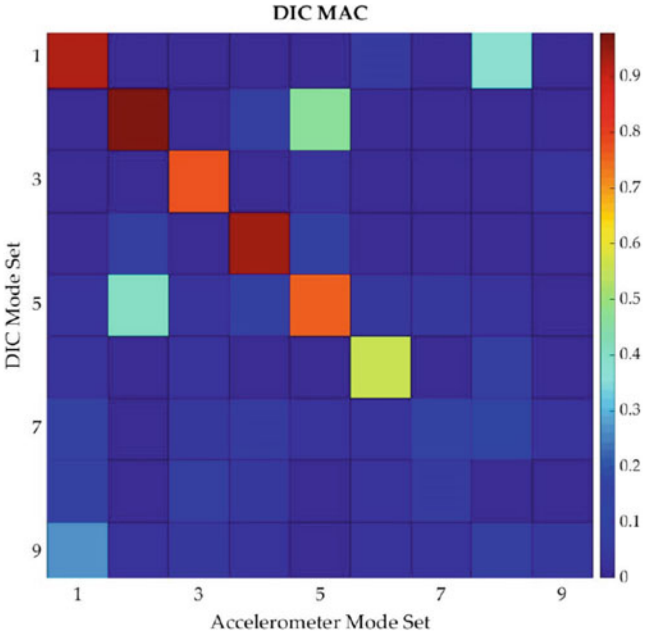

Fig. 10.4 MAC matrix

Table 10.2 Modal parameters comparison

	Accelerometers		DIC	
Mode	f_n (Hz)	ζ_n (%)	f_n (Hz)	ζ_n (%)
1	17.77	1	18.55	2.39
2	34.29	1.08	34.20	0.13
3	61.58	1.22	61.65	1.04
4	64.27	0.97	64.23	0.34
5	75.28	1.05	75.22	0.72
6	81.05	1.61	81.55	1.02
7	88.38	2.21	89.39	1.98
8	91.44	1.48	94.66	2.15
9	104.32	0.42	105.84	0.67

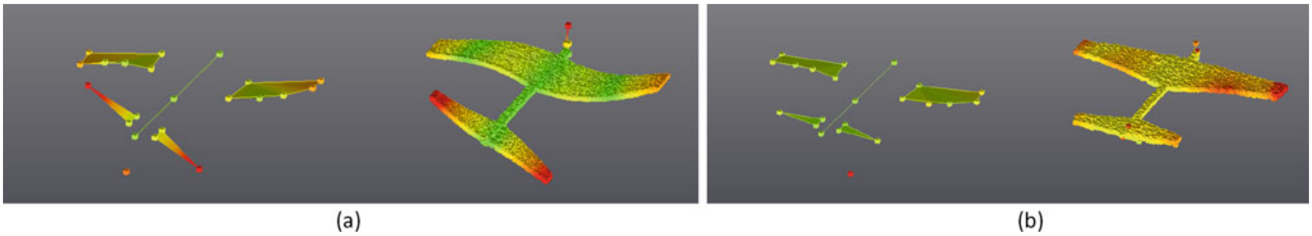
(a)
(b)

Fig. 10.5 Examples of mode shapes. (**a**) 2nd mode shape. (**b**) 5th mode shape

bottom of the tire. The output signal from the force cell, placed between the tire and the shaker, was used as a reference for the FRFs calculation, both for DIC and accelerometers.

Also in this measurement, two acquisition systems, the SCADAS, from Siemens Industry Software NV, and the TriggerBox, from MatchID, were used. During the demo airplane measurement, a not perfect synchronization between the two systems was detected due to the low slope of the sine in the zero crossing. Therefore, instead of using a sine signal, a sawtooth signal was designed to perform the synchronization. Based on this new signal, there was not any problem in aligning the displacement signal with the force cell signal for the FRFs calculation. Also the excitation signal sent to the shaker was changed. A more deterministic and appropriate signal for exciting the structures, a pseudo random signal, was used for this specimen. Following the same procedure of the previous test, for each period, a certain number of pictures are grabbed in order to reconstruct the output displacement signal using a camera sampling frequency minor with respect to the maximum

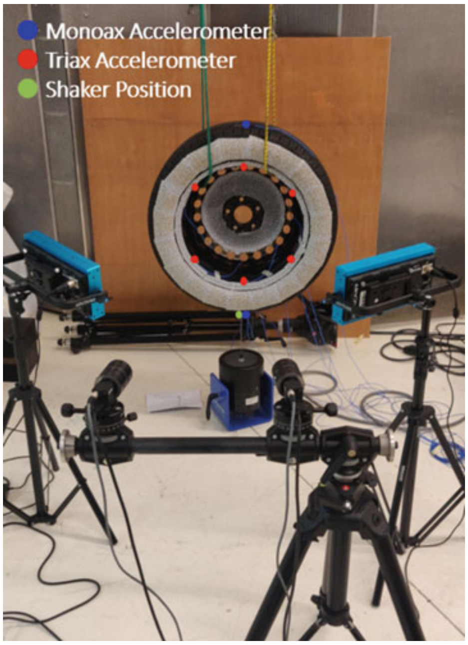

Fig. 10.6 Experimental setup

Table 10.3 Acquisition parameters

Signals specification	
Parameters	*Value*
Sawtooth frequency	0.1953125 Hz
Sawtooth amplitude	5 V
Pseudo random frequency	30–400 Hz
Pseudo random amplitude	0.5 V
Testlab acq. parameters	
Parameters	*Value*
Bandwidth	400 Hz
Spectral lines	512
Acquisition time	1.28 s
MatchID acq. parameters	
Parameters	*Value*
Sampling frequency	800 Hz
Camera frequency	12.5 Hz

pseudorandom sampling frequency. The acquisition parameters and the signals specifications used in this measurement campaign are shown in Table 10.3.

From the first investigation, it was noticed that the DIC dataset suffer from rigid body motion. This motion has a big impact on the reconstruction process. Due to the fact that the pictures are recorded in different cycles, the un-deformed configuration related to each excitation cycle it is not the same and therefore there is a drift in the data that has to be corrected in a post processing phase. A rigid body motion compensation algorithm was used for correcting the dataset. After this processing, 10 natural frequencies and mode shapes were identified in the bandwidth of interest. The modal parameters obtained from DIC and accelerometers are compared together in Fig. 10.7 and Table 10.4.

It is possible to see that there is a good correlation for some mode shapes between the 2 measurement systems and a bad correlation for others. Particularly, the 1st, 6th, 7th mode shapes are seen by the rigid body motion compensation as a rigid body motion and therefore are filtered out in the data. On the other side, we have a good correlation for the 2nd, 3rd, 4th, 5th, 8th, and 10th mode shapes. The high off diagonal cross correlation values are due to accelerometers spatial aliasing.

In Fig. 10.8, it is possible to see the 2nd and 5th mode shape.

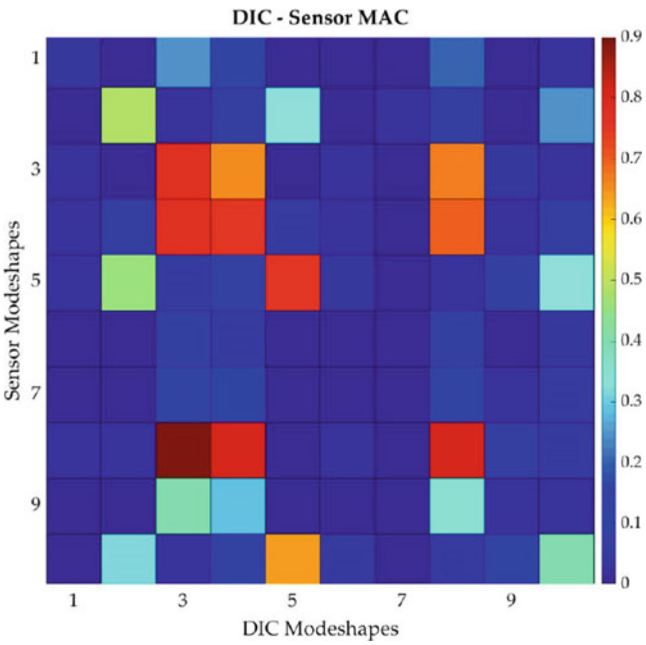

Fig. 10.7 MAC matrix

Table 10.4 Modal parameters comparison

	Accelerometers		DIC	
Mode	f_n (Hz)	ζ_n (%)	f_n (Hz)	ζ_n (%)
1	50.42	1.74	50.22	0.47
2	84.68	2.84	84.76	2.09
3	92.83	2.71	92.76	2.64
4	107.13	2.72	107.45	2.67
5	119.59	4.19	119.94	1.75
6	135.46	1.76	134.44	0.74
7	164.53	3.18	164.04	1.54
8	177.20	1.80	177.67	1.23
9	205.13	2.34	204.02	1.13
10	228.32	0.13	227.11	0.03


(a)
(b)

Fig. 10.8 Examples of mode shapes. (**a**) 2nd mode shape. (**b**) 5th mode shape

10.4 Conclusion

In this paper, the first attempt to use DIC for modal analysis is investigated. An experimental measurement result which combines conventional modal analysis (accelerometers) with the novel DIC experimental modal analysis is presented. The use of low speed camera for high speed vibration measurements seems to give very good results. However, the boundary conditions have to be controlled accurately for using this reconstruction method to guarantee that the test bed has a periodic behavior. The application of DIC in the modal analysis field in order to enrich the conventional modal analysis results with high density data is very promising. However, some limitations need to be taken into account:

- Data reduction techniques should be implemented to allow faster and accurate processing with current processors capabilities.
- A deeper investigation on the capabilities of using DIC with low displacements, which occurs at high frequency, should be done.
- A streamline solution covering the full measurement and processing chain is needed.
- A further investigation of the reconstruction method comparing results from high speed camera and low speed camera should be done.

Focusing on the tire, it is possible to understand the main advantages of having full-field mode shapes for a more reliable FE model validation and update. DIC shows also potential for identifying defects in lightweight strictures where the weight of sensors could be an issue when instrumenting the specimen for testing.

Acknowledgments The authors gratefully acknowledge the Flanders Innovation & Entrepreneurship for its support of the Baekeland project "Digital Image Correlation For Structural Dynamics Full-field Analysis". The authors would like to extend their gratitude to MatchID for their support during the experimental measurements.

References

1. Di Lorenzo, E., Lava, P., Balcaen, R., Manzato, S., Peeters, B.: Full-field modal analysis using high-speed 3d digital image correlation. J. Phys. Conf. Ser. **1149**, 012007 (2018)
2. Srivastava, V., Patil, K., Baqersad, J., Zhang, J.: A multi-view DIC approach to extract operating mode shapes of structures. In: Niezrecki, C., Baqersad, J. (eds.) Structural Health Monitoring, Photogrammetry & DIC, vol. 6, pp. 43–48. Springer International Publishing, Cham (2019)
3. Molina-Viedma, A., Lopez-Alba, E., Felipe-Sese, L., Diaz, F., Rodriguez-Ahlquist, J., Iglesias-Vallejo, M.: Modal parameters evaluation in a full-scale aircraft demonstrator under different environmental conditions using HS 3D-DIC. Materials **11**, 230 (2018)
4. Seguel, F., Meruane, V.: Damage assessment in a sandwich panel based on full-field vibration measurements. J. Sound Vib. **417**, 1–18 (2018)
5. Bharadwaj, K., Sheidaei, A., Afshar, A., Baqersad, J.: Full-field strain prediction using mode shapes measured with digital image correlation. Measurement **139**, 326–333 (2019)
6. Galeazzi, S., Chiariotti, P., Martarelli, M., Tomasini, E.: 3d digital image correlation for vibration measurement on rolling tire: procedure development and comparison with laser Doppler vibrometer. J. Phys. Conf. Ser. **1149**, 012010 (2018)
7. Ha, N.S., Vang, H.M., Goo, N.S.: Modal analysis using digital image correlation technique: an application to artificial wing mimicking beetle's hind wing. Exp. Mech. **55**, 989–998 (2015)
8. Yashar, A., Ferguson, N., Tehrani, M.G.: Measurement of rotating beam vibration using optical (DIC) techniques. Proc. Eng. **199**, 477–482 (2017). X International Conference on Structural Dynamics, EURODYN 2017
9. Baqersad, J., Carr, J., Lundstrom, T., Niezrecki, C., Avitabile, P., Slattery, M.: Dynamic characteristics of a wind turbine blade using 3d digital image correlation. Proc. SPIE - Int. Soc. Opt. Eng. **8348**, 74 (2012)
10. Peeters, B., Van der Auweraer, H., Guillaume, P., Leuridan, J.: The polymax frequency-domain method: a new standard for modal parameter estimation? Shock Vib. **11**, 395–409 (2004)

Chapter 11
Validating Complex Models Accurately and Without Contact Using Scanning Laser Doppler Vibrometry (SLDV)

Jerome Eichenberger and Joerg Sauer

Abstract The need to validate simulation models of complex mechanical structures has grown in importance for efficiency in the design process. This is especially true for non-linear structures (such as composite panels and jointed components) where it is critical to use an accurate full-field measurement method. This tutorial covers a how-to-guide and use cases of scanning laser Doppler vibrometry (SLDV) as a non-invasive technology to efficiently characterize critical mechanical structures.

Keywords Vibrometry · Non-contact · FE model validation · Vibration measurement · Quality control

11.1 Introduction

All mechanical structures fail sooner or later if the applied forces exceed the structural limits. What are these limits? How can they be established? What types of forces can be tolerated? These are questions design engineers ask themselves continuously. For example, this is important for aerospace, automotive, the development of medical devices, civil engineering, consumer electronics, and many other applications.

Simulation models that predict the dynamic behavior of critical structures are the bread and butter for the design engineer. These models not only enable safe designs but also give the engineer the capability to optimize for weight, efficiency, and performance. Needless to say, the models require accuracy. But how accurate do they need to be? How many prototype iterations need to be tested and evaluated until the final product can be released? Polytec provides state-of-the-art metrology to help the design engineer of today to test and optimize their designs. Non-contact laser Doppler vibrometers have been used in many industries for over 30 years and are continuously adapting to the ever-changing needs of the research and development process. The ability of laser vibrometry to provide fast, accurate measurements and map full-field responses as deflection shapes is instrumental for the short development time frames required in industry.

The diversity of vibrometer applications becomes evident when considering the versatile nature of laser light. Measurements are possible up to several GHz frequencies and down to the sub-Hz range with a flat frequency response and no mass loading. Any surface can be measured as long as there is visual access (even through glass and in water). Large objects like bridges and buildings can be targeted from as far as several 100 m. Microstructures can be characterized underneath a microscope. There are no measurement restrictions due to an object's surface color, texture, and curvature as long as there is some light being reflected back into the optics of the vibrometer. Furthermore, since the Doppler shifts are sensitive to variations of the refractive index of the medium, vibrometers are capable of directly measuring sound field distributions in water or in air using a technique called vibro refractometry.

The purpose of this tutorial is to provide general guidance to the user for making effective, accurate measurements using vibrometry. The tutorial also helps the user gain a basic understanding of the working theory of vibrometers that will enable him/her to generate test data efficiently. A best practices guide and measurement examples are included.

J. Eichenberger
Polytec, Inc., Irvine, CA, USA
e-mail: j.eichenberger@polytec.com

J. Sauer
Polytec GmbH, Waldbronn, Germany
e-mail: j.sauer@polytec.de

D. Di Maio, J. Baqersad (eds.), *Rotating Machinery, Optical Methods & Scanning LDV Methods, Volume 6*, Conference Proceedings of the Society for Experimental Mechanics Series, https://doi.org/10.1007/978-3-030-76335-0_11

11.2 Test Case Scenarios for Vibrometry

Choosing the correct vibrometer system as well as the best setup and measurement parameters can be straightforward once the purpose of test is defined. The most common test scenarios are as follows:

1. **Finite element (FE) model validation**. Finite element models are compared side by side with full-field 3D vibration data to see how well they match. This requires a high fidelity of the data. In order to compare the experimental modal parameters with the simulation, the vibration data needs to be curve fitted. For most accurate curve fitting, not only the resonance peaks need to be resolved clearly but also the response behavior of the anti-nodes, which, by nature, exhibit a much lower vibration amplitude. Some examples of model verification are shown in the following sections for turbine blades.
2. **Non-destructive evaluation (NDE)**. The location of defects can be determined by sending traveling ultrasonic waves through a material and seeing how they interact. A very high sensitivity vibrometer is required as the surface displacement of ultrasonic waves is very small (nm or even pm level) and a large amount of points need to be measured for visualization. Lack of sensitivity can be compensated by averaging, however, that will result in longer measurement times. Please see application example 2 for more details on NDE applications.
3. **Troubleshooting**. Finding an unwanted vibration for complicated structures can be difficult if you don’t know where to look. For example, in the case of electronic circuit boards, the acoustic noise emission can be excessive or damage the board. Vibration data quality is not as critical as in the case of modal validation as long as the vibration signature of the disturbing behavior is evident. A 1D scanning measurement and, in some cases, spot checks with a single point vibrometer at only a few locations are sufficient.
4. **Performance validation**. Determining if the design performs as expected is a critical aspect of R&D. For instance, verifying the efficiency of ultrasonically driven devices like an imaging arrays, cutting tools, or surgical tools can be critically important. Model validation is required in some cases, but mostly it is the performance parameters like frequency and vibration amplitude that are critical.
5. **Quality control**. Verifying that a product does not have defects for in-line manufacturing can improve yield. This can be true for mechanical structures such as bearings, motors, pumps, etc. In quality control usually only one location and one measurement are acquired. Measurement speed is of the essence to allow for maximum throughput.
6. **Basic research/learning from nature**. Vibrometry is used widely by many university labs and institutes for research. Often the mechanical behavior of a structure is typically not known beforehand. Thus, vibrometer systems provide important insights into the complex mechanical vibrations of experimental structures.

11.3 Measurement Principle of a Vibrometer

A laser Doppler vibrometer uses the light-based Doppler effect to determine the frequency and amplitude of an object’s motion in velocity, displacement, and acceleration. It is a point-and-shoot approach allowing for instant reading and recording of a vibration signal wherever the laser beam is pointed at.

Figure 11.1 depicts the optical layout of the laser Doppler vibrometer sensor head with laser source, interferometer, and photo-detector. The measurement beam is pointed at the vibrating sample, while the reference beam stays within the vibrometer head. The reflected light from the sample is captured by the photodetector where it is re-combined with the reference beam. The returned light is Doppler shifted in frequency by f_D, which is directly proportional to the object’s instantaneous velocity v according to the relationship in Eq. (11.1) below.

$$f_\mathrm{D} = \frac{2 \cdot n \cdot v}{\lambda}, \tag{11.1}$$

where λ is the wavelength of the laser source and n the refraction index of the medium the sample is contained in. Due to the simplicity of the optical design, vibrometers are accurate and versatile. The vibrometer is based on interferometry (measured against the wavelength of light) and is calibration free. In fact, it is used for primary calibrations of accelerometers. The interferometer is heterodyned by means of an acousto-optic modulator (Bragg cell) as depicted in Fig. 11.1. The vibrometer measures directionality of movement and achieves highest possible SNR even at low frequencies.

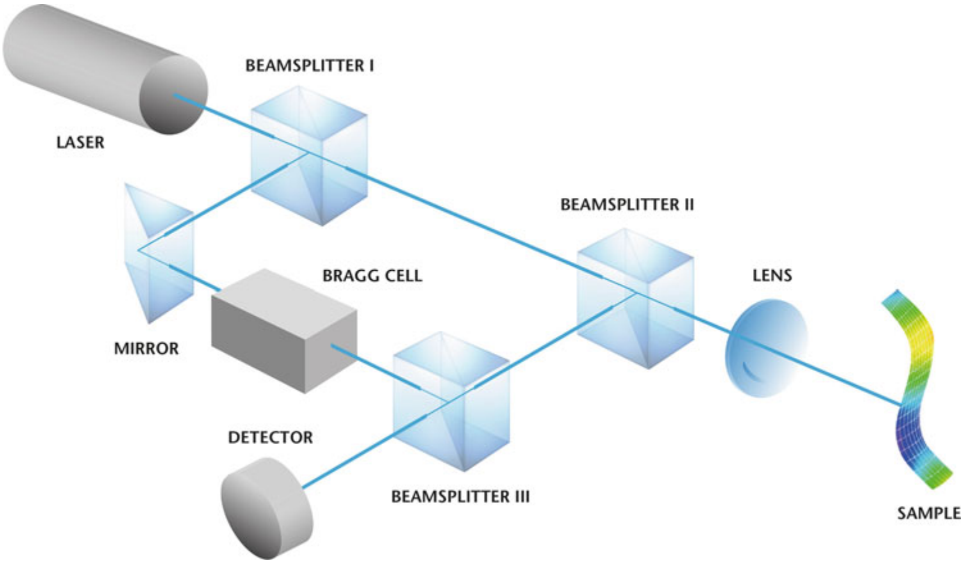

Fig. 11.1 Optical layout of a laser Doppler vibrometer

The electronics portion of the laser Doppler vibrometer takes the modulated carrier signal from the photo-detector and demodulates it for displacement using the ArcTan(I/Q) method. From this, velocity and acceleration can be derived easily. Since the demodulation occurs in the frequency domain, any amplitude fluctuations in the returned light intensity will not introduce any noise onto the vibration signal, similar to the benefits of FM radio versus AM radio.

In contrast to the heterodyne approach, as described above, a homodyne laser Doppler interferometer does not include a Bragg cell. The Doppler shift in frequency will be positive no matter in what direction the sample is moving; thus a homodyne vibrometer will not be able to inherently provide directionality information. Also, the noise floor of a homodyne-based vibrometer is typically higher at low frequencies. Yet another approach is the so called self-mixing interferometer. With the advent of solid-state diode lasers, a compact setup became possible: the light reflected from the sample interferes in the laser cavity leading to a modulation of the properties of the diode laser. This modulation can be detected and decoded to derive the displacement information. The phase noise for this technique tends to be higher compared to homodyne or heterodyne interferometers using external laser sources. For the purpose of this tutorial, only heterodyne laser Doppler vibrometers as depicted in Fig. 11.1 are considered.

There are two basic vibrometer types based on laser wavelength: (1) helium-neon (HeNe) laser-based vibrometers (633 nm) and (2) infrared (IR) solid-state laser-based vibrometers (1550 nm). Each type has it strength and weaknesses. The following overview shall provide the user with a guideline on when to choose which one:

1. Due to a short wavelength and very low phase noise of the HeNe laser tube, HeNe-based vibrometers have excellent sensitivity on surfaces with high reflectivity. They also work very well on submersed structures as long as the liquid is transparent. Visible laser-based vibrometers are recommended for applications requiring high beam positioning accuracy. Microscope-based vibrometers provide a submicron laser spot diameter, which is necessary for characterizing many microstructure devices.
2. IR laser-based vibrometers operate with a longer wavelength, which are less sensitive when compared to the HeNe-based design. However, the IR laser-based vibrometer performs better on surfaces with low reflectivity or at long stand-off distances. This is due to higher laser power (while still being eye-safe) and lower shot-noise on the photo-detector. IR laser-based vibrometers require a pilot laser for positioning which makes for a more complex vibrometer design. IR-based vibrometers are not able to measure on submersed structures as the absorption of IR light is too high.

There are some applications where either vibrometer system would work and the HeNe-based vibrometer is preferred due to its lower price point. Both vibrometer types employ the highest power laser possible while being eye-safe. Increasing laser power to a non-eye-safe laser class is not advised for lab environments, although it would theoretically provide even better signal-to-noise ratio (SNR).

11.4 Choosing a Vibrometer Configuration

In order to serve a wide range of applications, a variety of vibrometers are available. Single-point vibrometers measure at one location only, while full-field vibrometers measure a grid of measurement points upward to 1000s of locations.

A single-point vibrometer measures the vibration behavior of the test structure at a single laser spot location and in the direction of the laser beam. If the vibration vector is not parallel to the laser beam, the vibrometer will measure the component of the vibration vector that is projected onto the vector pointed along the direction of the laser beam. Complex structures move in multiple axes that need to be characterized with a 3D vibrometer. A 3D vibrometer, also called a tri-axial vibrometer, consists of three single-point vibrometers, which are pointing toward the same measurement location but at different angles. Using a coordinate transfer, the orthogonal x, y, and z vibration components can be calculated. Durability tests of small PCB-mounted components or bonding wires are a typical application for 3D vibrometry.

A rotational vibrometer measures the rotational dynamics of rotating objects (such as a shaft or a spindle). The rotational vibrometer consists of two vibrometers in parallel and is aligned perpendicularly to the rotation axis. This unique design measures RPM, dynamic angle, and angular velocity independent of the shape of the object or linear background vibration.

Full-field vibrometers measure a grid of points across a surface either sequentially using beam steering mirrors or simultaneously using a multi-sensor arrangement. In the case of a SLDV, a phase reference needs to be established to correlate the phase of the measurement points and to animate the deflection shapes. The phase reference can be the waveform driving the source of vibration, a voltage pulse from an impact hammer or a trigger signal. When working with complex structures, the SLDV requires geometry measurements for each point in the measurement grid. Alternatively, the SLDV can import a given mesh of points from a model and align itself with the coordinate system of the test structure. Maintaining a consistent coordinate system is critical especially when measuring an object from different sides and stitching scan data together.

11.5 Optimizing Setup and Test Parameters

Measurement quality and noise floor are directly related to the amount of return light captured by the vibrometer. This doesn't mean that measurements with low return light are invalid. Vibrometer accuracy is not affected by the amount of return light unless the SNR is low. Every vibrometer is equipped with a return signal indicator called RSSI (Received Signal Strength Indicator). During the measurement setup, it is advised to maximize the RSSI as a first priority. This can be done by properly focusing the beam, choosing an appropriate stand-off distance, and optimizing angle of incidence.

Figure 11.2 depicts a typical light scattering distribution on a rough surface. L_l is the incident light beam and the blue outline represents a typical light scattering distribution over all angles. As is obvious intuitively from Fig. 11.2, the preferred scattering direction (L_r) is at equal angle as the incoming beam. Measurements at an angle are possible with the IR vibrometer. However, a normal incidence provides the best SNR. All surfaces (including black surfaces) reflect light back. The following rule of thumb can be applied: if the laser spot can be seen by eye, the vibrometer is able to capture enough return light for a valid vibration signal in most cases.

The second priority of the setup is the optimization of the demodulation bandwidth. The demodulation bandwidth is directly correlated with the frequency range and the amplitude of the vibration. Minimizing frequency and velocity range on the demodulation side will automatically optimize the SNR.

Although laser light works well for vibrometry, speckle movement is a physical limitation that has to be considered when the test object exhibits large lateral movements. This is not a limitation of the vibrometer design but it is inherent for laser light scattering off a rough surface. For coherent light, constructive and destructive interference of reflected light generates a speckle pattern in the image plane. As the test object moves laterally, the speckle pattern moves as well, which can lead to temporary dropouts that manifest themselves as spikes in the measured vibration signal. In the early days of vibrometry,

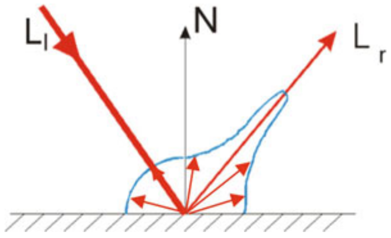

Fig. 11.2 Light scattering distribution on a rough surface

spikes in the velocity signal used to dramatically reduce the SNR, but current state-of-the-art technology doesn't exhibit dropouts for most applications. Polytec's upcoming generation of vibrometers will allow measurements without dropouts even under extremely challenging measurement conditions.

As mentioned above, measurement speed is affected by the number of required averages during the signal acquisition if a higher SNR is required. In order be able to minimize measurement time, let's first understand the contributing factors. The total scan time t is calculated in Eq. (11.2):

$$t = T * n_{\mathrm{p}} * n_{\mathrm{ave}} * \mathrm{OL} + t_{\mathrm{add}}, \tag{11.2}$$

where the variables are defined as

T length of one time record
n_{p} number of scan points
n_{ave} number of averages
OL overlap factor in percent (applies to frequency domain measurement only)
t_{add} additional time factors (scanner movement, software processing time, etc.)

T is determined by the required frequency resolution Δf of the test. The relationship is inverse proportional as shown in Eq. (11.3).

$$T = \frac{1}{\Delta f} \tag{11.3}$$

A high number of measurement points can be required for the validation of FE models. If the behavior is not known a priori when troubleshooting a part, the optimal number of points needs to be determined experimentally. Averaging helps lower the noise floor and thus improves the SNR but increases the measurement time. Optimizing the vibrometer configuration first will ensure best raw data quality and lessens the need for averaging. Additional time factors like the movement of the scanning mirrors and software processing can usually be neglected. Current scanning mirror technology allows for scanning up to 30 points per second. Completing scans of several thousand measurement points within a few minutes is possible, especially at high frequencies.

In a typical NDE scenario for measuring an ultrasonic traveling wave, scan grids using up to 1000s of points are often used. For a 100 kHz ultrasonic transducer, an FFT measurement with a frequency resolution of 10 Hz should be sufficient. Using five averages and a 50% overlap, the estimated measurement time is 500 s, which is equal to 8 min. In the case of a modal test of a large structure, 250 points are often sufficient. With a required frequency resolution of 1 Hz (e.g.) and five averages, the measurement time would be 10 min.

In contrast to scanning vibrometry, image-based techniques for capturing vibrations, like digital image correlation (DIC), capture the entire area at once. However, post-processing times can be significant. The displacement resolution of a DIC measurement depends on the field of view. In case the vibration amplitudes are in the μm range, DIC usually achieves sufficient SNR. However, DIC requires surface preparation with a speckle pattern to resolve deflection shapes. Importantly, the latest advances in vibrometry make it possible to measure successfully without any surface treatment.

11.6 Application Example 1: Modal Test on a Turbine Wheel [1]

During the design phase of turbine blades, a FE model is created using material parameters and boundary conditions. Once the first prototype is built, a modal test is performed allowing the design engineer to update the FE model. SLDVs provide the same high fidelity of FE modeling regarding the number of actual FRFs as the response can be measured at a high density of points. This eliminates the need for data interpolation. As laser Doppler vibrometry doesn't add mass to the structure, the measured frequency response functions (FRFs) represent the actual behavior of the blade and do not need to be corrected for any mass loading effects. The IR vibrometer is the ideal choice as no surface treatment is necessary for the measurement.

Figure 11.3 depicts a turbine wheel with 17 individual blades. The measurement grid was derived from the FE grid and coarsened to the necessary number or nodes for the test. As the wheel is lightly damped, accurate modal testing requires special care during the setup. Instead of attaching a shaker for excitation, an excitation method without mass loading is recommended. In this experiment an automated impact hammer from NV-Tech was used. The hammer head contained a

Fig. 11.3 Experimental setup of a 17-blade turbine wheel with PSV-500-3D SLDV

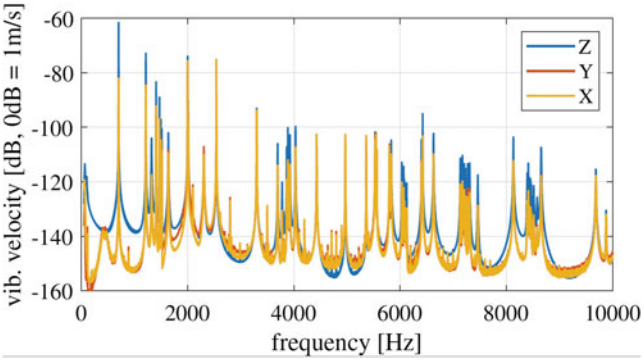

Fig. 11.4 Average FRF for *X*, *Y*, and *Z* across all measurement points

Fig. 11.5 Operational deflection shape (ODS) @ 700 Hz

force cell measuring the input force for each measurement point. Calculating the FRFs from the vibrometer response and the input force provides a normalized result. When exciting non-linear structures like composite panels or jointed structures, it is critical that the impact force is consistent during a scan such as to obtain high-fidelity FRF results and clean deflection shapes.

Figure 11.4 shows the average FRFs in the *x*, *y*, and *z* directions across all measurement points. The narrow resonance peaks are a clear indication of low damping. Figure 11.5 shows the deflection shape of the entire wheel at 700 Hz. The modal assurance criteria (MAC) in Fig. 11.6 confirm that there is a good correlation between simulation and measurement.

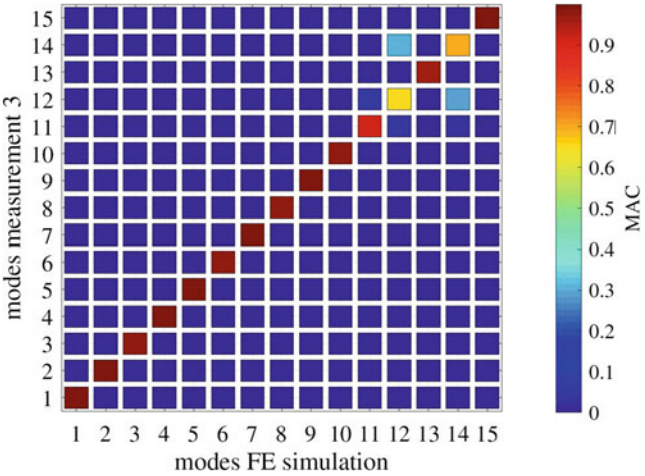

Fig. 11.6 MAC shows good agreement between model and test

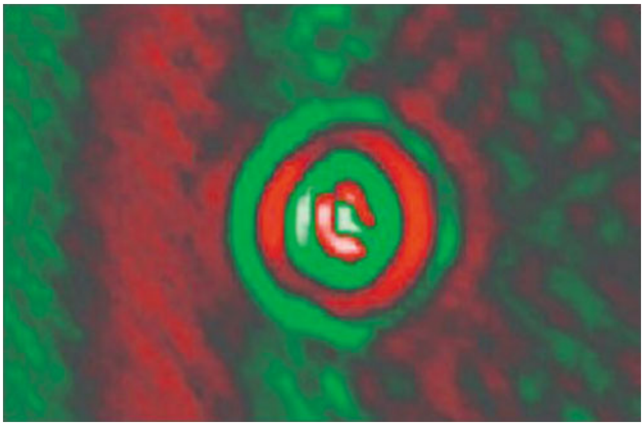

Fig. 11.7 Impact damage on composite panel, visualized by Lamb wave excitation using scanning vibrometry

11.7 Application Example 2: Traveling Ultrasonic Wave Analysis

Composite panels are used as lightweight materials for aerospace and automobiles. Defects on composite panels (like impact damage) weaken the structure, although the defect is not necessarily visible upon inspection by eye. For critical composite structures, sensor networks are embedded into the material for real-time monitoring. Understanding the ultrasonic wave characteristics is critical for accurate interpretation of the sensor data. Figure 11.7 shows the impact damage of a panel caused by a wrench being dropped on it. The defect was not visible by eye but could be visualized by capturing a Lamb wave traveling across the plate.

Figure 11.8 shows a side-by-side comparison of a measured and a simulated ultrasonic wave field across a thin metal plate. The simulated model was created by OnScale, the first cloud engineering simulation platform, combining powerful multiphysics solver technology with the limitless computational power of cloud supercomputers. Zooming into the area of the hole in the center of the plate (Fig. 11.9) shows that the ultrasonic wave is perturbed by the presence of the hole. The wave-hole interaction is weak because the wavelength of the ultrasonic wave is quite a bit larger than the diameter of the hole.

In another example, a traveling wave was measured across an aluminum plate that had a crack machined in the back side (Fig. 11.10). This measurement allowed the prediction of the wave-crack interaction based on crack length and orientation as can be seen in Fig. 11.11.

The IR SLDV is the best choice for these measurements to improve surface reflectivity. Since the surface displacements can be very small (order of nm), it is critical to set up the vibrometer for best SNR.

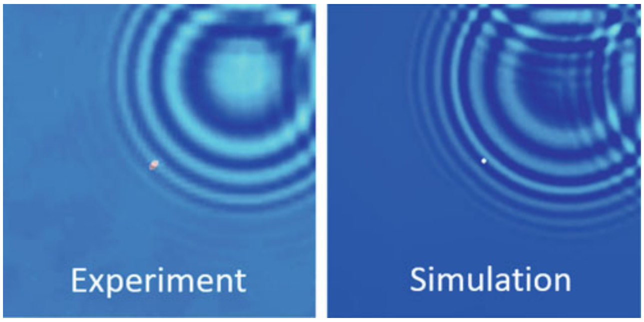

Fig. 11.8 Traveling ultrasonic wave visualization. Measured response (left) vs simulation by OnScale (right)

Fig. 11.9 Zoomed in area demonstrating wave interaction with the hole in the center of the plate

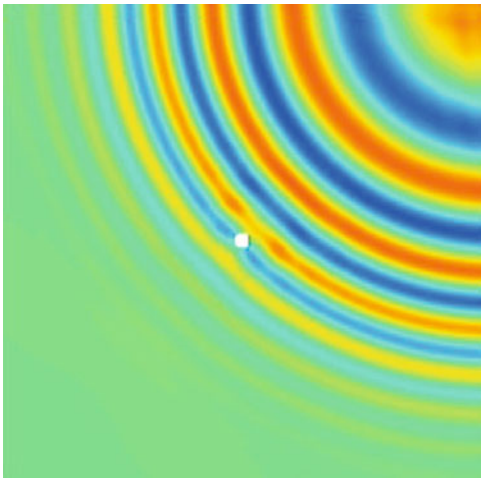

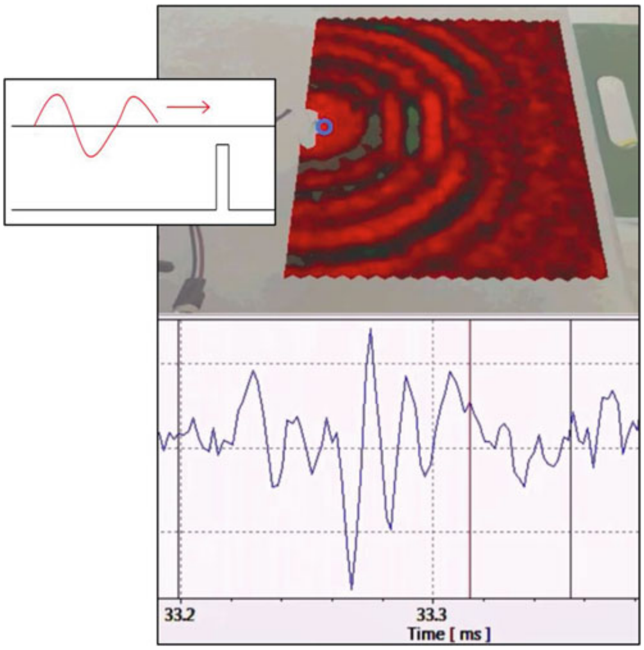

Fig. 11.10 Traveling wave measurement across aluminum plate with crack on opposite side

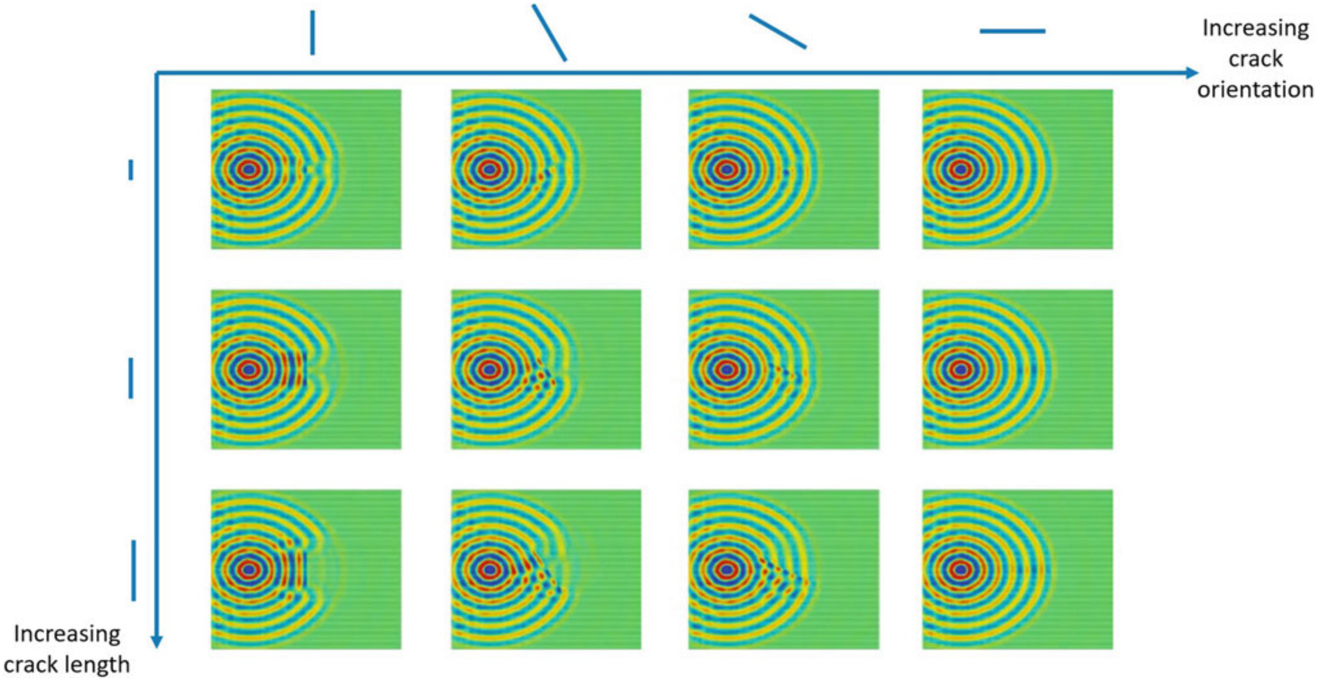

Fig. 11.11 Traveling wave measurement on hidden crack, as simulated by OnScale, allows simulation of various crack configurations

Fig. 11.12 Instrumented turbine blade (courtesy of Vrije Universiteit Brussel, S. Vanlanduit)

11.8 Application Example 3: Dynamic Stress and Strain Characterization [2, 3]

Three-dimensional SLDV data can be used to validate durability simulation models. Determining the location of the maximum stress is essential for the life time of components. In aerospace, turbine blades are conventionally instrumented with strain gauges (Fig. 11.12) in order to validate strain and stress models and for performing fatigue tests. In contrast to gluing strain gauges to the blade, non-contact vibrometer data can be used to obtain the dynamic strain distribution. As in the case of FE model validation, measuring without contact allows for a direct measurement of the response without having to correct for any mass loading effects.

Because of a small laser spot diameter (25–80 μm depending on stand-off distance) and very accurate beam positioning mechanics of the 3D SLDV, a deflection shape with high spatial density can be measured. By extracting the localized in-plane vibration component, strain values can be calculated for groupings of adjacent points. Overlaying the obtained strain values

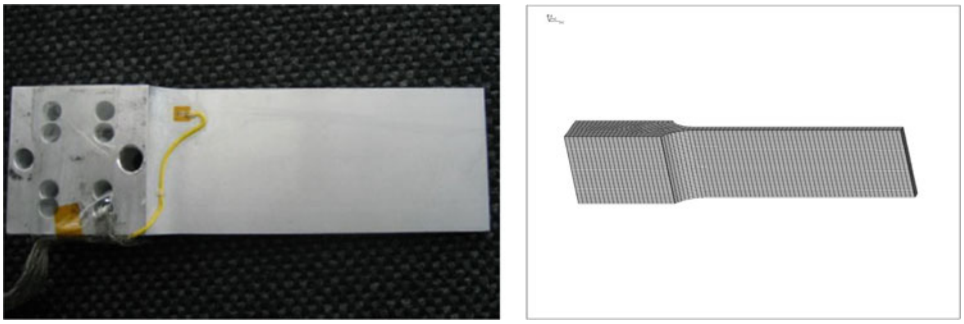

Fig. 11.13 Cantilever sample (left) and the corresponding model (right)

with an image of the part allows for the visualization of a strain distribution across the object surface. Linear as well as shear strain can be obtained. From the material properties, stress distributions can be calculated as well.

For strain measurements, exact overlap of the three laser beams is crucial. For that reason, alignment aides (like the machine vision procedure VideoTriangulation) are available to the user to ensure adequate spot overlap and thus reliable vibration data for the strain calculation. Equally important is the accuracy of the geometry measurement as the distance between adjacent measurement locations factors into the strain equation.

Figure 11.13 shows the image of an aluminum cantilever beam and the corresponding simulated model. The simulation was performed in a tool called Calculix by Klaus Wittig and measured under shaker excitation using a chirp signal. Strain and stress distributions of that beam are shown in Fig. 11.14 and compared with simulation. The quantitative comparison with a strain gauge (mounted on that cantilever beam at a few select locations) shows good agreement as shown in Fig. 11.15.

11.9 Conclusion

Scanning laser Doppler vibrometry (SLDV) is a unique measurement method that is used across a wide range of industries for FE model validation, NDE, troubleshooting, performance validation, quality control, or just basic research. The versatility of SLVD is evident when considering the myriad of applications for characterizing structures. This includes very large structures down to microscopic ones, frequency ranges from quasi-DC up to GHz, surfaces that are shiny or a dark, hot or cold objects, curved or flat structures, or from close up or far away. As discussed in this tutorial, choosing the correct vibrometer configuration is critical for obtaining accurate measurement data and fast, effective results.

Polytec offers PolyLab educational program free of charge with the goal to enable students to learn concepts such as vibration testing and modal parameters (natural frequency, damping, and mode shapes) and much more in a fun and exciting experiment. Learn more at www.polytec.com/us/polylab.

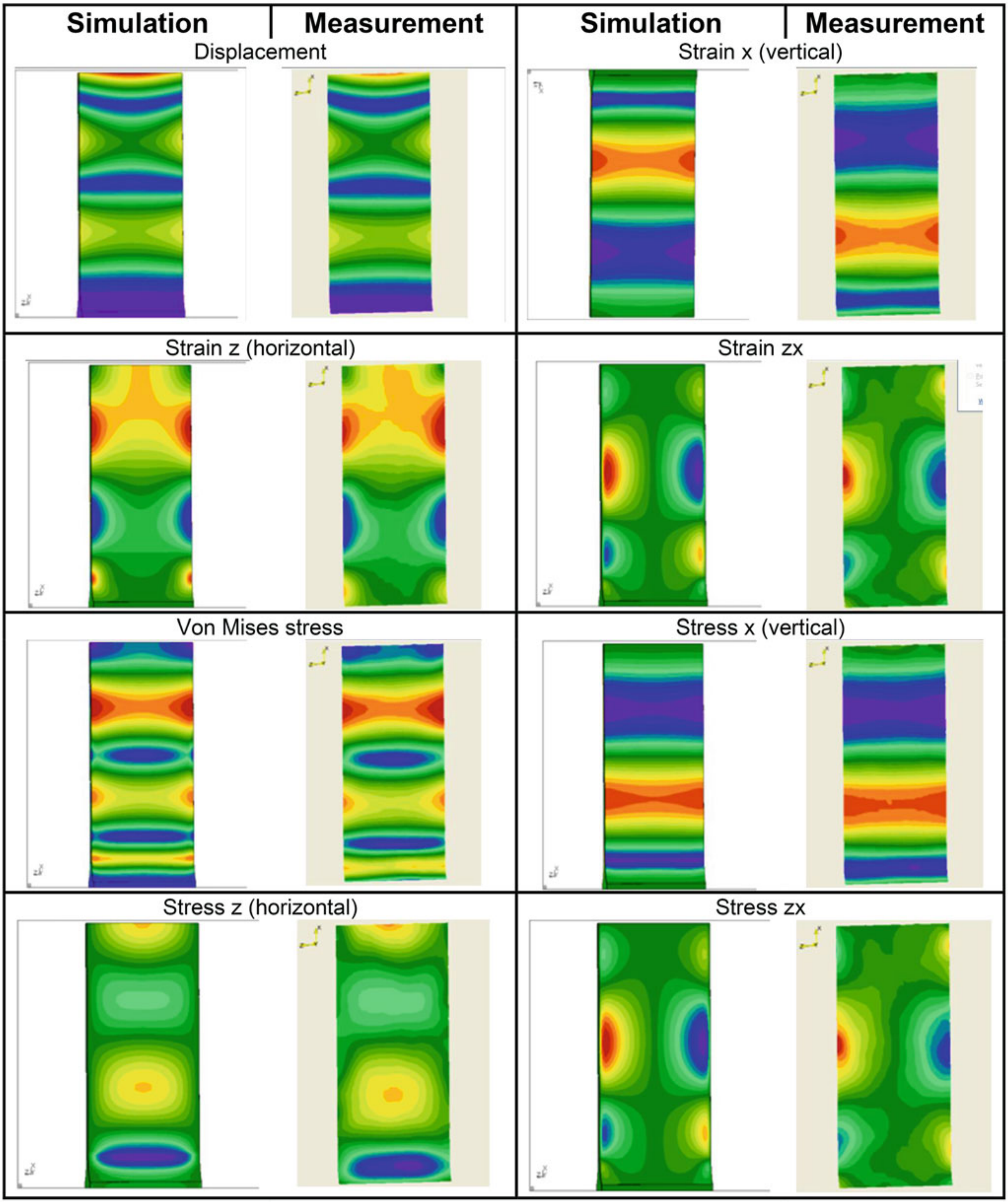

Fig. 11.14 Stress comparison of FEM and test

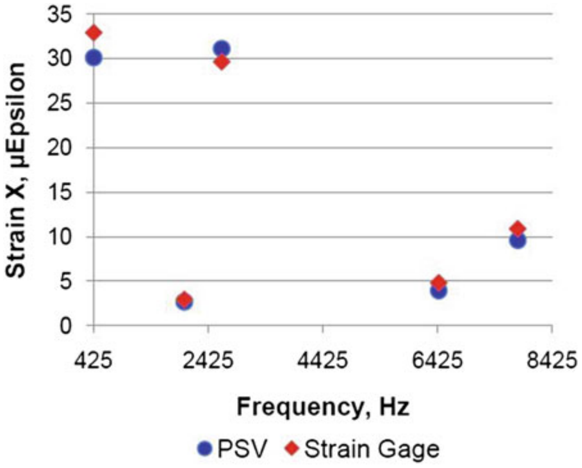

Fig. 11.15 Quantitative agreement of strain gauge data and vibrometer-based test results for a few select locations on the cantilever beam

References

1. Buchwald, P. et al.: Experimental and Numerical Modal Analysis of an Axial Compressor Blisk, APVC Sydney (2019). https://doi.org/10.1007/978-3-030-48153-7_48
2. Weisbecker H., Cazzolato, B.: Surface Strain Measurements Using a 3D Scanning Laser Vibrometer (2010). https://doi.org/10.1007/s11340-011-9545-5
3. Reyes, J., Avitabile, P.: Use of 3D Scanning Laser Vibrometer for Full Field Strain Measurements. https://doi.org/10.1007/978-3-319-15236-3_19

Chapter 12
Effect of Different Test Setup Configurations on the Identification of Modal Parameters from Digital Image Correlation

L. Marchetti, D. Mastrodicasa, E. Di Lorenzo, S. Manzato, L. Bregant, B. Peeters, and P. Lava

Abstract Over the past few years, the application fields for digital image correlation (DIC) have significantly broadened and are now extensively used not only for material characterization and deformation analysis but also for vibration and dynamic testing. The key advantage over more traditional technologies such as accelerometer- or laser-based measurement is the fact that all points of interest can be measured at once or over a limited number of repetitions without mass loading the structure or having to deal with complex cabling scenarios. While qualitative analysis, such as operational deflection shapes, proved to be very successful and straightforward, performing classical modal analysis on frequency response functions between a load cell signal and the deformations obtained by applying digital image correlation still requires extra care when setting up the experiments. In this paper, the effect of different cameras, camera settings, excitation levels, and speckle pattern on the modal parameters of a simple plate structure will be investigated and compared with classical acceleration measurement. The results will also be compared with numerical simulations where the accuracy of the mode shapes can be easily and quantitatively assessed.

Keywords Digital image correlation · FRF testing · Speckle patter · Modal analysis

12.1 Introduction

Nowadays, testing and validation for mechanical numerical models are mostly performed using a discrete number of transducers (e.g., accelerometers, strain gauges, fiber optics, etc.), which can only provide measurements at finite locations. Moreover, on lightweight structures, the accelerometers might impact the measurement because of mass loading. For these reasons there have been a growing research and industrial interest in contactless measurement technologies. Laser Doppler vibrometry is a quite established solution [1], but recently techniques based on images are attracting more and more interest and digital image correlation (DIC) in particular has recently received special attention in the structural dynamics field as a full-field measurement technique [2, 3]. In particular, DIC for vibration analysis is mostly performed on aerospace and automotive components [4–8] and rotating structures [9] like turbine blades [10] and helicopter rotors [2].

If the structure's high frequency behavior is investigated, high-speed cameras are needed in order to respect the Nyquist-Shannon's theorem. The principal drawback is that high-speed cameras present lower image resolution, which limits the

---

L. Marchetti
Siemens Digital Industries Software, Leuven, Belgium

Department of Mechanical Engineering, Università degli Studi di Trieste, Trieste, Italy

D. Mastrodicasa
Siemens Digital Industries Software, Leuven, Belgium

Acoustic & Vibration, Vrije Universiteit Brussels, Brussels, Belgium

E. Di Lorenzo · S. Manzato (✉) · B. Peeters
Siemens Digital Industries Software, Leuven, Belgium
e-mail: simone.manzato@siemens.com

L. Bregant
Department of Mechanical Engineering, Università degli Studi di Trieste, Trieste, Italy

P. Lava
MatchID, Ghent, Belgium

D. Di Maio, J. Baqersad (eds.), *Rotating Machinery, Optical Methods & Scanning LDV Methods, Volume 6*, Conference Proceedings of the Society for Experimental Mechanics Series, https://doi.org/10.1007/978-3-030-76335-0_12

vibration amplitude that can be measured. Higher resolution is usually available on lower-speed camera, so depending on the application, a compromise between speed and quality must be sought. The solution that allows to analyze high-frequency vibrations with high-quality images is the under-sampling technique [11, 12]. With this method it is possible to overcome the low sampling rate of high-resolution cameras by under-sampling and remapping the time histories to measure above their Nyquist frequency.

To measure FRFs, the camera images need to be perfectly synchronized with the excitation force and time-stamped using the same clock. This can be achieved by using external triggers on the camera, using external absolute clocks or by using reference signals that can be later on used to align the images with the samples acquired by the main data acquisition system. With the cameras used in this paper, using alignment with an artificial signal was the only option available.

In this paper DIC technique is used to get the full-field displacement time histories of three metal plates. These data are then processed and analyzed in order to obtain the FRFs and modal parameter [13] and will be validated against results from standard accelerometer measurements. The effect of different test setup configurations on the FRFs and modes will be investigated. In particular, the influence on results of the type of excitation used, the number of averages used for the calculation of FRFs, the frequency resolution, and the kind of speckling used on the plates will be evaluated.

12.2 Aliased Acquisition with Low-Speed Camera

In this study, the measurements were performed using two FLIR Blackfly S USB3 5 MP cameras, running at a max of 75 fps at max resolution. The measurements were also performed by directly streaming the images to the PC; this has the advantage that the images are already available, but if no dedicated is available, the camera speed is limited to max 25 fps because of the limited data transfer capacity of regular USB3 ports. Since the structure has been excited using periodic chirp and pseudo random signals having a maximum frequency higher than the camera frequency, the reconstruction technique is used.

This method is based on the requirement that the signal analyzed for the reconstruction must be periodic; under this assumption, it is possible to reconstruct it at a lower frequency using signal aliasing. The process is illustrated in Fig. 12.1. To measure the signal in blue in the left plot, at a frequency $f = f_{\text{signal}}$, a signal at sampling frequency $f_{\text{sample}} < f_{\text{signal}}$ can be used (purple signal in the center). This signal's frequency f_{r} is related both to f_{signal} and f_{sample}, and it is equal to:

$$f_r = f_{signal} \cdot f_{sample} \cdot \left(f_{sample}^{-1} - f_{signal}^{-1} \right) \tag{12.1}$$

The reconstructed signal has the same shape of the original signal, but it is scaled along the time axis. The purple signal is described by the equation:

$$S_r(t) = S_{signal} \cdot \left(\frac{f_r}{f_{signal}} \cdot t \right) \tag{12.2}$$

Using Eq. (12.2) it is now possible to obtain Eq. (12.3) and to reconstruct one period of the desired signal, as shown in Fig. 12.1 (right).

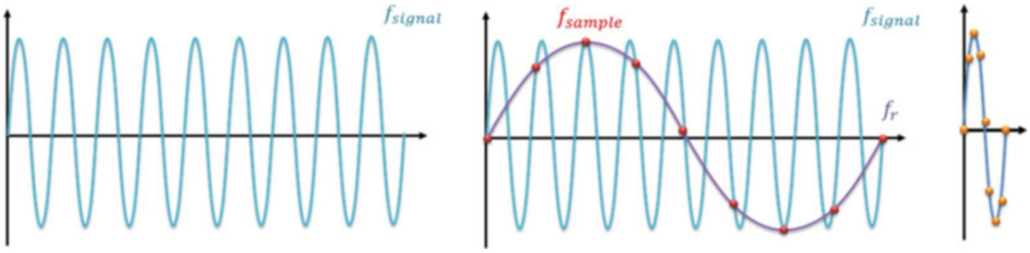

Fig. 12.1 Signal reconstruction process: (left) original signal; (center) original and sampled signal; (right) reconstructed signal

$$S_{artif}(t) = S_r \cdot \left(\frac{f_{signal}}{f_r} \cdot t \right) \tag{12.3}$$

Using this principle, it is possible to sample a very high-frequency signal with cameras operating at a low sample rate and then reconstruct it after the measurement. The main drawback of this approach is that the duration of the test is much longer than when using high-speed cameras, as the signal must be repeated until all samples to reconstruct the original signal have been acquired.

12.3 Experimental Setup

12.3.1 Test Item

The objective of this study is to perform a full-field modal analysis on a metal plate estimating FRFs using DIC. Since the effects of the test setup configurations are important to compare the influence of the different speckles, three different plates have been used. The original idea was to have three identical plates and to compare the results obtained on different plates using different settings. A big plate was then cut to obtain three plates with the same dimension (327 mm × 273 mm × 0.8 mm). However, as it will be shown later, the plates were hand-cut, resulting in local plastic deformations that influenced the structural properties of each one. Consequently, the analysis will be run on each of the three plates independently, and no-cross comparison, as was originally foreseen, can be performed.

Different speckle patterns were applied on the surface of each plate, as shown in Fig. 12.2, in particular:

- Plate 1: paint was sprayed on the plate and then dots were drawn with a pen.
- Plate 2: dots were printed on A4 paper. Then the plate was speckled using these A4 paper sheets glued on it.
- Plate 3: paint was sprayed on the plate and then dots were drawn with a pen on half plate. On the other half, speckle printed on paper has been glued.

12.3.2 FRF Testing

For each plate, reference properties were estimated by measuring FRFs using a shaker excitation at the center point of the plate before the speckle pattern was applied. The sensor setup is shown in Fig. 12.2, where the two accelerometers corresponding to the orange dots and the impedance head by the blue one are displayed on the three plates. The driving point FRFs measured on the three plates are shown in Fig. 12.3. As already mentioned, the three plates show a significantly different behavior in the complete frequency range. Due to the low weight and small thickness, even small differences cause significant effects on the natural frequencies, making it impossible to quantitatively compare the results between the three plates.

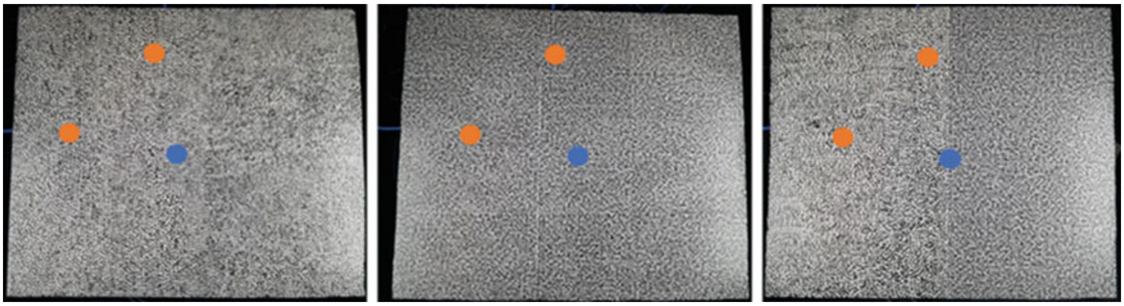

Fig. 12.2 Speckled plate. (Left) Plate 1 with painted speckle. (Center) Plate 2 with printed speckle. (Right) Plate 3 with half painted and half printed speckle. The blue dot indicates the excitation location (with impedance head), while the orange dot indicates response measurement locations with accelerometers

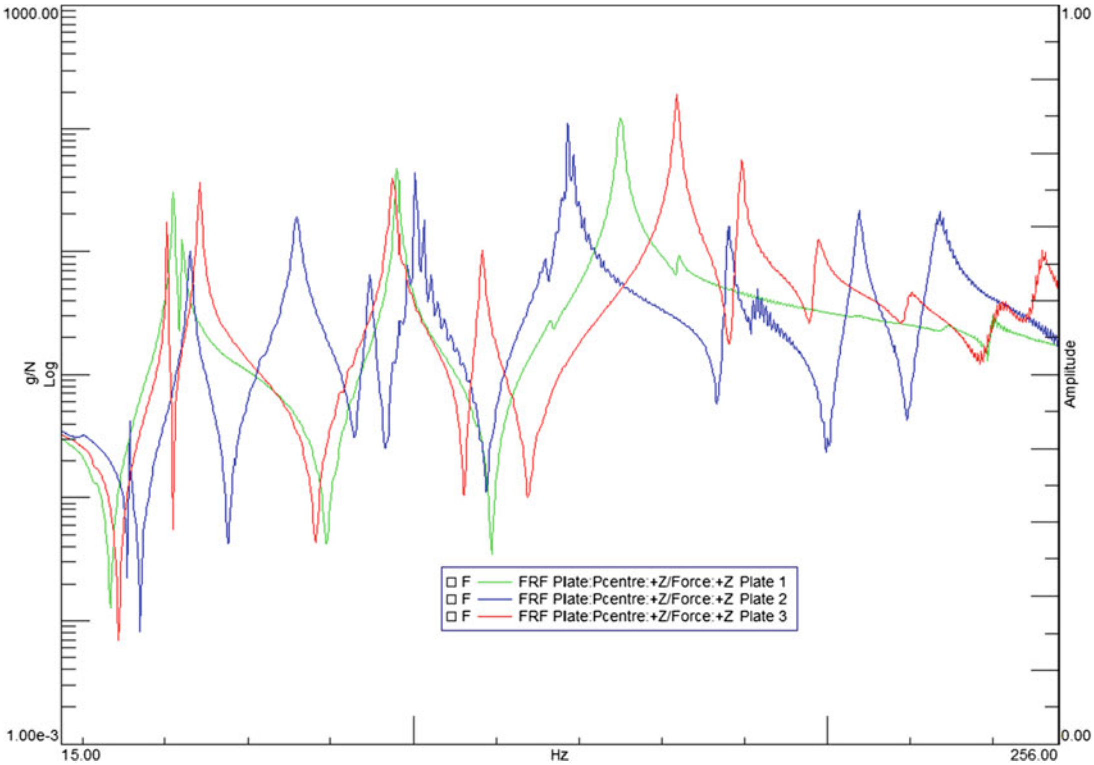

Fig. 12.3 Driving point FRFs measured on the three plates

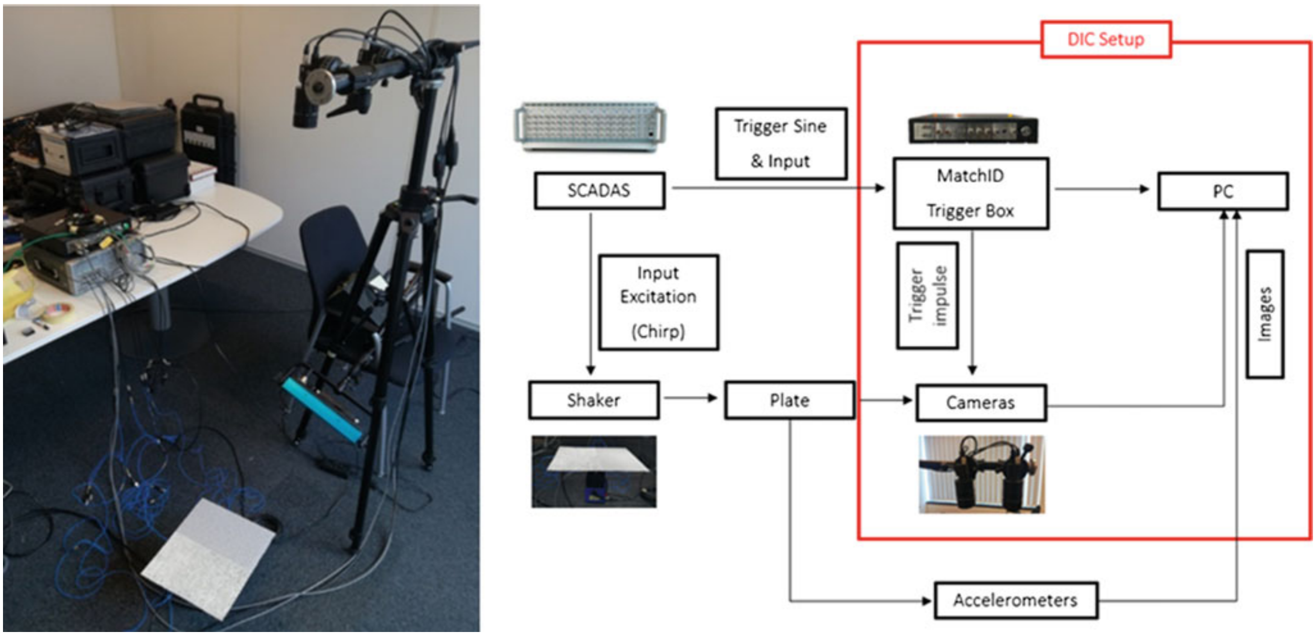

Fig. 12.4 Experimental setup with a schematic description of the connection between the different elements

12.3.3 *Camera Setup/Measurement Chain*

The experimental setup is shown in Fig. 12.4. The plate was excited using a shaker positioned at the center of the plate, while the response was captured using a pair of DIC cameras in a stereo configuration and three accelerometers placed under the plate.

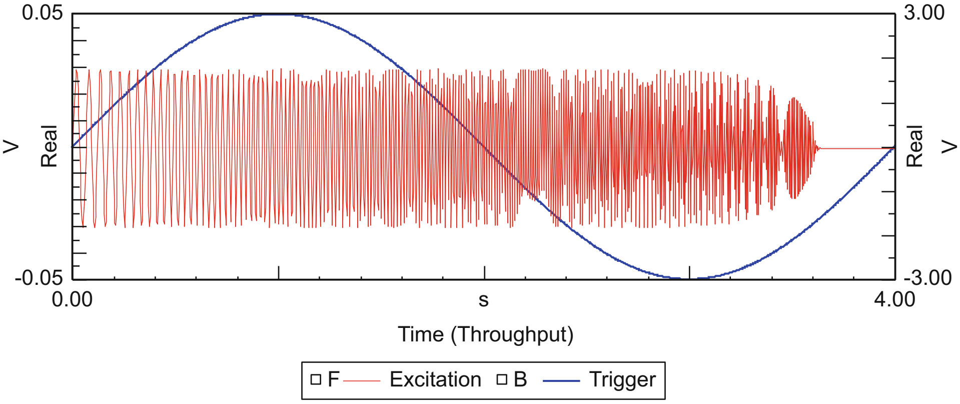

Fig. 12.5 Example of an excitation (chirp) and trigger signals

Table 12.1 Overview of excitation profiles

Technique	Pro	Cons
Chirp	Easy, quick test	Results not good
Pseudo random	1 realization, repeatable	More deterministic
Pseudo random averages	Repeatable, averages	More deterministic

The cameras were triggered by the MatchID TriggerBox, while the shaker was driven by the DAC of a Simcenter SCADAS that was also used to record the force and acceleration signals from the sensors. A reference signal was exchange between the two systems to synchronize the acquisition.

The DAC module of Simcenter SCADAS is used to generate two signals. One is used to excite the structure and must be a stationary and periodic signal. In this study, both chirp and pseudo random signals were used Table 12.1. The second generated signal is a sync signal, which is sent to the Triggerbox and used as a trigger. This is typically a sine whose period spans an integer number of excitation blocks. An example of these signals is shown in Fig. 12.5. The sine signals can then also be used to align the samples acquired in the two systems before applying post processing.

12.4 Results

In this section, the different experiments and the corresponding results will be presented. As the main objective is to assess the quality of the FRFs measured with DIC, the results will be compared with the FRFs obtained with the accelerometers in Fig. 12.2. In both cases, the FRFs are computed using the force signal measured with the load cell at the interface between the shaker and the plate.

The first goal is to find the excitation profile that gives the best results in terms of system's response, by comparing the DIC FRFs to those calculated using accelerometers. The second is to tune the level and bandwidth of the excitation to have displacements which are big enough for the cameras, but without overexciting the system.

12.4.1 Type of Excitation

The experiments started on plate 2 (the plate with the printed speckle pattern). The first excitation was a chirp of 4 s in the bandwidth of 15–128 Hz. At the same time, a sine with the same period of 4 s was sent to the TriggerBox to provide the timing for the aliased acquisition and the following reconstruction. The FRFs obtained with DIC identify the peaks correctly, but the magnitude and in particular the phase are noisy, due to the fact that no averaging is performed. Figure 12.6 shows the FRF calculated at the center point of plate 2 in red.

In order to improve the results, a pseudo random signal of 5.12 s and bandwidth 15–100 Hz was used. Also in this case, 1024 images were acquired to reconstruct the signal. The resulting FRF at the center point is now displayed in blue in

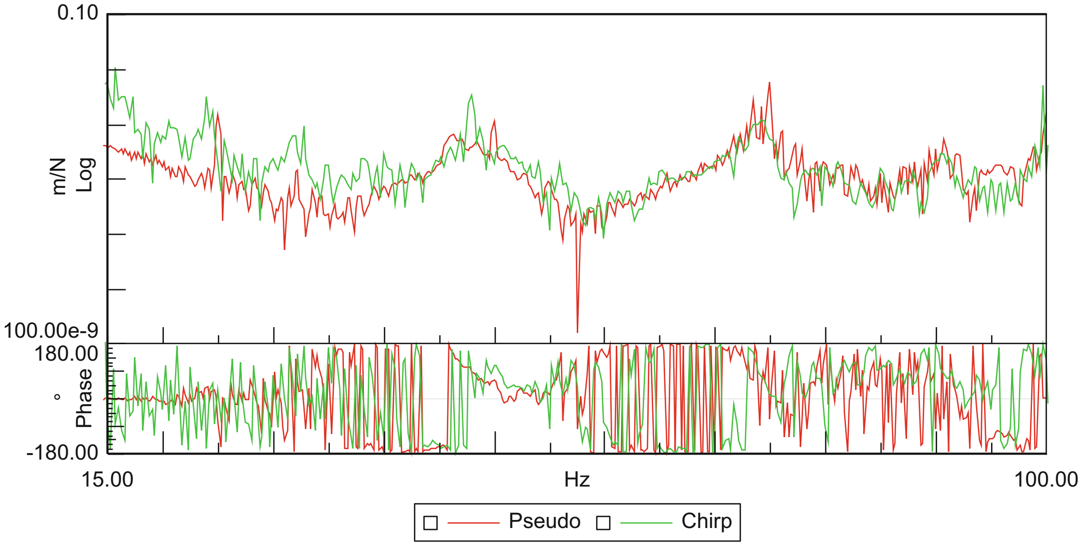

Fig. 12.6 FRF measured at the center of plate 2 with DIC for different excitations: Chirp (red) and pseudo random (blue)

Fig. 12.6. While the FRF remains noisy, the peaks are correctly captured, and, most importantly, the phase is more stable at lower frequencies. Because of the enhanced properties of a pseudo random signal (controlled amplitude and phase in the generation of the signal and inherently periodic excitation) versus a chirp, this was chosen as the reference excitation profile for the remaining of the investigation.

12.4.2 Number of Averages

The FRFs shown in Fig. 12.6 clearly show that averaging is required to further minimize noise and ensure that modal analysis can correctly extract the modal parameters from the data. As one of the limitations of DIC is the computational effort required to process the images, the effect of averaging was performed by fixing the number of images to 1024 and using the available samples to describe more cycles. The following tests were performed:

- One average with a block of 5.12 s, bandwidth 15–100 Hz, and resolution of 0.195 Hz.
- Two averages with block of 2.56 s, bandwidth of 15–100 Hz, and resolution of 0.391 Hz.
- Four averages with block of 1.28 s, bandwidth of 15–100 Hz, and resolution of 0.781 Hz.

The results of the different test will now be assessed in terms of modal parameters. Hence, they will be compared with the results obtained by processing the accelerometers' FRFs. To ensure consistency, the accelerometers were always attached to structure during the whole experimental campaign.

Figure 12.7 shows the stabilization diagram obtained by processing the FRFs with, respectively, two and four cycles. The case with only one cycle was not displayed as the results were noisy, and to identify the modes of interest, a very high model order had to be specified. The picture shows how the stabilization diagram built from the four averages FRFs is much cleaner than the other, allowing to correctly identify the five modes expected in this frequency region. While the same modes could be identified also using only two averages, the model order had to be doubled, and many more spurious poles could be observed. Although not reported here, the FRFs obtained by averaging 4 times had a much cleaner phase relation in the frequency range of interest.

.

The frequency and damping of the identified modes in the three DIC scenarios are compared in Table 12.2 with those obtained by processing the accelerometer FRFs. The results obtained with the four averages FRFs are those that best match the one from the accelerometers, which are considered here the reference. It can be then concluded that, as expected, sacrificing frequency resolution for a higher number of averages can significantly improve the quality of the estimated modal parameters. While for the first four modes the damping is accurately estimated, for mode 5 it is significantly underestimated if compared to the one obtained from the accelerometers. This is expected as the FRFs at higher frequency are still noisy,

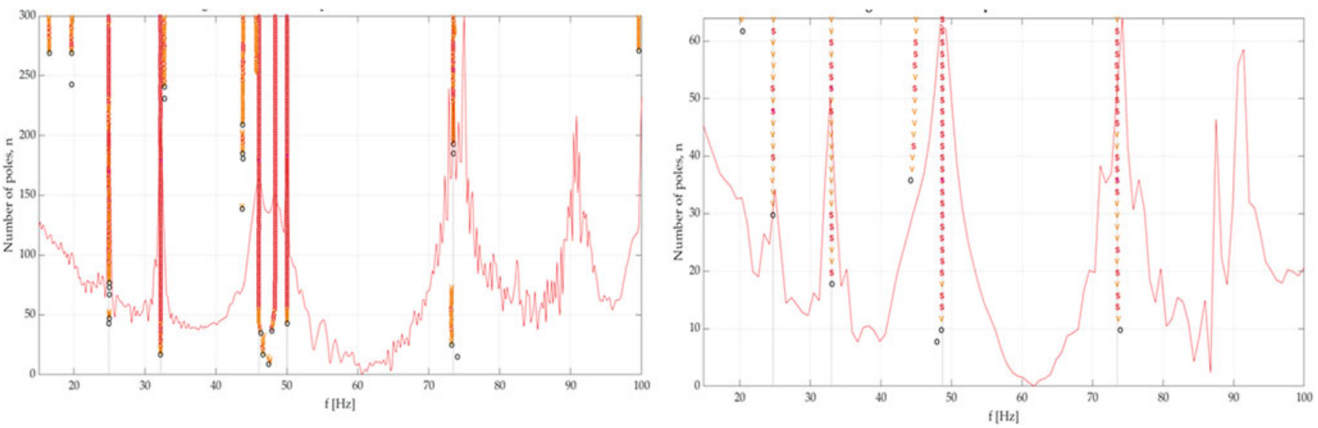

Fig. 12.7 Stabilization diagram built on the FRFs from the two cycles (left) and four cycles (right) test

Table 12.2 Comparison of modal parameters from accelerometer and DIC FRFs

Modes	Accelerometers		DIC 4 cycles		DIC 2 cycles		DIC 1 cycle	
\	f_n [Hz]	$d\%$	f_n [Hz]	$d\%$	f_n [Hz]	$d\%$	f_n [Hz]	$d\%$
1	24.2	1.02	25.1	1.02	25.7	0.10	20.8	1.17
2	31.7	0.15	32.0	0.11	32.6	0.13	33.3	0.08
3	47.1	1.89	47.1	1.41	48.0	1.36	46.1	1.29
4	73.8	0.52	73.8	0.52	74.2	0.15	77.5	0.05
5	89.5	0.49	91.4	0.07	92.1	0.03	92.2	0.05

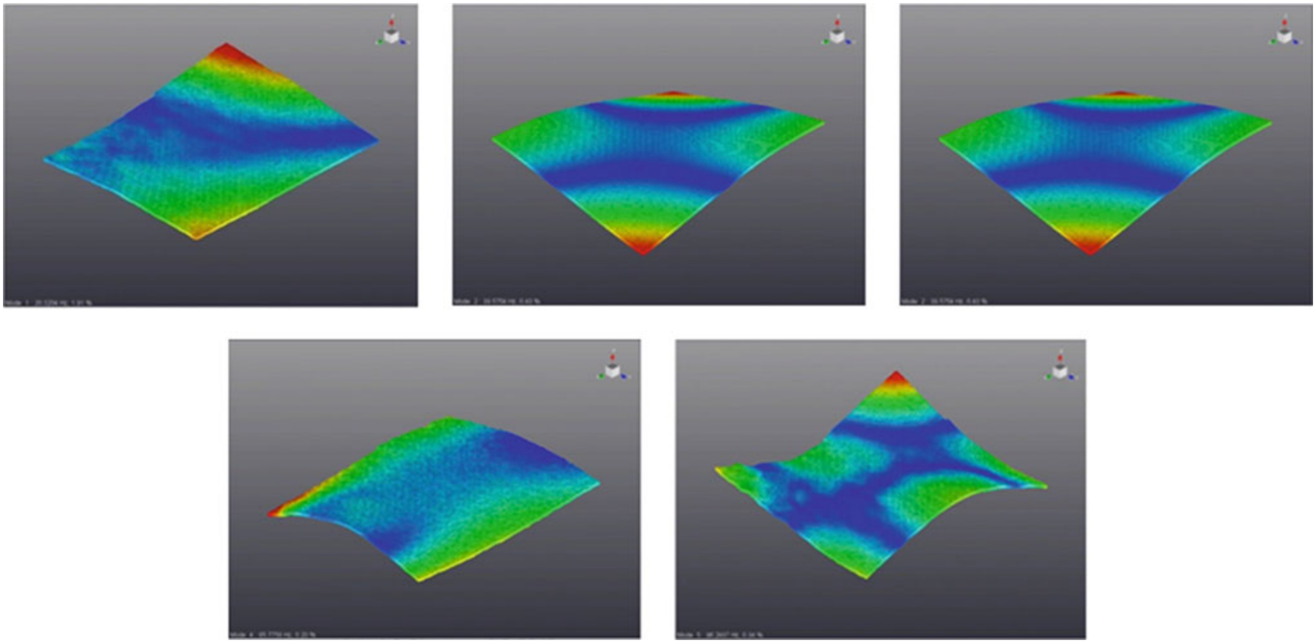

Fig. 12.8 Identified mode shapes for the five resonances identified in the frequency range of interest

affecting the stability of the estimation and causing the damping to be underestimated. The identified shapes for the four averages case are shown in Fig. 12.8.

A further validation of the obtained results can be obtained by comparing the DIC FRFs directly with the ones measured with the accelerometers. The DIC FRFs have been extracted trying to match the locations of the accelerometers and impedance head as shown in Fig. 12.2. As DIC usually extracts the displacements, after calculating the FRF, they have been differentiated twice to extract the corresponding accelerations. The results are shown in Fig. 12.9. The point which shows the best agreement between the two measurement techniques is point 2, which is the point at the center of the plate. The main

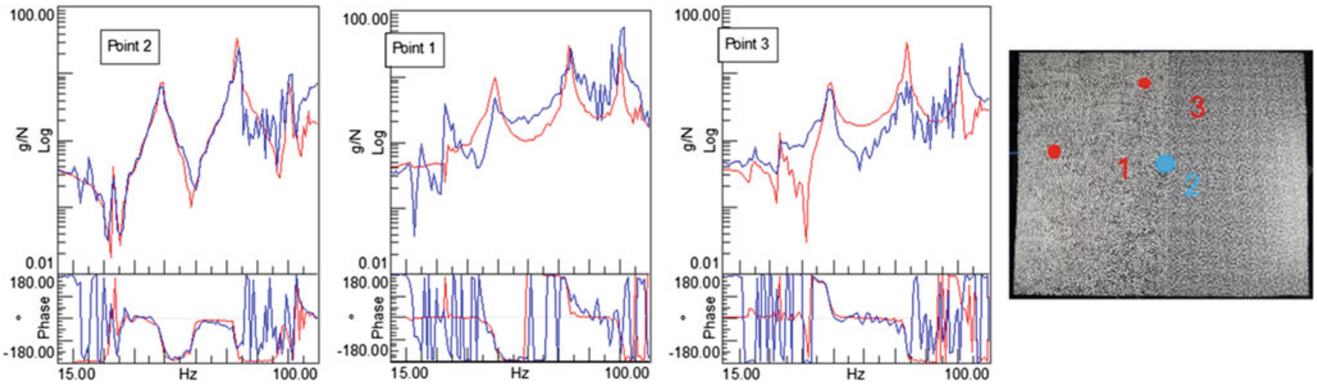

Fig. 12.9 Comparison between DIC (blue) and accelerometer (red) FRFs. Point locations on the plate are shown in the right

Table 12.3 Accelerometer vs DIC modes for plate 3 between 100 and 400 Hz

Modes	Accelerometers		DIC	
\	f_n [Hz]	$d\%$	f_n [Hz]	$d\%$
1	112.9	0.41	115.0	0.44
2	127.9	0.73	127.5	0.66
3	160.9	0.45	160.6	0.24
4	175.6	0.43	176.2	0.95
5	196.6	0.40	197.9	1.17
6	211.9	0.62	/	/
7	231.2	1.59	235.8	0.01
8	246.5	0.36	252.0	0.17
9	301.7	0.29	301.0	0.13
10	321.8	1.56	316.8	0.69
11	338.9	0.74	338.2	0.52
12	368.9	0.46	372.5	0.08

peaks match with those obtained from the accelerometers, both in frequency and in amplitude. In between resonances, the FRF is noisier, but this is limited impact in a modal analysis context. On the other points, while the peaks still align in terms of frequency, the amplitude shows some deviation and the response is generally noisier.

12.4.3 *Extended Frequency Range*

While testing plate 3 (half painted and half printed speckle), the excitation range was extended to 400 Hz to see whether the cameras could still capture displacement at these higher frequencies. To compensate for the quadratic decrease of displacements as the frequency increases, the excitation level had to be slightly increased compared to the previous test. Additionally, it was observed that if the excitation was applied in the whole range, from 15 to 400 Hz, the lower-frequency response was masking the dynamics above 100 Hz, with very noisy responses and response levels below the noise floor of the cameras. It was then decided to limit the excitation from 100 to 400 Hz, since the dynamics at lower frequencies have been already analyzed. This allowed to decrease the noise floor for the cameras, ensuring a better dynamic range in this frequency region. In total, 11 modes out of the 12 identified with the accelerometers were extracted, with damping values reasonably matching the reference ones. Table 12.3 gives a comparison of the frequency and damping extracted with the two methods, while Fig. 12.10 shows some of the shapes identified. In particular, the modes shapes extracted at all points (approx. 9000) allows to visualize the deformation shape very accurately, with a spatial resolution that would be nearly impossible to achieve with accelerometers.

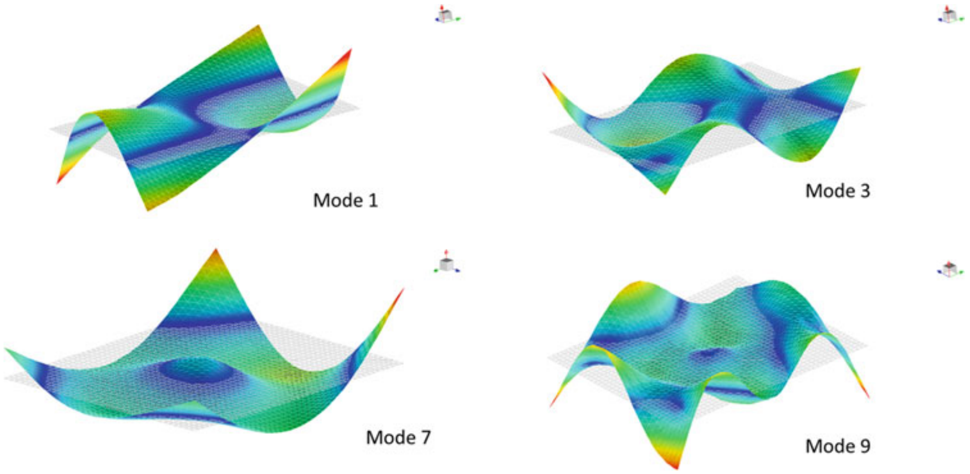

Fig. 12.10 Deformation shapes for some of the modes in Table 12.3

Table 12.4 Effect of speckle pattern on modal parameters of plate 3

Modes	Frequency			Damping		
\	No speckle	Paint	Paint + paper	No speckle	Paint	Paint + paper
\	[Hz]	[Hz]	[Hz]	%	%	%
1	40.5	39.2	39.1	0.1	0.04	2.91)
2	48.5	47.7	47.2	0.61	0.81	1.39
3	94.9	93.1	92.7	0.32	0.22	0.31
4	116.6	112.9	112.8	0.42	0.41	0.35
5	130.6	127.9	127.0	0.61	0.73	0.60
6	163.7	160.9	160.8	0.29	0.45	0.52
7	179.1	175.6	174.6	0.20	0.43	0.47
8	197.6	196.6	196.1	0.43	0.40	0.56
9	219.4	211.9	212.3	0.63	0.62	0.65

12.4.4 Effect of Speckling the Surface

Speckling the surface of a specimen could affect the structure's response, in particular if the object is light and thin like these plates. In order to evaluate the impact of the speckle, natural frequencies and damping have been identified on each plate before and after applying the speckle pattern. The analysis was carried out, in this case, using the FRF measured from the accelerometers. The locations of the accelerometers and the layout of the cables were carefully controlled between the different experiments, to limit as much as possible the impact of these factors on the results.

The results obtained on plate 3 are shown in Table 12.4. The table shows the results of modal analysis on FRF acquired before any speckles was applied, after applying the layer of paint and finally after gluing the printed speckles on half of the plate. By looking at the frequencies, it can be observed that adding more and more layers consistently decreases the estimated natural frequency, as expected when increasing the mass of the structures. In this case, where the plate was very light, this can cause natural frequency to shift 3–4 Hz for modes 4 and 5. Such variations are in line with the effect of adding locally few grams of mass on an FE model with equivalent properties.

For damping, in general it can also be observed that damping increases as the added material increases. Also in this case, however, the impact of adding accelerometers and cables on lightweight and lowly damped structure would cause similar variations. Similar trends were observed on the other two plates as well, so the results are omitted.

12.5 Conclusion

In this paper, the use of DIC for modal analysis is investigated. Different experiments were performed on a set of lightweight aluminum plate mounted on a shaker to analyze the effect of different setup and measurement options on the results.

First of all, it was observed that the type of excitation and the number of averages have a significant impact on the quality of the measurement and the FRFs. When using the aliased acquisition with low-speed cameras, it is of paramount importance that the excitation and response are as consistent as possible throughout the test. Using deterministic and controlled excitation such as pseudo random (multisine) profiles can significantly improve the quality of the data. Another important element is the number of averages to reduce noise. Finding the right balance between number of averages and computational time required for the DIC processing is important, but in general it was concluded that some compromise can be taken on the frequency resolution to obtain higher-quality data and more accurate modal estimates. When designing the experiment, the frequency range of interest was also shown to have an impact on the results. In general, it is suggested to repeat the test in different bandwidths, possibly progressively increasing the level to compensate for the lower displacement level at higher frequencies and avoid that low-frequency responses dominate the behavior at higher frequency.

Finally, applying speckle pattern on such a low weight structure was shown to have a limited impact on the results. Natural frequencies decreased due to increased mass and damping increased because of the extra layers of material applied, but these variations are in line with those caused by local accelerometers and cables.

References

1. Phillip, L., Reu, L., Rohe, D. and Jacobs, L.: Stereo-DIC vs 3D scanning LDV for modal. *Sandia National Laboratories*
2. Di Lorenzo, E., Lava, P., Balcaen, R., Manzato, S., Peeters, B.: Full-field modal analysis using high-speed 3d digital image correlation. J. Phys. **1149**(12), 012007 (2018)
3. Srivastava, V., Patil, K., Baqersad, J., Zhang, J.: A multi-view DIC approach to extract operating mode shapes of structures. Structural Health Monitoring, Photogrammetry & DIC. **6** (2019)
4. Molina-Viedma, A., Lopez-Alba, E., Felipe-Sese, L., Diaz, F., Rodriguez-Ahlquist, J.: Modal parameters evaluation in a full-scale aircraft demonstrator under different environmental conditions using hs 3d-dic. Materials. **11**, 230 (2018)
5. Seguel, F., Meruane, V.: Damage assessment in a sandwich panel based on full-field vibration measurements. J. Sound Vib. **417**, 1–18 (2018)
6. Bharadwaj, K., Sheidaei, A., Afshar, A., Baqer, J.: Full-field strain prediction using mode shapes measured with digital image correlation. Measurement. **139**, 326–333 (2019)
7. Galeazzi, S., Chiariotti, P., Martarelli, M., Tomasini, E.: 3d digital image correlation for vibration measurement on rolling tire: procedure development and comparison with laser Doppler vibrometer. J. Phys. Conf. Ser. **1149**, 012010 (2018)
8. Ha, N.S., Vang, H.M., Goo, N.S.: Modal analysis using digital image correlation technique: an application to artificial wing mimicking beetle's hind wing. Exp. Mech. **55**, 989–998 (2015)
9. Yashar, A., Ferguson, N., Tehrani, M.G.: Measurement of rotating beam vibration using optical (dic) techniques. Procedia Eng. **199**, 477–482 (2017)
10. Baqersad, J., Carr, J., Lundstrom, T., Niezrecki, C.: Dynamic characteristics of a wind turbine blade using 3d digital image correlation. Proc. SPIE Int. Soc. Opt. Eng. **8348**, 74 (2012)
11. Liu, Y., Gao, H., Zhuge, J., Zhao, J.: Research of under-sampling technique for digital image correlation in vibration measurement. In: Harvie, J.M., Baqersad, J. (eds.) Shock & Vibration, Aircraft/Aerospace, Energy Harvesting, Acoustics& Optics, vol. 9, pp. 49–58 (2017)
12. Endo, M.T., Montagnoli, A.N., Nicoletti, R.: Measurement of shaft orbits with photographic images and sub-sampling technique. Exp. Mech. **55**, 471–481 (2015)
13. Peeters, B., Van der Auweraer, H., Guillaume, P., Leuridan, J.: The polymax frequency-domain method: a new standard for modal parameter estimation? Shock. Vib. **11**, 395–409 (2004)

Chapter 13
WaveImage – Order ODS for Rotating Machineries

Matthias Urban, Daniel Herfert, and Maik Gollnick

Abstract Operational deflection shape (ODS) analysis is a method to determine the vibration pattern of a structure influenced by its own operating forces and can be applied to the time and frequency domain. For rotating machinery with rapidly changing numbers of revolutions, ODS analysis provides insufficient results in the frequency domain. This work introduces the novel order ODS from the software WaveImage. This approach applies order analysis (OA) techniques to the ODS analysis.

Classical OA deals with the analysis of structures which contain rotating elements such as engines or turbines. Each rotating element generates its own noise and vibration pattern which contributes to the overall vibration pattern. With OA these individual patterns can be identified and analyzed for each rotating element. During a run-up or run-down, relevant frequencies of the structure shift in relation to the current rotational speed and are therefore more difficult to evaluate. Furthermore, in OA each measuring channel is evaluated individually. The visualization of a complex geometry together with the simultaneous measurement of several measuring points is currently not applied in the field of OA.

To overcome these disadvantages, a new domain was introduced to the ODS analysis. The advantage is the possibility of visualizing the ODS for a certain rotational speed. In OA, digital resampling takes place in which the original time signal is transformed into the angular range. After that the result is transferred to the target domain by Fourier transformation. To carry out the order ODS, the RPM signal must be measured in addition to the response measurement.

For the validation of the order ODS approach, a structure was measured using acceleration sensors and a slow-motion video sequence. The acceleration data was used to perform a frequency ODS. To calculate the order ODS, the optical flow is used to determine the acceleration data from the recorded video. Finally the result of the frequency ODS was compared to the order ODS.

Keywords Operating deflection shape · Frequency ODS · Order ODS · Order analysis · Optical flow

13.1 Introduction

In the industrial environment, machines with rotating elements are subject to constant wear. To reduce maintenance costs and time loss due to production downtime, vibration analysis can be used for condition monitoring and improvements to the machine design to avoid unwanted vibrations.

For statically rotating machinery, the ODS analysis is suitable. The ODS analysis can be carried out in the time or frequency domain and is used to visualize the vibration patterns of the machine by means of a geometry. In contrast to the operational modal analysis, only the vibration patterns from the actual working range of the machine are considered. The ODS analysis is not suitable for non-stationary objects such as machines or engines which are operated at constant change in speed in case of a run-up or run-down. Due to the changing RPMs (revolutions per minute), the frequency lines in the spectrogram are unclear, and the Complex Mode Indicator Function (CMIF) is blurred by the RPM-related shift and makes further analysis difficult.

For machines with constantly changing speed signal, the OA is used. In contrast to the ODS analysis, OA includes a RPM signal of the machine in the analysis. The measurement data is converted from the time to the order domain where it is possible to assign a frequency with a high amplitude in the spectrum to a certain RPM value. Furthermore, the lines of the fast

---

M. Urban · D. Herfert (✉) · M. Gollnick
Department of Structural Dynamics / Pattern Recognition, Society for the Advancement of Applied Computer Science, Berlin, Germany
e-mail: herfert@gfai.de

D. Di Maio, J. Baqersad (eds.), *Rotating Machinery, Optical Methods & Scanning LDV Methods, Volume 6*, Conference Proceedings of the Society for Experimental Mechanics Series, https://doi.org/10.1007/978-3-030-76335-0_13

Fourier transform (FFT) in the spectrogram can be displayed more clearly by means of digital resampling. This technique transforms the original signal into the angular range. A further difference to ODS analysis is that in previous approaches to OA, the geometry of the structure is not used to display vibration patterns.

This paper introduces an approach implemented in the software WaveImage (gfai tech GmbH) [1] which applies the advantages of OA to ODS analysis. The so-called order ODS analysis extends the classical ODS analysis by the order domain.

In some cases, it can be difficult to mount sensors to the structure for vibration analysis. Either parts of the object are inaccessible, or it is not possible to stop the machine without major circumstances. Especially with complex structures, a lot of experience and a broad technical knowledge are needed for a high-quality measurement. Non-contact measuring instruments such as laser Doppler vibrometers are also expensive and require a lot of measuring experience.

In this paper an approach was validated which determines the vibration characteristics of a structure using a slow-motion video sequence. Therefore a method is used which calculates the optical flow of that sequence. This allows time signal shapes of rotating machines to be extracted from the video and the ODS of the structure to be visualized.

13.2 Background

13.2.1 Order Analysis

The analysis of noise and vibration signals for rotating machinery can be done with OA. FFT is hereby the most important method for the analyzation of such data.

Figure 13.1 shows the spectrogram (left) and the FFT (right) for a measurement of an acceleration sensor under stationary conditions at around 4300 RPM. For the constant RPM, the FFT shows a peak at 71.42 Hz which is also displayed in the spectrogram as a straight line.

Figure 13.2 shows the spectrogram (left) and FFT (right) for a run-down. The dominant spectral line moves over several frequencies according to the constant change in speed. This behavior can also be seen in the FFT plot where several peaks appear in the depiction and make a further analysis difficult.

For this reason the measurement data are transferred from the time to the order domain. An order is a frequency that corresponds to the RPM of a machine. The frequency equal to the RPM is called first order. In case of resonances, orders can be a fraction or multiples of the first order. By digital resampling the measured time signal is transformed into the angular range. Thus, RPM signal and time signal can be synchronized with each other [2]. If a FFT is applied to the resampled signal, the spectrogram shows the RPM signal above the order. Figure 13.3 shows the test measurement in the order domain. The FFT in Fig. 13.3 (right) shows a major peak at order 0.908 and is displayed in the spectrogram view in Fig. 13.3 (left) as a straight line. With this representation further analysis can be done.

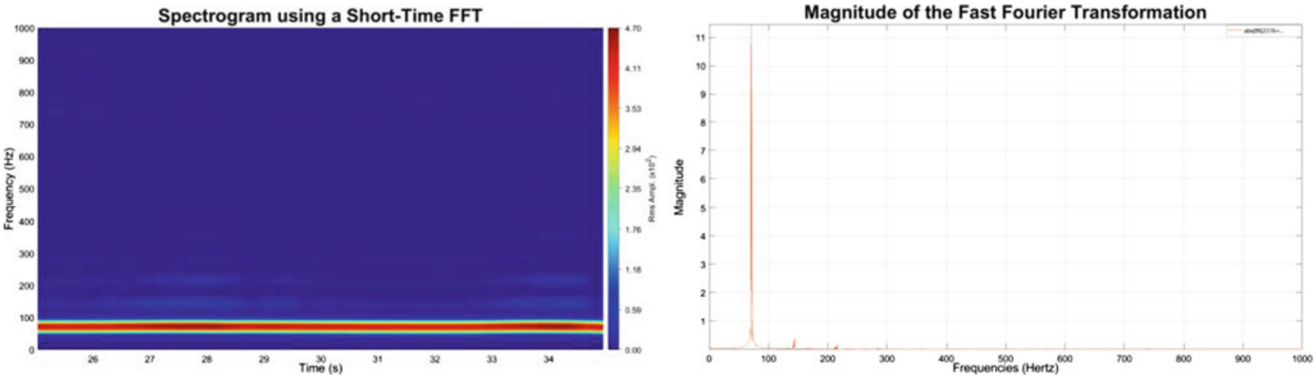

Fig. 13.1 Spectrogram (left) and FFT (right) representation of an acceleration measurement under stationary conditions

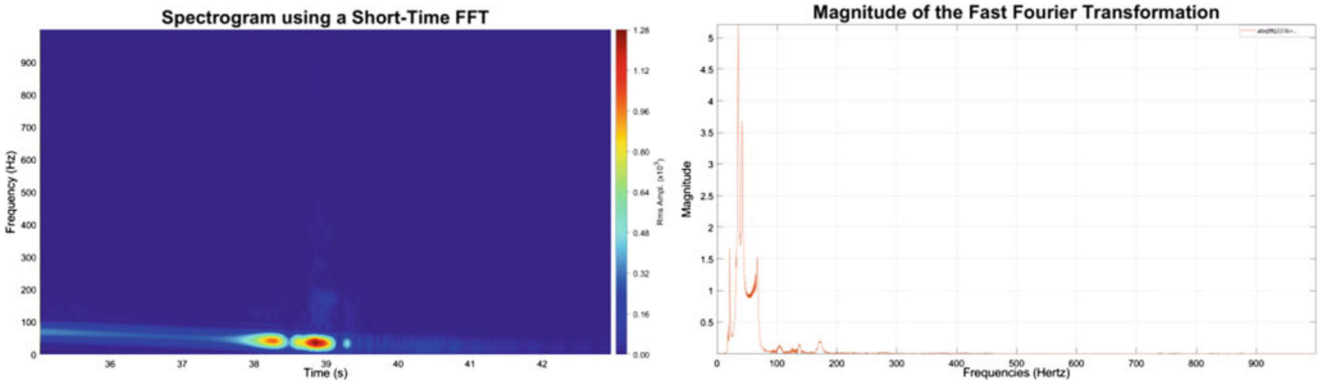

Fig. 13.2 Spectrogram (left) and FFT (right) representation of an acceleration measurement for a run-down

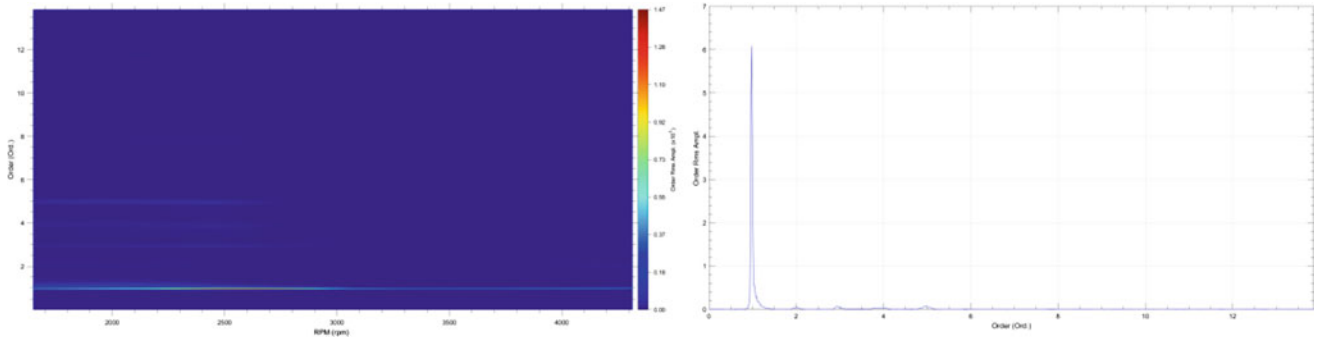

Fig. 13.3 Spectrogram (left) and FFT (right) representation of an acceleration measurement for a run-down transferred to the order domain

13.2.2 Operating Deflection Shapes

For vibration analysis, the structure is usually measured at several points that are called degrees of freedom (DOF). Each point can contain the measurement data of up to three directions (x, y, and z). To calculate the deflection shape, at least two points and a geometric model of the structure are needed. Points of the geometry which are not measured are interpolated. As the deflection is calculated while the structure is vibrating under its own operating forces like a changing RPM, flow, or pressure, it is called operating deflection shape. Having a geometrical model of the measured structure the ODS can be used to visualize the vibration pattern. With the help of ODS analysis, several questions can be answered. It is possible to detect how much a structure is moving and at which point and direction the highest motion occurs. If the structure is modified, for example, stiffened at some parts, it can be determined whether the sound and vibration characteristics have improved or worsened with respect to the desired values. Additionally structure-borne noise can be detected [3].

It can be distinguished between time ODS and frequency ODS. In time ODS velocities, displacements or accelerations are used for the deflection shape calculation. If two or more channels are simultaneously measured at different locations on the structure, the animation can be obtained by integrating or differentiating according to the sensor type. In frequency ODS linear spectra (FFT), auto power spectra (APS), cross power spectra (XPS), frequency response function (FRF), and ODS FRFs are used [3].

In the novel order ODS, only time data can be used for the calculation. In contrast to the time ODS, where the time series is applied as deflection shape, the RPM signal is used to resample the data to convert it from the time to the order or frequency domain. For selected channels different cuts can be extracted from the spectrogram in the order and frequency domain. These cuts from the spectrogram can be visualized and applied to the geometry for the animation of the deflection shapes. This allows the direct reference of the associated RPM signal to an ODS of the machine.

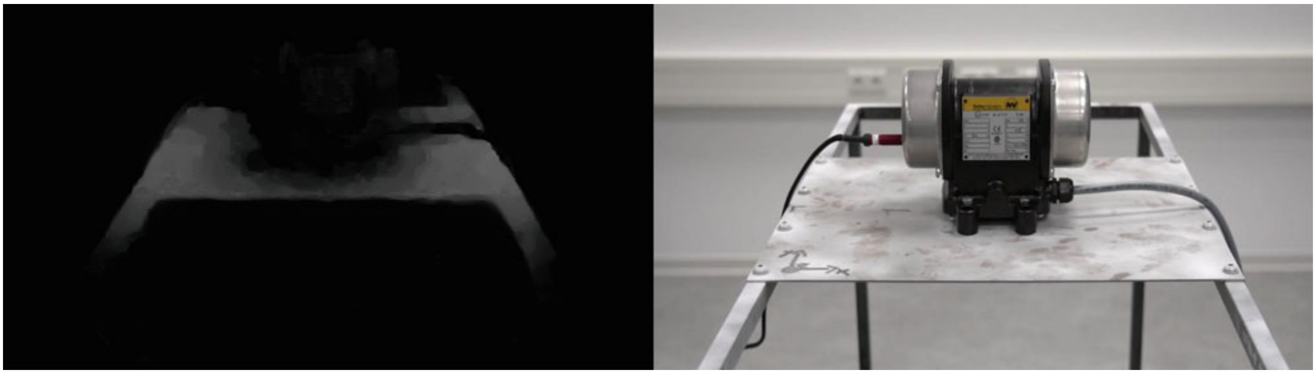

Fig. 13.4 Frame of the calculated optical flow during a run-down (left) and corresponding frame of the original video to the left image (right)

13.2.3 Optical Flow Analysis

The optical flow is the displacement vector of a pixel or an object in an image sequence relative to the image plane. With this technique, the movement of the pixel can be tracked and used for a variety of applications like object tracking and recognition, image segmentation, and video compression [4].

There are two approaches for calculating the optical flow. If only a few pixels of a frame are considered, for example, at edges or corners of an object, the flow field is sparse and thus called sparse optical flow. Calculating the flow vector for all image points is called dense optical flow. As all pixels in the image are considered, this method is more complex and time-consuming but has a higher accuracy as the sparse optical flow [5].

In terms of vibration analysis, the dense optical flow is used to calculate displacement vectors. The video recordings have the advantage that a non-contact measurement is possible. Due to the approach, each pixel in the image corresponds to a channel and is tracked over the length of the video sequence. This corresponds to a very high-resolution measurement with standard sensor technology. Imagine a video with full HD resolution which is the equivalent of over two million channels. Moreover, it would be very expensive to attach such a high number of sensors to the structure. Depending on the structure, the weight of the sensors can also influence the vibration shape.

Figure 13.4 (left) shows the length of the flow vector in image coordinates for one frame. The corresponding frame of the original video can be seen in Fig. 13.4 (right). If this procedure is done for all frames of the video sequence, an overlay video can be generated. Together with the original video, the displacements can be visualized. To generate channel data, which can be used in vibration analysis as equivalent to a displacement sensor measurement (triaxial), each pixel is transformed into 3D space obtaining x-, y-, and z-coordinates.

13.2.4 Measurement Setup

For the validation of the presented methods, a self-designed 500 × 500 × 1000 mm steel frame consisting of rectangular 20 × 20 mm solid profiles which are welded together was used. For the mounting of machines, a steel plate 500 × 400 × 2 mm was attached to the upper center of the frame. For the validation of the methods in the software, a CAD (computer-aided design) model of the steel frame was designed; see Fig. 13.5 (left). The rotating component is an electric external vibrator of the type Netter Vibration NEG 50200 which is used for loosening, conveying, compacting, and separating bulk materials. A Siemens SINAMICS V20 - 6SL3210-5BB17-5BV1 frequency converter was used to control the vibration frequency and force. To measure the speed signal, a magnetic speed sensor was installed inside the electric external vibrator. Six accelerometers were attached to the frame for a reference measurement, four at each corner at the upper side of the frame and two at the shorter sides of the steel plate. The position of each sensor is depicted in Fig. 13.5. The data acquisition was done with a data recorder of type SIRIUS from the company Dewesoft.

For the slow-motion video, two cameras were used: a Sony A7IV which captures a video with 120 fps and a resolution of 1920 × 1080 pixels and a GoPro Hero3+ black edition. The latter camera is able to capture a video with 240 fps and a resolution of 848 × 480 pixels. A measurement setup can be seen in Fig. 13.5 (right) which shows a recording of a slow-motion video during a run-down.

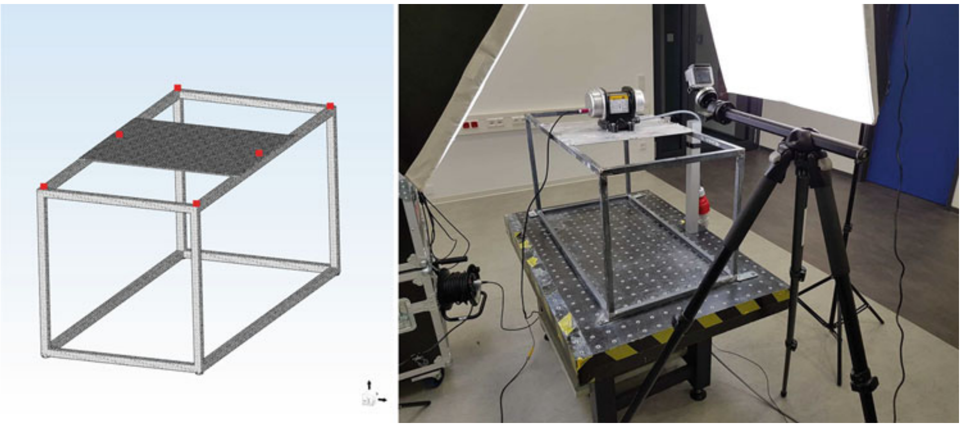

Fig. 13.5 Geometry of the steel frame which was used in the software and sensor positions (left) and measurement setup with steel frame, external electric vibrator, accelerometer, and camera (right)

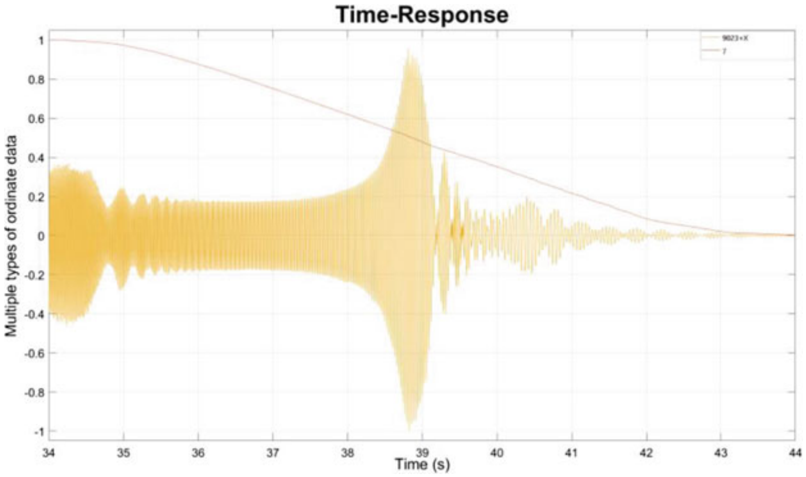

Fig. 13.6 Scaled data for the RPM signal (orange) and the response of an acceleration (yellow) sensor during the run-down

13.3 Analysis

For the analysis a run-down with a duration of 10 s was performed with the presented measurement setup. Figure 13.6 shows the speed signal and the response signal of an acceleration sensor. The signals were scaled for a better comparability. At the beginning of the measurement, the speed was about 4300 RPM. During the run-down, the sensor signal showed no continuous decrease in the amplitude. Excitations of the measured object during the measurement due to changes in the rotational speed can be seen.

The acceleration data of the six sensors were loaded into the frequency ODS module of the WaveImage software. For the time data, the respective ODS FRFs are calculated. Out of the ODS FRFs, the CMIF, which is shown in Fig. 13.7, is formed. The relevant frequencies are located in the range from 19 to 72 Hz. The highest amplitudes are reached at 18.95, 21.767, 31.754, 35.339, and 72.471 Hz. The peaks in the CMIF curve represent the system response. The larger the peak, the larger the system response. Without reference to a speed signal, no statement can be made about the speed range at which the maximum values are reached. The frequencies at the peaks do not represent the actual frequencies of the excitation because the frequency ODS does not consider the speed signal in the analysis.

When the acceleration data is loaded into the software—together with the speed signal—the data is converted from the time to the order domain. At this point it is possible to investigate each spectrogram for all sensors and their directions. The highest deflection is likely to occur at the mounted steel plate. Because of this we were mostly interested in the sensor information which were recorded at this position. Figure 13.8 shows the order cuts (left) and the frame with the highest amplitude in the animation related to the order cut (right) for the *x*-direction of the sensor. The cuts were taken from the order 0.908 which showed the highest amplitudes at this spectral line.

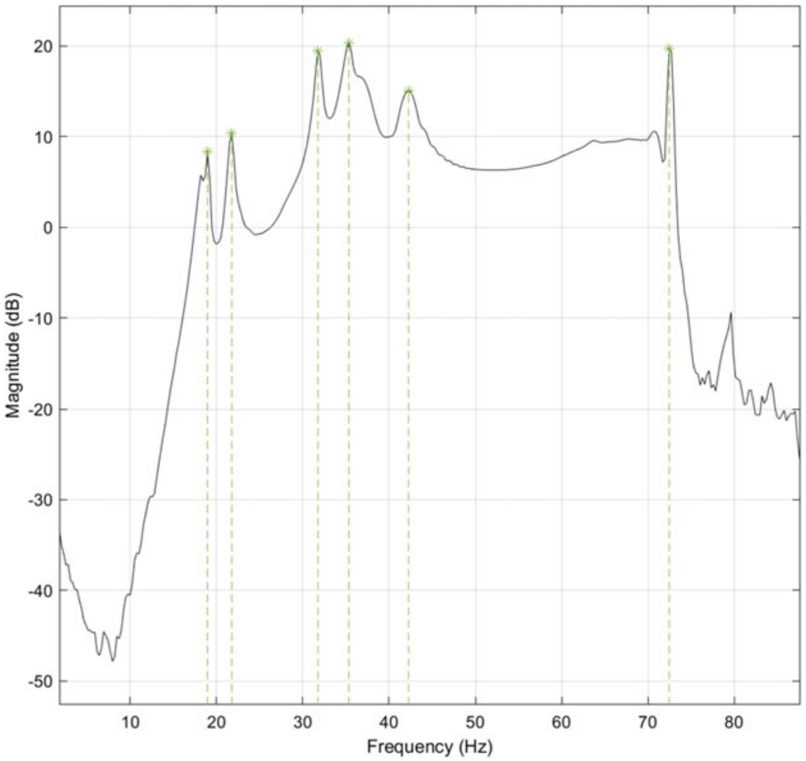

Fig. 13.7 CMIF of ODS FRFs from time data for the run-down measurement

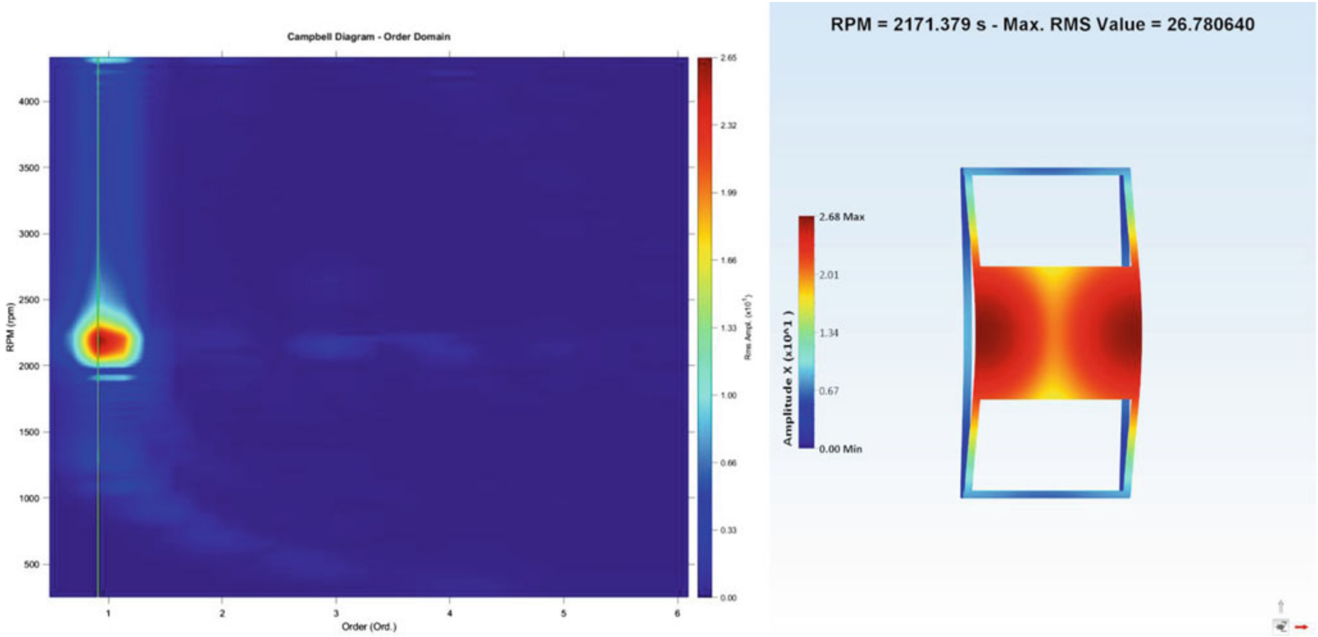

Fig. 13.8 Order cut of a channel in *x*-direction at order 0.908 (left) and frame with the highest amplitude of the order cut (right)

For the video recordings to calculate the optical flow, the same test setup as for the measurement using the acceleration sensors was used. Instead of attaching six sensors, only one sensor at the steel plate was used. To find out the best environmental and video conditions for our measurement scenario, we recorded the test object with the two cameras from different angles and distances and under varying lighting conditions. The recorded videos had a length of 32–34 s and consisted of up to 8000 single frames at a resolution of 240 FPS. The calculation of the dense flow was done by using several

Fig. 13.9 Frame of the original video together with the overlay video

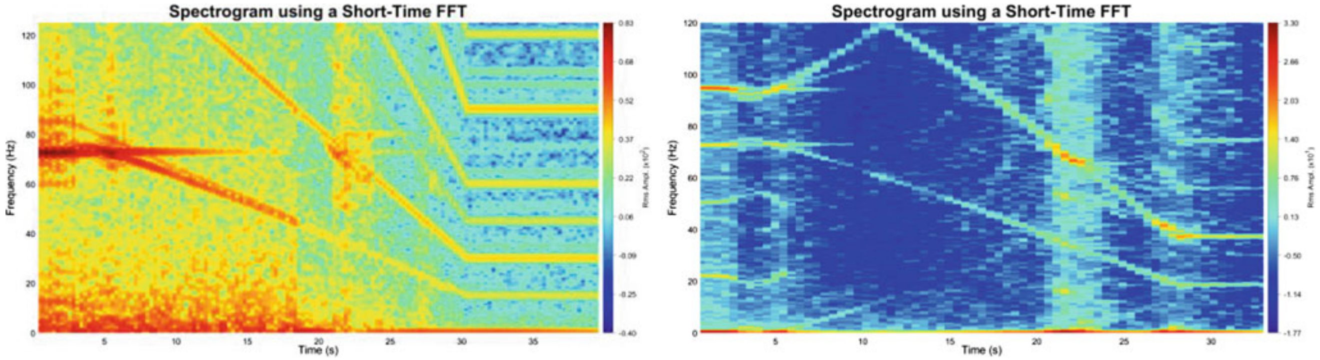

Fig. 13.10 Maximum of all spectrograms for the acceleration sensor (left) and the channels for the optical flow (right)

algorithms (Brox [6], TVL1 [7], and Farneback [8]) from the OpenCV library [9]. In order to find the best algorithm for the test scenario, several parameterizations were applied and validated. The TVL1 showed the best results for the overlay video. Visualization of the displacements on the steel plate creates a similar pattern to the animation of the deflection shapes from the order ODS; see Fig. 13.8 (right) and Fig. 13.9.

The spectrogram for the extracted channel data of the optical flow is shown in Fig. 13.10 (right). Compared to the spectrogram of the reference measurement with the acceleration sensor in Fig. 13.10 (left), a similarity can be seen. At least the main order can be identified. This observation can be explained by the low sampling rate of the camera.

13.4 Conclusion

In this paper, the novel order ODS implemented in the software WaveImage was presented on the basis of a measurement of a steel frame which was stimulated by an engine during a run-down. It was shown how the RPM signal can be related to the deflection shape of the structure. Additionally a slow-motion video sequence of the run-down was recorded to calculate the optical flow and generate channel data for vibration analysis from the video. It was demonstrated that the method provided good results considering the hardware. However, for future studies it would be necessary to use a camera with higher sampling rate to avoid aliasing effects. The generated channel data showed empty values in several locations of the vector. This problem could be reduced by using algorithms which apply backtracking techniques for pixel tracking.

References

1. Homepage of the software WaveImage Modal, https://wave-image.com/modalanalysis/?lang=en, 2020
2. Saavedra, P.N., Rodriguez, C.: Accurate assessment of computed order tracking. Shock. Vib. **13**, 13–32 (2006)
3. Schwarz, B., Richardson, M.H.: "Introduction to Operating Deflection Shapes" CSI Reliability Week, Orlando, FL, October 1999
4. O'Donovan, P.: Optical flow: techniques and applications. Int. J. Comput. Vis. pp. 1–26. https://www.dgp.toronto.edu/~donovan/stabilization/opticalflow.pdf, 2005

5. Spruyt, V., Ledda, A., & Philips, W.: Sparse optical flow regularization for real-time visual tracking. Proceedings – IEEE International Conference on Multimedia and Expo. 1–6, 2013
6. Brox, T., Bruhn, A., Papenberg, N., and Weickert, J.: High accuracy optical flow estimation based on a theory for warping. In Computer Vision-ECCV 2004, pages 25–36. Springer (2004)
7. Zach, C., Pock, T., Bischof, H.: A duality based approach for realtime TV-L1 optical flow. In: Hamprecht, F.A., Schnörr, C., Jähne, B. (eds.) Pattern Recognition. DAGM 2007. Lecture Notes in Computer Science, vol. 4713. Springer, Berlin, Heidelberg (2007)
8. Farnebäck, G.: Two-frame motion estimation based on polynomial expansion. In: Bigun, J., Gustavsson, T. (eds.) Image Analysis. SCIA 2003. Lecture Notes in Computer Science, vol. 2749. Springer, Berlin, Heidelberg (2003)
9. OpenCV, Open source computer vision library, 2015

Chapter 14
Multi-Level Damage Detection Using Octree Partitioning Algorithm

Mehrdad S. Dizaji and Zhu Mao

Abstract This research proposes a damage detection methodology that takes advantages of full-field sensing of structural elements via 3D digital image correlation (3D-DIC) within a new optimization algorithm. To get a unique solution for a finite element model updating problem in detecting internal properties of a structure by topology optimization method, a novel strategy is proposed termed as octree partitioning algorithm (OPA). Damage detection is attained using minimizing a defined objective function of residuals between the observed and corresponding mimicked responses, resulting in the identification of the underlying material distribution. This brief paper explores this concept through a case study on a series of small structural test specimens with fabricated damage on the specimens. The results show that the proposed OPA has capability of tuning the initial model to find the ideal partition configuration for the proposed model updating process.

Keywords Multi-level damage detection · Finite element model updating · Octree partitioning algorithm

14.1 Introduction

Internal properties of a sample such as defects can be detected by inverse problems such as finite element model updating strategy or topology optimization strategies [1–3]. To establish and minimize the objective function of residuals between the observed and corresponding mimicked responses, it is necessary to attain experimental data using full-field measurements. Experimental measurements can be acquired using 3D digital image correlation technique.

In the proposed inverse problem, the unknown design variables are initial elasticity modulus distribution all over the entire component. There are two ways to assign the unknown parameters to the initial model: either *partition by partition* or *element by element* approach. In this study, the partition-by-partition way is studied. Initial finite element model is divided into partitions and assigned an initial elasticity modulus distribution to be optimized according to the proposed approach. However, it is challenging to find a proper partitioning of the initial model such that the existence defects can be found appropriately. Therefore, it is necessary to investigate the effect of different partitioning configurations of the initial finite element model on the size and location of the discovered damaged region. Therefore, a novel sensitivity analysis based on octree partitioning strategy is proposed in order to find a proper partitioning strategy for the initial finite element model and inverse problem. This strategy is demonstrated in Fig. 14.1 schematically. Assuming there is a structure component with a defect inside, the new defined sensitivity method is applied to find the whereabouts location and size of the defect iteratively. In each step different partition configurations are selected to find the best configuration by evaluating the objective function using optimization algorithm. In the end of each step (i.e., the objective function does not change significantly), the partitions with no dramatic change in their values will be freeze for the next step. Following the next step, the active partitions will be considered in the optimization process. This process will be continued until the objective function has met the minimum criteria. The sensitivity strategy can help to not only increase the chance of having a unique answer but also to decrease extra computational cost.

M. S. Dizaji (✉) · Z. Mao
Department of Mechanical Engineering, University of Massachusetts Lowell, Lowell, MA, USA
e-mail: mehrdad_shafieidizaji@uml.edu

D. Di Maio, J. Baqersad (eds.), *Rotating Machinery, Optical Methods & Scanning LDV Methods, Volume 6*, Conference Proceedings of the Society for Experimental Mechanics Series, https://doi.org/10.1007/978-3-030-76335-0_14

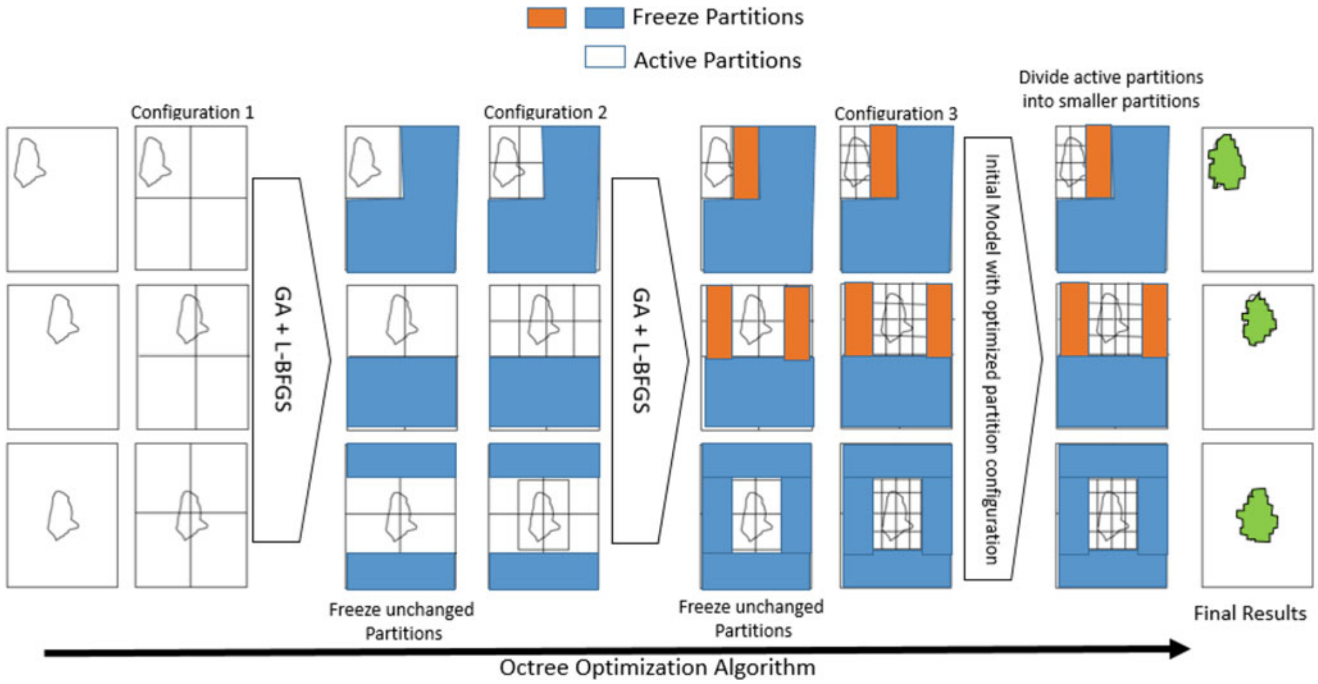

Fig. 14.1 Schematic diagram of the octree partitioning algorithm

14.2 The Proposed Algorithm

The whole point of the proposed idea is to discover the size and location of the defects without any prior information of the defects. This concept is studied by selecting different configurations for partitioning of the initial model. The purpose is to show that the proposed algorithm has the capability of realizing the location and size of the defects without any prior information about the defects. The selected partition configurations are plotted in Fig. 14.2. Several partition configurations are applied on the initial finite element model of the coupon specimen, and the performance of the proposed algorithm is evaluated and the results are shown in Fig. 14.3. Also, in Table 14.1, the elasticity values for the different configurations before and after optimization process are shown. The results show that the proposed OPA has capability of tuning the initial model to find the ideal partition configuration for the proposed model updating process. The partitioning algorithm for updating of partition configurations is demonstrated as follows:

0. Create initial partition and assign initial design variables for the partitions.
1. Start optimization process based on the hybrid algorithm (GA + L-BFGS).
2. Continue the optimization process until the criteria is satisfied.
3. Stop the optimization if gradient of objective function is less than 5 percent of the previous step.
4. Compare updated design variables with target values.
5. If the values for the partition are less than target value, then keep it for the next step; if not, extract the partition from next model updating process.
6. Continue to implement step 5 until all the partitions are covered.
7. Create second configuration based on the previous results and go to step 2.
8. Stop the procedure if there is no change in gradient of objective function.
9. The final partition will be used in the second round of optimization process.
10. The small partitions will be updated based on GA + L-BFGS-B algorithm.
11. It will be continued until the gradient of the objective function does not change.
12. End.

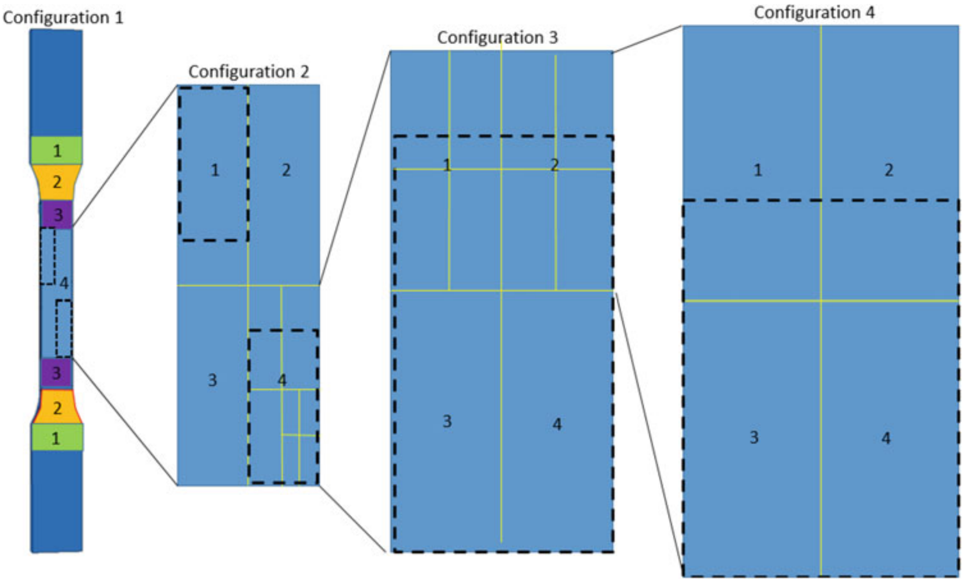

Fig. 14.2 OPA for a coupon specimen

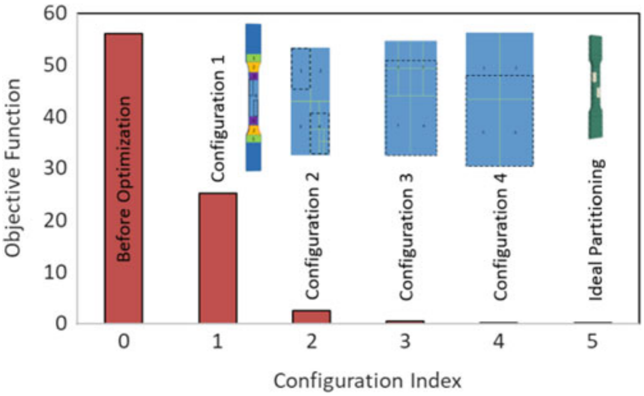

Fig. 14.3 Final objective values at the end of each optimization process for different configurations

Table 14.1 Elasticity modulus before and after running the optimization algorithm for different configurations

	Elasticity Modulus							
	Configuration 1		Configuration 2		Configuration 3		Configuration 4	
Partition number	Before	After	Before	After	Before	After	Before	After
1	150,000	204,768	110,334	34,033	28,223	10,333	1546	120
2	320,000	193,003	110,334	105,443	28,223	12,545	1546	111
3	220,000	191,000	110,334	98,003	28,223	2433	1546	78
4	55,000	110,334	110,334	28,223	28,223	1546	1546	56
Objective function	57	25	10	2.6	1.2	0.2	0.12	0.02

14.3 Conclusion

The proposed OPA is designed to maximize the sensitivity to damage of measurements collected through the experimental testing in the lab, where damage has been considered as a local reduction of the stiffness of the hosting structure. Based on Fig. 14.3 and Table 14.1, it can be concluded that even though there were not any prior knowledge about the location of the defects, only by creating a random partitioning of the initial model, the proposed method will work. Using the proposed partitioning algorithm, and by conducting a few random initial partitioning for the model, not only can we obtain some prior knowledge regarding the location of the defects but also get unique solution for the objective function.

Acknowledgments Research was sponsored by the Army Research Laboratory and was accomplished under Cooperative Agreement Number **W911NF-17-2-0211**. The views and conclusions contained in this document are those of the authors and should not be interpreted as representing the official policies, either expressed or implied, of the Army Research Laboratory or the US Government. The US Government is authorized to reproduce and distribute reprints for government purposes notwithstanding any copyright notation herein.

References

1. Dizaji, M. S., Alipour, M., Harris, D. K.: Subsurface damage detection and structural health monitoring using digital image correlation and topology optimization. Engineering Structures, 230, 111712 (2021)
2. Dizaji, M.S., Alipour, M., Harris, D.K.: Leveraging full-field measurement from 3D digital image correlation for structural identification. Exp. Mech. **58**(7), 1049–1066 (2018)
3. Bendsoe, M.P., Sigmund, O.: Topology Optimization: Theory, Methods, and Applications. Springer Science & Business Media (2013)

Chapter 15
Photogrammetry-Based Experimental Modal Analysis for Plate Structures

J. S. Kim and Y. F. Xu

Abstract A photogrammetry-based vibration measurement method was first developed and applied to beam structures for modal parameter estimation and structural damage identification. In this work, the photogrammetry-based method is experimentally investigated for its application to modal parameter estimation of plate structures. A single-point laser equipped with a diffractive optical element projected a grid consisting of 100 laser spots to a plate structure in a fully non-contact, non-destructive manner. Deformations of the plate were measured by tracking the projected spots that served as external optical features to be tracked in the photogrammetry-based method. A scanning laser Doppler vibrometer was also used to measure deformations of the plate for comparison purposes. The accuracy of the photogrammetry-based method and its three-dimensional kinematic relation for plate structures were studied by comparing its measurements and modal parameter estimation results with those by the scanning laser Doppler vibrometer. The three-dimensional kinematic relation between a point on a field-of-view plane of the plate and that on an image plane of a camera was experimentally verified. Both rigid body and elastic modes of the plate were identified, and their modal parameters were estimated. Mode shapes of the plate estimated using the photogrammetry-based method were compared with those from a finite element model, and their modal assurance criterion values were all over 90%, which verified the accuracy of the EMA method.

Keywords Experimental modal analysis · Photogrammetry · Plate structure · Laser object tracking · Image processing

15.1 Introduction

Recently, using photogrammetry to measure dynamic parameters of structures became more popular due to developments in cameras [1]. Photogrammetry is one of optical measurement technique to extract a geometry, displacement, and deformations of a test object using digital images. Optical technology has been developed in last few decades due to advances in camera sensors, storage abilities, and processing power. It can be categorized into two parts: one is by laser beams such as laser Doppler vibrometry (LDV) and the other is by while lights such as photogrammetry-based techniques. Advantages of optical technology are non-contact and non-destructive compared to conventional measurement sensors such as accelerometers. LDV can served as an accurate non-contact measurement technique; however, generally point-by-point measurements are required for any number of measurement points which can lead experiments to be expensive and inefficient. On the other hand, photogrammetry-based measurement techniques can be processed multiple measurement points so that measurements can be efficient and full-field manner.

Photogrammetry technique can be approached with three categories: point-tracking (PT), digital image correlation (DIC), or target-less approaches. PT technique is used with optical targets attached on the test object, and displacements can be extracted by tracking those optical targets. Olaszek [2] developed a real-time photogrammetry measurement technique to measure dynamic properties of bridges with optical targets attached. Morlier [3] also used point-tracking method to inspect bridges and extracted displacements to obtain natural frequencies and mode shapes. Ryall et al. [4] developed a measurement technique that can extract three-dimensional displacement using a single camera. Attaching optical targets could be a challenge in point tracking method because test object surface profile might get modified and mass load can be introduced to the system. DIC, on the other hand, is used with non-repeatable pattern (speckle pattern) painted on a dedicated surface of the test object for extracting displacements. Helfrick et al. [5] used a signal mode excitation to extract mode

---

J. S. Kim · Y. F. Xu (✉)
Department of Mechanical and Materials Engineering, University of Cincinnati, Cincinnati, OH, USA
e-mail: xu2yf@uc.edu

D. Di Maio, J. Baqersad (eds.), *Rotating Machinery, Optical Methods & Scanning LDV Methods, Volume 6*, Conference Proceedings of the Society for Experimental Mechanics Series, https://doi.org/10.1007/978-3-030-76335-0_15

shapes of a dryer cabinet. Full-field vibration measurement can be performed using DIC, but processing data is required with memory and computational power [6]. Peters and Ranson [7] investigated the concept of the photogrammetry and applied to measure mechanical stress and strain during deformations. From their work, an idea of subset in an image and combined digital imaging technique were proposed to analyze stress of structures. Sutton and Chu [8, 9] further investigated the idea and introduced three-dimensional digital image correlation (3D DIC) measurement technique. This technique includes the following: image processing to obtain deformations of structures, kinematic relation between a camera and a specimen is determined by tracking unique patterns in each subset of an image. To improve accuracy and resolution, stereo cameras or multiple-camera measurement [10] is used to obtain a dynamic parameter of structures. In mentioned DIC measurement technique by using the speckle pattern requires equally distributed light intensities throughout a specimen. Multiple lighting sources are recommended for this technique, and the results have high sensitivities about light sources . Another approach to reduce efforts on painting the pattern is to apply projected pattern. Papa et al. [11, 12] used DIC for three-dimensional shape extraction instead of deformations of the structures. They used projected pattern on a very thin layer to measure dynamic properties to avoid any changes in the sensitive boundary conditions of the thin layer. Yang et al. [13] used projected pattern to extract mode shapes of a simple cantilever beam vibrating at its resonant frequency. Targetless approaches were also widely used to study dynamic properties of structures. Especially, edge detection algorithm is widely accepted to extract dynamic properties of a structure including slender parts such as cables where optical targets cannot be attached. Ji, Change et al. [14] used the edge detection algorithm to extract mode shapes of a thin cantilever bar and further investigated to extract dynamic properties of a cable of a bridge [15, 16]. Kim et al. [17] used the algorithm to perform rigid-body correction for large structures. Chen et al. [18] introduced a motion magnification approach to show amplified visions of small deformations in digital images for mode shapes.

In this work, a photogrammetry-based experimental modal analysis (EMA) method is experimentally investigated, where a digital camera is used to measure displacements of a test object under small deformations. Instead of using speckle patterns for point-tracking, projected laser spots were used to serve as an image target. A kinematic relation between the displacement of the laser spots and that of its associated image target was used to obtain three-dimensional kinematic model. Point tracking using the laser spots was used to measure the displacement of tracked image targets on an image plane. To validate accuracy of the EMA method and kinematic relation, experimental investigation was conducted. Experimental results from the kinematic relation and EMA method were compared with those from a finite element model.

The remaining part of this paper is outlined as follows. The kinematic relation is demonstrated in Sect. 15.3.1, and the point-tracking method is described in Sect. 15.3.2. The photogrammetry-based EMA method is described in Sect. 15.3.3. The experimental investigations of EMA method including kinematic relation and point-tracking method are demonstrated in Sect. 15.3. Conclusions of this paper are presented in Sect. 15.4.

15.2 Methodology

In this section, the photogrammetry-based measurement method is described for its application to modal parameter estimation of plate structures. This method uses a point-tracking technique, where a single-point laser equipped with a diffractive optical element was used to project a laser spot grid to a plate structure, and the laser spots serve as trackable optical targets. A single-camera system was used instead of a stereo-camera system to reduce processing time and avoid complicating the kinematic relation between cameras and a test object. An image plane can be defined in front of the lens of the camera. The image plane is parallel with the surface of the test object, as shown in Fig. 15.1a, where the position and orientation of the camera are depicted by dashed lines. The camera is then tilted by an angle θ and a field-of-view plane can be defined by projecting the image plane to the flat surface, as shown in Fig. 15.1b. A three-dimensional kinematic relation is derived in Ref. [1], where restrictions were imposed on the test object: (1) the structure undergoes small deformation and (2) it has a flat surface. The kinematic relation was previously validated on beam structures with flat surfaces.

15.2.1 *Kinematic Relation*

A random measurement point is formed at point P on the field-of-view plane, and an associated image target is formed at point P_i on the image plane, as shown in Fig. 15.1. As shown in the Fig. 15.2a, when the test object vibrates, P moves to point P' in the out-of-plane direction and P_i moves to point P_i' on the image plane. The kinematic relation between the displacement of P in the out-of-plane direction and that of P_i on the image plane can be derived based on a geometric

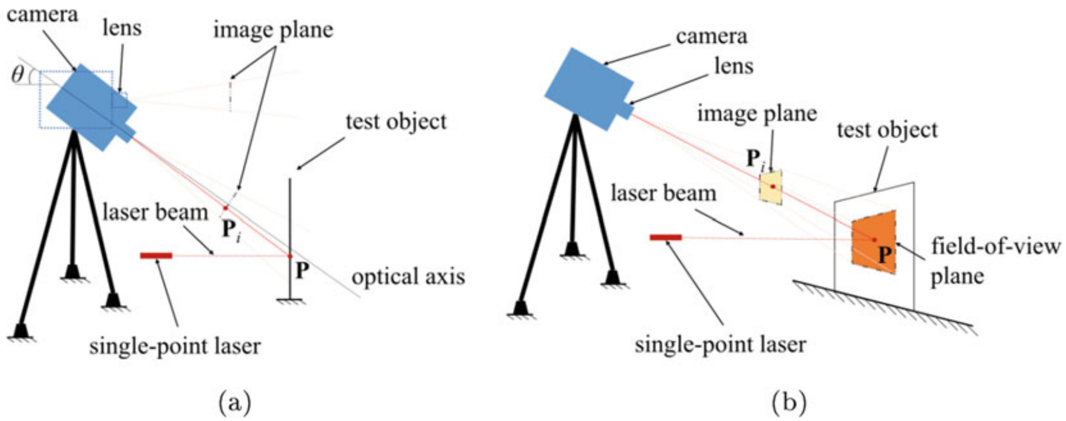

Fig. 15.1 (**a**) Schematic view of a test object for the photogrammetry-based vibration measurement method and (**b**) a three-dimensional view of the schematic view in (**a**). The position and orientation of the camera before it is tilted are depicted using dashed lines in (**a**) [1]

description of a three-dimensional kinematic model shown in Fig. 15.2b. A Cartesian coordinate system $C - xyz$ is defined: the origin and x-axis of the coordinate system coincide with the lens center C and optical axis of the camera, respectively. The coordinate system is oriented so that the image plane of the camera will be parallel with a plane formed by its y- and z-axes. The out-of-plane displacement of P, i.e., the length of PP', is denoted by w. A projective ray starting from C to P intersects the image plane at P_i and that starting from C to P intersects the image plane at P_i. The out-of-plane displacement of the test object PP' is projected to $\overrightarrow{P_i P_i'}$ on the image plane, and the length of $\overrightarrow{P_i P_i'}$ is denoted by w_i. As shown in Fig. 15.2c, the optical axis of the camera intersects the field-of-view plane and image plane at R and R_i, respectively. Lengths of CR and CR_i are denoted by d and d_0, respectively. Point P'' can be defined by projecting P to a line that is defined by intersecting a plane formed by the x- and y-axes and the field-of-view plane. Point P''' can be defined by projecting P to a plane formed by the x- and z-axes. Lengths of PP'' and PP''' are denoted as h and l, respectively, as shown in Fig. 15.2c and d. The line RP is projected to $R_i P_i$ on the image plane. The length of RP is denoted by h_0, as shown in Fig.15.2c, and it is directly related to h [1]. Three-dimensional linearized kinematic relation for $\overrightarrow{P_i P_i'}$ can be expressed by,

$$\overrightarrow{P_i P_i'} = \left(0, \frac{d_0 l \cos\theta}{(d - h\sin\theta)^2} \times w, \frac{d_0(d\sin\theta - h)}{(d - h\sin\theta)^2} \times w\right) \tag{15.1}$$

Coefficients $\frac{d_0 l \cos\theta}{(d-h\sin\theta)^2}$ and $\frac{d_0(d\sin\theta-h)}{(d-h\sin\theta)^2}$ are called as correction factors.

15.2.2 Point-Tracking Technique

In this work, a point-tracking technique is applied to calculate the centroid of each laser spot on subsets of an image, and the y- and z-coordinates of centroid of a spot, denoted by $y_{i,c}$ and $z_{i,c}$, respectively, are calculated by

$$y_{i,c} = \frac{\sum[y_i \times I_i(y_i z_i)]}{\sum I_i(y_i z_i)}, \qquad z_{i,c} = \frac{\sum[z_i \times I_i(y_i z_i)]}{\sum I_i(y_i z_i)} \tag{15.2}$$

respectively, y_i and z_i denote y- and z-coordinates of the optical intensity on the subset, $\sum$ denotes summation on all pixels of the subset, and I_i denotes the optical intensity at (y_i, z_i). A term $y^0_{i,c}$ is defined as $y_{i,c}$ value at the reference image, and the same rule is applied for $z^0_{i,c}$. The first captured image is denoted as the reference image. A term $y^n_{i,c}$ is defined as $y_{i,c}$ value at n-th measurement point where $n = 1, 2 \ldots N$ and N is a total number of captured images. A step-by-step description of the point-tracking technique for one image is provided below:

- Step 1. Set the first captured image as the reference image.
- Step 2. Locate a measurement point on the reference image with a threshold to locate the highest optical intensity.

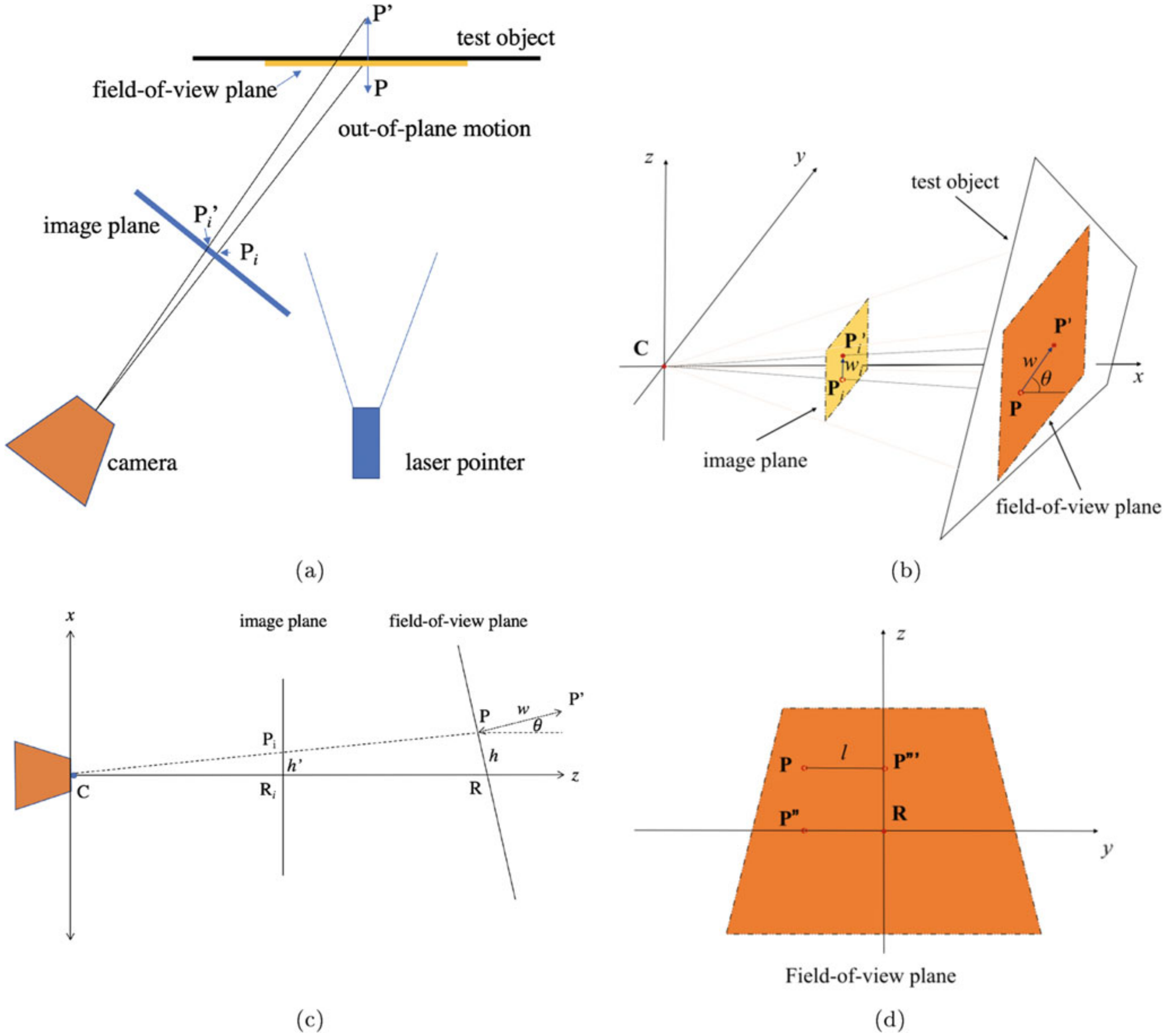

Fig. 15.2 (**a**) Three-dimensional kinematic model of the measurement point on the flat surface before and after deformation of the test object and the associated image target on the image plane, (**b**) a three-dimensional geometric description of the kinematic model in (**a**), (**c**) the side view of the field-of-view plane in (**b**) along the y-axis, and (**d**) the side view of the field-of-view plane in (**b**) along the x-axis [1]

- Step 3. Create an identical subset centered at each located measurement point. Subset size should not be bigger than the length from two measurement points in order to avoid any errors by putting two measurement points in one subset.
- Step 4. Calculate $y^0_{i,c}$ and $z^0_{i,c}$ on the reference Image, and geometry properties such as a width and length of subsets are fixed for all images.
- Step 5. Calculate $y_{i,c}$ and $z_{i,c}$ for each projected laser spot.

The length w_i can be calculated by subtracting $y_{i,c}$ and $z_{i,c}$ from the first captured image, which is referred to as the reference image, from $y_{i,c}$ and $z_{i,c}$ from the second through last images. The $w_{i,y}$ and $w_{i,z}$ can be calculated by Eq. (15.3) for each measured images.

$$w_{i,y} = \sum y^n_{i,c} - y^0_{i,c}, \qquad w_{i,z} = \sum z^n_{i,c} - z^0_{i,c} \tag{15.3}$$

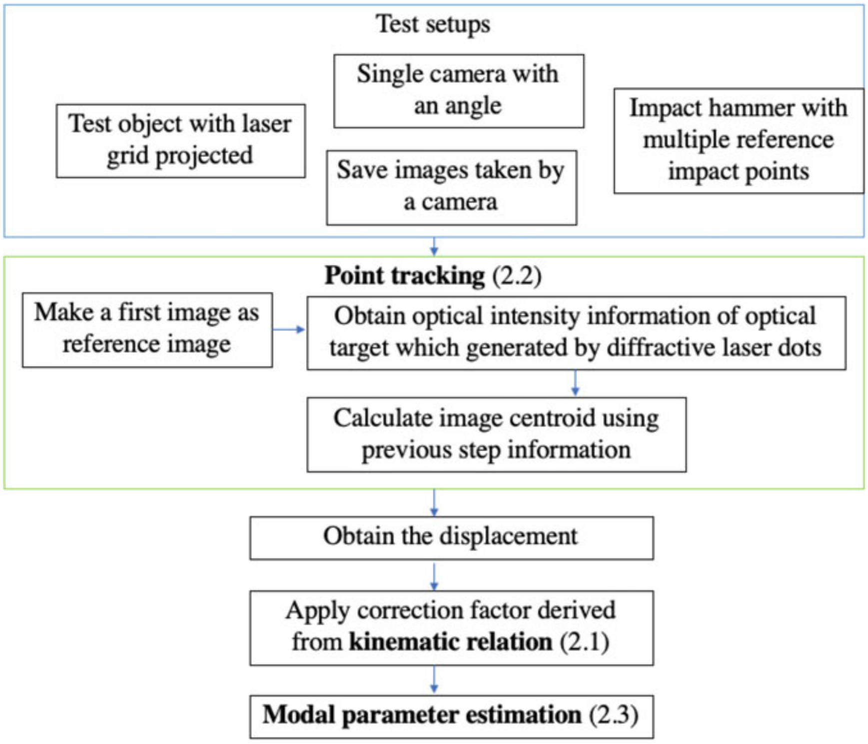

Fig. 15.3 Flowchart for experimentally investigating a photogrammetry-based vibration measurement methodology

where $\sum$ denotes summation of all measurement points. Finally w can be presented as a displacement vector in time domain with each $w_{i,y}$ and $w_{i,z}$ values.

15.2.3 Photogrammetry-Based EMA

Based on the kinematic relation and point-tracking technique, a photogrammetry-based EMA method is described here, and its flowchart is shown in Fig. 15.3. A test object is excited with single impulsive force, and its responses are measured by a digital camera. A measurement point and impact point are denoted as a and b, $a = 1, 2, \ldots A$ with A being the total number of measurement points and $b = 1, 2, \ldots B$ with B being the total number of impact points. A FRF between the displacement at point a and single impulsive force at point b can be expressed by

$$H_{ab} = \frac{W_a(\omega)}{F_b(\omega)}$$

where ω is the circular frequency, and $W_a(\omega)$ and $F_b(\omega)$ are defined as Fourier transforms of the displacement at point a and the single impulsive force at point b. Dynamic parameters such as natural frequencies and corresponding mode shapes are estimated by processing FRFs using an ordinary experimental modal analysis algorithm.

15.3 Experimental Investigation

15.3.1 Experimental Setup

In this section, the EMA of a plate structure was conducted in the form of impact tests. Test setup is shown in Fig. 15.4a. Free boundary conditions of the test plate were simulated by hanging the plate with two cotton ropes through the small holes at corners of the plate as shown in Fig. 15.4b. Dimensions of the plate are shown in Fig. 15.4b. An impact hammer PCB 068C05 was used to excite the plate in the form of single impact. A single-point laser with a diffractive optical element was used to project laser spots to the plate structure. A digital camera, Photron AX200, was used to capture images of the plate vibrating. Nine impact points and 100 measurement points were selected. The EMA method with the point-tracking technique under the three-dimensional kinematic relation was conducted on a square plate made of low carbon steel. The location of the impact point was determined based on the first six out-of-plane elastic mode shapes from the finite element model of the plate to avoid most nodal lines.

To validate the results, a LDV and a finite element model of the test object were used. The LDV was used for comparison of natural frequencies. Both laser vibrometer and the camera measurement operated simultaneously. A finite element model of the plate was constructed using ABAQUS. In the finite element model, the plate had a mass density of 7900 kg/m^3, Young's modulus of 210 GPa, and Poisson's ratio of 0.26. A total number of nine impact locations were tested to be compared well with the finite element model.

15.3.2 Data Processing

At each measurement points, five sets of excitation and response measurement data were collected and used to calculate the associate averaged FRF with the H$_1$-algorithm. Exponential window was applied to the collected response measurement data. To reduce any random error caused by excessive optical intensities that might cause error in calculating the centroids, external lights were turned off during the experiment as shown in Fig.15.4a (Table 15.1).

Images taken from the camera were calibrated using Matlab Image Tool box with 20 checkerboard images with different angles. Once images were taken, each image was divided into subsets with one side length of 36 pixels. Reference image was used to locate the highest optical intensity point of 100 measurement points. Using the aforementioned location, subsets were created and centroids of light intensities of each subset was calculated using Eq. (15.2). The centroids from the reference

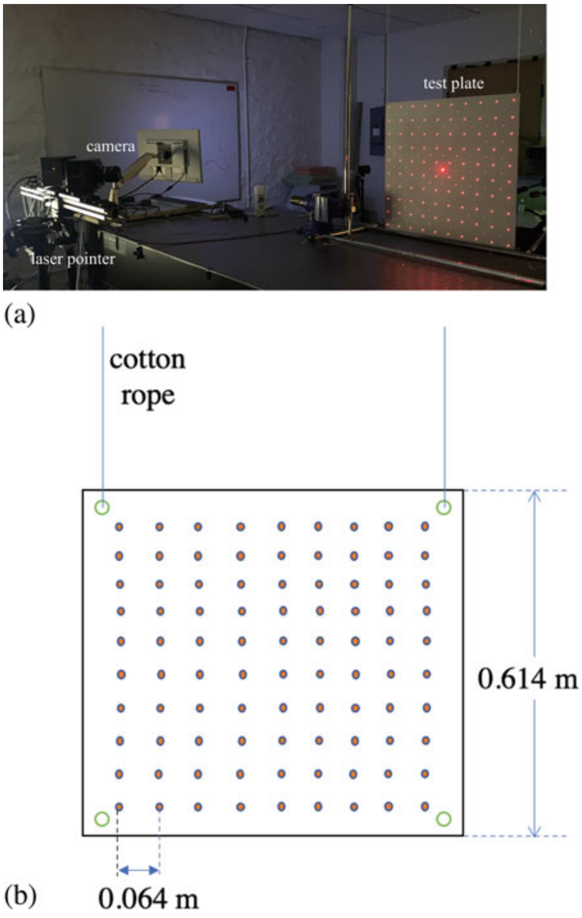

(a)

(b)

Fig. 15.4 (**a**) Test setup of the photogrammetry-based EMA technique and (**b**) sketch of the tested plate with indicated measurement points

Table 15.1 MAC values in percent between the first six mode shapes of the test plate from the photogrammetry-based EMA method (row) and from the finite element model (column)

Mode	1	2	3	4	5	6
1	95.8	0.02	0.008	0.2	0.1	0.005
2	0.02	94.0	2.4	0.02	0.04	0.1
3	0.03	2.1	94.68	0.6	0.06	0.01
4	1.2	0.01	0.5	91.3	7.5	0.1
5	0.02	0.2	0.6	6.2	90.9	0.08
6	0.03	0.9	0.1	0.01	0.4	94.5

Table 15.2 MAC values in percent using w_i and w to demonstrate the effect of the correction factors

Mode	w_i	w
1	97.2	99.4
2	95.6	96.76
3	94.9	95.05
4	88.67	91.29
5	88.61	90.92
6	92.61	94.5

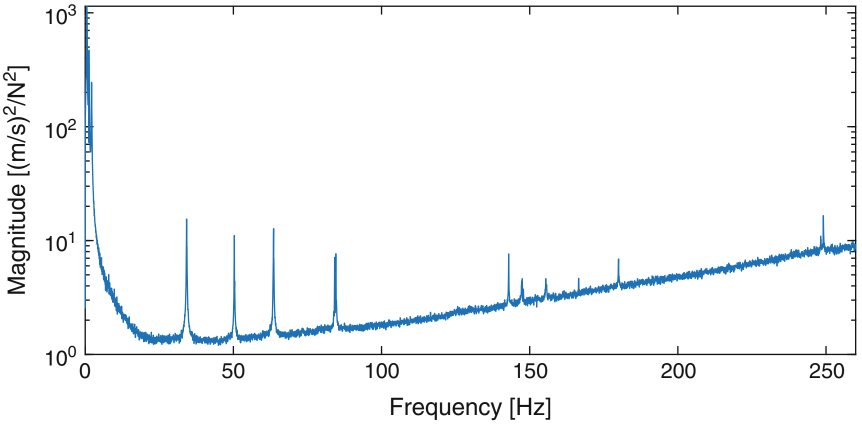

Fig. 15.5 Sum of auto spectra of measured FRFs associated with the 100 measurement points. Each peak in the sum indicates a possible mode of the test plate

image were compared with other centroids from other images to obtain displacements w. The calculated correction factors from the kinematic relation was used to correct the displacements obtained from measured data and the effects of correction factors are shown in Table 15.2.

15.3.3 EMA Method Results

FRFs associated with the 100 measurement points were analyzed by the modal parameter estimation algorithm PolyMax in LMS Test Lab 17 [19]. The sum of auto spectra of the 100 analyzed FRFs is shown in Fig. 15.5 to assist identification of the elastic modes of the plate. Based on the measured FRFs, estimated natural frequencies and mode shapes associated with the first 6 out-of-plane elastic modes of the plate were obtained.

To validate results, LDV and a finite element model of the test object were used. Laser vibrometer was used for comparison of natural frequencies where both laser vibrometer and the camera measurement operated simultaneously. The estimated natural frequencies were validated by the natural frequencies of LDV measurement results. The finite element (FE) model of the plate was constructed using ABAQUS. In the finite element model, the plate had a mass density of 7900 kg/m^3, Young's modulus of 210 GPa, and Poisson's ratio of 0.26. The experimentally estimated mode shapes associated with the first four out-of-plane elastic modes are shown in Fig. 15.6. A modal assurance criterion (MAC) matrix [20] between the first six out-of-plane mode shapes from the FE model and experimentally estimated ones was calculated and all diagonal entries of the MAC matrix were over 90%, indicating that the mode shapes of the same modes were highly correlated.

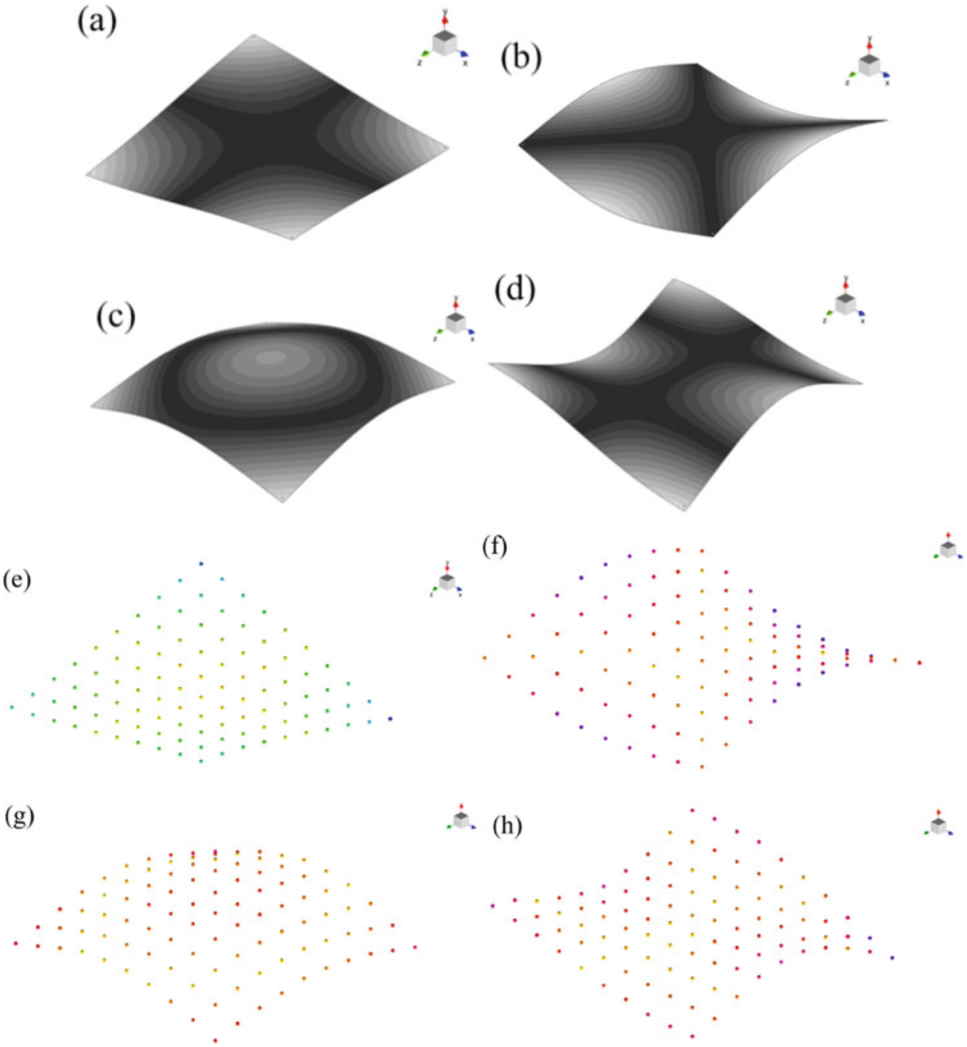

Fig. 15.6 (**a**) First, (**b**) second, (**c**) third, and (**d**) fourth mode shapes of the test plate and they were calculated from the FE model; the (**e**) first, (**f**) second, (**g**) third, and (**h**) fourth experimentally estimated mode shapes of the test plate

Based on the comparison of the MAC matrix, as shown in Table 15.1 photogrammetry EMA method for plate structures was experimentally validated.

15.4 Conclusion

An expanded experimental investigation of the proposed photogrammetry-based EMA method [1] is conducted and validated. Test setup had a square steel plate sheet instead of a cantilever beam [1], leads to more investigation on both axis small amplitude displacements oriented at the image plane. The correction factor of the measured displacements was calculated from a three-dimensional kinematic relation model between a camera's image plane and a plane oriented at the test plate and applied. Modified displacements and single impulsive forces were used to obtain FRFs. Mode shapes of obtained FRFs were compared with those from a finite element model. Their MAC values for the first six out-of-plane displacements were all over 90% which supports the accuracy of the EMA method.

References

1. Xu, Y.F.: A photogrammetry-based experimental modal analysis method by tracking visible laser spots. Measurement **151**, 106963 (2020)
2. Olaszek, P.: Investigation of the dynamic characteristic of bridge structures using a computer vision method. Measurement **25**, 227–236 (1999). https://doi.org/10.1016/S0263-2241(99)00006-8
3. Morlier, J., Salom, P., Bos, F.: New image processing tools for structural dynamic monitoring. Key Eng. Mater. **347**, 239–244 (2007). Trans Tech Publications
4. Ryall, T., Fraser, C.: Determination of structural modes of vibration using digital photogrammetry. J. Aircraft **39**, 114–119 (2002)
5. Helfrick, M.N., Niezrecki, C., Avitabile, P., Schmidt, T.: 3D digital image correlation methods for full-field vibration measurement. Mech. Syst. Signal Process. **25**, 917–927 (2011)
6. Baqersad, J., Poozesh, P., Niezrecki, C., Avitabile, P.: Photogrammetry and optical methods in structural dynamics–a review. Mech. Syst. Signal Process. **86**, 17–34 (2017)
7. Peters, W.H., Ranson, W.F.: Digital imaging techniques in experimental stress analysis. Opt. Eng. **21**(3), 427–431 (1982)
8. Sutton, M., Wolters, W., Peters, W., Ranson, W., McNeill, S.: Determination of displacements using an improved digital correlation method. Image Vis. Comput. **1**, 133–139 (1983)
9. Chu, T., Ranson, W., Sutton, M.: Applications of digital-image-correlation techniques to experimental mechanics. Exp. Mech. **25**, 232–244 (1985)
10. Luo, P., Chao, Y., Sutton, M., Peters Iii, W.: Accurate measurement of three-dimensional deformations in deformable and rigid bodies using computer vision. Exp. Mech. **33**, 123–132 (1993)
11. Pappa, R., Black, J.T., Blandino, J.R., Jones, T.W., Danehy, P.M., Dorrington, A.A.: Dot-projection photogrammetry and videogrammetry of gossamer space structures. J. Spacecraft Rock. **40**, 858–867 (2003)
12. Pappa, R.S.: Photogrammetry and videogrammetry methods for solar sails and other gossamer structures. In: 45th AIAA/ASME/ASCE/AHS/ASC Structures, Structural Dynamics & Materials Conference 2004
13. Yang, F.J., He, X.Y.: Digital speckle projection for vibration measurement by applying digital image correlation method. In: Key Engineering Materials, pp. 99–102 (2006). Trans Tech Publications, Stafa-Zurich
14. Ji, Y., Chang, C.C.: Identification of structural dynamic behavior for continuous system based on videogrammetric technique. In: Proceedings of the SPIE 6173, Smart Structures and Materials 2006: Smart Structures and Integrated Systems, 2006, pp. 61731I-61731I-61712. https://doi.org/10.1117/12.657828
15. Chang, C.C.: From photogrammetry, computer vision to structural response measurement. In: Proceedings of the SPIE 6529, Sensors and Smart Structures Technologies for Civil, Mechanical, and Aerospace System, 2007, pp. 652903-652903-652915
16. Ji, Y.F., Chang, C.C.: Nontarget image-based technique for small cable vibration measurement. J. Bridge Eng. **13**(1), 34–42 (2008)
17. Kim, S.-W., Kim, N.-S.: Dynamic characteristics of suspension bridge hanger cables using digital image processing. NDT E Int. **59**, 25–33 (2013). https://doi.org/10.1016/j.ndteint.2013.05.002
18. Chen, J.G., Wadhwa, N., Cha, Y.-J., Durand, F., Freeman, W.T., Buyukozturk, O.: Modal identification of simple structures with high-speed video using motion magnification. J. Sound Vib. **345**, 58–71 (2015). https://doi.org/10.1016/j.jsv.2015.01.024
19. LMS International, LMS Test, Lab Modal Analysis, Leuven, 2017
20. Ewins, D.J.: Modal Testing: Theory, Practice and Application, 2nd edn. Wiley, New York (2000)

Chapter 16
An Optical Mode Shape-Based Damage Detection Using Convolutional Neural Networks

Celso T. do Cabo and Zhu Mao

Abstract One of the most widely used methods for structural health monitoring (SHM) is vibration-based, in which changes of the dynamics of a structure are collected and associated to damages. While the change of the natural frequencies may be influenced by many different factors, mode shapes provide a more informative feature set in identifying damages. However, most of the sensing hardware, such as accelerometers, and even some of the noncontact techniques, such as laser Doppler vibrometer, are only able to take measurements from specific locations, leading to a limited spatial resolution of deformation field. The use of camera-based sensing allows the extraction of information at much denser locations on a structure. Among the current techniques for motion sensing, phase-based motion estimation (PME) and phase-based motion magnification (PMM) aim to extract and amplify subtle motions, allowing the extraction of full-field mode shapes with an enhanced visibility. Convolutional neural network (CNN) is applied to metamodel the amplified mode shapes extracted from both undamaged baseline and damaged conditions. A lab-scale testbed is employed to provide data to validate the damage identification approach via the CNN algorithm under different operational conditions.

Keywords Structural health monitoring · Convolutional neural network · Phase-based motion magnification · Machine learning · Optical measurement

16.1 Introduction

Among the variety of possible methods for applying structural health monitoring (SHM) in structures, vibration-based approach is widely used for its clear physics and easy implementation. Commonly, the damage-induced structural dynamics changes which led to nonlinearities may serve as a possible feature to identify structural damage according to Chanpheng et al. [1] and Worden et al. [2]. Such detection of damages may not always be straightforward due to the complexity of the system and environmental uncertainties; therefore, machine learning is oftentimes applied, such as the work done by Gordan et al. [3], using data mining-based algorithms.

However, for complex structures such as truss bridges, the application of a structural health monitoring system will require the installation of an acquisition system dedicated exclusively to the structure, leading to an increasing cost. Aiming to reduce the costs and increasing the portability of the data acquisition hardware, many researches are focusing on the use of camera-based sensing for online structural health monitoring. There is a rich literature such as the use of cameras to estimate load by Zaurin and Catbas [4] and measure static deformation in Dong et al. [5]. In addition, investigation on the reliability of video processing techniques was done previously by Sarrafi et al. [6], and particularly, Poozesh et al. [7] studied the feasibility to apply phase-based motion magnification to extract operational mode shapes of structures. do Cabo et al. [8] also investigated the use of phase-based motion estimation and magnification to identify shifts of structural frequency to identify damages. Yang et al. [9] also developed a method to blindly identify a mode shape and then apply motion magnification to it.

Other approaches with video-based information were adopted to determine full-field mode shapes, such as using drones and capturing partial mode shapes of a large structures before assembling the full field by Hoskere et al. [10]. Also, Javh et al. [11] used cameras with a low-frequency acquisition alongside with accelerometers to extract high-frequency mode shapes. Gorjup et al. [12] used a single camera at different observation points to extract 3D mode shapes of a complex structure. Damage localization was also studied by Yang et al. [13] applying fractal dimensions in full-field mode shapes of beams.

C. T. do Cabo (✉) · Z. Mao
Department of Mechanical Engineering, University of Massachusetts Lowell, Lowell, MA, USA
e-mail: celso_docabo@student.uml.edu

D. Di Maio, J. Baqersad (eds.), *Rotating Machinery, Optical Methods & Scanning LDV Methods, Volume 6*, Conference Proceedings of the Society for Experimental Mechanics Series, https://doi.org/10.1007/978-3-030-76335-0_16

The objective of the presented work is to use the full-field mode shape information obtained by camera as input for a convolutional neural network (CNN) in order to recognize whether or not the structure has a damage. Phase-based motion magnification (PMM) is adopted to isolate and highlight the first bending mode of a laboratory scale truss bridge. Later motion-magnified video is processed through the CNN algorithm. This paper has initially a brief introduction on phase-based motion magnification and convolutional neural networks. Afterward there are the experimental data obtained of a laboratory scale truss bridge, with the data processing and the results. Finally, a conclusion is given.

16.2 Phase-Based Motion Magnification

Inside the field of motion estimation using optical flow, there are many techniques presented in researches. Wadhwa et al. [14] developed an algorithm capable of amplifying subpixel motions and generating a new video permitting the user to see the subtle motion. According to Poozesh et al. [7] and Sarrafi et al. [15], the use of phase-based motion is a robust method in order to avoid disturbance and noise. It also has a higher accuracy, permitting a subpixel accuracy if compared to other techniques. First, the intensities, I(x, y, t), in the time domain are gathered which permits a transition into the complex domain via a convolution using directional Gabor wavelets. Equation 16.1 describes the complex polar form containing the phase and amplitude of each pixel.

$$C_\theta = A_\theta e^{i\phi_\theta(x,y,t)} \tag{16.1}$$

The pixel phase, $\phi_\theta(x, y, t)$, is then band-passed between a frequency range which contains an a priori natural frequency from experimental testing. Following the band-passing of pixel phase, $\psi_\theta(x, y, t)$, a magnification factor, α, is then applied to amplify subtle movements. Equation 16.2 describes the reformulation of each frame with corresponding phase and magnification factor.

$$\widetilde{C}_\theta = A_\theta e^{i\alpha\psi_\theta(x,y,t)} \tag{16.2}$$

In this paper, the phase-based motion magnification is applied in truss bridge structures in order to obtain its vibration information, as the motions of the structure are amplified; it is possible to extract subtle movements and its natural frequencies, to later, identify shifts on those frequencies that can be caused by damage.

16.3 Convolutional Neural Networks

Convolutional neural networks (CNN) are a particular category of deep learning algorithms capable to classify information, such as images, texts, or sounds, with outstanding performance. It is a supervised learning technique, in which two or more classes of sets are used as training sample and testing. For image applications, it converts the image into a matrix and then applies a convolution operation with a feature detector in order to create a feature map. Later the pooling operation is applied, subsampling the layer and highlighting its features. These processes can be repeated; it is common to have convolutional neural networks with two or three layers. After this process is finished, the matrix is flattened into a vector which will be used as input for the neural network. Fig. 16.1 demonstrates an example of the convolutional neural network process.

16.4 Methodology

In order to train the convolutional neural network algorithm, labeled information is needed. For that reason, tests were done on a laboratory-scale bridge with different labels in those training conditions. Using a loaded mass cart as input, videos are recorded at 120 frames per second with the response of the bridge in different conditions, starting with the healthy condition and then with different damage locations. The damages were simulated by extracting members from the bridge. Applying phase-based motion magnification, it is possible to isolate one specific mode from the rest, which is, in this case, the first bending mode. Figure 16.2(a) shows the laboratory-scale bridge during the test and Fig. 16.2(b) shows the same image with the amplified motion. An exaggerated motion may be found at the bottom of the mid-span.

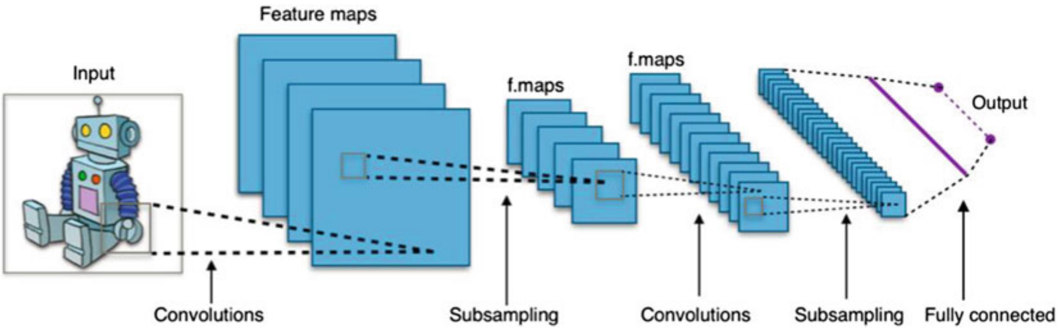

Fig. 16.1 Convolutional neural network Scheme [16]

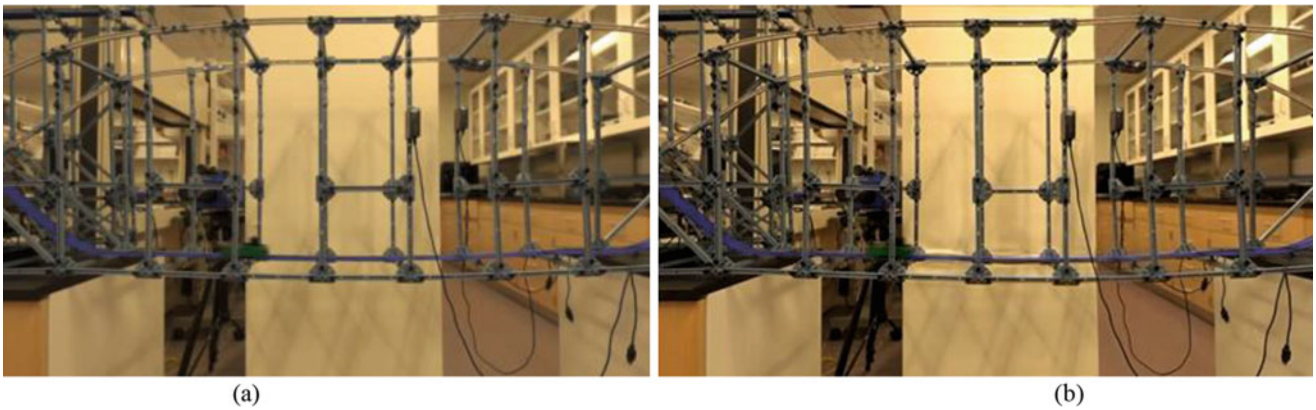

Fig. 16.2 Bridge model testing (**a**), bridge model testing with motion magnification (**b**)

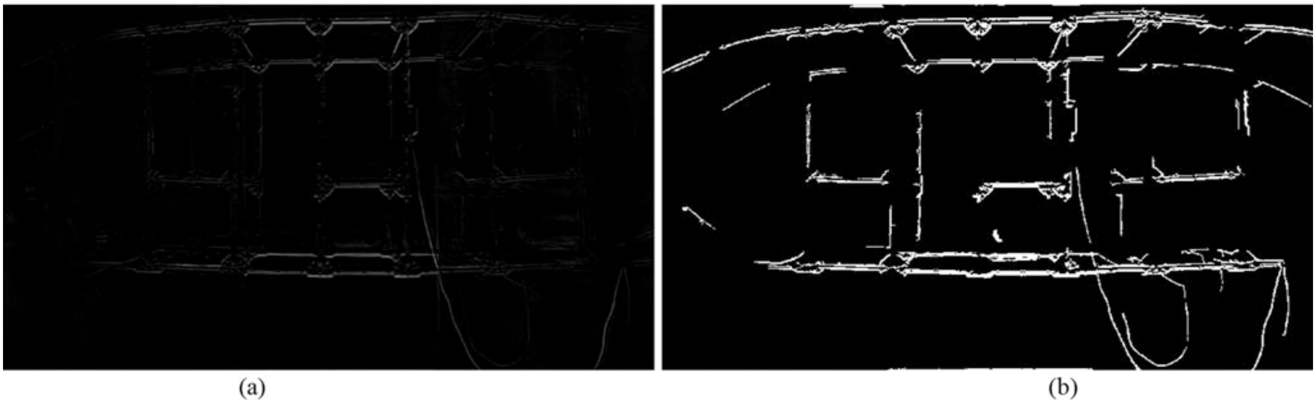

Fig. 16.3 Subtraction of frames (**a**), subtraction of frames with contrast increased (**b**)

However, as the background of the video has many details and the frames are similar to a high degree, information could be lost, and the model accuracy would be reduced during the convolution operation and subsampling of the algorithm. To mitigate this issue, one frame in the video is employed as reference, and the subsequent frames are subtracted from this first one, generating images similar to Fig. 16.3(a). Therefore, only the difference from frame to frame is saved. Since the movements, even with the magnified motion, are small, the contrast of the image is increased too as shown in Fig. 16.3(b).

In Fig. 16.3, the frame has information of the entire structure, and since the damage applied was the extraction of one component, it actually can be seen in the frame itself, even with the subtraction of the frames. In Fig. 16.4, it can be observed a section of the healthy (a) and damaged case (b), and it is easily visible where the damaged is located; in the figure, it is highlighted in red. Therefore, aiming to hide the damage to the algorithm, it was selected a region of the frame to be the new input for the algorithm, and it can be seen in Fig. 16.4 for a healthy scenario (c) and damaged scenario (d). By doing this, the

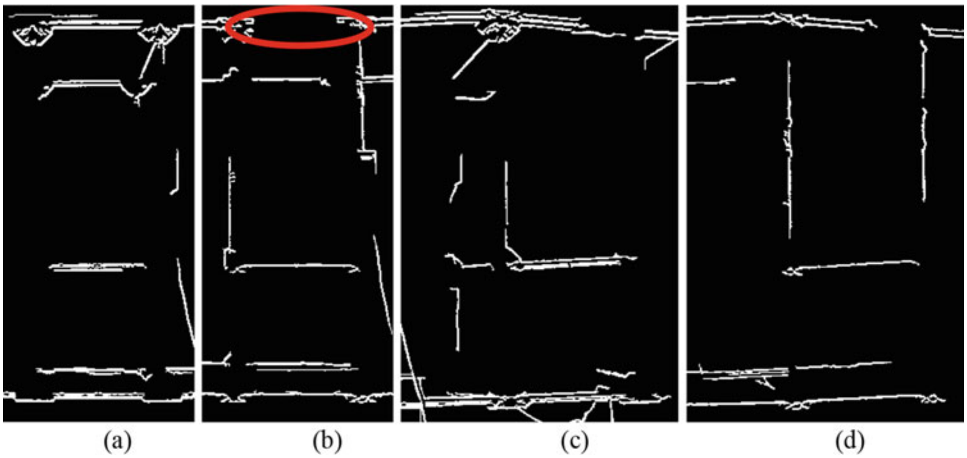

Fig. 16.4 Section with damage for a healthy (**a**) and a damaged case (**b**), section selected without damage for a healthy (**c**) and a damaged case (**d**)

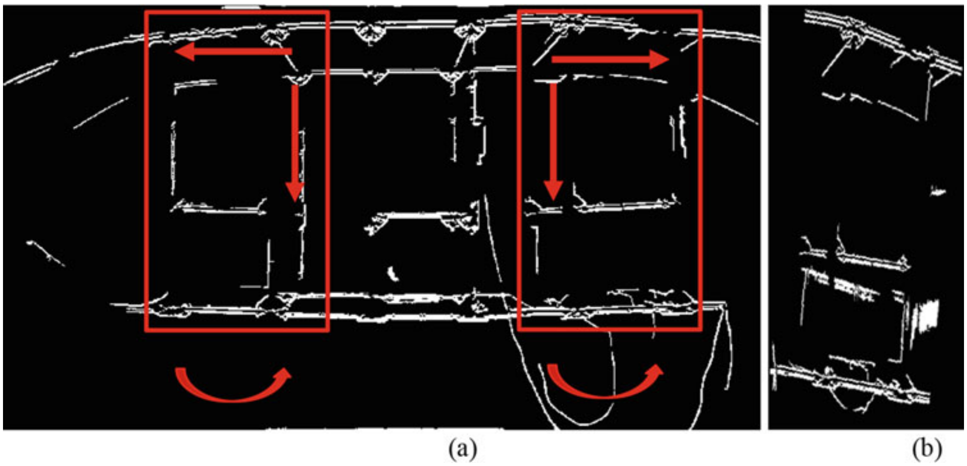

Fig. 16.5 Highlight of the selected sections and explanation on the data augmentation (**a**) and a sample of one of the selections (**b**)

difference of extracted deformation of the operating deflection shape will be used for the damage localization, rather than the missing part of the geometry.

Considering cases where the data collected is limited, the number of frames for each case was limited to 2000 for training. However, decreasing the quantity of data in a deep learning algorithm may lead to a degraded accuracy and robustness. Techniques of data augmentation were applied in this study. The three most common techniques for data augmentation were considered, which are adding random noise and rotating and translating the images. Since the frames were saved as a binary matrix to increase contrast, it was decided to apply just rotation and translation for the data augmentation as Fig. 16.5 demonstrates.

Section on both left and right sides of the bridge is selected, shown by the red boxes in Fig. 16.5(a). For the data augmentation, this box was translated in the vertical and horizontal as shown by the arrows in the figure, at a random number of pixels, and rotated at a random angle as well. Repeating this procedure, 20,000 more frames were generated for both damage conditions, leading to 40,000 frames in total and 28,000 frames for training and 12,000 frames for testing. Figure 16.5(b) shows an example of the section with a random translation and rotation.

The parameters of the convolutional neural network algorithm are presented in Table 16.1 above. The loss function was calculated using the mean absolute error (MAE) and can be seen in Fig. 16.6(a). As the result shows, error during the training was around 0.1, which is still considered high for a machine learning algorithm. However, after the data augmentation, it can be seen that the error for the testing sample is also of the same magnitude, while for preliminary trainings the loss function for testing reached values 10 times higher than in the testing. This model predicted 60% of the healthy frames and 69% of the damaged for validation correctly; a graphic form of the results can be seen in Fig. 16.4(b).

Table 16.1 Parameters of the convolutional neural network

	Layer 1	Layer 2	Layer 3
Convolutional layer	*k*(3*3)/*c*(32)	*k*(3*3)/*c*(32)	*k*(3*3)/*c*(64)
Max pooling layer	*k*(4*4)	*k*(4*4)	*k*(4*4)
Activation function	ReLU	ReLU	Sigmoid
Epochs	20		
Batch size	32		

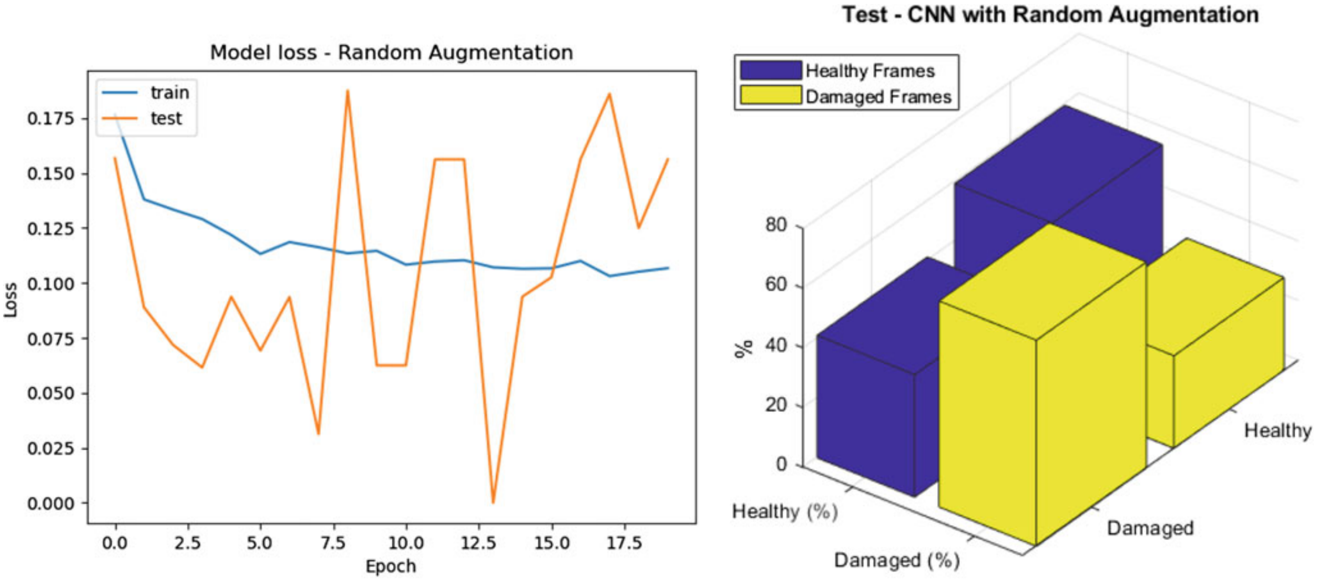

(a) (b)

Fig. 16.6 Loss function of the convolutional neural network model (**a**) and the results from the validation test (**b**)

16.5 Conclusion

Video-based techniques for dynamic identification of structures show a great potential in the past decade. It has great aptitude to extract full-field mode shapes, which is not easily achievable with traditional sensing techniques. The better portability enables faster test setup and lowers the costs with dedicated data acquisition systems. It is also proved that the data collected by cameras has a good accuracy compared to traditional sensing techniques.

The use of PMM can help and enhance the extraction of structural frequencies and full-field mode shapes, and the convolutional neural network (CNN) adopted in this paper shows a powerful deep learning capability to classify damages from individual snapshots of a vibrating structure. Although its parameter tuning may be time-consuming, with a sufficient number of images/frames, it demonstrates an improvement in the accuracy. Without time-dependent information, such as natural frequencies or the change of mode shapes with time, it can classify differences in a vibrating structure.

Acknowledgments Funding for this research is provided by the Transportation Infrastructure Durability Center at the University of Maine under grant 69A3551847101 from the US Department of Transportation's University Transportation Centers Program.

References

1. Chanpheng, T., Yamada, H., Katsuchi, H., Sasaki, E.: Nonlinear features for damage detection on large civil structures due to earthquakes. Struct. Health Monit. **11**, 482–488 (2012). https://doi.org/10.1177/1475921712437182
2. Worden, K., Farrar, C., Haywood, J., Todd, M.: A review of nonlinear dynamic applications to structural health monitoring. Struct. Control. Health Monit. **15**, 540–567 (2008). https://doi.org/10.1002/stc.215

3. Gordan, M., Ismail, Z., Razak, H.A., Ghaedi, K., Ibrahim, Z., Tan, Z.X., Ghaayeb, H.H.: Data mining-based damage identification of a slab-on-girder bridge using inverse analysis. Measurement. **151**, 107175 (2020)
4. Zaurin, R., Catbas, N.: Structural health monitoring with emphasis on computer vision, damage indices, and statistical analysis. Ph.D. dissertation, College of Eng. and Computer Sc., University of Central Florida, Orlando (2009)
5. Dong, C., Bas, S., Catbas, N.: A completely non-contact recognition system for bridge unit influence line using portable cameras and computer vision. Smart Struct Syst. **24**, 617–630 (2019). https://doi.org/10.12989/sss.2019.24.5.617
6. Sarrafi, A. & Poozesh, P. & Mao, Z.: “A comparison of computer-vision-based structural dynamics characterizations,” model validation and uncertainty quantification, Volume 3: Proceedings of the 35th IMAC, A Conference and Exposition on Structural Dynamics, pp. 295–301 (2017)
7. Poozesh, P., Sarrafi, A., Mao, Z., Avitabile, P., Niezrecki, C.: Feasibility of extracting operating shapes using phase-based motion magnification technique and stereo-photogrammetry. J. Sound Vib. **407**, 350–366 (2017)
8. do Cabo, C., Valente, N., Mao, Z.: Motion magnification for optical-based structural health monitoring. Proc SPIE. **11381** (2020). https://doi.org/10.1117/12.2559266
9. Yang, Y., Dorn, C., Mancini, T., Talken, Z., Kenyon, G., Farrar, C., Mascareñas, D.: Blind identification of full-field vibration modes from video measurements with phase-based video motion magnification. Mech. Syst. Signal Process. **85**, 567–590 (2017a)
10. Hoskere, V., Park, J., Yoon, H., Spencer, B.: Vision-based modal survey of civil infrastructure using unmanned aerial vehicles. J Struct Eng (US). **145** (2019). https://doi.org/10.1061/(ASCE)ST.1943-541X.0002321
11. Javh, J., Slavič, J., Boltežar, M.: Experimental modal analysis on full-field DSLR camera footage using spectral optical flow imaging. J. Sound Vib. **434**, 213–220 (2018). https://doi.org/10.1016/j.jsv.2018.07.046
12. Gorjup, D., Slavič, J., Boltežar, M.: Frequency domain triangulation for full-field 3D operating-deflection-shape identification. Mech. Syst. Signal Process. **133**, 106287 (2019). https://doi.org/10.1016/j.ymssp.2019.106287
13. Yang, Y., Dorn, C., Mancini, T., Talken, Z., Theiler, J., Kenyon, G., Farrar, C., Mascareñas, D.: Reference-free detection of minute, non-visible, damage using full-field, high-resolution mode shapes output-only identified from digital videos of structures. Struct. Health Monit. **17** (2017b). https://doi.org/10.1177/1475921717704385
14. Wadhwa, N., Rubinstein, M., Durand, F., Freeman, W.: Phase-based video motion processing. ACM Trans. Graph. **32**(4), 80 (2013)
15. Sarrafi, A., Mao, Z., Niezrecki, C., Peyman, P.: Vibration-based damage detection in wind turbine blades using phase-based motion estimation and motion magnification. J. Sound Vib. **421**(12), 300–318 (2018)
16. Kone, C.: Introducing convolutional neural networks in deep learning. https://towardsdatascience.com/introducing-convolutional-neural-networks-in-deep-learning-400f9c3ad5e9. 2019

Chapter 17
Full-Field 3D Experimental Modal Analysis from Dynamic Point Clouds Measured Using a Time-of-Flight Imager

Moisés Silva, Andre Green, John Morales, Peter Meyerhofer, Yongchao Yang, Eloi Figueiredo, and David Mascareñas

Abstract The ability to measure static, high-resolution 3D point cloud data has existed for multiple decades and has been used to great benefit in both civil and mechanical engineering applications. Recently, time-of-flight imagers have emerged that are capable of measuring 3D dynamic point clouds at rates as high as 30 point cloud captures per second with resolutions approaching the millimeter scale. Conventional modal analysis utilizes contact measurements that are captured in the Lagrangian (i.e., material) coordinate system. Imager measurements such as used for DIC are captured in what is approximately an Eulerian frame of reference. However, oftentimes the imager measurements are captured in a small-motion, sub-pixel regime and can be assumed to be captured in a Lagrangian reference frame. As a result, most experimental modal identification algorithms are designed to operate on data captured in a Lagrangian reference frame. Measurements of 3D point clouds of vibrating structures do not necessarily fit into either an Eulerian or Lagrangian framework, particularly in the case where motion of the structure is large. An additional feature of these measurements is that the number of points measured on the structure can change significantly through time as a result of occlusions, the change in angle of the structure, or simply noise in the measurement. This feature of point clouds is significantly different from imagers and contact sensors in which the dimensionality of the measurements does not change through time. In this work we present the first known technique for extracting structural dynamics information from dynamic point clouds.

Keywords 3D mode identification · 3D dynamic point clouds · Time-of-flight imaging · Blind source separation

17.1 Introduction

The most common approach to perform experimental and operational modal analysis requires physically attached wired or wireless sensors, such as accelerometers or vibrometers [1]. Those sensor networks can only provide measurements at discrete spatial points (i.e., sensors positioned at sparse locations of the structure result in poor spatial resolution) and are usually limited to only a small number of sensors that can be placed over the structure's surface. For all those cases, video-based approaches provide attractive alternatives, as their implementation can provide high-spatial resolutions since they consider each pixel as a potential displacement sensor, achieving full-field measurements with the same resolution as the number of pixels in the video. Amid the various imaging technologies available, laser-based imagers, such as Lidar mapping systems [1, 2], have particularly become important tools to rapidly acquire large-scale 3D point cloud data for real-time monitoring. These sensors provide accurate 3D geometrical information and additional features about the reflection properties and compactness of the surfaces [2]. Related time-of-flight (ToF) imagers can immediately indicate the distance to an object and its direction based on the time difference between the emission of a light pulse and its return, resulting in highly dense 3D point clouds.

M. Silva
Applied Electromagnetism Laboratory, Federal University of Pará, Belém, Brazil

A. Green · J. Morales · P. Meyerhofer · D. Mascareñas (✉)
Engineering Institute, Los Alamos National Laboratory, Los Alamos, NM, USA
e-mail: dmascarenas@lanl.gov

Y. Yang
Department of Mechanical Engineering, Michigan Technological University, Houghton, MI, USA

E. Figueiredo
Faculty of Engineering, Universidade Lusófona de Humanidades e Tecnologias, Lisbon, Portugal

D. Di Maio, J. Baqersad (eds.), *Rotating Machinery, Optical Methods & Scanning LDV Methods, Volume 6*, Conference Proceedings of the Society for Experimental Mechanics Series, https://doi.org/10.1007/978-3-030-76335-0_17

This paper introduces an initial step toward transitioning the current modal analysis techniques to full-field 3D measurements using a cheap and ready-to-use commercial imager. By exploring the ToF sensors built into the Azure Kinect [3], we are able to estimate real-time dynamic point clouds at high spatial resolution, with the potential for capturing many thousands of measurement points at 30 fps. In dynamic point clouds, the number of points changes dynamically over time due to changes in environmental noise, illumination conditions, and the dynamics of moving objects. This problem motivated the development of an imager-based sensing approach to emulate the sampling strategy often performed with physically attached sensors. We create a dense mesh of virtual sensors that capture real-time 3D motion from the dynamic point cloud, from which solutions to the blind source separation (BSS) problem are employed to identify modal parameters and extract dynamic 3D mode shapes. Next, we show how bending and torsional modes can be comfortably estimated from this point cloud-based strategy in a complete unsupervised and output-only fashion with small amounts of user intervention.

17.2 Background

The proposed output-only 3D modal identification technique can be blindly and autonomously performed using the steps in Fig. 17.1, summarized in the following:

1. The dynamic tracking maps a mesh of virtual sensors onto the structure to capture the motion of the structure at several locations along time. Note that the number of points in the dynamic point clouds is not constant. As a result this modelling step is imperative to enable the measurement of motion in the same structure locations over time. The goal is to define a set of fixed positions on the structure's point cloud data from which the motion is tracked over time to create motion time series, similarly to what is performed with conventional physically attached sensors. This motion tracking is carried out by a three-dimensional polynomial model fitted over the point cloud data and may or not involve a down sampling step to speed up the processing. This step could also conceivably be accomplished using other interpolation techniques such as Gaussian process regression [4, 5].
2. As this mesh of virtual sensors must be densely populated to achieve high-resolution estimation, the estimated motion time series are temporally decomposed by PCA to obtain r active principal components η with active non-zero singular values. Then perform BSS on η to obtain the modal coordinates q_i ($i = 1, \dots, r$), from which modal frequencies, damping ratios, and mode shapes ϕ can be estimated using former solutions for mode estimation from video [6, 7].
3. Finally, one can visualize the 3D mode dynamics by scaling and reconstructing the ith mode ϕ_i using a visualization factor α and a decaying term β. The end result is a scaled version of the original ith mode by a factor α while removing the other modes using the term β. Other modes can be arbitrarily recovered for visualization purposes following the same procedure.

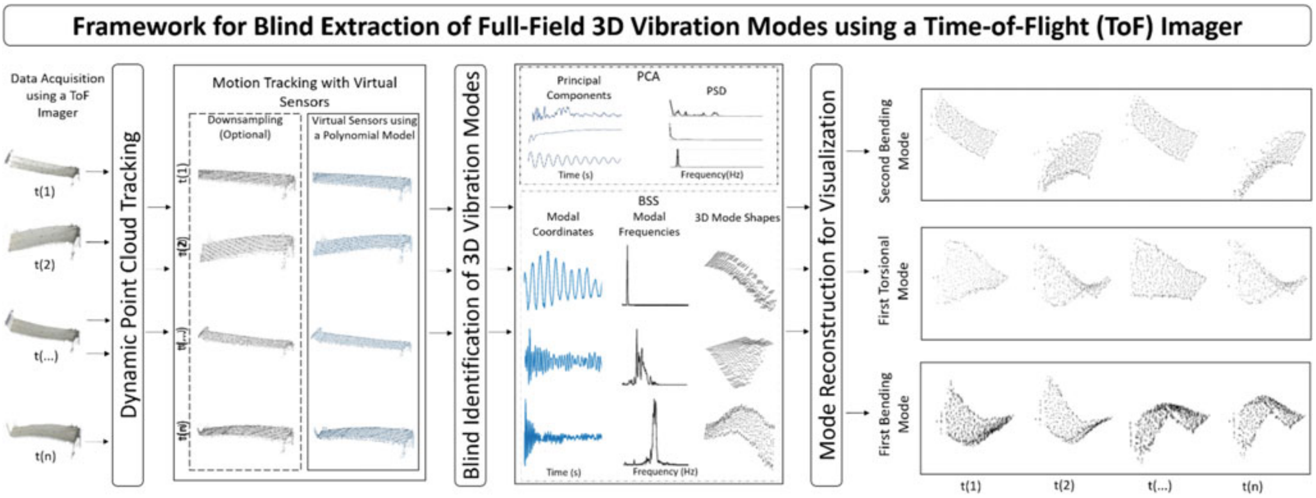

Fig. 17.1 We introduce the first attempt extract 3D modal parameters from dynamic point cloud data in a complete automated and unsupervised fashion. The key feature of this technique is the estimation of displacements from the dynamic cloud

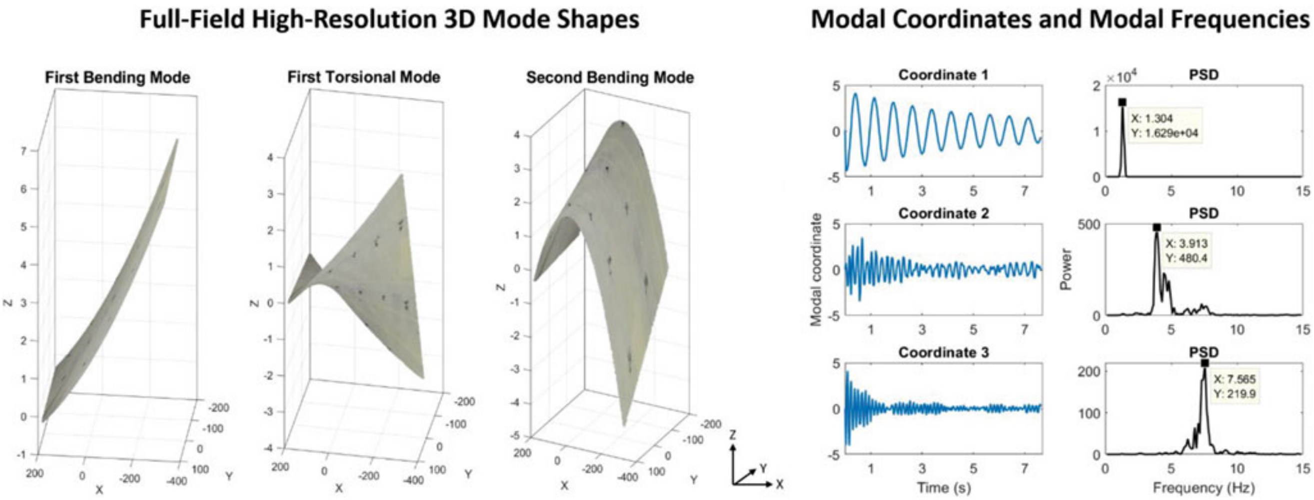

Fig. 17.2 Very high-resolution 3D mode shapes (number of points equal to the number of virtual sensors), modal coordinates, and their power spectral densities (PSD) estimated using the imager-based blind identification approach

17.3 Analysis

Laboratory tests were carried out with a stainless steel plate measuring 65 cm long by 30.5 cm wide. Data acquisition was performed using a Microsoft Azure Kinect camera featuring a ToF sensor. For comparison purposes, three laser displacement sensors were used along with an oscilloscope to estimate displacements at different locations of the plate. The excitation source is a modal hammer, used to impact the plate with a single hit. From the proposed technique, 90.186 virtual sensors were defined throughout the point cloud data (on average, each dynamic cloud has 110.000 points). From the estimated motion time series, the first three individual modes estimated are as follows: first bending mode (at 1.30 Hz), first torsional mode (at 3.91 Hz), and the second bending mode (at 7.56 Hz). In comparison, from the laser data, the same modes were estimated with the following frequencies: 1.35, 4.10, and 7.45 Hz. The recovered mode shapes and modal coordinates are visualized in Fig. 17.2.

17.4 Conclusions

This paper presented a novel formulation for video-based modal analysis and identification using dynamic point cloud data. The BSS paradigm is utilized for unsupervised and output-only parameter estimation. As dynamic point clouds are inherently 3D data sets, the end result is the estimation of 3D high-resolution full-field modal parameters. Here, polynomial functions are used for fitting the data due to its simplicity and broad use in other related applications, such as finite element analysis. Alternatively, other models could be employed; radial basis functions are a suitable alternative to fit more complicated shapes to data. To the authors' best knowledge, the processing of dynamic point clouds for modal analysis has never been attempted before, which endorses the unique contributions here stated.

Acknowledgments This study was financed in part by the CAPES - Brazil - Finance codes 88882.445119/2018-01 and 88881.190499/2018-01. This work was supported by the US Department of Energy through the Los Alamos National Laboratory. Los Alamos National Laboratory is operated by Triad National Security, LLC, for the National Nuclear Security Administration of US Department of Energy (Contract No. 89233218CNA000001). This work was partially funded by the US Department of Energy Microreactor Project.

References

1. Mistretta, F., Sanna, G., Stochino, F., Vacca, G.: Structure from motion point clouds for structural monitoring. Remote Sens. **11**, 1940 (2019)
2. Jo, H.C., Sohn, H.-G., Lim, Y.M.: A lidar point cloud data-based method for evaluating strain on a curved steel plate subjected to lateral pressure. Sensors. **20**, 721 (2020)

3. Bamji, C., et al.: “Impixel 65nm bsi 320mhz demodulated tof image sensor with 3um global shutter pixels and analog binning”, in: *2018 IEEE International Solid - State Circuits Conference* - (ISSCC) (2018)
4. Williams, C.K.I.: Prediction with Gaussian processes: from linear regression to linear prediction and beyond. Learn Graphic Models, 599–562 (1998). https://doi.org/10.1007/978-94-011-5014-9_23
5. Wahaba, G.: Spline models for observational data. SIAM. **59** (1990). https://doi.org/10.1137/1.9781611970128
6. Yang, Y., Dorn, C., Mancini, T., Talken, Z., Kenyon, G., Farrar, C., Mascarenas, D.: Blind identification of full-field vibration modes from video measurements with phase-based video motion magnification. Mech. Syst. Signal Process. **85**, 567 (2017)
7. Silva, M., Martinez, B., Figueiredo, E., Costa, J., Yang, Y., Mascarenas, D.: Nonnegative matrix factorization-based blind source separation for full-field and high-resolution modal identification from video. J. Sound Vib. **487**, 115586 (2020)

Chapter 18
Application of a U-Net Convolutional Neural Network to Ultrasonic Wavefield Measurements for Defect Characterization

Joshua D. Eckels, Isabel F. Fernandez, Kelly Ho, Nikolaos Dervilis, Erica M. Jacobson, and Adam J. Wachtor

Abstract Recent advances in nondestructive evaluation (NDE) techniques have sought to improve the testing speed and accuracy of automatic flaw detection algorithms to minimize the costly downtime of removing in-service parts and components for testing and maintenance. Acoustic wavenumber spectroscopy (AWS) is a rapid NDE technique that utilizes steady-state ultrasonic excitation and laser Doppler vibrometer (LDV) measurements to identify component flaws orders of magnitude faster than traditional time-of-flight ultrasonic NDE techniques. However, current AWS technology is limited when applied to larger domains, such as rooms and larger structures, due to increased processing needs, and it is limited in accuracy and spatial resolution when applied to smaller defects on the order of one wavelength in size as well as defects on the edges of the structure. This paper presents the novel application of a U-Net style convolutional neural network (CNN) to improve the processing speed and spatial resolution of current AWS technology by performing semantic segmentation on simulated ultrasonic wavefield images of a steady-state, single-tone excitation of an aluminum plate. The well-adopted ResNet architecture, which was pre-trained on the large and openly available ImageNet dataset, was trained by transfer learning on the augmented wavefield dataset for the purpose of defect localization and characterization in aluminum plates. Finally, the performance of the CNN processing time and spatial resolution accuracy were shown to improve upon the processing methods of current AWS technology.

Keywords Convolutional neural network · Nondestructive evaluation · Structural health monitoring · Ultrasonic wavefield measurements · Acoustic wavenumber spectroscopy

18.1 Introduction

The identification of material flaws in engineering components and structures for the purpose of performance assessment, testing, and maintenance is collectively referred to as structural health monitoring (SHM) [1]. It is desirable in the engineering community to quickly and efficiently assess the performance capability of in-service parts and components by detecting component flaws and defects, such as corrosions, cracking, and delaminations, to minimize the costly downtime of part inspection and to maximize the safety and lifetime of in-service components. Nondestructive evaluation (NDE) is an essential form of SHM that ensures structural integrity using non-invasive procedures to estimate material properties and the presence of defects without damaging or removing key components from the structure. Much research in the field of NDE focuses on ultrasonic inspection technology for damage identification and quantification [2].

J. D. Eckels
Department of Mechanical Engineering, Rose-Hulman Institute of Technology, Terre Haute, IN, USA

I. F. Fernandez
Daniel Guggenheim School of Aerospace Engineering, Georgia Institute of Technology, Atlanta, GA, USA

K. Ho
Department of Electrical & Computer Engineering, University of Washington, Seattle, WA, USA

N. Dervilis
Department of Mechanical Engineering, The University of Sheffield, Sheffield, UK

E. M. Jacobson · A. J. Wachtor (✉)
NSEC-EI, Los Alamos National Laboratory, Los Alamos, NM, USA
e-mail: ajw@lanl.gov

D. Di Maio, J. Baqersad (eds.), *Rotating Machinery, Optical Methods & Scanning LDV Methods, Volume 6*, Conference Proceedings of the Society for Experimental Mechanics Series, https://doi.org/10.1007/978-3-030-76335-0_18

Recent advances in ultrasonic NDE seek to minimize part inspection downtime and improve the accuracy, reliability, and usability of the technique by reducing processing time and utilizing full-field, non-contact, guided wave measurements of the part or component response. Staszewski et al. [3] and Aryan et al. [4] used a 3D laser Doppler vibrometer (LDV) to obtain the surface velocity response of a plate-like structure to ultrasonic excitation from a piezoelectric transducer (PZT). Local cracks or holes in the plate were detected and quantified by alterations in the transient Lamb wave propagation pattern near the location of the defects. Michaels and Michaels identified bonding flaws in an aluminum plate using acoustic wavefield imaging of transient propagating Lamb waves with a non-contact, air-coupled transducer [5]. Studies by Rogge and Leckey [6] and Ruzzene [7] used a 3D Fourier transform of LDV velocity measurements to visualize defects in the frequency/wavenumber domain. Mesnil et al. improved the processing time of these methods by an order of magnitude by performing frequency/wavenumber domain analysis on a steady-state LDV measurement [8].

Acoustic wavenumber spectroscopy (AWS) is a modern ultrasonic NDE technique that overcomes the noise level and delay issues associated with previous transient wave interaction LDV studies by utilizing the full-field, single-tone, steady-state surface response and wavenumber-domain processing to rapidly visualize and characterize defects in a plate-like structure [9, 10]. A single-tone ultrasonic excitation is applied to the surface of a structure by a PZT, and a 2D scanning LDV obtains the steady-state, out-of-plane surface velocity response of the structure. While most LDV measurements rely on transient Lamb wave interactions with defects for damage detection, AWS uses time-invariant properties of the wave, such as wavenumber, to indicate structural damage [9]. The frequency-wavenumber processing described by Flynn et al. [10] produces a full-field map that estimates the local wavenumber on a pixel-by-pixel basis over the scan area of the structure. For a given excitation frequency and wave mode, local changes in wavenumber correspond to changes in plate geometry or material properties, which is often indicative of damage. Plate thickness can be obtained from Lamb wave dispersion relationships, which relate the frequency and thickness to the wavenumber for different wave modes for a given material [11]. Like wavenumber, changes in plate thickness in a local region of a structure can correspond to areas of hidden damage, such as corrosion, indentation, or delamination underneath the surface of the component.

Despite its performance improvements from previous ultrasonic NDE techniques, AWS has several limitations. In a recent study that explored the performance limits of AWS, O'Dowd et al. noted that wavenumber estimates lose accuracy as the diameter of a defect decreases below the nominal wavelength of the propagating waves [11]. Similarly, wavenumber estimates are inaccurate along the edges of the LDV scan area. Because the AWS algorithm utilizes a spatial Fourier transform to process data in the wavenumber domain, regions of the scan area with limited wavelength information show limited wavenumber estimation accuracy, including smaller diameter defect regions and the regions around the edges of the scan area. O'Dowd et al. also reported lower accuracy in wavenumber estimation for defects with thicknesses slightly lower than the nominal plate thickness [11]. Regions of similar thicknesses correspond to defects with more subtle changes in wavenumber, which are more difficult to distinguish from surrounding undamaged regions. Obtaining the local thickness of the plate from the local wavenumber and Lamb wave dispersion relationships loses accuracy when there are subtle changes in wavenumber, or when the thickness is closer to the plateau region of the dispersion curves [11]. This method of obtaining the local thickness is less precise and can lead to missed detection of defects with a similar thickness as the nominal plate thickness. Another limitation of AWS is the rate at which computational time scales with increasing scan area. As a result, AWS provides full-field response measurements in larger structures and domains at an increased computational expense.

The motivation behind this work was to improve the processing time of AWS and to account for its main limitations in spatial resolution. The limited accuracy of AWS in detecting smaller diameter defects and in regions along the edges of the scan area can be improved by avoiding the resolution artifacts resulting from the spatial Fourier transform. The loss in precision of obtaining plate thickness in regions of subtle changes in wavenumber can be improved by detecting and using plate thickness directly, rather than wavenumber, to indicate and quantify the damage. This work looked into tackling these goals by training a convolutional neural network (CNN) to recognize wave-pattern features directly from a steady-state ultrasonic wavefield image and to classify regions of the image by plate thickness on a pixel-by-pixel basis for damage visualization and quantification, eliminating the intermediate step of wavenumber estimation.

This paper will first provide background information on CNNs, image segmentation, and related work. Then, the methodologies used in this study will be explained in detail. Next, several results will be presented, comparing the performance of the CNN model to current AWS technology. Finally, the paper will discuss the major strengths of the CNN model and areas for future work.

18.2 Background

18.2.1 Convolutional Neural Networks

CNN finds its roots in the Neocognitron [12], a neural network framework proposed by Fukushima that can learn visual patterns based on geometrical similarity without a teacher. A CNN takes in a 2D image as an array of pixel information and passes it through a series of hidden layers. In each layer, a set of filters are passed over the input image to produce an array of filtered images—a process known as convolution. The array of filtered images typically pass through a nonlinear activation function, such as the rectified linear unit (ReLu) function, and a max pooling operation to clean the images and reduce parameter size. Grouped together, this set of operations is known as a convolutional layer. The addition of each convolutional layer allows the CNN to detect a hierarchy of features from pixel values, ranging from simple edges and shapes to more complicated figures and features. After passing through several convolutional layers, the array of images passes through several fully connected (dense) layers that eventually connect to the output layer, which is a list of all possible desired object classifications [13].

The CNN contains a set of parameters, weights, and biases that control the propagation of information between each internal layer. The values of these parameters are learned by the CNN by passing several labeled images through the network and computing the total error between the expected output and the output of the CNN. By passing several training images through the network, the total error is minimized by optimizing the set of weights and biases through stochastic gradient descent and backpropagation [14]. A trained CNN model is good at detecting features in an image and classifying objects invariant of viewpoint, perspective, illumination, scale, background, clutter, or intra-class variation.

Several hyperparameters must be set before training any CNN model. These hyperparameters include the number, type, order, and depth (number of filters) of each layer, the stride length and size of each filter (kernel), and the learning rate. Several mature software platforms exist for the development of CNN models, including Berkeley's *Caffe* platform [15] and Google Brain's *TensorFlow* [16]. Because the setting of hyperparameters highly contributes to the success or failure of any CNN model, it is important to understand the functionality of each layer within the CNN for the model's success in its intended application. The majority of beginning users do not have the depth of experience required to tune these hyperparameters successfully. The lesser-known and forthcoming *Fast.ai* library [17] achieves greater usability by setting these parameters for the user to enable a faster on-ramp in applying CNN models to solve novel engineering problems. The *Fast.ai* library with a *PyTorch* backend [18] was used in the current study.

Recent advancements in CNNs have made them a primary tool for a variety of image processing and computer vision applications, including image classification, object detection and tracking, scene labeling, and visual saliency detection [13]. Of interest to the current study are applications of CNNs to the fields of SHM and NDE. Oliveira et al. proposed the application of a CNN to electromagnetic impedance measurements of an aluminum plate [19]. After exciting a boundary-free aluminum plate with a piezoelectronic transducer and measuring the impedance signal of the plate, the signal was converted to an RGB image for classification by a CNN as a damaged or undamaged plate. Ren et al. developed a modified image segmentation-based CNN for the purpose of identifying cracks in concrete civil infrastructure on a pixel-wise basis [20]. The proposed CNN was capable of outperforming conventional crack detection methods. A deep neural network (DNN) was utilized along with a sliding-window approach to locate welding defects in radiographic NDE X-ray images [21]. Munir et al. compared the performance of a CNN and a DNN in classifying weldment flaws from ultrasonic measurements [22]. The authors reported that the CNN outperformed the conventional DNN in nearly every case in classifying cracks, porosity, slags, and other weldment defects from a noisy ultrasonic signal. Ultrasonic weldment flaws were further studied in [23] where noise was first removed from the data by an autoencoder—a type of DNN—before being passed through a CNN for flaw classification. Virkkunen et al. demonstrated extensive data augmentation on phased-array ultrasonic data for flaw classification with a CNN [24]. In the study, the trained CNN model outperformed human inspection in ultrasonic flaw classification. Meng et al. rearranged the wavelet transform coefficients from A-scan ultrasonic signals into a 2D matrix to be fed into a CNN for feature extraction [25]. The proposed algorithm demonstrated better performance than conventional A-scan pattern recognition techniques. These studies demonstrate the applicability and high performance of CNNs in the field of structural damage detection.

18.2.2 Image Segmentation

Image segmentation, or semantic segmentation, is an important task in the field of computer vision where regions or pixels in an image are classified and color-coded by class or object type. Image segmentation has seen significant development recently in several different fields, including autonomous driving, robotic navigation, remote sensing, and medical imaging [26]. Deep neural networks have shown promising results when applied to image segmentation tasks, including the use of conditional random fields (CRFs) [27, 28], feedback CNNs [29], feedforward labeling of superpixels [30], region-based CNNs (R-CNNs) [31], flexible segmentation graphs (FSGs) [32], fully convolutional networks (FCNs) [33], and up-sampling and deconvolutional layers with multi-path fusion [34–36]. Ronneberger et al. [37] proposed a U-Net style architecture for image segmentation with symmetry between the down-sampling (encoder) and up-sampling (decoder) paths of the neural network, as shown in Fig. 18.1.

Feature maps in the encoder are carried over to the decoder by the horizontal paths in Fig. 18.1 for improved pixel-wise prediction and resolution in the output segmentation map. The U-Net model is a type of FCN, where all model parameters in both the encoder and decoder can be optimized by training the network on a labeled image segmentation dataset. An altered version of the U-Net style architecture was used in the current study. Further detail on image segmentation and object detection can be found in the surveys by Lateef and Ruichek [26] and Liu et al. [38].

18.3 Methodology

18.3.1 Project Overview

Figure 18.2 provides a high-level conceptual map detailing the flow of data between each working subprocess and software component in this study.

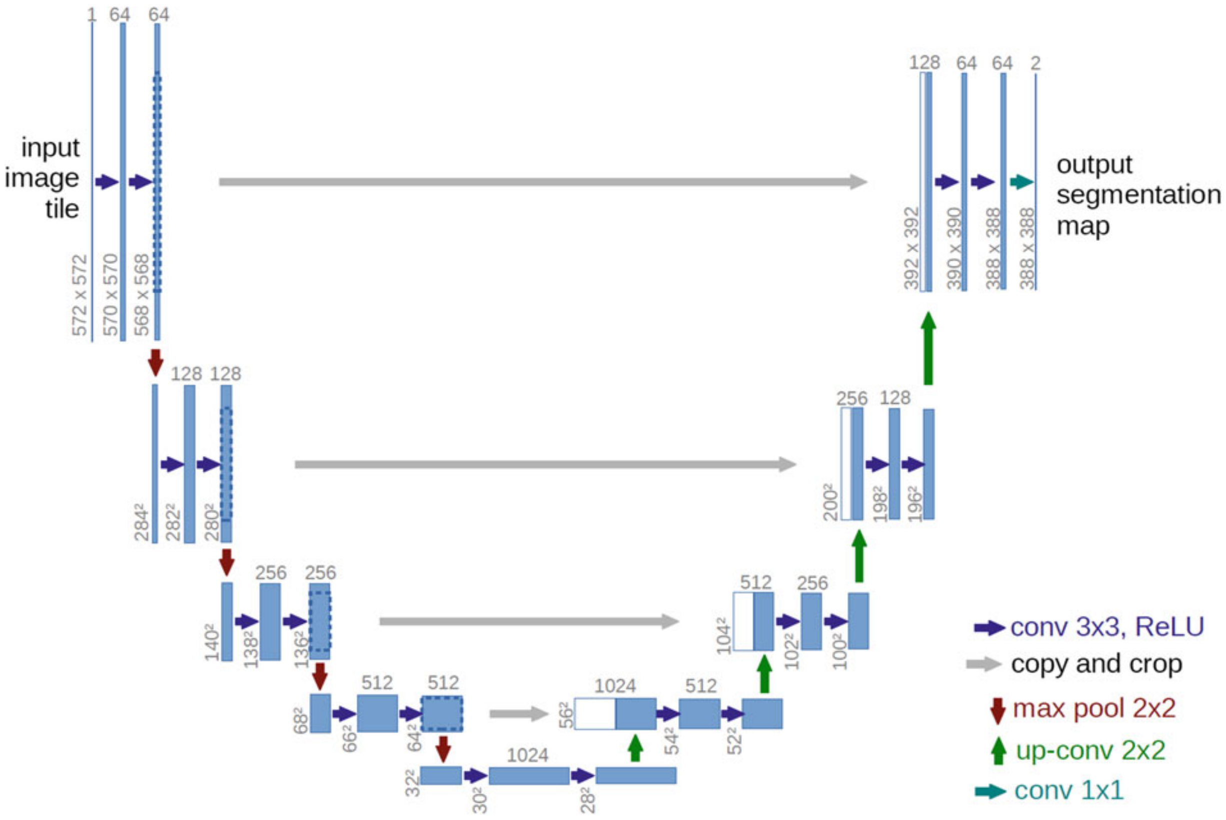

Fig. 18.1 U-Net style CNN architecture for image segmentation [37]

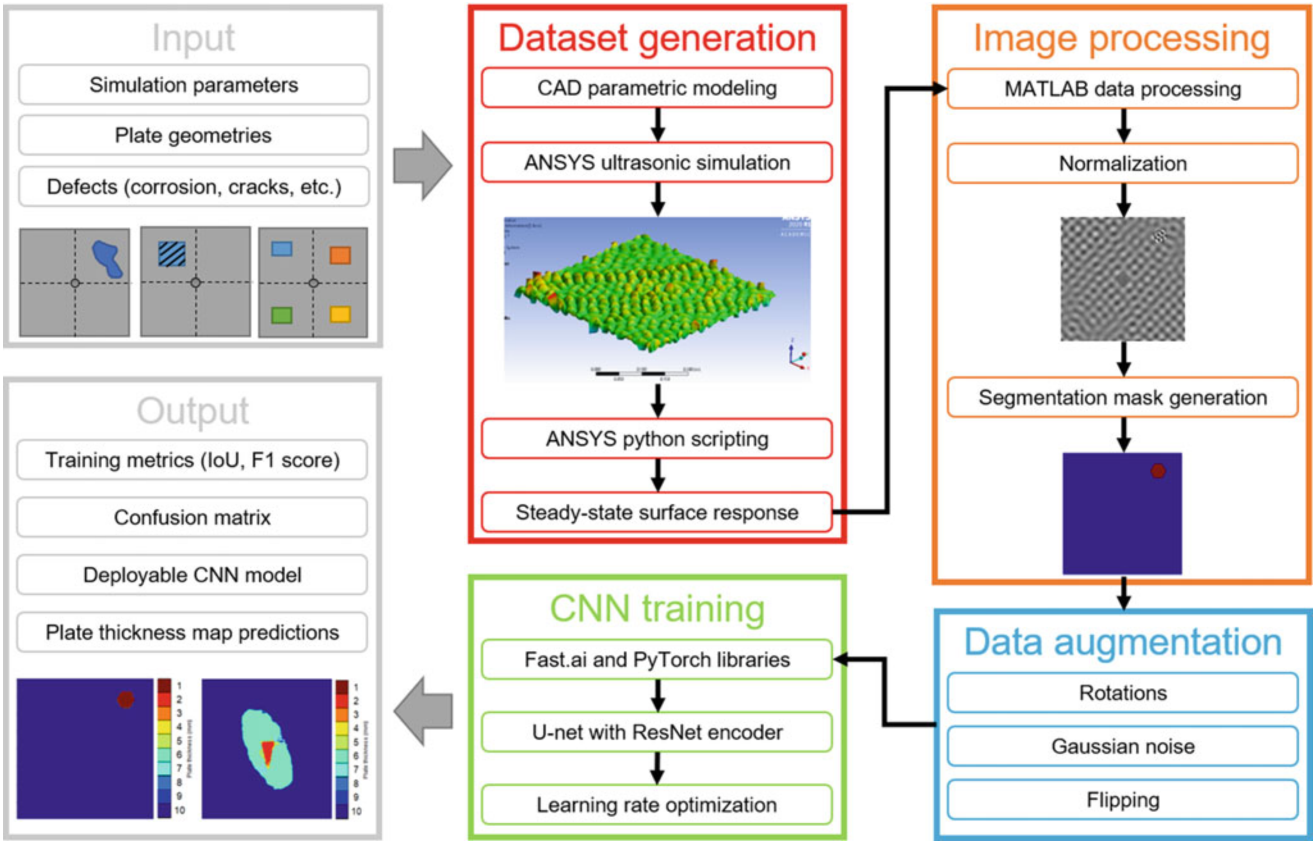

Fig. 18.2 High-level project conceptual map

The desired output of the system is a trained and deployable CNN model that can produce plate thickness maps from an ultrasonic wavefield measurement. Because the CNN model must be trained on a large dataset, the data was generated by simulation in a finite element analysis (FEA) software to efficiently increase the number of samples that would be available from experimental studies. The input to the system was a simulation scheme that varies simulation parameters, plate geometries, and defect characteristics (shape, depth, location, etc.) to account for different real-world plate damage scenarios. Damages were prescribed to the back of the plates to mimic hidden structural damage by altering the plates' thickness in a computer-aided design (CAD) software. Python was used to batch run steady-state ultrasonic simulations for each plate to generate a dataset. After processing the images and creating the segmentation maps, the dataset size was increased using data augmentation techniques. The CNN model was trained on the augmented dataset using open-source software and learning rate optimization. Finally, the model was deployed and tested for damage visualization and quantification. Each component in the diagram in Fig. 18.2 is explored in further detail in the following sections.

18.3.2 Dataset Generation

Initially, a training dataset was conceptualized by generating a simulation scheme. Several simulations and geometry parameters were varied to imitate thickness damage or defects that can occur in plate-like structures. The parameters examined in this study were transducer excitation frequency, transducer location, number of defects, plate thickness, defect location and geometry, and plate size and material. Among these, plate material, plate size, and transducer frequency were held constant. Thin plates were modeled as 400 mm × 400 mm and assigned the generic Aluminum Alloy material within ANSYS. The excitation frequency was set at 80 kHz. Five datasets were devised to account for variability in all other parameters, as summarized in Table 18.1.

Dataset 1 consisted of one defect in 1 of 9 locations in the upper-right quadrant of the plate, as shown in Fig. 18.3. In each of the 9 locations, the plate thickness was varied (9 different thicknesses) and the shape was varied (3 different shapes), for a

Table 18.1 Geometry and simulation parameters for dataset generation

Parameter	Value	Dataset 1	Dataset 2	Dataset 3	Dataset 4	Dataset 5
Number of defects	Variable	1	1	1	0	1
Transducer location	Variable	Center	Upper right quad. (4 locations)	Lower left	Upper right quad. (4 locations)	Center
Plate thickness	Variable	10 mm	10 mm	2–9 mm	1–10 mm	10 mm
Plate thickness at defect	Variable	1–9 mm	1–9 mm	1–8 mm	n/a	1–9 mm
Defect location	Variable	Upper right quad. (9 locations)	Center	Center	n/a	Top edge
Defect shape	Variable	circle, square, rectangle	Circle	Square	n/a	Rectangle
Defect size (width)	Variable	50 mm	50 mm dia.	10, 30, . . . , 90 mm	n/a	10, 20, . . . , 60 mm
Dataset size	**Total: 503**	243	36	130	40	54

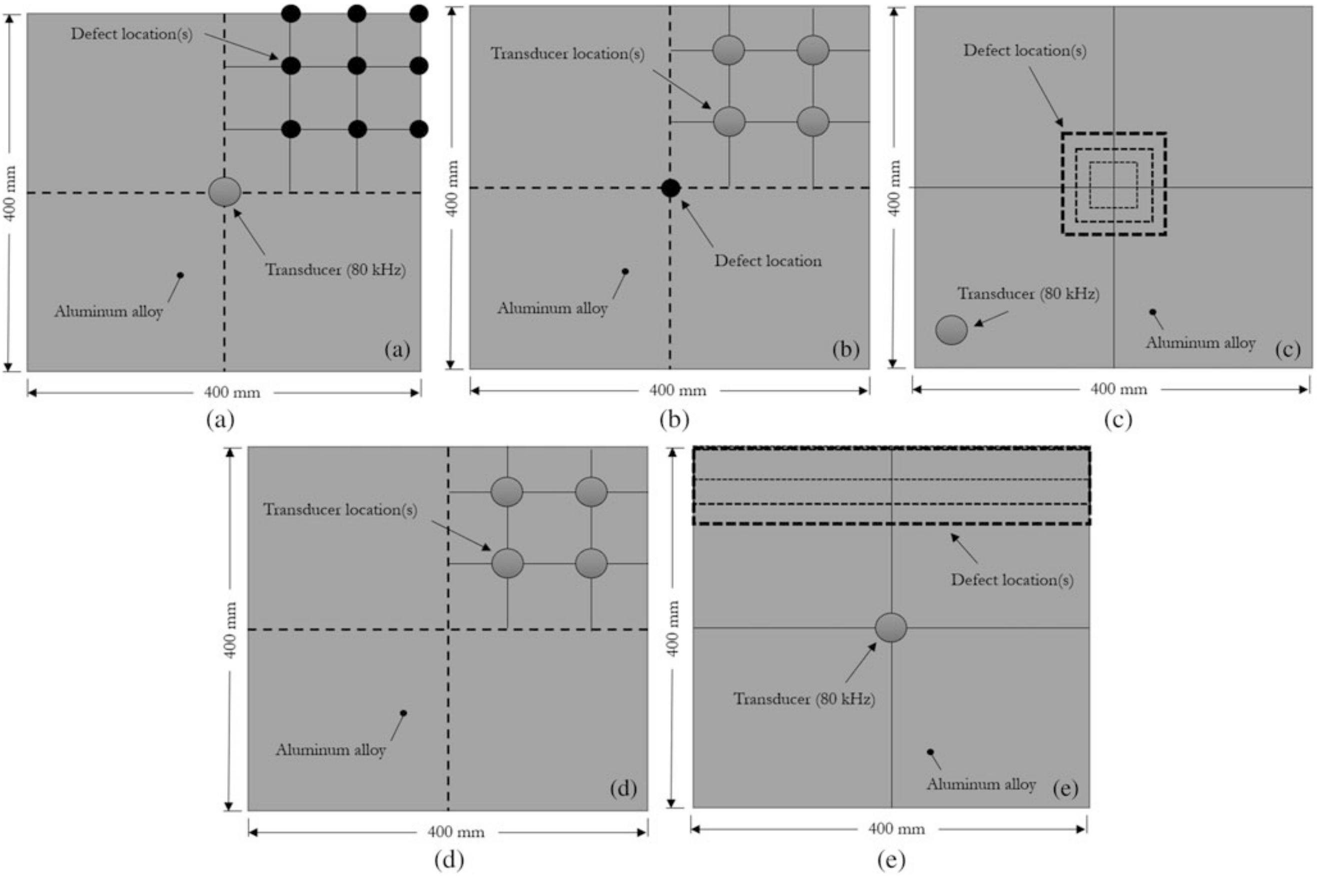

Fig. 18.3 Visual summary of datasets in Table 18.1. (**a**) Dataset 1. (**b**) Dataset 2. (**c**) Dataset 3. (**d**) Dataset 4. (**e**) Dataset 5

total dataset size of 243. For dataset 2, the transducer was placed in 1 of 4 locations in the upper-right quadrant, and the plate thickness at the defect was varied between 1–9 mm. For dataset 3, one square defect was placed at the center of the plate, and the characteristic length was varied in 20 mm increments from 10 mm to 90 mm. The thickness reduction percentage at the defect was kept to roughly 50%. Dataset 4 consisted of 10 different plate thicknesses, each with the transducer at 1 of 4 locations in the upper-right quadrant, for a total dataset size of 40. For dataset 5, one rectangular defect was placed at the top edge of the plate, and its width was varied in 10 mm increments from 10 mm to 60 mm. The total dataset size for all 5 datasets was 503.

The combination of these 5 datasets exposed the CNN to a variety of plate damage and experimental setup scenarios, making it invariant to the shape, size, location, and orientation of the defect, as well as to the location of the transducer on the plate. In this way, the CNN learned general characteristic features inherent within the different wavefields rather than the specific shape or size of any particular defect.

The plate geometry files were created in CAD software and the steady-state ultrasonic excitation response of each plate was obtained using an FEA harmonic response simulation in ANSYS Mechanical. Simulation setup procedures were followed from previous work by O'Dowd et al. [11]. Ultrasonic excitation was simulated by applying a 0.1 MPa pressure at 80 kHz on the top face of the transducer. A constant damping ratio of $\zeta = 0.001$ was used in the analysis. The mesh size was tuned to 2 mm to obtain accurate solutions at reasonable computation times. ANSYS ADPL commands were used to export the real and imaginary components of the steady-state harmonic response of the plate for further processing. Finally, ANSYS Python scripting was used to automate the simulation process for all 503 models in the dataset.

18.3.3 Image Processing

The real and imaginary components of the steady-state harmonic response of the plate were read directly into MATLAB for initial processing. MATLAB was used to filter out the surface mesh points, interpolate the response to an evenly spaced grid of 400 × 400 mm, normalize the data, and generate a grayscale wavefield image for all of the real component, imaginary component, and magnitude of the steady-state response of the plate for each simulation. Next, MATLAB was used to generate segmentation masks of the plate indicating the location and thickness of defects on a pixel-by-pixel basis from the CAD file geometry. A resolution of 1 mm^2 to 1 pixel was used in the segmentation masks. In this study, there were 10 plate thickness classes to identify in each image. Numeric class identifiers from 0 to 9 corresponded to plate thicknesses of 1 mm to 10 mm, with a 10 mm thickness having an identifier of 0.

For example, in a given 10 mm thick plate with no defects, every single pixel value in the segmentation label image would have an RGB value of (0, 0, 0), equivalent to its class identifier. If a thickness defect, such as that which would result from corrosion, was introduced to the back of the plate, causing the thickness of the plate in that region to be reduced to 7 mm, then all pixel values in that region of the segmentation label image would have an RGB value of (3, 3, 3). Thus, the CNN model is given wavefield images of a plate and it will be told (via the label images) which wave patterns and regions in the image correspond to which plate thickness value. Figure 18.4 shows an example of a grayscale wavefield image and a segmentation mask for a 10 mm plate with a 1 mm thick hexagonal defect in the upper-right corner. Figure 18.4b is colored for better visualization—10 mm correspond to dark blue and 1 mm correspond to dark red.

The hexagonal defect region is evident in the wavefield image where the wavenumber sharply increases compared with the nominal plate wavenumber, indicating a region of the plate with reduced thickness. Only the real-component surface response wavefield images were used in this study.

18.3.4 Data Augmentation

The process of generating new data from available data without changing its nature is known as data augmentation [13]. Data augmentation is often used to increase dataset size or is performed on-the-fly between training rounds to improve the accuracy

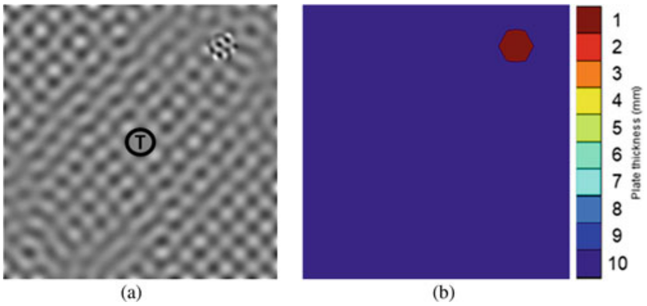

(a) (b)

Fig. 18.4 Wavefield and segmentation mask images for a 1 mm thick hexagonal defect. (**a**) Wavefield image. (**b**) Ground truth segmentation mask and generalizability of a CNN. Common data augmentation techniques on images include geometric transformations such as windowing, rotating, and shifting, as well as photometric transformations such as lighting, hue, and color alterations. Since the goal of the present study is to recognize features in an ultrasonic wavefield, any augmentation techniques that alter or distort the appearance of the propagating waves were excluded. The dataset of 503 was doubled in size by applying a 180° rotation to the entire dataset. The dataset was doubled in size again by applying white Gaussian noise with a variance of $\sigma^2 = 0.004$ to all of the images, for a total dataset size of 2012. In between training rounds, images also had a random chance of being horizontally or vertically flipped before passing through the network. The combination of the augmentation techniques described here and the quadrant-based simulation scheme described in Sect. 18.3.2 exposed the CNN to defects in all quadrants of the plate with no duplication and with some levels of noise to reduce the risk of overfitting.

18.3.5 CNN Training

The *Fast.ai* library with a *PyTorch* backend was used in the current study as the CNN development platform [17, 18]. The chosen CNN model had a U-Net based architecture [37] with 36 convolutional layers in the encoder and 18 convolutional layers in the decoder. The encoder was constructed based on the ResNet-34 model proposed by He et al. [39] with batch normalization and a ReLu activation function in between convolutional layers. The encoder was also pre-trained on the ImageNet database [40] before ever seeing the ultrasonic wavefield dataset. This form of training, known as transfer learning, is generally accepted to produce better results on a significantly smaller dataset than training all CNN parameters from scratch [17]. After the U-Net CNN was constructed, the ultrasonic wavefield dataset was randomly split into training and validation sets (80% and 20%, respectively), with a batch size of 16. Before training, the learning rate was optimized by plotting the value of the loss function as a function of learning rate using tools within the *Fast.ai* library, as shown in Fig. 18.5.

The learning rate is a hyperparameter that must be set by the user that controls the step size of the gradient descent on the overall training loss function. The maximum learning rate was chosen where the maximum rate of decrease in the loss function with respect to the learning rate was experienced. This occurred in the region of the steepest negative slope in Fig. 18.5 [17]. The learning rate was then smoothly varied during training iterations up to the maximum learning rate and then back down to traverse the loss landscape in the most efficient manner, as shown in Fig. 18.6.

This technique of varying the learning rate has been shown to avoid small local minimums in the loss function while ramping the learning rate up, then smoothly approaching a more global minimum in the loss function while refining the learning rate back down. After optimizing the learning rate, the network was trained on the ultrasonic wavefield dataset in two consecutive phases. During the first phase, all parameters in the hidden layers of the network were frozen and the head of the network, which is responsible for the final pixel-by-pixel classification, was left unfrozen. The learning rate was optimized again after the first phase of training to account for the change in parameters at the head of the network. During the second phase, all hidden layers were unfrozen and the entire network was trained again on the dataset. Figure 18.7 shows the training and validation set losses over training iterations.

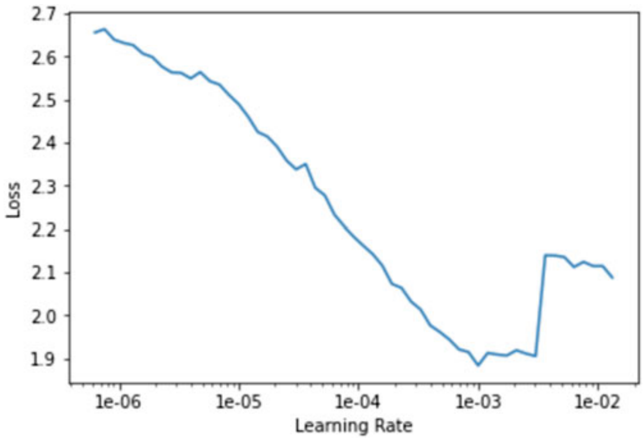

Fig. 18.5 Loss as a function of learning rate

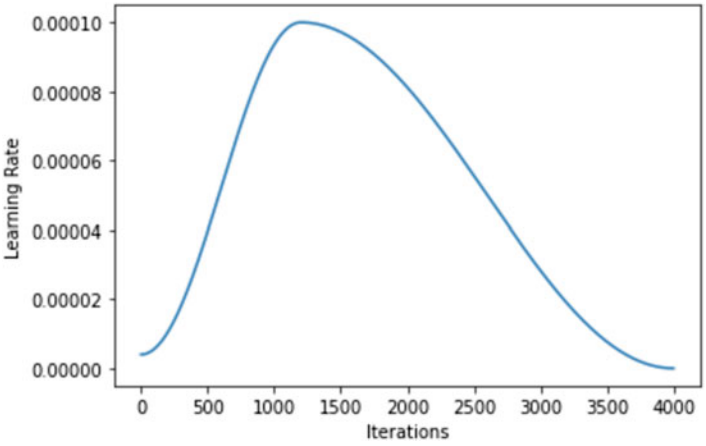

Fig. 18.6 Learning rate distribution over training iterations

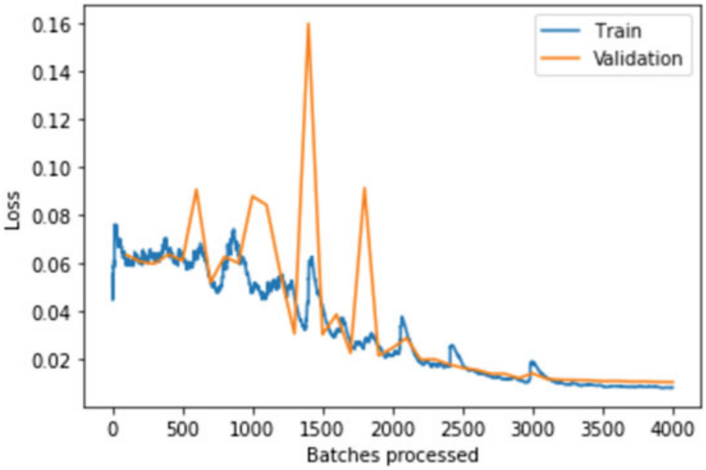

Fig. 18.7 Training and validation loss over training iterations

Fig. 18.8 Intersection over Union (IoU) metric

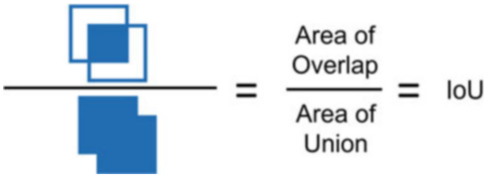

During the early iterations, the loss is shown to rapidly spike up and down due to the increased learning rate, with an overall decreasing trend. During later iterations, the loss decreases more steadily and progresses toward a more global minimum as the learning rate is refined. The training process was continued until the loss leveled to an asymptotic value.

After training of the CNN was completed, its performance on the validation set was evaluated by a classic object detection metric, Intersection over Union (IoU). For a semantic segmentation task, IoU is defined as the area of overlap between the predicted pixel classifications and the ground truth labels divided by the area of the union, averaged over all segmentation classes, as illustrated in Fig. 18.8.

The IoU metric is the most commonly reported benchmark for comparison against previously published models. In order to benchmark the training performance of the CNN, the final IoU value of the model was compared with previously reported values of other image segmentation CNN models, such as RefineNet [35] and DeepLab [27]. These results are summarized in Table 18.2.

The final IoU value of the wavefield CNN was 76.3%. It is noted that the DeepLab and RefineNet IoU scores are not directly comparable to the wavefield CNN, since they were trained on a different test set (PASCAL VOC 2012 test set). They are provided here, however, to give a general sense of the range of IoU values reported by state-of-the-art image

Table 18.2 Intersection over Union (IoU) training performance

CNN model	IoU
Wavefield CNN	76.3%
DeepLab[a] [27]	72.7%
RefineNet[a] [35]	83.8%

[a] Based on PASCAL VOC 2012 test set

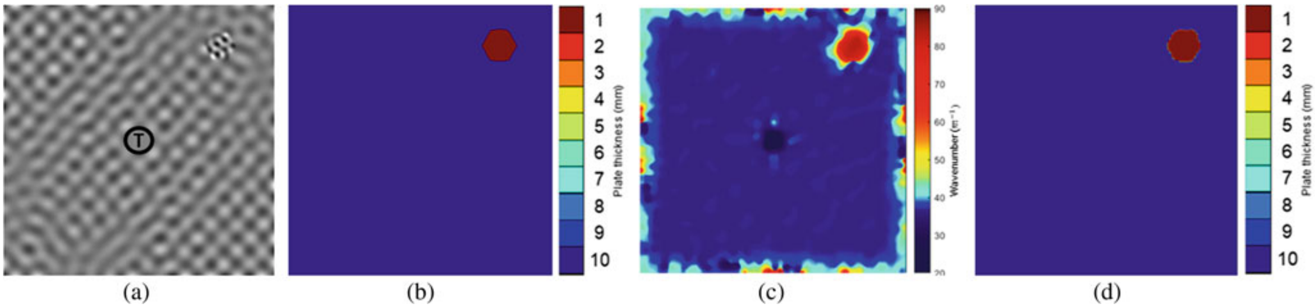

Fig. 18.9 AWS v. CNN prediction maps for a 1 mm thick hexagonal defect. (**a**) Wavefield image. (**b**) Ground truth. (**c**) AWS prediction. (**d**) CNN prediction

segmentation models. Even though the IoU score reported here is not directly comparable, it is on par with accuracy metrics reported elsewhere in the literature, despite the abstract nature of the ultrasonic wavefield images.

18.4 Results and Discussion

After training, several test geometries were created and passed through the CNN for inference. The test geometries were also processed using the AWS algorithm described by Flynn et al. [10] and compared with the results of the CNN inference. Because the CNN outputs a thickness prediction map and AWS outputs a wavenumber prediction map, the wavenumbers of the dominant A0 wave mode were mapped through Lamb wave dispersion curves to the corresponding plate thickness at a given excitation frequency. The CNN's plate thickness maps were color-coded linearly with plate thickness between 1 mm to 10 mm. The log scale of the AWS wavenumber maps was adjusted so that A0 wavenumbers corresponding to plate thicknesses of 1 mm to 10 mm were colored the same as the thickness maps. This allowed a more direct visual comparison between AWS and CNN results.

Six test sets are presented here to test the generalizability of the CNN in detecting unseen damages, as well as to test its improvements on the current AWS method. Each of the following figures shows the raw real-component surface response wavefield image that was processed by both AWS and the CNN, as well as the ground truth segmentation mask showing the exact location of the defects in the plate. The AWS wavenumber map predictions and the CNN thickness map predictions are compared side-by-side with the ground truth masks. Each of the test geometries is a nominally 10 mm thick, 400 mm × 400 mm aluminum plate excited at a frequency of 80 kHz. Figure 18.9 shows a test geometry with a small hexagonal defect in the upper-right corner of the plate with a plate thickness in the defect region of 1 mm. The transducer is labeled in the center of the plate.

Due to the large thickness reduction percentage and visual saliency of the defect, both AWS and the CNN can identify the hexagonal defect region clearly. The CNN provides a sharper outline of the defect with a lower noise level compared with the AWS prediction. The CNN correctly classifies the rest of the plate as a uniform 10 mm, whereas AWS exhibits high variance in the prediction around the edges of the plate, due to the Fourier transform limitations described in Sect. 18.1.

The next test plate has an irregularly shaped defect in the upper-right corner of the plate to mimic amorphous corrosion on the back of the plate with an 80% thickness reduction. The prediction results are shown in Fig. 18.10. The transducer is located at the center of the plate.

The significance of this result is that the CNN was able to correctly classify a defect region of the wavefield image irrespective of its shape, showing that it has learned the features inherent to the wavefield itself rather than the geometry of

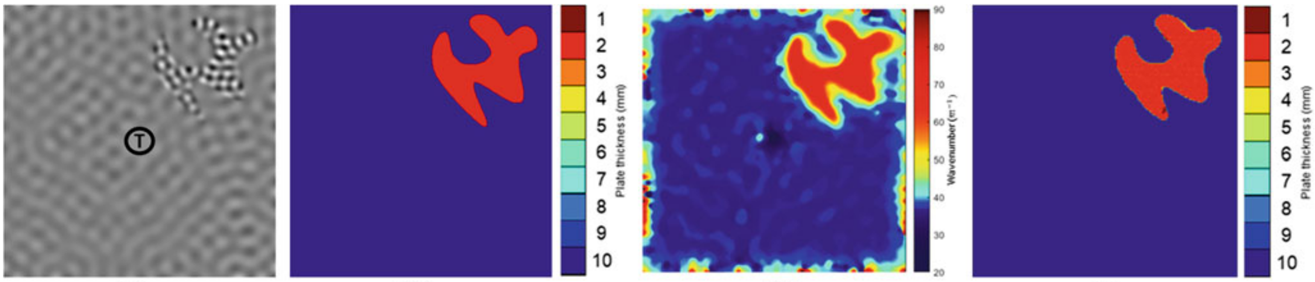

(a) (b) (c) (d)

Fig. 18.10 AWS v. CNN prediction maps for a 2 mm thick irregular defect. (**a**) Wavefield image. (**b**) Ground truth. (**c**) AWS prediction. (**d**) CNN prediction

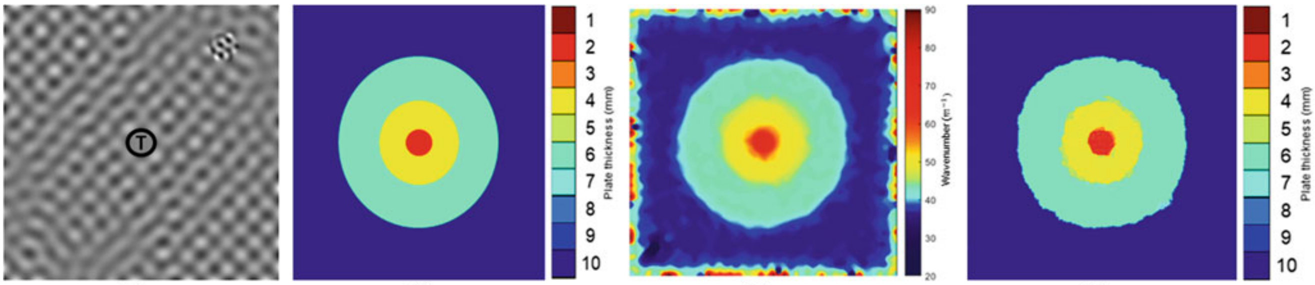

(a) (b) (c) (d)

Fig. 18.11 AWS v. CNN prediction maps for a nested circular defect region. (**a**) Wavefield image. (**b**) Ground truth. (**c**) AWS prediction. (**d**) CNN prediction

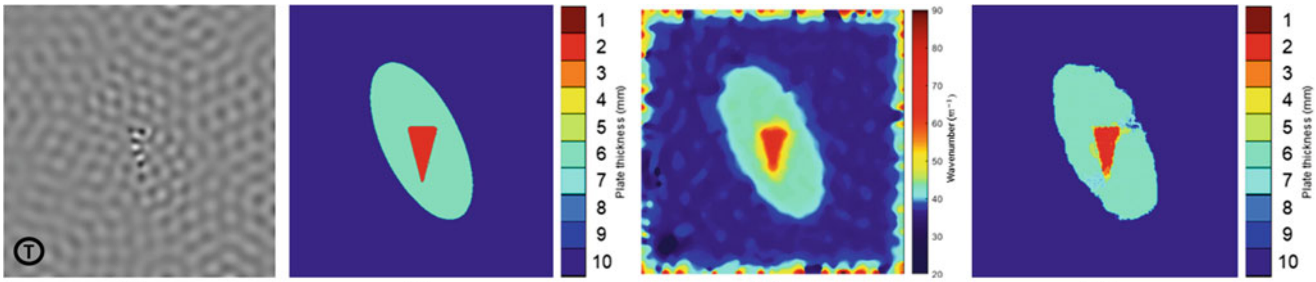

(a) (b) (c) (d)

Fig. 18.12 AWS v. CNN prediction maps for nested oval and triangle defects. (**a**) Wavefield image. (**b**) Ground truth. (**c**) AWS prediction. (**d**) CNN prediction

the defects in the training set. The CNN results again show the same sharpness and improved prediction at the edges of the plate in comparison to AWS.

Figures 18.11 and 18.12 show multiple, nested defects in the center of the plate, with the transducer in the lower left corner.

Even though the CNN was only trained on plates with a single defect of a single thickness, it was able to generalize to scenarios with nested defects present in the plate. These two cases also show the same performance improvements over AWS as the previous test results.

The next test geometry has a small, irregularly shaped defect in the upper-right corner of the plate with a 50% thickness reduction, and the transducer is in the center of the plate. The test results are shown in Fig. 18.13.

Although the AWS prediction picks up an anomaly in the upper-right corner where the defect is, the adverse Fourier transform artifacts around the edges of the plate disrupt the clarity of the defect. This makes it more likely to obtain a false negative when there is an obscured defect along the edge, or to obtain a false positive when there are no defects along the edge but the AWS prediction indicates there is. In contrast, the CNN prediction clearly outlines the location of the defect and correctly predicts the plate thickness in the defect region.

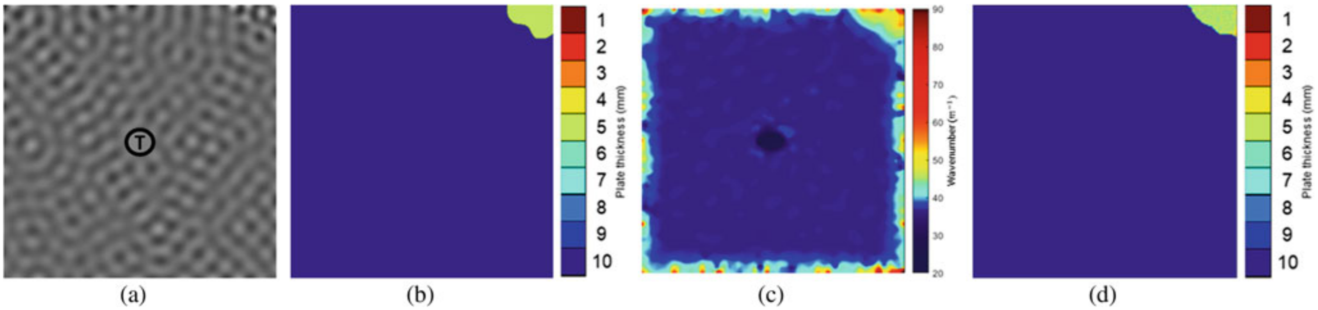

(a) (b) (c) (d)

Fig. 18.13 AWS v. CNN prediction maps for a small edge defect. (**a**) Wavefield image. (**b**) Ground truth. (**c**) AWS prediction. (**d**) CNN prediction

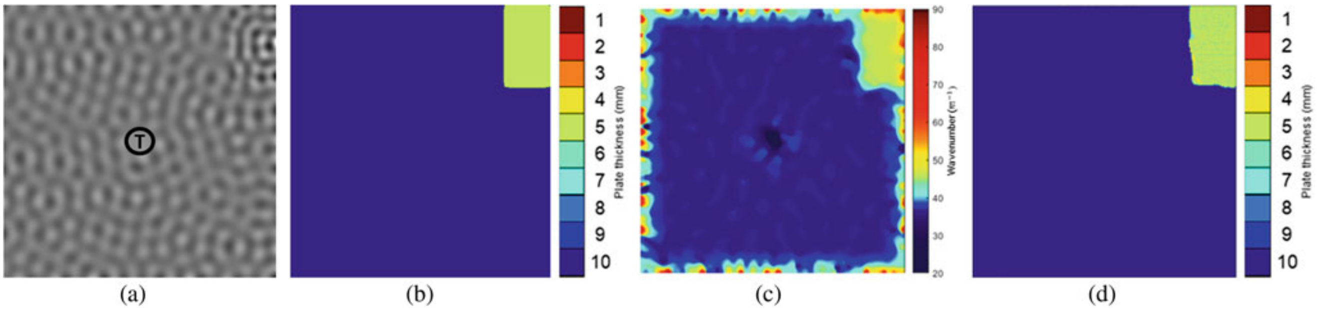

(a) (b) (c) (d)

Fig. 18.14 AWS v. CNN prediction maps for a rectangular internal crack. (**a**) Wavefield image. (**b**) Ground truth. (**c**) AWS prediction. (**d**) CNN prediction

The next test geometry also tests the ability of AWS and the CNN to identify defects along the edges of the plate. In this case, a small, 0.5 mm thick internal crack was introduced to the top-right corner of the plate, causing a 50% thickness reduction in the cracked region. The results are shown in Fig. 18.14.

The AWS results again show high variability around the edges of the plate and an unreliable prediction in the defect region, whereas the CNN correctly classifies and clearly outlines the edge defect. It is also important to note that the CNN was only trained on corrosion or indentation-like defects, yet shows generalizability to other defect types, such as internal cracks.

In the preliminary tests presented here, the average processing time of the AWS algorithm from ultrasonic wavefield to wavenumber prediction map was approximately 7 s, while the CNN inference time was approximately 0.1 s. It is noted that the processing time was not extensively tested in this study, although early results show decreased processing time can be achieved via CNN inference compared with AWS processing.

The previous test cases showed performance against AWS for 10 mm plates only, and a limited number of thickness reduction percentages. The following cases provide a brief, preliminary study into the performance of the CNN with respect to plate thickness and thickness reduction percentage. In order to assess the performance of the CNN with respect to thickness reduction percentage, the hexagonal defect from Fig. 18.4 was varied from 10% to 90% thickness reduction of the nominal value of 10 mm in Fig. 18.15.

For higher reduction defects, the defect is clearly outlined and the hexagonal shape is visible (Fig. 18.15a). As the reduction decreases, the defect is detected and classification is still correct, but the definition of the hexagonal shape is harder to discern (Fig. 18.15i). In general, the accuracy of the reported thickness in the defect region decreases with decreasing percent reduction, similar to the findings in O'Dowd et al. [11]. This effect can be mostly attributed to the convergence of the wave-pattern in the defect region to the wave-pattern in the rest of the plate. As the two wave patterns become more visually similar, the CNN prediction accuracy of the boundaries decreases.

The performance of the CNN with respect to changes in the nominal plate thickness was investigated by varying the plate thickness from 2 mm to 10 mm with a small triangular defect located consistently for all cases. The thickness reduction at the triangular defect was kept to 50% as best as possible (i.e. rounding up to the nearest integer value was necessary). The results for changing plate thickness are shown in Fig. 18.16.

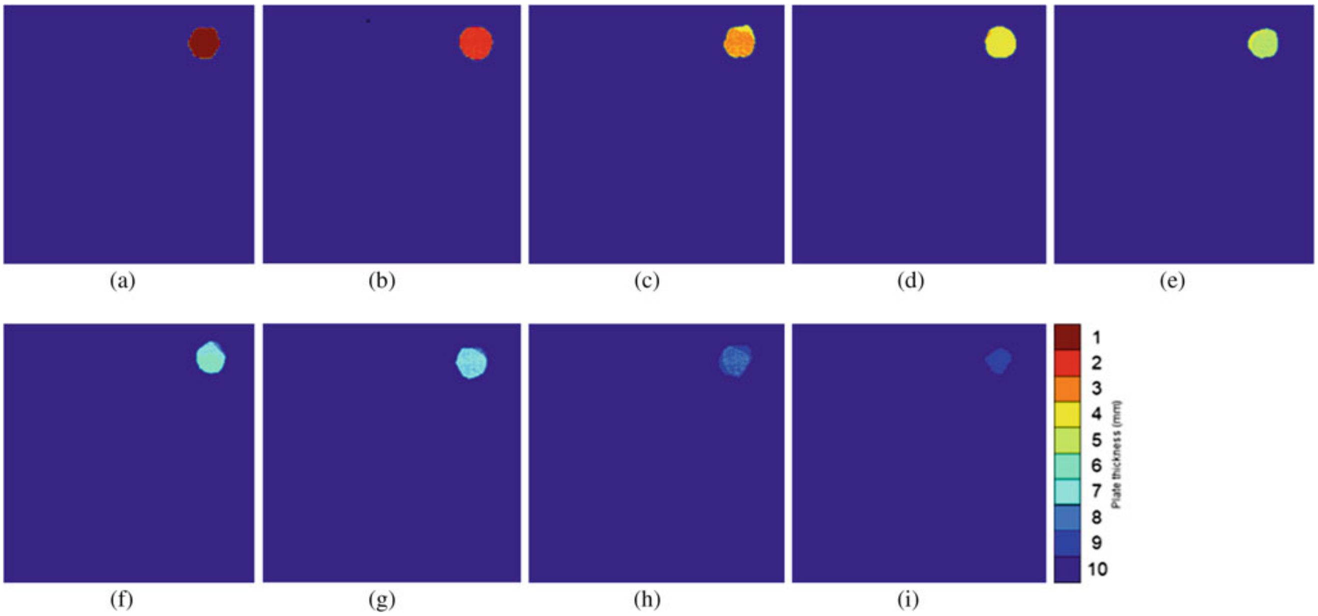

Fig. 18.15 Comparison of CNN prediction for hexagonal defect of 10–90% thickness reduction. (**a**) 90% reduction. (**b**) 80% reduction. (**c**) 70% reduction. (**d**) 60% reduction. (**e**) 50% reduction. (**f**) 40% reduction. (**g**) 30% reduction. (**h**) 20% reduction. (**i**) 10% reduction

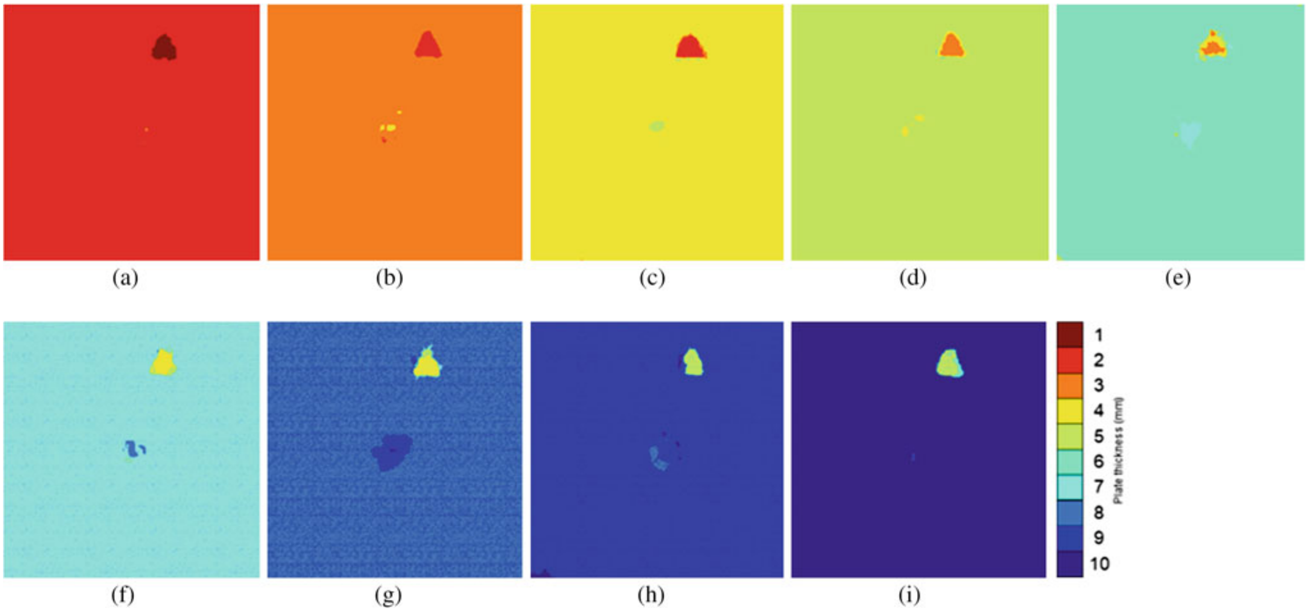

Fig. 18.16 Comparison of CNN prediction of triangular defect for varying plate thicknesses. (**a**) 2 mm plate. (**b**) 3 mm plate. (**c**) 4 mm plate. (**d**) 5 mm plate. (**e**) 6 mm plate. (**f**) 7 mm plate. (**g**) 8 mm plate. (**h**) 9 mm plate. (**i**) 10 mm plate

The CNN is able to identify the triangular defect well on these plates of varying thickness, as well as correctly classify the nominal thickness of the plate. Some inaccuracies are noticeable in the center of the plate where the transducer was located. Because the transducer was extruded above the plate, there was a lack of wavefield data at the transducer location and in the wavefield images. The transducer was still labeled the same as the nominal plate thickness in each case, which may have caused inconsistent training results in the transducer region. Despite inaccuracies near the transducer, this result shows that although the majority of the training dataset was on 10 mm plates, the CNN can generalize learned features of other thicknesses over the entire area of the plate.

18.5 Conclusion

This paper has presented the novel application of a CNN to steady-state ultrasonic wavefield measurements for NDE on plate-like structures. A U-Net style architecture was used for image segmentation on wavefield images to visualize and characterize damages and defects on a pixel-by-pixel basis. The results presented in this study provide proof-of-concept that a CNN framework can be successfully applied to steady-state ultrasonic measurements used in AWS techniques for the purpose of NDE. The trained CNN model overcomes the problems for AWS when estimating wavenumber near the edges of the scan area and provided sharper, more accurate, and reliable detection of defect boundaries in the cases investigated. The CNN model also has been shown to provide an order of magnitude speed-up in processing time compared with the current AWS method. The most prominent limitation and area for future work of the current study is the limitation of the CNN to classifying 10 discrete thickness values in a problem that is inherently one of regression rather than classification. Another area for future work is more extensive testing and improvement on the CNN's performance when decreasing the signal-to-noise ratio, decreasing thickness reduction percentage, decreasing defect size, different plate sizes, materials, and excitation frequencies, and applying it to experimental datasets. As with any neural network, these limitations can be addressed by increasing the network's exposure to them during training. Future work in this study would focus on implementing a regression model and generating a broader dataset to overcome these limitations.

Acknowledgments This research was funded by Los Alamos National Laboratory (LANL) through the Engineering Institute's Los Alamos Dynamics Summer School. The Engineering Institute is a research and education collaboration between LANL and the University of California San Diego's Jacobs School of Engineering. This collaboration seeks to promote multidisciplinary engineering research that develops and integrates advanced predictive modeling, novel sensing systems, and new developments in information technology to address LANL mission relevant problems.

References

1. Farrar, C.R., Worden, K.: An introduction to structural health monitoring. Philos. Trans. R. Soc. A Math. Phys. Eng. Sci. **365**(1851), 303–315 (2007)
2. Thompson, R.B., Thompson, D.O.: Ultrasonics in nondestructive evaluation. Proc. IEEE **73**(12), 1716–1755 (1985)
3. Staszewski, W.J., Lee, B.C., Traynor, R.: Fatigue crack detection in metallic structures with lamb waves and 3D laser vibrometry. Measure. Sci. Technol. **18**(3), 727–739 (2007)
4. Aryan, P., Kotousov, A., Ng, C.T., Cazzolato, B.S.: A baseline-free and non-contact method for detection and imaging of structural damage using 3D laser vibrometry. Struct. Control Health Monit. **24**(4), e1894 (2017)
5. Michaels, T.E., Michaels, J.E.: Application of acoustic wavefield imaging to non-contact ultrasonic inspection of bonded components. AIP Conf. Proc. **820**(1), 1484–1491 (2006)
6. Rogge, M.D., Leckey, C.A.: Characterization of impact damage in composite laminates using guided wavefield imaging and local wavenumber domain analysis. Ultrasonics **53**(7), 1217–1226 (2013)
7. Ruzzene, M.: Frequency–wavenumber domain filtering for improved damage visualization. Smart Mater. Struct. **16**(6), 2116–2129 (2007)
8. Mesnil, O., Yan, H., Ruzzene, M., Paynabar, K., Shi, J.: Fast wavenumber measurement for accurate and automatic location and quantification of defect in composite. Struct. Health Monit. **15**(2), 223–234 (2016)
9. Flynn, E.B., Jarmer, G.S.: High-speed, non-contact, baseline-free imaging of hidden defects using scanning laser measurements of steady-state ultrasonic vibration. In: Structural Health Monitoring 2013: Proceedings of the Ninth International Workshop on Structural Health Monitoring, September 10–12, 2013, vol. 1, pp. 1186–1193. Stanford University, Standard, CA (2013)
10. Flynn, E.B., Chong, S.Y., Jarmer, G.J., Lee, J.: Structural imaging through local wavenumber estimation of guided waves. NDT& E Int. **59**, 1–10 (2013)
11. O'Dowd, N.M., Han, D., Kang, L., Flynn, E.B.: Exploring the performance limits of full-field acoustic wavenumber spectroscopy techniques for damage detection through numerical simulation. In: 8th European Workshop on Structural Health Monitoring, July 5–8, 2016, Bilbao
12. Fukushima, K.: Neocognitron: a self-organizing neural network model for a mechanism of pattern recognition unaffected by shift in position. Biol. Cybernet. **36**, 193–202 (1980)
13. Gu, J., et al.: Recent advances in convolutional neural networks. Pattern Recogn. **77**, 354–377 (2018)
14. Rumelhart, D.E., Hinton, G.E., Williams, R.J.: Learning representations by back-propagating errors. Nature **323**(6088), 533–536 (1986)
15. Jia, Y., et al.: Caffe: convolutional architecture for fast feature embedding. Preprint. arXiv:1408.5093. Jun. 2014
16. Abadi, M., et al.: Tensorflow: a system for large-scale machine learning. In: 12th USENIX Symposium on Operating Systems Design and Implementation (OSDI 16), Novembe 2016, pp. 265–283. USENIX Association, Savannah, GA (2016)
17. Howard, J., Gugger, S.: Fastai: a layered API for deep learning. Information **11**(2), 108 (2020)
18. Paszke, A., et al.: PyTorch: an imperative style, high-performance deep learning library. In: Advances in Neural Information Processing Systems, vol. 32, pp. 8024–8035 (2019)
19. De Oliveira, M.A., Monteiro, A.V., Vieira Filho, J.: A new structural health monitoring strategy based on PZT sensors and convolutional neural network. Sensors **18**(9), 2955 (2018)

20. Ren, Y., et al.: Image-based concrete crack detection in tunnels using deep fully convolutional networks. Construct. Build. Mater. **234**, 117367 (2020)
21. Hou, W., Wei, Y., Guo, J., Jin, Y., Zhu, C.: Automatic detection of welding defects using deep neural network. J. Phys. Conf. Ser. **933**, 012006 (2018)
22. Munir, N., Kim, H.-J., Park, J., Song, S.-J., Kang, S.-S.: Convolutional neural network for ultrasonic weldment flaw classification in noisy conditions. Ultrasonics **94**, 74–81 (2019)
23. Munir, N., Park, J., Kim, H.-J., Song, S.-J., Kang, S.-S.: Performance enhancement of convolutional neural network for ultrasonic flaw classification by adopting autoencoder. NDT E Int. **111**, 102218 (2020)
24. Virkkunen, I., Koskinen, T., Jessen-Juhler, O., Rinta-Aho, J.: Augmented ultrasonic data for machine learning (2019). Preprint. arXiv:1903.11399
25. Meng, M., Chua, Y.J., Wouterson, E., Ong, C.P.K.: Ultrasonic signal classification and imaging system for composite materials via deep convolutional neural networks. Neurocomputing **257**, 128–135 (2017)
26. Lateef, F., Ruichek, Y.: Survey on semantic segmentation using deep learning techniques. Neurocomputing **338**, 321–348 (2019)
27. Chen, L., Papandreou, G., Kokkinos, I., Murphy, K., Yuille, A.L.: Deeplab: semantic image segmentation with deep convolutional nets, atrous convolution, and fully connected CRFs. IEEE Trans. Pattern Anal. Mach. Intell. **40**(4), 834–848 (2018)
28. Liu, F., Lin, G., Shen, C.: CRF learning with CNN features for image segmentation. Pattern Recogn. **48**(10), 2983–2992 (2015)
29. Cao, C., Huang, Y., Yang, Y., Wang, L., Wang, Z., Tan, T.: Feedback convolutional neural network for visual localization and segmentation. IEEE Trans. Pattern Anal. Mach. Intell. **41**(7), 1627–1640 (2019)
30. Mostajabi, M., Yadollahpour, P., Shakhnarovich, G.: Feedforward semantic segmentation with zoom-out features. In: Proceedings of the IEEE Conference on Computer Vision and Pattern Recognition, June 2015, pp. 3376–3385
31. He, K., Gkioxari, G., Dollár, P., Girshick, R.: Mask R-CNN. IEEE Trans. Pattern Anal. Mach. Intell. **42**(2), 386–397 (2020)
32. Zhou, Q., Zheng, B., Zhu, W., Jan Latecki, L.: Multi-scale context for scene labeling via flexible segmentation graph. Pattern Recogn. **59**, 312–324 (2016)
33. Shelhamer, E., Long, J., Darrell, T.: Fully convolutional networks for semantic segmentation. IEEE Trans. Pattern Anal. Mach. Intell. **39**(4), 640–651 (2017)
34. Badrinarayanan, V., Kendall, A., Cipolla, R.: SegNet: a deep convolutional encoder-decoder architecture for image segmentation. IEEE Trans. Pattern Anal. Mach. Intell. **39**(12), 2481–2495 (2017)
35. Lin, G., Liu, F., Milan, A., Shen, C., Reid, I.: RefineNet: multi-path refinement networks for dense prediction. IEEE Trans. Pattern Anal. Mach. Intell. **42**(5), 1228–1242 (2020)
36. Gao, H., Yuan, H., Wang, Z., Ji, S.: Pixel transposed convolutional networks. IEEE Trans. Pattern Anal. Mach. Intell. **42**(5), 1218–1227 (2020)
37. Ronneberger, O., Fischer, P., Brox, T.: U-Net: convolutional networks for biomedical image segmentation. In: International Conference on Medical Image Computing and Computer-Assisted Intervention, November 2015, pp. 234–241. Springer, New York (2015)
38. Liu, L., et al.: Deep learning for generic object detection: a survey. Int. J. Comput. Vis. **128**(2), 261–318 (2020)
39. He, K., Zhang, X., Ren, S., Sun, J.: Deep residual learning for image recognition. In: Proceedings of the IEEE Conference on Computer Vision and Pattern Recognition, 2016, pp. 770–778
40. Deng, J., Dong, W., Socher, R., Li, L.-J., Li, K., Fei-fei, L.: ImageNet: a large-scale hierarchical image database. In CVPR, 2009

Chapter 19
Application of the RASTAR Method to Continuous Scanning LDV Measurements

D. Di Maio and S. Bruinsma

Abstract This paper presents the application of RASTAR method to diagnostics performed by continuous scanning spectral sidebands. In a previous investigation, RASTAR proved to detect damage condition of a cantilever beam which was continuously scanned along a line by a laser beam. The objective of this paper is to extend the method to two-dimensional scan rather than one. As the method is based on spectral sidebands, the access to spectral lines for deflections in both directions in space should enhance the detection of damage for structures which are lookalike panels. The research is focused on numerical simulations where the LDV was synthesized using continuous scanning approach. The results are encouraging and show that two-dimensional scans can be more useful for RASTAR to detect damage.

Keywords Continuous SLDV · Damage detection · RASTAR

19.1 Introduction

Damage identification by continuous scanning methods has seen an interesting development over recent years. The modulated laser Doppler vibrometry (LDV) signal can be translated into strain field which could be processed further into a damage indicator, as presented in several works by Zhu, Xu, and Chen [1–9]. The use of modal strain analysis proved successful both for detection and identification of the damage. However, those methods were mainly attempted on academic structures. Alongside such developments, the author of this paper attempted the exploitation of the spectral sidebands for the damage detection, avoiding the use of reconstructed deflection shapes from the LDV modulated signal which might be biased by curve-fitting artefacts. A research presented at IMAC XXXIV [10] attempted the direct exploitation of spectral sidebands using numerical generated LDV modulated signals. That paper showed that by using a mere root mean square (RMS) error between the pristine and damaged case, one could detect signature of damage, but the RMS also showed to be a very limited option.

This research work represents an improvement of recent advances made on the development of the RASTAR method applied to continuous scanning laser measurements. The exploitation of spectral sidebands for the detection of damage was first presented in [11] where the research proposed few methods which failed to work properly. However, the novelty of research was to develop some algorithms to process sidebands more effectively than attempted earlier in [10]. RASTAR algorithm was born soon after that piece of research and overcame limitations of previous algorithms. The major difference of RASTAR is to calculate the ratio between a single sideband over the total sum of all sidebands and sum the differences of all the ratios between the damaged and pristine cases. The research was fully published in [12] where the method was tested both on numerical and experimental test cases. Despite the successful investigation, the researched focused on a cantilever beam only, which was measured by continuous straight-line method, therefore analysing the spectral sidebands produced by that line.

The step forward of this short paper is to extend the test cases to two-dimensional structures where sidebands are created along both directions that are in x- and y-axis. It is worth reminding that the a single axis scan measures a number of sidebands which are proportional to the complexity of the deflection shape; those sidebands show as a single cluster of harmonics. Scanning along the two axes, the number of sidebands increases exponentially as one cluster of harmonics now repeats as many times as the shape complexity is measured by the other scan direction. The numerical simulation presented

---

D. Di Maio (✉) · S. Bruinsma
Department of Applied Mechanics, Mechanical Engineering, University of Twente, Enschede, Netherlands
e-mail: d.dimaio@utwente.nl

D. Di Maio, J. Baqersad (eds.), *Rotating Machinery, Optical Methods & Scanning LDV Methods, Volume 6*, Conference Proceedings of the Society for Experimental Mechanics Series, https://doi.org/10.1007/978-3-030-76335-0_19

in [10, 13] is repurposed here. Two finite element models of plates embedding two types of damages of different severity are used for the calculation of the ODSs and LDV output signal modulation. The RASTAR algorithm is applied to some of these cases and conclusions are drawn from this attempt.

19.2 Test Structure, Setup, and Experimental Method

As already introduced earlier, the RASTAR method performed well on both numerical and experimental cases involving a cantilever beam with damage which was continuously scanned by a straight-line measurement. The goal in this paper is to investigate how the algorithm performs when a two-dimensional scan is carried out, and therefore a numerical test case is analysed. A finite element model of a plate is built with four different severity damages, severity increasing in both area and thickness as shown in Fig. 19.1. Two types of damage were created such as (a) damage-*n* and (b) damage-A*n*. The first one has got the "damaged" element thickness of 4.5 mm instead of 5 mm for a pristine one, whereas for the second type, the "damaged" element thickness was set to 4 mm. The model is built in shell elements to facilitate the extraction and polynomial fitting of the mode shapes which are used in Eq. 19.4. The same model was already used in [10] and more details can be found in that publication. Upon the extraction of the mode shapes and natural frequencies, the operational deflection shapes are calculated by Eq. 19.1.

$$\{X\} = \sum\nolimits_{r=1}^{N} \frac{\{\varphi\}_r^T \{F\} \{\varphi\}_r}{\omega_r^2 - \omega^2 + i\eta_r\omega_r^2} \tag{19.1}$$

where η_r is damping loss factor, which was set 0.001 for all modes.

The type of test simulated here is an area scan and it is briefly described hereafter. The laser beam can continuously scan over a structure which is vibrating sinusoidally at any frequency. The measured LDV output signal can be quickly post-processed to obtain the spectral sidebands. All continuous scanning techniques employed in ODS recovering involve sinusoidal excitation of the structure; so the response at any point, measured at any direction, is also sinusoidal at the same excitation frequency, assuming the linearity of the structure. The vibration response measured by the SLDV system, which can be expressed as velocity in the z-direction, perpendicular to the structure surface nominally in the *X*-*Y* plane and measured at any point (*x*, *y*) along the scan path *s(x, y)* will be:

$$v_z\,(s,t) = V_R(s)\cos(\omega t) + V_I(s)\sin(\omega t) \tag{19.2}$$

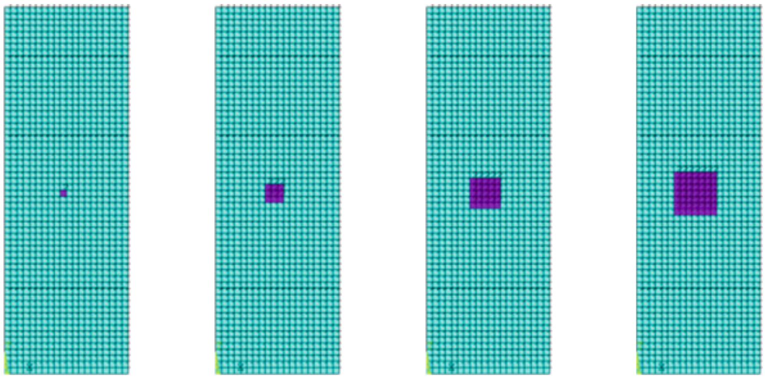

Damage-1 Damage-2 Damage-3 Damage-4

Fig. 19.1 Finite element models showing the damage location

When the *X*-*Y* mirrors of the scanning device are driven sinusoidally by two functions at two non-fractional frequencies, Ω_x and Ω_y, the laser beam will perform an area scan which describes an open Lissajous figure. Hence, in order to sweep a normalized area of dimension 2 × 2, with zero position the centre of the square, the mirror drivers should be fed by two sinewaves of equations:

$$\begin{aligned} x(t) &= \cos\left(\Omega_x t\right) \\ y(t) &= \cos\left(\Omega_y t\right) \end{aligned} \tag{19.3}$$

Expanding out trigonometrically, the following representation of the vibration signal is derived:

$$v_z(t) \approx \sum\nolimits_{m,n=0}^{p,q} V_{Rn,m} \cos\left[\left(\omega \pm n\Omega_x \pm m\Omega_y\right) t\right] \tag{19.4}$$

Once the LDV output signal is simulated, the spectral sidebands are calculated and fed into the RASTAR error calculations.

The RASTAR algorithm is described by Eq. 19.5 as follows:

$$\epsilon(t) = \sum_{j=1}^{n} \left(\frac{\mathrm{SBA_P}\left(\omega \pm \Omega j\right)}{\sum_{i=1}^{n} \mathrm{SBA_P}\left(\omega \pm \Omega i\right)} \cdot 100\% - \frac{\mathrm{SBA_D}\left(\omega \pm \Omega j\right)}{\sum_{k=1}^{n} \mathrm{SBA_D}\left(\omega \pm \Omega k\right)} \cdot 100\% \right) \tag{19.5}$$

where the SBA indicates spectral sidebands and the subscript *p* pristine and *D* damage. The RASTAR is calculated for the number of sidebands required (or desired) for the ODS reconstruction. Figure 19.2 shows an example of selected sidebands (in the shaded area) for the RASTAR calculation. The sidebands are symmetric to the central one, at the excitation frequency, so one side is enough for the calculation. RASTAR mainly highlights the error between pristine and damage at every individual sideband, where the error is calculated as the spectral amplitude of a sidebands over the total sum of the selected sidebands. The method is indifferent to overall amplitude change and is focused on the difference in distribution of the total amplitude over the sidebands.

An area scan measures the sidebands in *x*- and *y*-coordinates providing much more information than a line scan. Figure 19.3 shows the spectrum of a numerically generated LDV signal from ODS of the model plate. One can appreciate that the spectrum is composed by several clusters (only some selected and plotted) of sidebands because of the scan carried out in both spatial coordinates. Every cluster is made of 19 sidebands which are frequency spaced by 1 Hz, which is the scan frequency along one direction, and the whole spectrum is made of 19 clusters spaced by 10 Hz which is the scan frequency along the other direction.

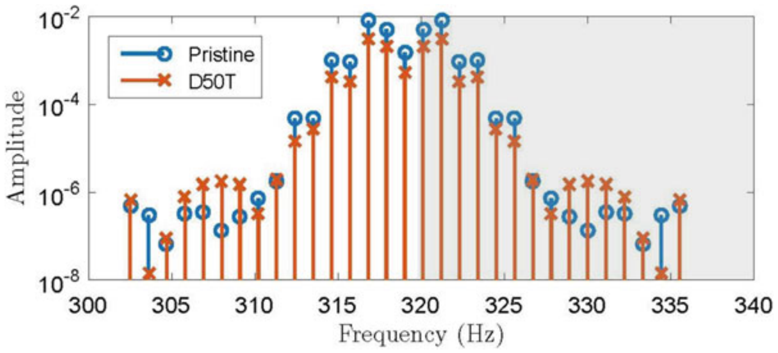

Fig. 19.2 Example [12] of spectrum from straight-line scan and the spectral sidebands used for the RASTAR in shaded area

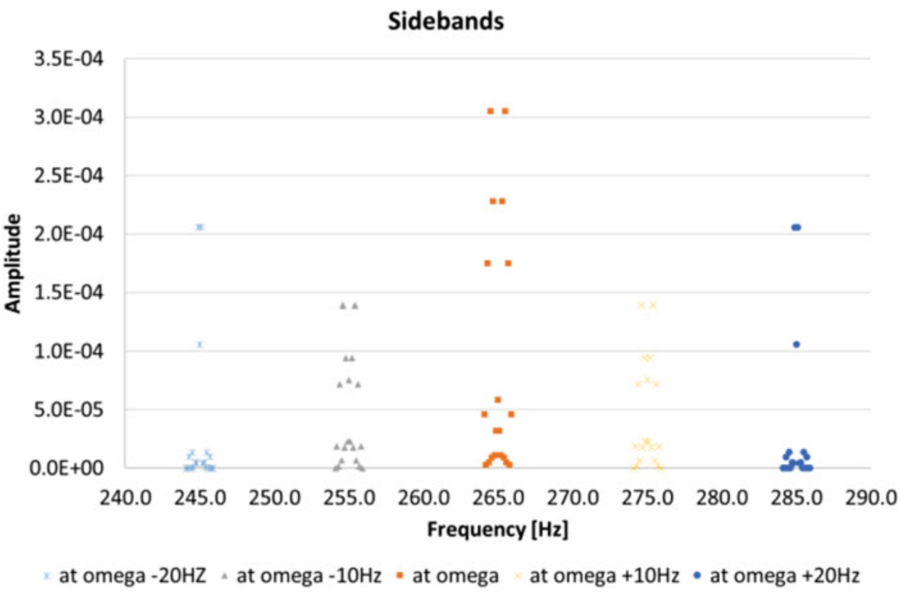

Fig. 19.3 Spectrum of area scan simulated from the numerically generated ODS

Table 19.1 Selection of the first five clusters of sidebands at 265 Hz excitation frequency

	ω−50	AMP	ω−40	AMP	ω−30	AMP	ω−20	AMP	ω−10	AMP	ω	AMP	ω+10	AMP	ω+20	AMP	ω+30	AMP	ω+40	AMP	ω+50	AMP
ω−9.9	214.1	8.4E-12	224.1	8.4E-12	234.1	8.3E-12	244.1	8.3E-12	254.1	8.3E-12	264.1	**4.6E-05**	274.1	8.3E-12	284.1	8.3E-12	294.1	8.3E-12	304.1	8.3E-12	314.1	8.3E-12
ω−8.8	214.2	8.3E-12	224.2	8.3E-12	234.2	8.3E-12	244.2	8.3E-12	254.2	1.9E-05	264.2	**2.7E-06**	274.2	1.9E-05	284.2	8.2E-12	294.2	8.2E-12	304.2	8.2E-12	314.2	8.2E-12
ω−7.7	214.3	8.5E-12	224.3	8.5E-12	234.3	8.5E-12	244.3	9.7E-06	254.3	1.3E-06	264.3	**1.7E-04**	274.3	1.3E-06	284.3	9.7E-06	294.3	8.4E-12	304.3	8.4E-12	314.3	8.4E-12
ω−6.6	214.4	8.2E-12	224.4	8.2E-12	234.4	1.3E-07	244.4	7.5E-09	254.4	7.2E-05	264.4	**4.5E-06**	274.4	7.2E-05	284.4	7.5E-09	294.4	1.3E-07	304.4	8.2E-12	314.4	8.1E-12
ω−5.5	214.5	8.6E-12	224.5	2.2E-06	234.5	5.9E-08	244.5	1.4E-05	254.5	6.4E-06	264.5	**3.0E-04**	274.5	6.4E-06	284.5	1.4E-05	294.5	5.9E-08	304.5	2.2E-06	314.5	8.7E-12
ω−4.4	214.6	1.0E-06	224.6	1.3E-07	234.6	3.9E-06	244.6	3.8E-07	254.6	1.4E-04	264.6	**8.7E-06**	274.6	1.4E-04	284.6	3.8E-07	294.6	3.9E-06	304.6	1.3E-07	314.6	1.0E-06
ω−3.3	214.7	9.2E-08	224.7	2.6E-07	234.7	4.4E-07	244.7	4.9E-06	254.7	1.7E-05	264.7	**2.3E-04**	274.7	1.7E-05	284.7	4.9E-06	294.7	4.4E-07	304.7	2.6E-07	314.7	9.2E-08
ω−2.2	214.8	9.3E-07	224.8	3.5E-07	234.8	7.0E-06	244.8	4.2E-06	254.8	9.4E-05	264.8	**1.1E-05**	274.8	9.4E-05	284.8	4.2E-06	294.8	7.0E-06	304.8	3.5E-07	314.8	9.3E-07
ω−1.1	214.9	8.0E-08	224.9	1.5E-05	234.9	6.4E-07	244.9	2.1E-04	254.9	2.3E-05	264.9	**3.2E-05**	274.9	2.3E-05	284.9	2.1E-04	294.9	6.4E-07	304.9	1.5E-05	314.9	8.0E-08
ω	215.0	**9.0E-07**	225.0	**8.7E-06**	235.0	**8.8E-06**	245.0	**1.1E-04**	255.0	**7.6E-05**	265.0	**5.8E-05**	275.0	**7.6E-05**	285.0	**1.1E-04**	295.0	**8.8E-06**	305.0	**8.7E-06**	315.0	**9.0E-07**
ω+1.1	215.1	8.0E-08	225.1	1.5E-05	235.1	6.4E-07	245.1	2.1E-04	255.1	2.3E-05	265.1	**3.2E-05**	275.1	2.3E-05	285.1	2.1E-04	295.1	6.4E-07	305.1	1.5E-05	315.1	8.0E-08
ω+2.2	215.2	9.3E-07	225.2	3.5E-07	235.2	7.0E-06	245.2	4.2E-06	255.2	9.4E-05	265.2	**1.1E-05**	275.2	9.4E-05	285.2	4.2E-06	295.2	7.0E-06	305.2	3.5E-07	315.2	9.3E-07
ω+3.3	215.3	9.2E-08	225.3	2.6E-07	235.3	4.4E-07	245.3	4.9E-06	255.3	1.7E-05	265.3	**2.3E-04**	275.3	1.7E-05	285.3	4.9E-06	295.3	4.4E-07	305.3	2.6E-07	315.3	9.2E-08
ω+4.4	215.4	1.0E-06	225.4	1.3E-07	235.4	3.9E-06	245.4	3.8E-07	255.4	1.4E-04	265.4	**8.7E-06**	275.4	1.4E-04	285.4	3.8E-07	295.4	3.9E-06	305.4	1.3E-07	315.4	1.0E-06
ω+5.5	215.5	8.3E-12	225.5	2.2E-06	235.5	5.9E-08	245.5	1.4E-05	255.5	6.4E-06	265.5	**3.0E-04**	275.5	6.4E-06	285.5	1.4E-05	295.5	5.9E-08	305.5	2.2E-06	315.5	8.4E-12
ω+6.6	215.6	8.3E-12	225.6	8.3E-12	235.6	1.3E-07	245.6	7.5E-09	255.6	7.2E-05	265.6	**4.5E-06**	275.6	7.2E-05	285.6	7.5E-09	295.6	1.3E-07	305.6	8.4E-12	315.6	8.4E-12
ω+7.7	215.7	8.3E-12	225.7	8.4E-12	235.7	8.4E-12	245.7	9.7E-06	255.7	1.3E-06	265.7	**1.7E-04**	275.7	1.3E-06	285.7	9.7E-06	295.7	8.4E-12	305.7	8.4E-12	315.7	8.4E-12
ω+8.8	215.8	8.4E-12	225.8	8.4E-12	235.8	8.4E-12	245.8	8.4E-12	255.8	1.9E-05	265.8	**2.7E-06**	275.8	1.9E-05	285.8	8.4E-12	295.8	8.4E-12	305.8	8.4E-12	315.8	8.4E-12
ω+9.9	215.9	8.4E-12	225.9	8.4E-12	235.9	8.4E-12	245.9	8.4E-12	255.9	8.4E-12	265.9	**4.6E-05**	275.9	8.4E-12	285.9	8.4E-12	295.9	8.4E-12	305.9	8.4E-12	315.9	8.5E-12

Table 19.2 Natural frequencies present between 20 and 265 Hz

Mode shape	Mode 0	Mode 1	Mode 2	Mode 3	Mode 4	Mode 5	Mode 6
Natural frequency [Hz]	29.64	53.78	82.24	113.54	161.69	184.94	263.90

Table 19.1 shows an example of how the data of the sidebands and clusters are stored for a selection. The table is colour-coded to match with the sidebands plotted in Fig. 19.3. The sidebands are spaced about 1.1 Hz column-wise and 10 Hz row-wise from the excitation frequency at ω. The amplitudes of the sidebands used for the RASTAR calculations are in bold. The clusters are both on the right and the left of the excitation frequency, and one can immediately notice that the sidebands are symmetric by looking at the actual numbers. Finally, one can notice by looking at the fifth cluster from the middle that four spectral lines are meaningful out of the nine sidebands. The two-dimensional scan enables RASTAR to analyse much more test data than available with a single scanned line. However, this paper will only analyse the data highlighted in bold in Table 19.1.

19.3 Results and Analysis

The simulations of the spectral sidebands were carried out in a frequency range between 20 and 265 Hz with a frequency step of 1 Hz. Table 19.2 shows that six modes are present in that frequency range.

As already introduced, the RASTAR algorithm will be used for one row and one column of data as shown in Table 19.1. It is worth noting that the bold column entails data spaced by 1 Hz and the bold row entails data spaced by 10 Hz.

The simulations of the LDV output signal were carried out in three scenarios: without added noise and with an excitation force of 1 N, with broadband noise 100 mV and excitation force of 1 N, and with broadband noise 100 mV and excitation force 10 N, respectively.

Table 19.3 shows the RASTAR errors for four different damage severities, levels 1–4. The red colour identified the RASTAR calculated using data row-wise and the black using the data column-wise. The most interesting result comes from observing the data for the lowest damage level, damage 1, which shows how sensitive the algorithm is when spectral sidebands are taken along the row instead of the column. The red plot shows clearly a peak value for RASTAR error at around 148 Hz. A less clear result can be observed in the plots for damages 2–4, where high spikes are calculated. The calculations were checked, and they did not reveal issues about the method of selecting data points between the pristine and damaged case.

Table 19.4 shows the RASTAR error plots for damage levels, A1–A4. Even for this case, the smallest damage A1 shows much better plot than the ones obtained for larger damages. Such a behaviour of the damage indicator seems suggesting that the damage scenarios created are far too severe for the RASTAR method to yield a sensible result. Anyhow, both Table 19.3 and Table 19.4 present plots which are coherent at least for the damage 1 and damage A1.

Figure 19.4 shows the RASTAR error calculated row-wise plotted together with a frequency response function in an attempt to observe how the error peaks related to the resonance peaks.

As already demonstrated in [12], the RASTAR method seems to be very sensitive in regions of anti-resonances as shown in Fig. 19.4 where a max error peak is located between the resonances at approx. 113 and 161 Hz (disregarding a probable numerical error at approx. 233 Hz).

Table 19.3 Table of plots of RASTAR errors calculated for different damage severities, levels 1–4

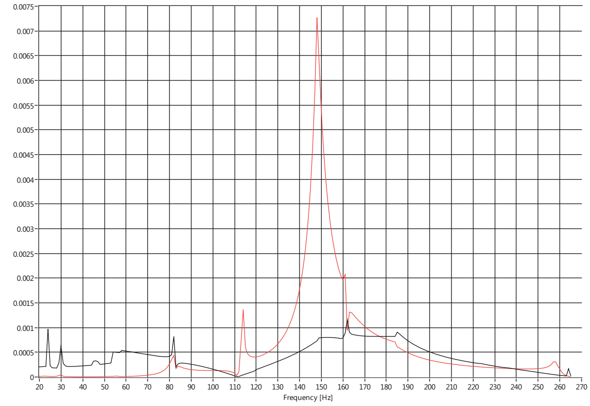 Damage-1	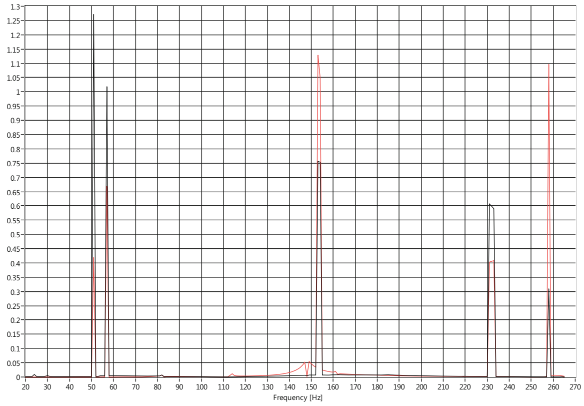 Damage-2
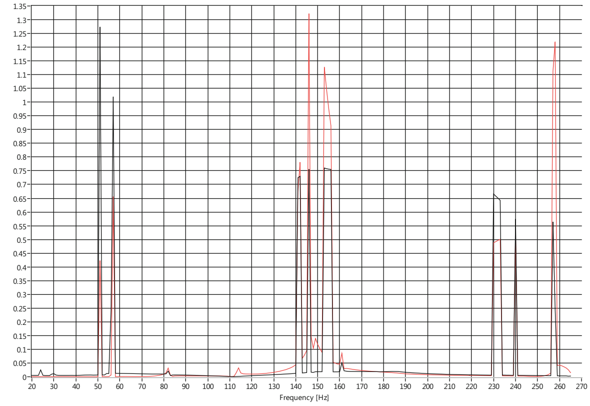 Damage-3	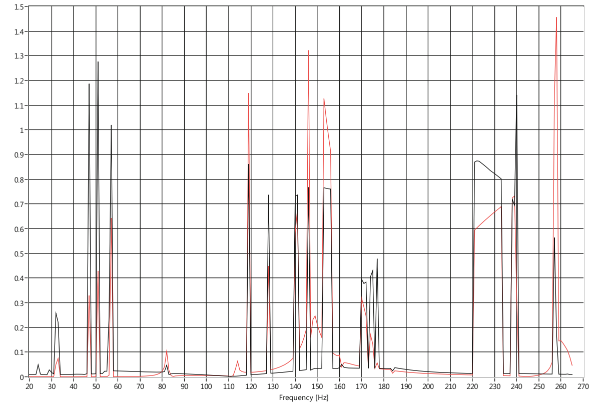 Damage-4

Table 19.4 Table of plots of RASTAR errors calculated for different damage severities, levels A1–A4

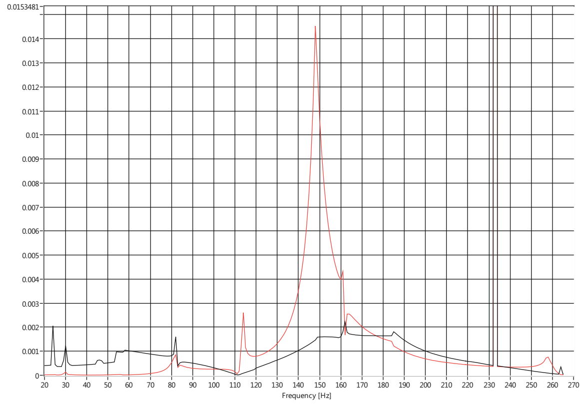 Damage-A1	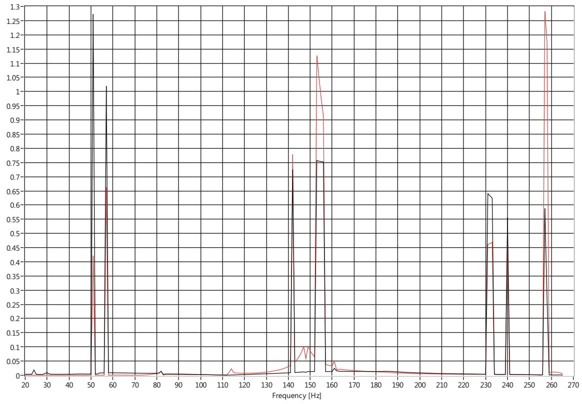 Damage-A2
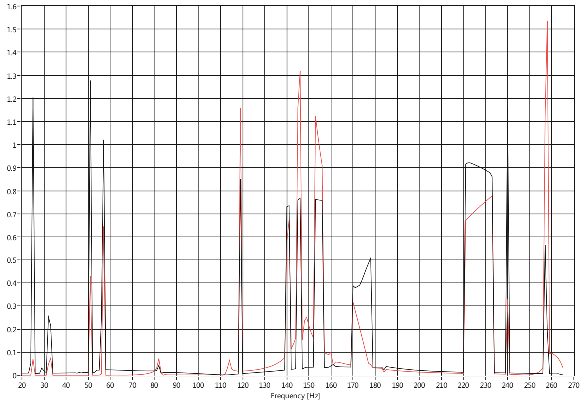 Damage-A3	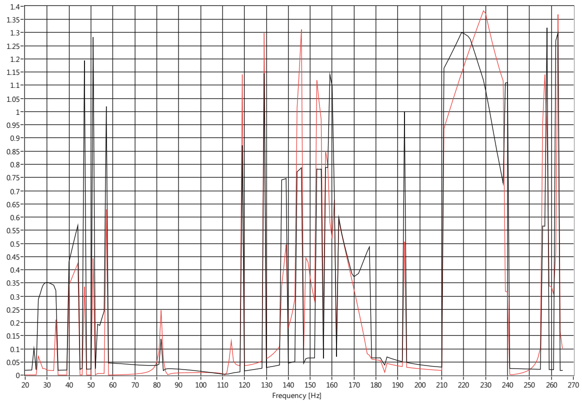 Damage-A4

The final set of plots presented in this paper are relative to analysis carried out on LDV output signal with added noise, for cases where the excitation force was low at 1 N and high at 10 N. The data reported are for the damage cases A1 and A4. Table 19.5 shows the four plots from which one can clearly notice how severe the effect of noise is on the RASTAR error. The damage case A1 for low level excitation force does not clearly reveal damage indictor peak, whereas for the higher force at 10 N, one can notice a consistent higher error level when the row-wise data are selected. It is worth mentioning that the RASTAR error for the resonance between 50 and 60 Hz is nearly null, thus indicating that mode of vibration is very insensitive to the damage location and severity A1 but very opposite behaviour for damage A4. However, when the damage severity is the highest, A4, the error plots both for low and high excitation forces show that RASTAR mean value is definitely high. Especially in the low excitation force case, the highest peaks seem to match with resonances. The noise affects more the anti-resonance regions as the RASTAR is unable to return the same error peaks identified in absence of noise in the LDV simulated signal.

19.4 Conclusions

This research work introduces an innovative technique to investigate damage by continuous scanning measurements (CSLDV). Prior researches have demonstrated that the RASTAR technique is able to calculate errors by exploiting the spectral amplitude of the sidebands measured by the CSLDV method. Those error plots indicated the frequency regions

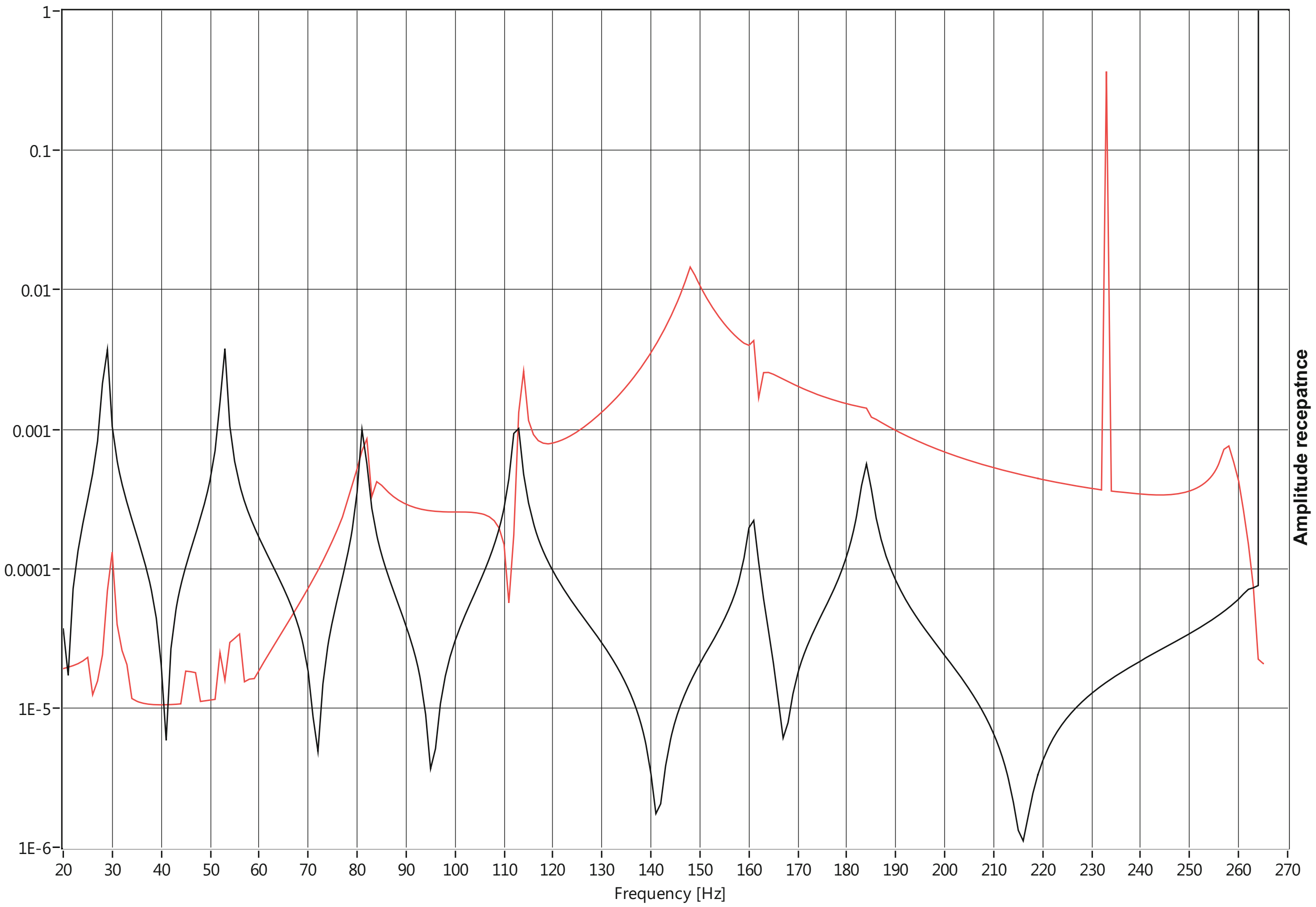

Fig. 19.4 Damage A1 rows only with FRF of pristine sample log scale, left scale RASTAR error and right scale amplitude of receptance

where the ODSs between the pristine and damage cases diverges the most. However, these calculations are done without recovering any ODS but straight from the LDV output spectral sidebands. This paper extends the investigation of RASTAR from the single to the two-dimensional scan in an attempt to show that area might be more effective than the single line scan. A numerical investigation was therefore designed to prove such goal. The results indicate that the RASTAR technique benefits of accessing data in both directions, as it showed for the damage cases level 1 and A1 where the row-wise data can be more effective than the column-wise ones. Higher damage levels, however, did not identify frequencies of interest, which will require further investigations. The RASTAR was evaluated in terms of noise, and it showed that error plots indicate better peaks when the excitation force is higher as expected, showing that a better signal-to-noise ratio leads to better error plots.

Table 19.5 Table of plots of RASTAR errors calculated for different damage severities, levels A1–A4, and added noise

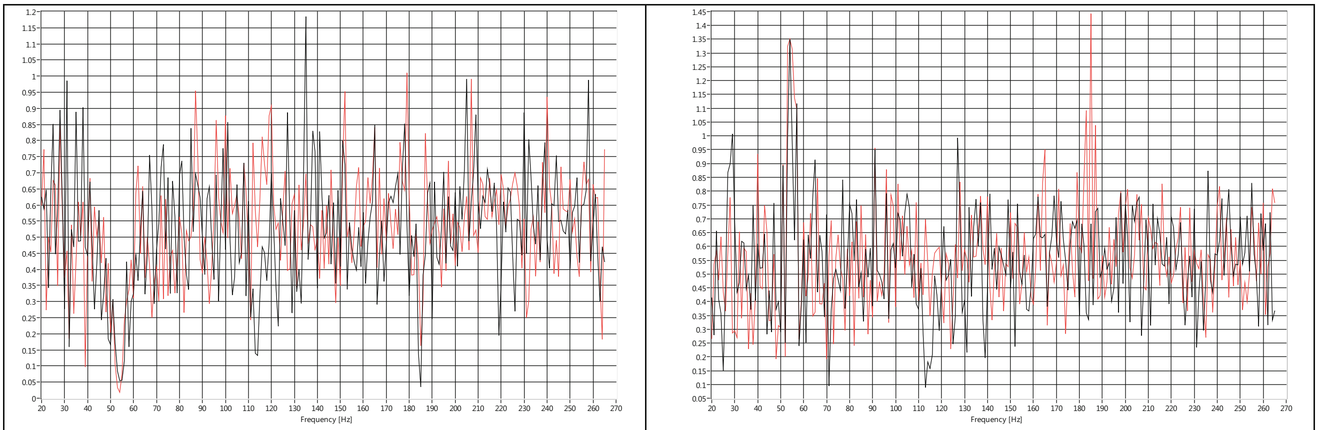

DamageA1+noise100mV and 1N force

DamageA4+noise100mV and 1N force

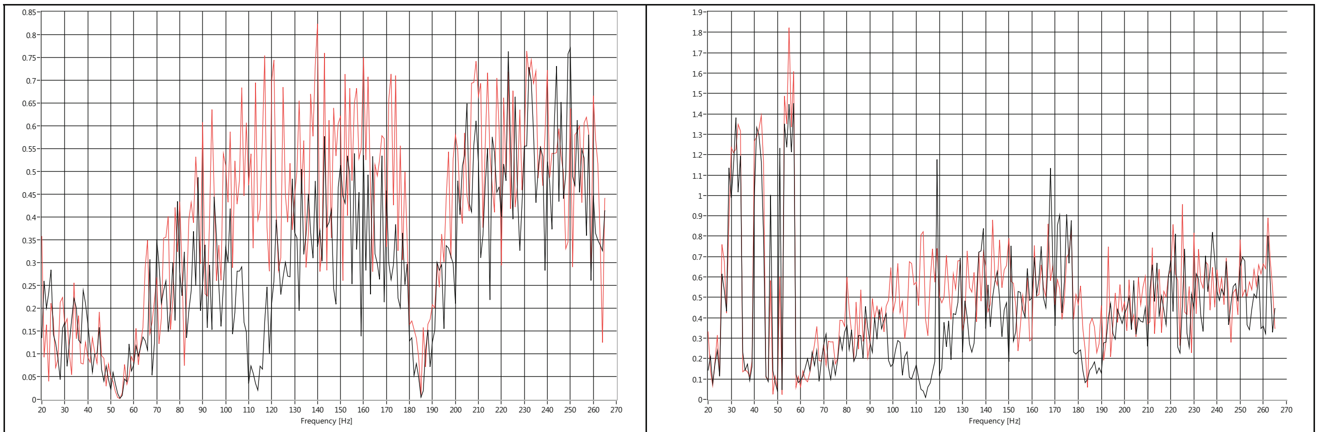

DamageA1+noise100mV and 10N force

DamageA4+noise100mV and 10N force

References

1. Chen, D., Xu, Y.F., Zhu, W.D.: Identification of damage in plates using full-field measurement with a continuously scanning laser Doppler vibrometer system. **422**, 542–567 (2018). https://doi.org/10.1016/j.jsv.2018.01.005
2. Chen, D.-M., Xu, Y.F., Zhu, W.D.: Damage identification of beams using a continuously scanning laser Doppler vibrometer system. J. Vib. Acoust. **138**, 5 (2016)
3. Chen, D.-M., Xu, Y.F., Zhu, W.D.: Non-model-based multiple damage identification of beams by a continuously scanning laser Doppler vibrometer system. Measurement. **115**, 185–196 (2018)
4. Chen, D.-M., Xu, Y.F., Zhu, W.D.: Non-model-based identification of delamination in laminated composite plates using a continuously scanning laser Doppler vibrometer system. J. Vib. Acoust. **140**, 4 (2018)
5. Xu, Y.F., Chen, D.-M., Zhu, W.D.: Modal parameter estimation using free response measured by a continuously scanning laser Doppler vibrometer system with application to structural damage identification. J. Sound Vib. **485**, 115536 (2020)
6. Xu, Y.F., Chen, D.-M., Zhu, W.D.: Damage identification of beam structures using free response shapes obtained by use of a continuously scanning laser Doppler vibrometer system. Mech. Syst. Signal Process. **92**, 226–247 (2017)
7. Chen, D.-M., Xu, Y.F., Zhu, W.D.: A comprehensive study on detection of hidden delamination damage in a composite plate using curvatures of operating deflection shapes. J. Nondestruct. Eval. **38**(2), 54 (2019)
8. Xu, Y.F., Chen, D.-M., Zhu, W.D.: Operational modal analysis using lifted continuously scanning laser Doppler vibrometer measurements and its application to baseline-free structural damage identification. J. Vib. Control. **25**(7), 1341–1364 (2019)
9. Chen, D.-M., Xu, Y.F., Zhu, W.D.: Experimental investigation of notch-type damage identification with a curvature-based method by using a continuously scanning laser doppler vibrometer system. J. Nondestruct. Eval. **36**(2), 38 (2017)
10. Di Maio, D.: Use of continuous scanning LDV for diagnostics. in *Conference Proceedings of the Society for Experimental Mechanics Series*, 2016, vol. 8, doi: https://doi.org/10.1007/978-3-319-30084-9_11
11. Bruinsma, S., Di Maio, D., Tinga, T.: Diagnostics based on continuous scanning LDV methods: numerical study. J. Phys. Conf. Ser. **1149**(1), 12012 (2018)
12. Di Maio, D., Bruinsma, S., Tinga, T.: Diagnostics based on continuous scanning LDV measurements and RASTAR analysis method. Exp. Tech., 1–18 (2020)
13. Di Maio, D.: Damage monitoring using Continuous Scanning LDV methods: numerical approach. in *OPTIMESS2015* (2015)